Imperial College London
Department of Mechanical Engineering

# Vibration Isolation With Periodic Structures

Junyi Lee

March 2016

Supervised by Daniel Balint

Submitted in part fulfilment of the requirements for the degree of
Doctor of Philosophy in Mechanical Engineering of Imperial College London
and the Diploma of Imperial College London

# Declarations

## Declaration of Originality

I, Junyi Lee, hereby declare that that this thesis is an original work conducted by myself under the supervision of Dr. Daniel Balint and Prof. John Dear in Imperial College London during the period of 1 October 2012 to 4 February 2016.

## Copyright Declaration

The copyright of this thesis rests with the author and is made available under a Creative Commons Attribution Non-Commercial No Derivatives licence. Researchers are free to copy, distribute or transmit the thesis on the condition that they attribute it, that they do not use it for commercial purposes and that they do not alter, transform or build upon it. For any reuse or redistribution, researchers must make clear to others the licence terms of this work.

# Abstract

Vibrations are undesirable and cause many problems in engineering. Among the many techniques to reduce vibrations, phononic crystals and elastic metamaterials, that have periodic variations in geometry or material properties, have the potential to attenuate vibrations over a large range of frequencies. These classes of materials attenuate vibrations via the band gap mechanism that stops elastic waves from propagating.

Additionally, periodic structures can possess high effective stiffness or strength to density ratios. This makes them ideal for lightweight structural applications. Furthermore, their periodic nature allows band gaps to be generated in them. These features can be combined to produce lightweight structural components with vibration isolation properties. Currently, very few studies of this class of materials for practical applications were made. Therefore, the goal of the work done in this thesis is to develop techniques and perform analyses to promote their implementation.

A literature review has been performed on the techniques to determine the band structures and effective properties of lattice materials. A novel method coined the wave superposition method (WSM) to measure the band structure was developed. This method allows band structures to be determined experimentally using simple equipment with a small number of measurements. The method was then validated experimentally.

A parametric study on the mechanical and dispersion properties of cubic lattice structures were conducted to assess the viability of designing a multifunctional lattice structure with excellent properties to be used as multifunctional lightweight and vibration attenuating components. Important trends relating to the geometric parameters to the performance of the lattice structures were found. Lastly, an experimental study was performed on a selected design to demonstrate the vibration attenuation characteristic of this material. The techniques and findings in this thesis, have laid the foundations for future development of periodic structures for both structural and vibration isolation applications.

# Acknowledgements

This thesis is the final product of three years of labour and its completion would not have been possible without the support from many people. Therefore, I would like to take this opportunity to express my appreciate to everyone who have supported me throughout this time.

First of all, I would like to thank my family who have been very supportive of my studies. I would also like to express my deepest gratitude to my supervisor, Dr. Daniel Balint for his guidance and constant encouragement throughout this project. I would also like to thank the Aviation Industry Corporation of China (AVIC) and the First Aircraft Institute (FAI) for funding my PhD project and the academic visitors from FAI Qifeng and Xiangying. I would also like to thank Prof. Jianguo Lin, Prof. Dear, and Dr. Liliang Wang who have offered invaluable advice during my project.

Thanks also to the technicians in the student teaching workshop, the research workshop, and the laboratories for helping me with my jobs. I would like to thank Valentina and her supervisor for providing me with the equipment and technical help for my experiments. Additionally, I would like to thank Val and Kate for dealing with all the paperwork at lightning pace and also to Mark from the ME stores.

I would also like all my friends and colleagues to know I am grateful for the time we've spent together, my life here would have been very dull without all of you. So a quick thank you to (in no particular order) Kai Lun, Yu Long, Shouhua, Joseph, Dennis, Nick, Tom, Panos, Erie, Ali, Liu Jun, Charles, Lawrence, Mani, Jasmine, Adithya, Li Nan, Jinghua, Bai Qian, Li Yong, James, Irfan, Zhou Jie, Wang Yi, and Wang Yi, Haoxiang, Pan Ran, Yiran, and many others. If I've missed you, please don't worry, you are included in "many others". In all seriousness, I would like to specially thank Yo-Lun helping me in times of need.

Last but not least, my deepest gratitude goes to my wife, Irène, who have always been there for me throughout this time.

# Contents

**Nomenclature** **xvi**

**1 Introduction** **1**
1.1 General background of vibration isolation . . . . . 1
1.2 Thesis outline . . . . . 4

**2 Periodic structures and modelling techniques** **6**
2.1 Phononic crystals and elastic metamaterials . . . . . 6
2.1.1 Background . . . . . 6
2.1.2 Phononic crystals and elastic metamaterials in vibration isolation applications . . . . . 7
2.1.3 Band structure analysis techniques . . . . . 17
2.2 Lightweight periodic lattice materials . . . . . 51
2.2.1 Introduction . . . . . 51
2.2.2 Homogenisation techniques . . . . . 52

**3 An inverse method to determine the dispersion curves of periodic structures based on wave superposition** **81**
3.1 Introduction . . . . . 81
3.2 Theory . . . . . 83
3.2.1 Superposition of elastic waves . . . . . 83
3.2.2 Single wave . . . . . 86
3.2.3 Two coupled waves . . . . . 87
3.2.4 Generalising to systems with multiple degrees of freedom or waves 91
3.2.5 Calculating the eigenvectors and predicting response of periodic structures with different numbers of unit cells . . . . . 94
3.3 Virtual experiment: demonstration and validation of the method . . . . 95
3.3.1 Structure . . . . . 96
3.3.2 Calculation of band structure using the wave superposition method 97
3.3.3 Transfer Matrix Method . . . . . 98
3.4 Results and discussion on band structure . . . . . 99
3.4.1 Response functions . . . . . 99
3.4.2 Dispersion curves . . . . . 102

3.4.3 Components of the eigenvectors . . . 107
3.4.4 Transmissibilities . . . 108
3.4.5 Effects of finiteness of the periodic structure . . . 112
3.5 Extending method to 2D and 3D structures: Potential and limitations . 115
3.5.1 Generalising equations for 2D and 3D structures . . . 116
3.5.2 Numerical example of 2D phononic crystal . . . 120
3.5.3 Results for two dimensional phononic structures . . . 122
3.6 Summary and conclusion . . . 126

**4 Measuring the band structures of periodic beams using the wave superposition method 128**
4.1 Introduction . . . 128
4.2 Experimental setup . . . 129
4.2.1 Beam properties . . . 129
4.2.2 Experimental procedure . . . 131
4.3 Results and discussions . . . 132
4.3.1 Frequency response function . . . 132
4.3.2 Dispersion curves . . . 133
4.3.3 Frequency response predictions . . . 138
4.4 Conclusion . . . 141

**5 A parametric study on the mechanical and dispersion properties of cubic lattice structures 144**
5.1 Introduction . . . 144
5.2 Selected Topologies And Analysis Procedures . . . 145
5.2.1 Selected topologies and resonators . . . 145
5.2.2 Analysis of mechanical properties . . . 150
5.2.3 Dispersion analysis . . . 151
5.3 Stiffness and strength properties of lattice materials . . . 154
5.3.1 Simple cubic lattice . . . 154
5.3.2 Body-centred cubic (BCC) lattice . . . 156
5.3.3 Face-centred cubic (FCC) . . . 157
5.3.4 Regular Octet . . . 159
5.3.5 General discussion of the static properties of the lattice structures 160
5.4 Band gaps in optimal lattice structure . . . 161
5.4.1 Optimal lattice for stiffness constrained panel structure (simple cubic lattice) . . . 163
5.4.2 Optimal lattice for strength constrained panel structure (octet lattice) . . . 166

5.4.3 Optimal lattice for stiffness constrained beam structure (FCC lattice) . . . 168
5.4.4 Optimal lattice for strength constrained beam structure (FCC lattice) . . . 172
5.4.5 General discussion on band gap behaviour of lattice with oscillators 174
5.5 Conclusion . . . 175

**6 Design and testing of a three dimensional periodic lattice structure with elastic band gap 177**
6.1 Introduction . . . 177
6.2 Design of periodic lattice structure . . . 178
6.2.1 Selected topology and geometry . . . 178
6.2.2 Finite element and band structure calculations . . . 178
6.3 Experimental set up . . . 183
6.4 Results and discussion . . . 185
6.5 Summary and conclusion . . . 187

**7 Conclusions and future work 189**
7.1 Summary and conclusion . . . 189
7.2 Suggestions for future work . . . 193

**A Appendices 215**
A.1 Solution for two waves with one degree of freedom . . . 215
A.2 Example of eigenvector component calculations using force measurements 216
A.3 Publications . . . 217

# List of Tables


2.1 Properties and geometry of the material in the unit cell. . . . . 23
2.2 Properties and geometry of the materials in steel/epoxy phononic crystal. [100] . . . . . 30
2.3 Properties and geometry of the materials in FCC composite material. [141] 45
2.4 Ratios to maximise for beam and plate configurations [158]. . . . . 52
2.5 Definition of sets used in analysis. . . . . 72

3.1 Number of equations for a system with a single wave; where $n$ is the number of nodes. . . . . 86
3.2 Number of equations required for a periodic system with two waves; where $d$ is the number of degrees of freedom and $n$ is the number of nodes required. 90
3.3 Number of equations required for a periodic system with arbitrary number of degrees of freedom; where $d$ is the number of degrees of freedom and w is the number of waves. . . . . 92
3.4 Properties and geometry of the beams in the unit cell. . . . . 97
3.5 Boundary conditions of beams in the virtual experiment. . . . . 97
3.6 Material properties for 2D phononic crystal . . . . . 122
3.7 Summary of cases studied for 2D phononic crystals . . . . . 122

4.1 Properties and geometry of the beams in the unit cell. . . . . 129

5.1 Ratios to maximise for achieving minimum mass while fulfilling the stiffness and strength requirements for beam and plate configurations [158]. 148
5.2 Dimensions of the selected topologies shown in Figure 5.1 that were investigated in this study. . . . . 149
5.3 Mechanical properties of ABS [217]. . . . . 149
5.4 Optimal normalised parameters for cubic topologies studied (Panel Configuration). . . . . 161
5.5 Optimal normalised parameters for cubic topologies studied (Beam Configuration). . . . . 162

# List of Figures


1.1 Anti-vibration mount. . . . . 2
1.2 Transmissibility of a single degree of freedom linear viscoelastic isolator. 2
1.3 Damping treatments (a) Free layer damping (b) Constrained layer damping. 2

2.1 (a) Phononic crystal beam (b) Band structure and transmissibility curve of the beam in bending. Reprinted from [43] with kind permission from AIP Publishing. . . . . 8
2.2 A vibration isolation structure. Reprinted from [43] with kind permission from AIP Publishing. . . . . 8
2.3 (a) Unit cell of lattice structure (a grid made from beams with different thickness) (b) Full lattice structure, the red dot denotes excitation point while the blue dot denotes the point where the transmissibility was measured. Reprinted from [44] with kind permission from SPIE. . . . . 9
2.4 (a) Band structure of first unit cell (b) Transmissibility curve. The grey region denotes the calculated band gap while the red lines denote the band gaps based on the measured response. Reprinted from [44] with kind permission from SPIE. . . . . 10
2.5 (a) Measured response outside of band gap, 2500 Hz. (b) Measured response within band gap, 3000 Hz. Reprinted from [44] with kind permission from SPIE. . . . . 10
2.6 Conventional phononic crystal and elastic metamaterial designs for vibration isolation (a) Beam with periodic variations [50] (b) Beam with local resonator [46] (c) Lattice structure [23] (d) Lattice structure with local resonator [36] (e) Periodic material [59] (f) Periodic material with local resonator [54]. Reprinted from various sources with kind permission from ASME, Elsevier and Sage Publishing . . . . . 11
2.7 (a) Undeformed lattice (b) Deformed lattice (c) Band structure of deformed lattice (d). Reprinted from [60] with kind permission from APS Publishing. . . . . 12
2.8 Elastic metamaterial made from periodic shunted piezoelectric patch arrays. (a) Full array (b) Unit cell front view (c) Unit cell side view. Reprinted from [61] with kind permission from Elsevier. . . . . 13

2.9 Periodic rod vibration isolator. Reprinted from [68] with kind permission from Hindawi. . . . . 14
2.10 Active elastic metamaterial by [69] (a) CAD model (b) Physical system. Reprinted from [69] with kind permission from IOP publishing. . . . . 14
2.11 Elastic metamaterial design (a) from [70] (b) from [71]. Reprinted with kind permission from APS and Elsevier. . . . . 15
2.12 FRF of inertia amplification elastic metamaterial. Reprinted from [71] with kind permission from Elsevier. . . . . 16
2.13 (a) Nacreous composite material design (b) Band structure of nacreous composite material. Reprinted from [74] with kind permission from Elsevier. . . . . 16
2.14 Design of vibration isolator using elastic band gap by [75]. Reprinted with kind permission from Elsevier. . . . . 17
2.15 Typical band structure of a 2D phononic crystal (a) Common representation (b) Complete surface. Grey regions denote the band gaps. . . . . 18
2.16 (a) Direct lattice (b) Reciprocal lattice. . . . . 18
2.17 Typical band structure of a 1D phononic crystal (a) Real part (b) Imaginary part. Grey regions denote the band gaps. . . . . 21
2.18 Unit cell of phononic crystal. . . . . 22
2.19 Distribution of density and Young's modulus (a) Density with 7 waves (b) Density with 21 waves (c) Young's modulus with 7 waves (d) Young's modulus with 21 waves. . . . . 23
2.20 Band structure of phononic crystal. . . . . 27
2.21 Band structure of a phononic crystal. Curves represent bands calculated using EPWE while markers represent band calculated using PWE. Reprinted from [100] with kind permission from APS Publishing. . . . . 29
2.22 Unit cell of phononic crystal studied. . . . . 29
2.23 Band structure of the 2D phononic crystal in Figure 2.18 (a) Comparison of mesh sizes (b) Comparison between PWE and FE. Grey regions denote the band gaps. . . . . 32
2.24 (a) Arranged nodes for the phononic crystals. . . . . 34
2.25 Band structure comparison between finite element and transfer matrix method. . . . . 35
2.26 Example of discretised grid. ©IEEE. Reprinted from [131] with kind permission from IEEE. . . . . 37
2.27 (a) 2D phononic crystal made from epoxy and steel cylinder (b) Calculated band structure [131] . . . . . 39

2.28 (a) Tested periodic beam (b) Measured frequency response, the legend shows the magnitude of the velocity measured in the transverse direction (c) Warped frequency response (d) Frequency response after removing reflection. Reprinted from [138] with kind permission from IOP Publishing. 40
2.29 Band structure of tested periodic piezopatches. The red lines are the analytical predictions and the coloured contours show the amplitudes calculated using the 2D Fourier transform with the values stated in the legend. Reprinted from [138] with kind permission from IOP Publishing. 41
2.30 (a) Band structure of an FCC Au/Si composite (b) First Brillouin Zone of FCC structure. Reprinted from [141] with kind permission from APS. 45
2.31 (a) Periodic rod-joint structure (b) unit cell of the rod-joint structure (c) rod element [47] . . . . . 46
2.32 Mass spring element for the joint. Reprinted from [141] with kind permission from Elsevier. . . . . 48
2.33 Schematic of combining spectral matrices. Reprinted from [141] with kind permission from Elsevier. . . . . 49
2.34 Frequency response function of the final node of the system with 10 unit cells. Reprinted from [141] with kind permission from Elsevier. . . . . 49
2.35 Ashby charts (a) Stiffness versus density (b) Strength versus density. Reprinted from [159] with kind permission from the Royal Society Publishing. . . . . 53
2.36 Unit cells of common lattice structures (a) Chiral (b) 2D Kagomé (c) 3D Kagomé [149] (d) Honeycomb [23] (e) Simple cubic (f) BCC (g) FCC (h) Octet truss [29]. Reprinted from various sources with kind permission from Elsevier. . . . . 54
2.37 (a) Unit cell model (b) Deformed unit cell. Reprinted from [161] with kind permission from Cambridge University Press. . . . . 55
2.38 Truss structure showing joint equilibrium. Reprinted from [166] with kind permission from Elsevier. . . . . 56
2.39 (a) Kagomé lattice (b) Primitive unit cell (c) Alternative unit cell. Reprinted from [166] with kind permission from Elsevier. . . . . 57
2.40 Kagomé lattice bases: (a) direct translation vectors (b) joint vectors (c) bar vectors (d) illustration of lattice position vectors. Reprinted from [166] with kind permission from Elsevier. . . . . 58
2.41 Modelling approach [29]. Reprinted with kind permission from Elsevier. 61
2.42 (a) Example BCC lattice (b) Unit cell. Reprinted from [29] with kind permission from Elsevier. . . . . 63
2.43 RVE analysis concept. Reprinted from [160] with kind permission from Elsevier. . . . . 67

2.44 Periodic boundary conditions on the opposite edges of the RVE. Reprinted from [160] with kind permission from Elsevier. . . . . 69
2.45 Illustration of beam element. Reprinted from [179] with kind permission from Otto-von-Guericke-University Magdeburg. . . . . 72
2.46 A material with microstructure under load. Reprinted from [184] with kind permission from Elsevier. . . . . 80

3.1 (a) A structure with infinitely repeating unit cells (b) Superposition of two infinite structures. . . . . 84
3.2 (a) Unit cell of structure (b) Five unit cell structures used in the numerical example. . . . . 96
3.3 Frequency response of bi-material beam at various locations (a) Node 0 (b) Node 1 (c) Node 2 (d) Node 3 (e) Node 4 (f) Node 5 (Free-Fixed is 0 and not plotted). The band gaps calculated from the TM method are highlighted in grey. . . . . 100
3.4 Wave profiles for infinite structures at different frequencies and waves where the values are normalised, each unit cell is 2 metres (a) Point A - 9 Hz (b) Point B - 9 Hz (c) Point C - 855 Hz (d) Point D - 855 Hz (e) Point E - 625 Hz (f) Point F - 1063 Hz . . . . . 104
3.5 Dispersion curves for the undamped bi-material beam in the transverse direction (a) Real part (b) Imaginary part. Solid lines (–) denote results using transfer matrix method while square markers (□) denote results using the wave superposition method. The band gaps are highlighted in grey. . . . . 105
3.6 Dispersion curves for the undamped bi-material beam in the longitudinal direction (a) Real part (b) Imaginary part. Solid lines (–) denote results using transfer matrix method while square markers (□) denote results using the wave superposition method. The band gaps are highlighted in grey. . . . . 105
3.7 Dispersion curves for the damped bi-material beam in the transverse direction (a) Real part (b) Imaginary part. Solid lines (–) denote results using transfer matrix method while square markers (□) denote results using the wave superposition method. Band gaps of the undamped case are highlighted in grey. . . . . 106
3.8 Dispersion curves for the damped bi-material beam in the longitudinal direction (a) Real part (b) Imaginary part. Solid lines (–) denote results using transfer matrix method while square markers (□) denote results using the wave superposition method. Band gaps of the undamped case are highlighted in grey. . . . . 106

3.9 Magnitudes of eigenvectors components (a) $v_\phi$ Undamped (b) $v_\phi$ Damped (c) $v_F$ Undamped (d) $v_F$ Damped (e) $v_M$ Undamped (f) $v_M$ Damped (g) $v_T$ Undamped (h) $v_T$ Damped. Band gaps for the undamped cases are highlighted in grey and each colour corresponds to the values for a given wave. . . . . 109
3.10 Transmissibility for the bi-material beam structure for the free-free case (a) Transverse direction (b) Longitudinal direction. Legend: (A) analytical solution; (W) Wave superposition method; N represents the number of unit cells. The band gaps are highlighted in grey. . . . . 110
3.11 Decomposition of elastic waves for free-free axial vibration (a) 835 Hz, N=2 (b) 824 Hz, N=2 (c) 835 Hz, N=5 (d) 835 Hz, N=10 (e) 835 Hz, forward waves (f) 835 Hz, reverse waves. Each unit cell is 2 m long. N represents the number of unit cells. . . . . 113
3.12 Periodic bar with massless spring at the end. . . . . 114
3.13 Transmissibility vs number of unit cells (a) Axial vibration with different values of spring stiffness at 835 Hz (b) Transverse vibration at free-free condition at different frequencies . . . . . 115
3.14 (a) Real portion of band structure of 2D phononic crystal shown in Section 3.5.3 (b) Contour plot of real portion of band structure of 2D phononic crystal shown in Section 3.5.3, the numbers on the contour denote the frequency. . . . . 118
3.15 (a) A two dimensional phononic crystal in with periodic boundary conditions in the y direction (b) Single row of two dimensional phononic crystal (c) Single row of two dimensional phononic crystal with free boundary conditions. . . . . 119
3.16 (a) Dimensions of a unit cell of the 2D phononic crystal studied (b) Mesh of a unit cell used in the finite element analysis. . . . . 121
3.17 Band structure of 2D phononic crystal $k_y = 0$ (a) 10 Unit cells (b) 20 Unit cells. Real and Com in the legend denotes real waves and complex waves respectively, full band gaps are highlighted by grey regions. . . . . 124
3.18 Band structure of 2D phononic crystal (a) $k_x = 0$, 20 Unit cells (b) $k_y = 0$, 20 Unit cells free boundaries. Real and Com in the legend denotes real waves and complex waves respectively, full band gaps are highlighted by grey regions. . . . . 125

4.1 Illustration of beam dimensions. . . . . 130
4.2 Dispersion curve for Beam 1 (a) Real part (b) Imaginary part. . . . . 130
4.3 Dispersion curve for Beam 2 (a) Real part (b) Imaginary part. . . . . 131
4.4 Experimental setup. (a) Schematic (b) Photo of experiment. . . . . 131
4.5 Placement of accelerometer and stinger on beam. . . . . 132

4.6 Frequency response function of polycarbonate and aluminium bi-material beam (Beam 1). (a) Point 2 (b) Point 3 (c) Point 4 (d) Point 5 (e) Point 6. Analytical band gaps using the transfer matrix method are highlighted in grey. . . . . 134
4.7 Frequency response function of aluminium beam with varying geometry (Beam 2). (a) Point 2 (b) Point 3 (c) Point 4 (d) Point 5 (e) Point 6 (f) Point 7 (g) Point 8 (h) Point 9. Analytical band gaps predicted using the transfer matrix method are highlighted in grey. . . . . 135
4.8 Dispersion curve for Beam 1. (a) Wave A (real part) (b) Wave A (imaginary part) (c) Wave B (real part) (d) Wave B (imaginary part). Analytical band gaps are highlighted in grey. . . . . 136
4.9 Dispersion curve for Beam 2 (combined). (a) Wave A (real part) (b) Wave A (imaginary part) (c) Wave B (real part) (d) Wave B (imaginary part). Analytical band gaps are highlighted in grey. . . . . 139
4.10 Dispersion curve for Beam 2 from points 2-7. (a) Wave A (real part) (b) Wave A (imaginary part) (c) Wave B (real part) (d) Wave B (imaginary part). Analytical band gaps are highlighted in grey. . . . . 140
4.11 Frequency response function predictions of aluminium beam with different widths. (a) Point 8 (b) Point 9. Analytical band gaps are highlighted in grey. . . . . 142

5.1 Selected topologies and the added resonators (a) Simple Cubic (b) BCC (c) FCC (d) Octet truss. . . . . 146
5.2 Beam and panel being loaded. . . . . 147
5.3 First Brillouin Zone of (a) Simple Cubic Lattice (b) BCC Lattice (c) FCC and Octet Lattice . . . . . 153
5.4 Static properties of the simple cubic structure with different radii for panel configurations (a) Normalised stiffness parameter (b) Normalised strength parameter. . . . . 154
5.5 Static properties of the simple cubic structure with different radii for beam configurations (a) Normalised stiffness parameter (b) Normalised strength parameter. . . . . 155
5.6 Static properties of the BCC lattice structure with different radii for panel configurations (a) Normalised stiffness parameter (b) Normalised strength parameter. . . . . 156
5.7 Static properties of the BCC lattice structure with different radii for beam configurations (a) Normalised stiffness parameter (b) Normalised strength parameter. . . . . 157
5.8 Normalised strength parameter versus $\frac{r_2}{r_1}$ for the BCC lattice. . . . . 158

5.9 Static properties of the FCC structure with different radii for panel configurations (a) Normalised stiffness parameter (b) Normalised strength parameter. . . . . 158
5.10 Static properties of the FCC with different radii for beam configurations (a) Normalised stiffness parameter (b) Normalised strength parameter. . 159
5.11 Normalised strength parameter versus $\frac{r_2}{r_1}$ for FCC lattice. . . . . 159
5.12 Static properties of the regular octet structure with different radii for panel configurations (a) Normalised stiffness parameter (b) Normalised strength parameter. . . . . 160
5.13 Static properties of the regular octet structure with different radii for beam configurations (a) Normalised stiffness parameter (b) Normalised strength parameter. . . . . 161
5.14 Band structure comparing different mesh density at (a) 0 to 3000 Hz (b) 480 to 530 Hz for the simple cubic lattice with a resonator. . . . . 163
5.15 Band structures of simple cubic lattice studied with and without local resonators (a) 0 to 1000 Hz (b) 400 to 800 Hz. . . . . 164
5.16 (a) Upper and lower bounds of the first band gaps (b) width of first band gap for different resonator configurations for simple cubic structure. . . 164
5.17 Density increment with the addition of resonators for simple cubic lattice. 165
5.18 (a) Overlap of density increment and band gap width contour plot, red contour denote density increment while the other contour denotes band gap width (b) Band gap width per unit density increment contour plot for simple cubic structures. . . . . 166
5.19 (a) Upper and lower bounds of the first band gaps (b) width of first band gap for different resonator configurations for regular octet lattice. . . . . 167
5.20 Density increment with the addition of resonators for regular lattice. . . 167
5.21 (a) Overlap of density increment and band gap width contour plot, red contour denote density increment while the other contour denotes band gap width (b) Band gap width per unit density increment contour plot for the regular octet lattice. . . . . 168
5.22 Band structures of FCC studied with and without local resonators (a) 0 to 2000 Hz (b) 400 to 600 Hz. . . . . 169
5.23 (a) Upper and lower bounds of the first band gaps (b) width of first band gap for different resonator configurations for the FCC structure. . . . . 169
5.24 Density increment with the addition of resonators for FCC lattice. . . . 170
5.25 Overlap of density increment and band gap width contour plot, red contour denote density increment while the other contour denotes band gap width (a) Original gap (b) Resonator gap for the FCC lattice. . . . . 171

5.26 Band gap width per unit density increment contour plot (a) Original gap (b) Resonator gap for the FCC lattice. . . . . 172
5.27 (a) Upper and lower bounds of the first band gaps (b) width of first band gap for different resonator configurations for the FCC lattice. . . . . 173
5.28 Density increment with the addition of resonators for the FCC lattice. . 173
5.29 (a) Overlap of density increment and band gap width contour plot, red contour denote density increment while the other contour denotes band gap width (b) Band gap width per unit density increment contour plot for the FCC lattice. . . . . 174

6.1 Finite structure that is printed and boundary conditions in finite element analysis. . . . . 179
6.2 Surface showing values that gives the local resonators a natural frequency of 500 Hz. . . . . 180
6.3 Unit cell used to calculate band structure where the nodes denoted by prime have Bloch wave periodic conditions. . . . . 180
6.4 Band structure of structure (a) with local resonators (b) without local resonators. . . . . 181
6.5 Frequency response functions from finite element calculations (a) with local resonators (b) without local resonators. . . . . 182
6.6 Bloch modes at the points shown in Figure 6.4 (a) Point A (b) Point B (c) Point C (d) Point D. . . . . 184
6.7 Experimental setup. . . . . 184
6.8 Frequency response functions from experiments (a) with local resonators (b) without local resonators, band gaps are predicted based on the finite element analysis. . . . . 186

# Nomenclature

### Acronyms

| | |
|---|---|
| ABS | Acrylonitrile butadiene styrene |
| BCC | Body centre cubic |
| EPWE | Extended plane wave expansion |
| FCC | Face centre cubic |
| FDTD | Finite difference time domain |
| FE | Finite element |
| KKR | Korringa, Kohn, Rostoker |
| LR | Local resonance |
| MST | Multiple scattering theory |
| PWE | Plane wave expansion |
| SE | Spectral element |
| SLA | Stereolithography |
| TM | Transfer matrix |
| WSM | Wave superposition method |

### Latin Symbols

| | |
|---|---|
| $A$ | Area |
| $\mathscr{B}(\bar{b})$ | Set of beams numbered $\bar{b}$ |
| $\mathbf{C}$ | Elasticity tensor |
| $c$ | Speed of sound |
| $\mathbf{D}$ | Transfer matrix |

| | |
|---|---|
| $d$ | Displacement |
| $\bar{\mathscr{E}}(\bar{n})$ | Set of nodes at the sides of beams |
| $\mathscr{E}(\bar{n})$ | Set of nodes at the ends of beams |
| $E$ | Young's modulus |
| $\mathbf{F}$ | Force vector |
| $F$ | Force |
| $f$ | Force |
| $\mathbf{G}$ | Reciprocal lattice vector |
| $G$ | Shear modulus |
| $h$ | Field variable |
| $h_l$ | Hankel function of the first kind |
| $\mathbf{I}$ | Second moment of area |
| $j_l$ | Spherical Bessel function |
| $\mathbf{K}$ | Stiffness matrix |
| $\tilde{\mathbf{K}}$ | Reduced stiffness matrix |
| $k$ | Wave vector |
| $\mathbf{L}$ | Elasticity tensor |
| $L$ | Length |
| $l$ | Length |
| $\mathbf{M}$ | Mass matrix |
| $\tilde{\mathbf{M}}$ | Reduced mass matrix |
| $\mathscr{N}(\bar{n})$ | Set of nodes numbered $\bar{n}$ |
| $\mathscr{O}(\bar{n})$ | Set of nodes at the origins of beams |
| $\mathbf{Q}$ | Transformation matrix |
| $r$ | Radius |
| $\mathbf{T}$ | Transfer matrix |

| | |
|---|---|
| $t$ | Time or thickness (depending on context) |
| $\ddot{u}$ | Acceleration |
| $\dot{u}$ | Velocity |
| $\mathbf{U}$ | Displacement matrix |
| $U$ | Displacement |
| $u$ | Displacement |
| $V$ | Volume |
| $\mathbf{W}$ | Transverse displacement matrix |
| $\mathbf{w}$ | Transverse displacement matrix |
| $W$ | Transverse displacement |
| $w$ | Transverse displacement |
| $x$ | Position |

**Greek Symbols**

| | |
|---|---|
| $\boldsymbol{\alpha}$ | Simplification matrix for complicated matrices |
| $\nu$ | Poisson's ratio |
| $\rho$ | Density |
| $\sigma$ | Stress |
| $\boldsymbol{\sigma}$ | Stress tensor |
| $\phi$ | Shear rotation angle |
| $\omega$ | Radial frequency |
| $\mathit{\Gamma}$ | Matrix containing wave vector and reciprocal lattice vector |
| $\delta$ | Dirac delta |
| $\boldsymbol{\varepsilon}$ | Strain matrix |
| $\varepsilon$ | Strain |
| $\eta$ | Mechanical loss coefficient |
| $\kappa$ | Timoshenko shear coefficient |

| | |
|---|---|
| $\lambda$ | Eigenvalue or Lame constant (depending on context) |
| $\mu$ | Lame constant (depending on context) |

# 1 Introduction

## 1.1 General background of vibration isolation

Vibrations are undesirable in the field of engineering as they cause reduced component life, user discomfort, damage in components, and many other negative effects [1]. Unfortunately, vibrations are generated through various means, such as imbalances in rotating machinery, seismic activities, turbulent flow conditions, etc., some of which cannot be easily eliminated. Several strategies have been devised in order to either damp or isolate unwanted vibrations in structures. The most common strategies include anti-vibration mounts (also known as vibration isolators), damping treatments, and active control. Each of these strategies have their benefits and disadvantages.

Anti-vibration mounts, as seen in Figure 1.1, can be used to reduce vibrations, where the vibrations are isolated from the source to prevent it from being transmitted to the structure. In general, anti-vibration mounts isolate vibrations in two ways, firstly by reducing the natural frequency of the system to attenuate high frequency vibrations, and secondly damping to reduce the vibration amplitude around the natural frequency. However, this type of anti-vibration mount will result in conflicting requirements because low stiffness is required to reduce vibrations and this will cause large static displacements, which are undesirable for load bearing structures [2, 3]. Additionally, the increase in damping to reduce the vibration amplitude at the natural frequency will result in an increase in amplitude at higher frequencies, as illustrated by the transmissibility of a single degree of freedom system shown in Figure 1.2. Transmissibility is defined as the ratio of the response at a given point to the response of a reference point, usually the input. Although other designs of vibration isolators have been devised to overcome these issues, they add complexity to the system. For example many non-linear vibration isolators, such as the X-pendulum isolation table, anti-spring devices, and other systems listed in [4] have either complicated designs or possible instabilities, while shape memory isolators discussed in [5–7] require large amplitudes to be effective.

On the other hand, damping treatments are performed by bonding a high damping material, such as a viscoelastic polymer, to the structure, as seen in Figure 1.3. This is a common method to increase damping in the aerospace and automotive industry. The damping material reduces vibrations by dissipating mechanical energy into heat due to the hysteresis during cyclic loading when the damping material is deformed

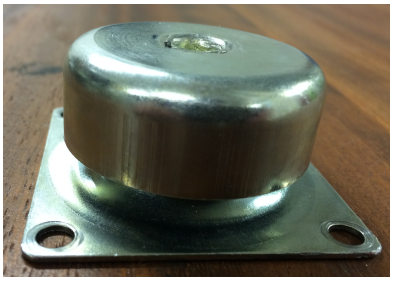


Figure 1.1: Anti-vibration mount.

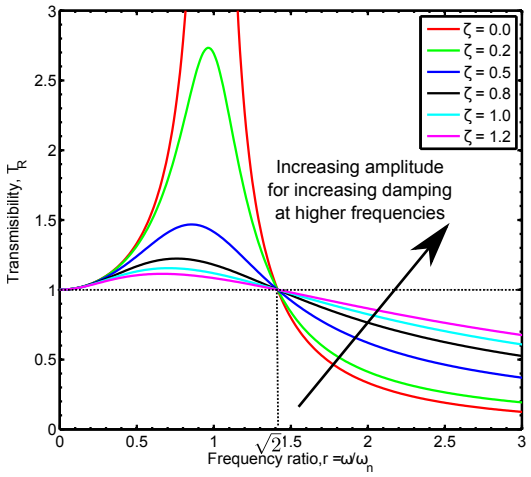



Figure 1.2: Transmissibility of a single degree of freedom linear viscoelastic isolator.

with the base material [8, 9]. The advantages of this technique are that the amount of damping is limited only by weight and size restrictions and it is independent of the mode shape of the vibrations at the region where it is applied [8, 9]. However, it has several disadvantages. Firstly, it is most effective when the treatment is applied to regions where bending moments are high and it is sensitive to temperature, in which damping is highest near the glass transition temperature of the material [8, 9].

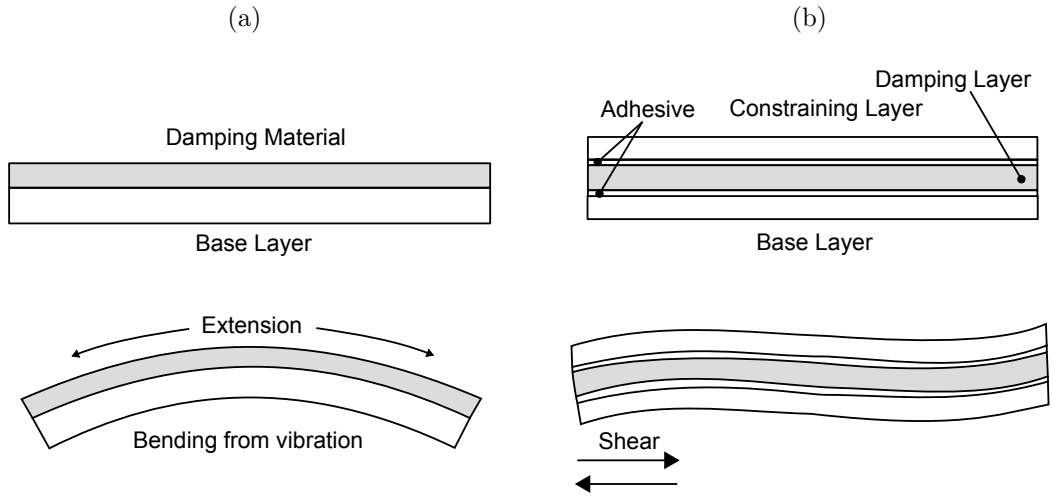



Figure 1.3: Damping treatments (a) Free layer damping (b) Constrained layer damping.

Another potential solution for controlling vibrations in structural components is active control that uses actuators mounted on structural components to minimise the vibration [10]. The actuators are usually controlled by a control system with inputs from sensors, such as microphones or piezoelectric patches. The key advantage of active

acoustic control is that the control system can be designed to damp vibrations over a large range of frequencies and a lightweight system can be designed by using piezoelectric actuators, which is why they are considered to be implemented in the aerospace industry [10]. However, the addition of actuators, sensors, and a sufficiently sophisticated control system can significantly increase the costs of the system [10], while piezoelectric components are brittle and their actuation strength is limited to low frequencies [10]. Furthermore, since all active control schemes work based on creating a field to cancel the source of the vibration [11], active controls require the incoming field to be accurately represented in the control scheme. This results in many active control schemes being sensitive to the incoming field changes.

Ideally, the solution for vibration control of a load bearing structure should have the following criteria.

- high static stiffness.
- high attenuation of vibrations over a large range of frequencies.
- low density.
- high strength.
- capable of operating in a variety of environments.
- simple design.

Although the conventional vibration control solutions described previously are capable of achieving several of these criteria, they do possess their respective drawbacks. An overlooked method for vibration isolation is the use of elastic band gaps. Elastic band gaps are regions of frequencies in a periodic medium in which elastic waves or vibrations cannot propagate. Therefore, a periodic medium with a large band gap can attenuate vibrations over a large range of frequencies. It is important to point out that the energy from the vibration is being reflected back to the source via the Bragg scattering or local resonance mechanism [12] and dissipation of the energy is not necessary. Additionally, the band gap mechanism does not involve low stiffness or material damping and does not require active control. Hence, there is a potential to create a strong, stiff, and lightweight structure that can also attenuate vibrations with the material.

Although elastic band gaps have been known to exist since the 1940s [13] and the wave propagation characteristics have been widely studied [14], elastic band gaps have not been exploited for vibration isolation purposes. This is mainly because the known mechanism to produce elastic band gaps in the past is Bragg scattering, which is produced by changes in geometry or material properties within a periodic structure. Since Bragg scattering can only occur when the lattice constant is larger or equal to the

wave length [15], the minimum frequency range to create the band gap is limited by the size and speed of sound in the periodic medium. Unfortunately, this limitation results in the periodic structure required to produce band gaps around common low operating frequencies to be too large for practical implementation [16]. This issue with Bragg scattering also applies to acoustic waves and electromagnetic waves. For acoustic waves, the use of Helmholtz resonators, that were invented in the 19th century [17], were used to overcome this issue, for example in [18]. Similarly split ring resonators, introduced in 1999 [19] were used in photonic metamaterials to overcome this limitation. The corresponding solution for elastic waves was found very recently in 2000, when Liu. et. al. [20] introduced the local resonance mechanism to produce band gaps for elastic waves with wave lengths larger than the lattice structures. This new mechanism allows periodic structures with local resonators to be designed to have low frequency elastic band gaps that cannot be achieved previously. This enables the design of new lightweight structural components with excellent vibration isolation characteristics as many lightweight structural components, such as honeycomb cores, periodic lattices, and stiffened panels, are periodic and several studies [21–26] have demonstrated that these structures can produce band gaps by either the local resonance or Bragg scattering mechanism.

Although, a large number of studies that have been conducted on the analysis of the static mechanical (stiffness and strength) [27–34] and dispersion properties of lattice materials [21–26], only a few studies [2, 3, 35, 36] have investigated these two types of properties in tandem or design a stiff structural material with desirable dynamic characteristics. Therefore, this project aims to develop methods to facilitate the analysis of the band structures of such structures and to devise strategies to the design of periodic structures. Although periodicity is not required if the local resonators are used to produce the band gaps, this work will focus on periodic lattice structures, with desirable dynamic properties while possessing other qualities, like high stiffness, for practical implementations. This is an important feature of such materials as highlighted in [37]. The parametric study of the effects of the geometry on the static mechanical properties and dispersion properties will serve as a guide for future design of these multi-functional components.

## 1.2 Thesis outline

This thesis is organised as follows. The next chapter, Chapter 2, is a literature review on the topics relating to the project, which are the application of phononic crystals and elastic metamaterials for vibration isolation purposes and the static mechanical analysis for periodic structures. This is in order to identify the techniques available for the analysis of these structures. Chapter 3 will then describe the development of a novel

technique based on the superposition of elastic waves to measure the band structure of periodic structures with equipment that are familiar to engineers. In Chapter 4, the experiments conducted to validate the method and experimental issues related to the method are described.

Since periodic lattice structures have been identified as a candidate to create lightweight materials with vibration isolation properties, the remaining chapters will be dedicated to the study of these systems. Chapter 5 details a parametric study on both the mechanical and dispersion characteristics of common periodic lattice structures to be used as sandwich core materials. A prototype of a selected lattice structure based on the results of the parametric study has been manufactured and tested experimentally as a proof of concept. The experiment is described in Chapter 6. Lastly, Chapter 7 will summarise potential areas for future development of the design of lightweight structure components with vibration isolation characteristics before concluding the thesis.

# 2 Periodic structures and modelling techniques

## 2.1 Phononic crystals and elastic metamaterials

### 2.1.1 Background

A *periodic medium* is a material or structure that has spatial periodicity in constituent material properties, geometry, and/or boundary conditions [37]. Early studies of acoustics and vibrations within periodic structures dates back to the $17^{\text{th}}$ century when Isaac Newton investigated sound propagation in air and in the $19^{\text{th}}$ century Rayleigh studied the speed of sound of sound in continuous media [14, 37, 38]. Further studies in wave propagation of periodic structures were made in modern times, for example wave propagation properties in crystal lattices [13], periodic beams [39–41], stiffened panels [14], and other structures.

Elastic band gaps, which are frequency ranges where elastic waves cannot propagate, can be produced when there are periodic variations in the speed of sound within a material or component [12]. Elastic band gaps are the mechanical analogue to the band gaps of electromagnetic waves in electrical insulators. However, unlike electromagnetic waves that only have two independent polarisations, an elastic wave has a total of three polarisations, which are two shear waves and a longitudinal wave [12]. This complicates the analysis of such materials. Wherever there is a variation in the speed of sound within a unit cell, the incident wave is reflected and transfers part of its energy to the reflected wave [12]. These waves then interfere with each other and if the interference is constructive, the entirety of the energy of the incident wave will be reflected and the wave cannot propagate [12]. Conversely, during destructive interference, the waves are not reflected entirely and the wave propagates. This mechanism is known as *Bragg scattering* and periodic materials that produce band gaps via this mechanism are now commonly referred to as *phononic crystals* or *phononic structures* [37]. The path differences, defined as the differences between the distances travelled by waves originating at the same location, between the interfering waves must be equal to multiples of their wave lengths, $\Lambda$, for constructive interference to occur. Since the wave length is determined by the lattice constant, $L$, or the length of the unit cell, constructive interference can only occur when the lattice constant is comparable to or smaller than $\Lambda$ [12]. Further-

more, the frequency of the band gaps are inversely proportional to the lattice constants resulting in large structures being needed to produce band gaps at low frequencies. This limitation hinders the use of phononic crystals for practical applications as large scale structures, approximately the size of outdoor sculptures [16, 42], are needed to produce band gaps in the audible frequency range.

In 2000, Liu. et. al. [20] proposed a sonic crystal with locally resonant components, which is able to produce sub-wavelength band gaps that can overcome this limitation. This mechanism has been coined as *local resonance*, and the basic concept was inspired by the strong scattering of light by gases with atoms smaller than the light's wavelength that occurs when the light frequency coincides with the difference between two electronic energy levels within the atoms in the Lorentzian formulation of atom-light interaction [16]. The local resonance mechanism has led to further development in the field of phononics. Periodic structures that utilises this mechanism are known as *acoustic* or *elastic metamaterials*. Additionally, with the local resonance mechanism, periodic structures can now be designed with sizes and with band gaps at frequencies that are suitable for practical and engineering applications.

### 2.1.2 Phononic crystals and elastic metamaterials in vibration isolation applications

The presence of band gaps, which prevents elastic waves and hence vibrations from being transmitted, makes phononic crystals and elastic metamaterials ideal for vibration isolation and wave filtering purposes. Since the band gap mechanism does not rely on large material damping or low stiffness, this class of material has the potential to be used as a load bearing component. Additionally, if no active components are used, a passive broadband vibration isolator can be designed. Despite their potential benefits, there were no studies in using phononic crystals and acoustic metamaterials for vibration isolation applications until the mid-2000s.

Among the earliest studies for vibration isolation using phononic crystals and elastic metamaterials is the study conducted by Wen et. al. [43], and Jeong and Ruzzene [44] that were published in 2005. In [43], Wen et. al. presented the concept of using a periodic beam made from aluminium and lucite, as seen in Figure 2.1 (a), for vibration isolation. In their study, they calculated the band structure of the periodic beam using the plane wave expansion method (PWE) and the response of a finite beam using the finite element method (FEM). Based on their analysis shown in Figure 2.1 (b), the predicted transmissibility at the band gaps are low, which demonstrates that the band gaps are capable of isolating vibrations. Additionally, they have also conducted an experiment to measure the transmissibility of the beam and the experimental transmissibility are also low at the band gap, although there are discrepancies between the predicted and measured values. They then made further improvements to their structure and in-

troduced a vibration isolation structure made from their beams, as shown in Figure 2.2, where the shoring is placed at the ends or the middle of the lucite beams in alternating layers in order to minimise the wave being transmitted from the bottom of the structure to the top of it.

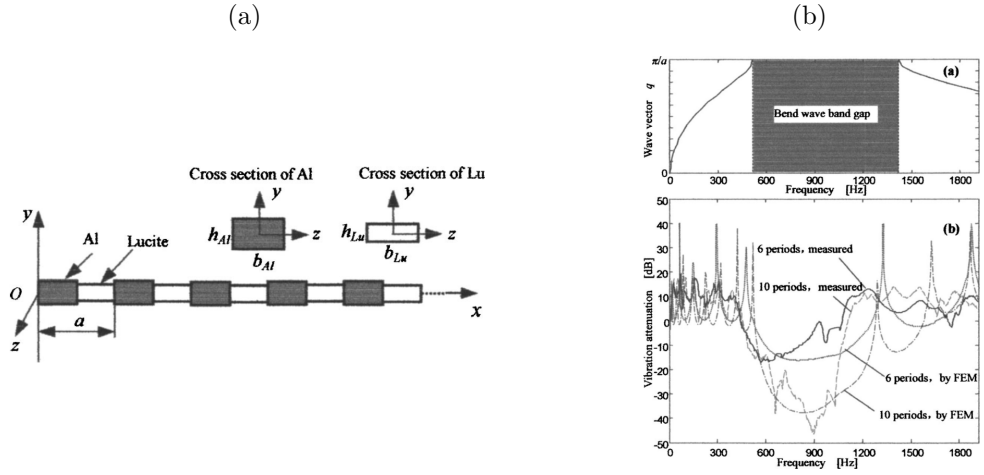



Figure 2.1: (a) Phononic crystal beam (b) Band structure and transmissibility curve of the beam in bending. Reprinted from [43] with kind permission from AIP Publishing.

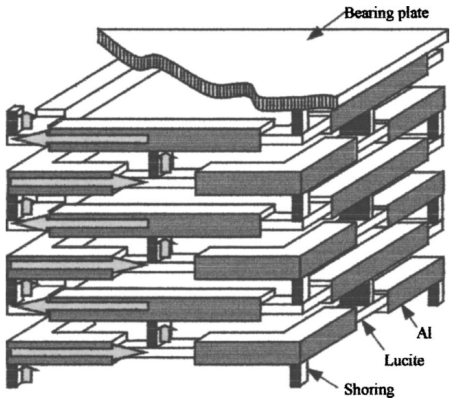



Figure 2.2: A vibration isolation structure. Reprinted from [43] with kind permission from AIP Publishing.

Similarly, Jeong and Ruzzene [44] have considered a two dimensional (2D) lattice structure made from aluminium beams with different thickness and width, as shown in Figure 2.3, to be a suitable candidate for a passive vibration isolator. In their study, they calculated the dispersion curve within the first Brillouin zone, which is the primitive cell in reciprocal space, of the unit cell of the lattice structure to determine the band gap, as seen in Figure 2.4 (a). They then manufactured the 2D lattice structure by machining an aluminium plate and used a scanning laser vibrometer to measure the

response of the entire lattice structure. Similar to the observations by Wen et. al. [43], the transmissibility within the band gap is low, as seen in Figure 2.4 (b). Furthermore, the vibration amplitude of the entire lattice structure outside the band gap as shown in Figure 2.5 (a) was found to be large across the entire system. On the other hand, the response of the lattice structure decays away from the excitation point as shown in Figure 2.5 (b). These results demonstrate that the band gaps are capable of broadband attenuation.

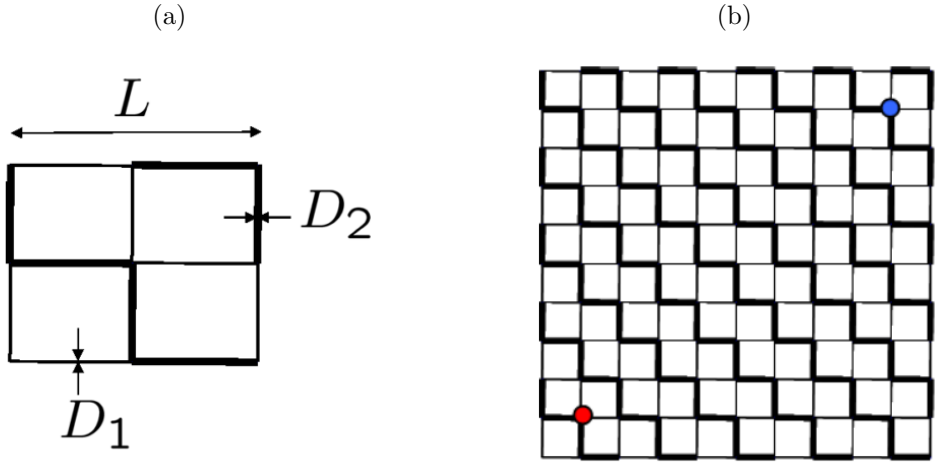



Figure 2.3: (a) Unit cell of lattice structure (a grid made from beams with different thickness) (b) Full lattice structure, the red dot denotes excitation point while the blue dot denotes the point where the transmissibility was measured. Reprinted from [44] with kind permission from SPIE.

Since then, a large amount of studies have been performed on phononic crystals and elastic metamaterials for vibration isolation applications. The most common types of periodic structures used for vibration isolation purposes are lumped masses systems [45], periodic beam or bar structures [46–50], lattice structures [23, 25, 36, 51, 52], and materials with inclusions or holes [53–59]. Some of these designs have been manufactured and tested, for example in [50, 58]. The designs introduced in these studies are considered to be conventional in the literature, in which the periodic systems are designed to have band gaps at the frequencies of interest. This is done by either designing the systems to have periodic variations in density, stiffness, and geometry or by introducing local resonators, as seen in Figure 2.6.

In general, many studies on conventional designs like the ones shown in Figure 2.6, focuses on the design of the local resonators or structure and optimisation of the design parameters to obtain the widest band gap at the desired frequencies. The basic mechanisms for the band gap creation are still Bragg scattering and local resonance. However, in recent years, several new designs with additional features for vibration isolation using band gaps have been proposed.

(a) (b)

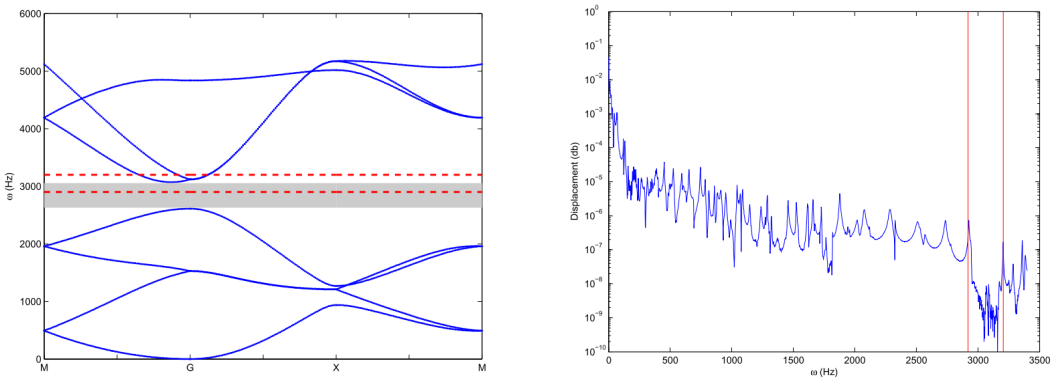



Figure 2.4: (a) Band structure of first unit cell (b) Transmissibility curve. The grey region denotes the calculated band gap while the red lines denote the band gaps based on the measured response. Reprinted from [44] with kind permission from SPIE.

(a) (b)

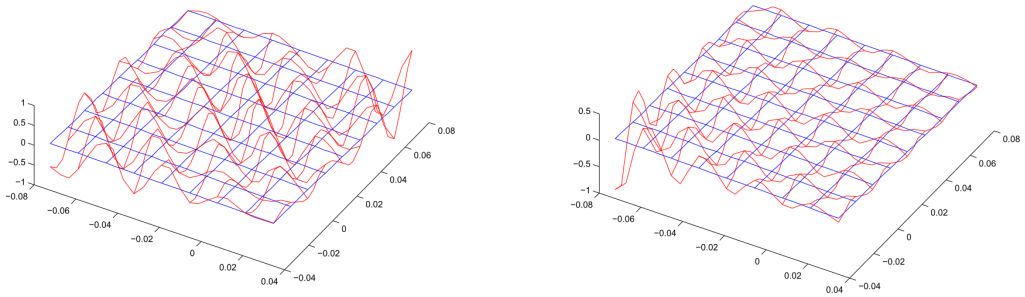


Figure 2.5: (a) Measured response outside of band gap, 2500 Hz. (b) Measured response within band gap, 3000 Hz. Reprinted from [44] with kind permission from SPIE.

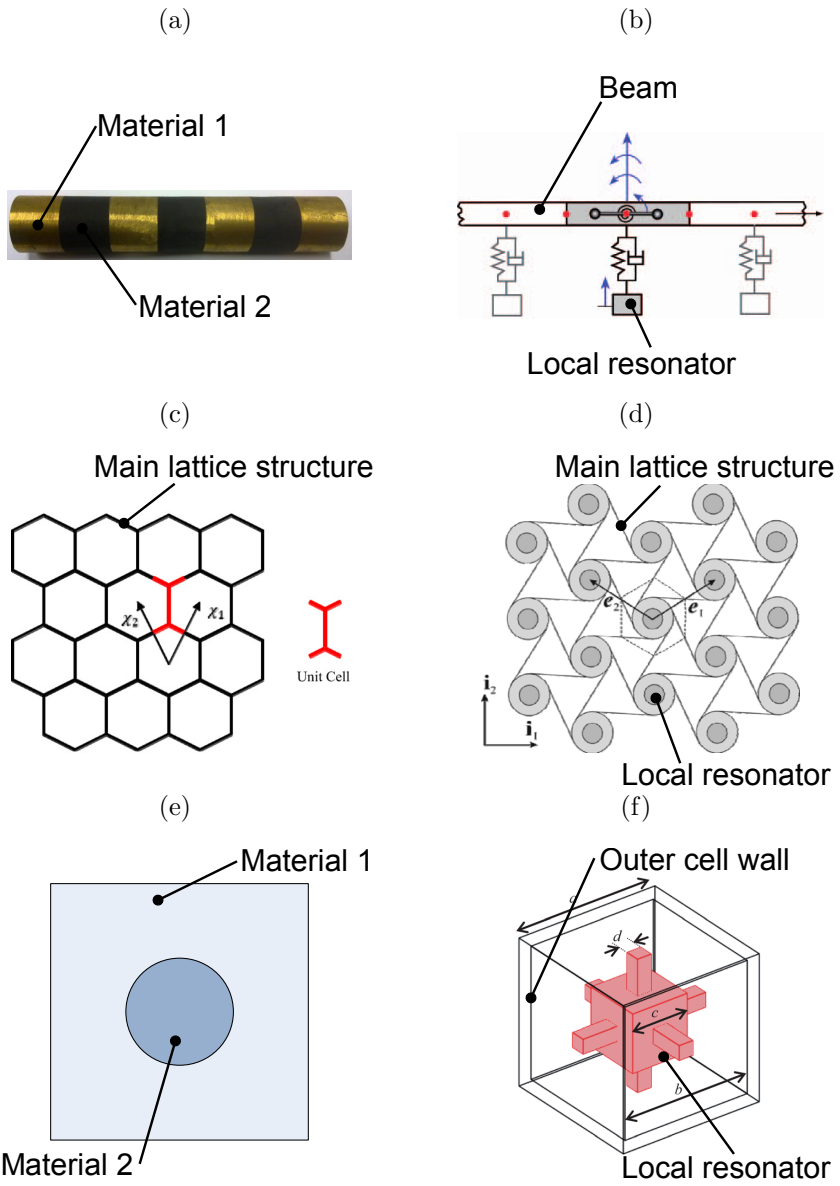



Figure 2.6: Conventional phononic crystal and elastic metamaterial designs for vibration isolation (a) Beam with periodic variations [50] (b) Beam with local resonator [46] (c) Lattice structure [23] (d) Lattice structure with local resonator [36] (e) Periodic material [59] (f) Periodic material with local resonator [54]. Reprinted from various sources with kind permission from ASME, Elsevier and Sage Publishing

One interesting feature that have been in incorporated into the periodic structure for vibration isolation is the tunability of the band gaps. This means that the periodic structure have been designed to vary its band gap, allowing it to be able to attenuate vibrations at different frequencies based on the excitation conditions. The tunability of the band gaps in periodic structures can be achieved in a few ways. Firstly, the band gaps can be tuned by varying the geometry of the periodic structure. Since the band gaps of periodic structures depend on the geometry and material properties of the structure, the band gap can be tuned to the desired frequencies by deforming the periodic structure as proposed in [60], which not only changes the geometry of the structure but also the material properties if a non-linear material is used. This concept can be illustrated in Figure 2.7, where the band structure changes from Figure 2.7 (c) to (d), when the structure is deformed from Figure 2.7 (a) to (b).

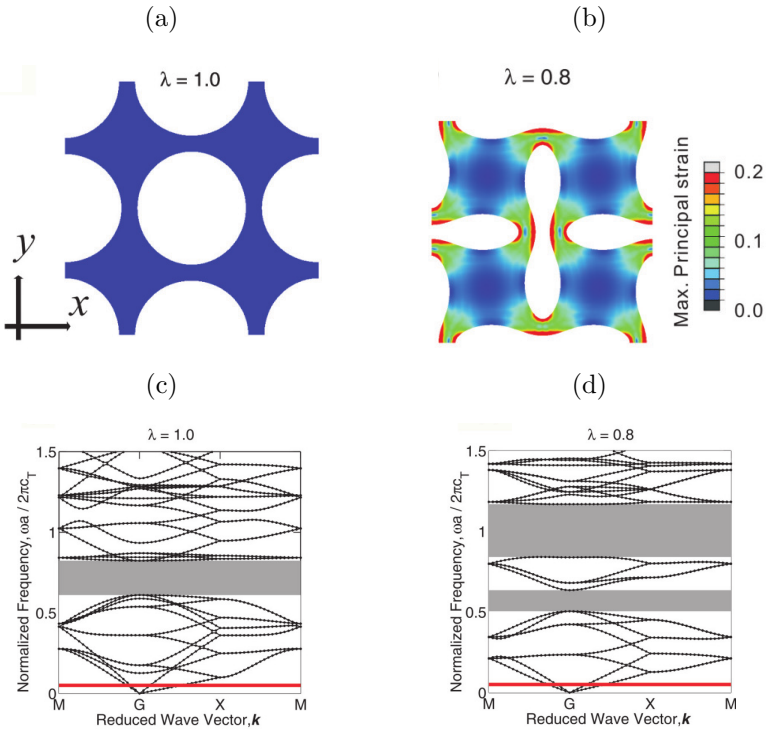



Figure 2.7: (a) Undeformed lattice (b) Deformed lattice (c) Band structure of deformed lattice (d). Reprinted from [60] with kind permission from APS Publishing.

Alternatively, tunability can also be introduced via materials that respond to electrical and/or magnetic excitation, such as piezoelectric [61–63], magnetoelectroelastic [64, 65], or magnetorheological materials [66]. Among these techniques, shunted piezoelectric patch arrays on beams or plates, in which periodic piezoelectric patches are connected to a passive shunt shown in Figure 2.8, are most common. For the shunted piezoelectric patch arrays, resistive-inductive (RL) shunts [61], which emulate dynamic absorbers or resonators, are usually used to tune the band gap by setting the system to have natural

frequencies that corresponded to the desired band gap location. However, other shunts, such as the negative capacitance shunt [67], have also been demonstrated to provide broadband frequency attenuation.

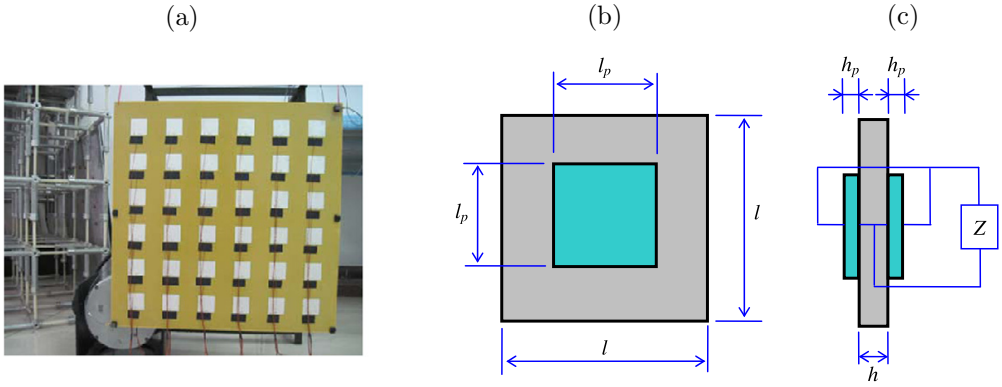



Figure 2.8: Elastic metamaterial made from periodic shunted piezoelectric patch arrays. (a) Full array (b) Unit cell front view (c) Unit cell side view. Reprinted from [61] with kind permission from Elsevier.

There are significantly less studies on using magnetoelectroelastic and magnetorheological materials to achieve tunability. In Bou Matar et. al. [65], a phononic crystal was designed with magnetoelectroelastic materials embedded in an epoxy matrix and placed within an external magnetic field. In their design, large variations in the elastic properties of the magnetoelectroelastic material and hence band structure, can be achieved by using the external magnetic field via giant magnetostriction and spin-reorientation phase transition effects. Conversely, Bayat and Gordaninejad [66], created a phononic crystal using magnetorheological elastomers, which are subjected to an external magnetic field. For the phononic crystal in [66], the external magnetic field causes changes to both the geometry of the phononic crystal and the properties of the magnetorheological elastomers, which in turn changes the band structure. According to their study, the higher the applied magnetic induction, the wider the band gaps but the band gaps shifts to higher frequencies [66].

Apart from passively tuning the band gaps, active control systems have also been proposed to improve the vibration isolation performance of periodic systems. In [68], a periodic one dimensional structure made from aluminium rods with actuators in between them have been proposed and tested, as seen in Figure 2.9. The control system in [68] uses a phase shifter to create a feedback signal to the actuators that causes destructive interference of waves. Their active system managed to attenuate the transmission of vibration effectively over a large range of frequencies of 150-4000 Hz using control voltages lower than 5 V.

Similarly, active control was used in conjunction with the band gap phenomenon to improve the vibration attenuation of elastic metamaterials in [69]. The metamaterial

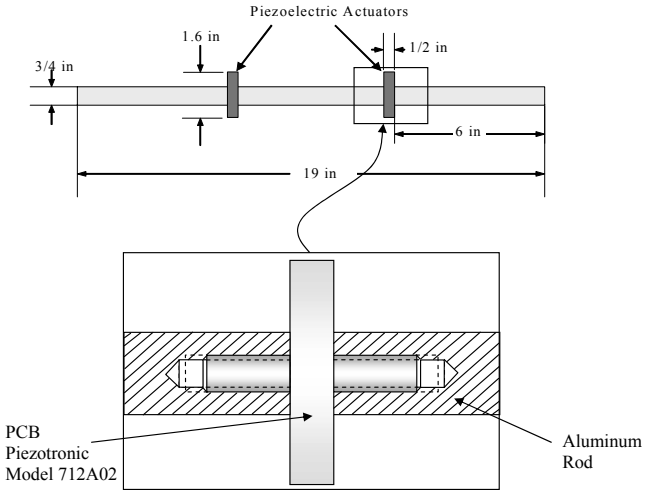



Figure 2.9: Periodic rod vibration isolator. Reprinted from [68] with kind permission from Hindawi.

is made from titanium discs connected together via coil springs as the transmission medium, while a resonator mass is connected between each transmission layer using leaf springs. The design is shown in Figure 2.10 and voice coil type reactive actuators are installed in the empty compartments in the resonator masses, so that the control forces can be applied to the masses. The control system used in [69] is an adaptive feedforward algorithm called FxLMS. Based on their experimental results, the active systems can produce excellent isolation performance of up to 40 dB over a broad frequency range, with the largest attenuation occurring in the passive band gaps. These active systems show the potential for further development in for phononic crystals and elastic metamaterials.

(a) (b)

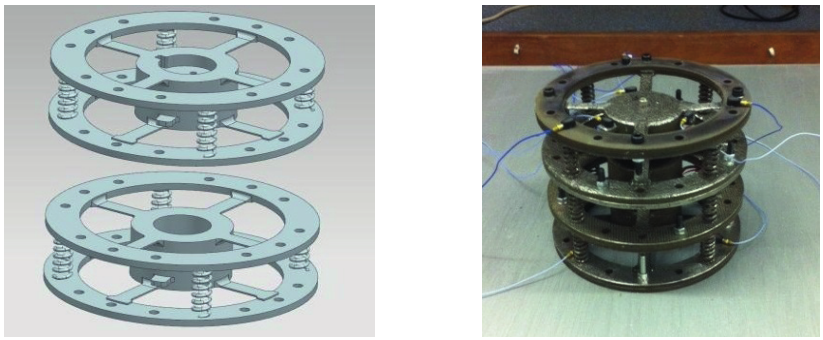


Figure 2.10: Active elastic metamaterial by [69] (a) CAD model (b) Physical system. Reprinted from [69] with kind permission from IOP publishing.

Apart from active systems, the inertia amplification effect introduced by Yilmaz et.

al. [70–72] can be used to create deep (or high attenuation) low frequency band gaps and is considered to be an alternative method to produce elastic band gaps. The inertia amplification effect increases the effective inertia or mass of the wave propagation within a medium by using systems, such as levers, to amplify the motions of small masses that increases the effective inertia and produce low frequency band gaps [70, 71]. The inertia amplification offers a solution to alleviate the problem of having large structures required to generate low frequency band gaps using the Bragg scattering. It also resolves the problem of having narrow band gaps produced using the local resonance method [71]. Several elastic metamaterials using the inertia amplification effect, as shown in Figure 2.11, have been proposed. Experiments have been carried out and these systems have been shown to produce low frequency, wide and deep band gaps, for example in Figure 2.12 where the band gaps have low frequencies from around 300 to 600 Hz

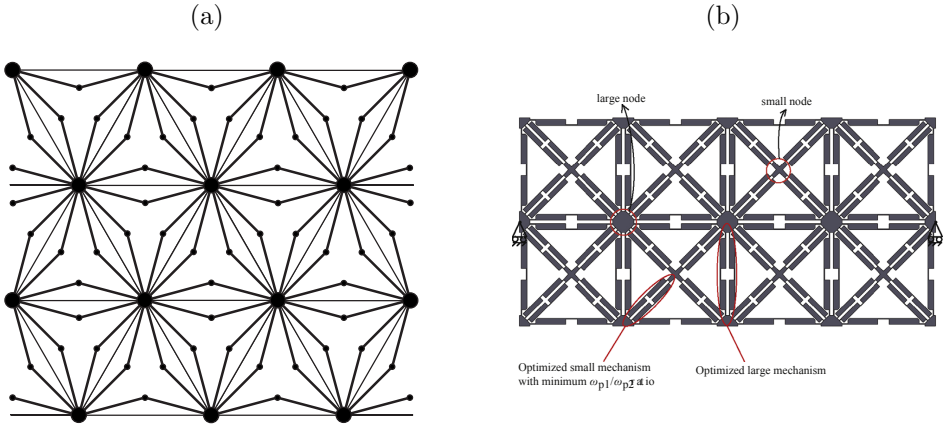



Figure 2.11: Elastic metamaterial design (a) from [70] (b) from [71]. Reprinted with kind permission from APS and Elsevier.

Furthermore, several more designs have been introduced very recently to make use of band gaps for vibration isolation. One notable new design is the nacreous composite material [73, 74], inspired by natural occurring nacreous materials, seen in seashells. The nacreous composite material, as seen in Figure 2.13 (a), can not only be designed to have elastic band gaps but can also possess other desirable properties such as excellent mechanical properties and resistance to impulsive loading [74]. As studied by Yin et. al. in [73, 74], the nacreous composite materials can be designed to have low frequency band gaps that are fairly wide, as seen in Figure 2.13, where the band gap spans from approximately 100 to 450 Hz for a nacreous composite material made from aluminium and silicone rubber.

Lastly, other simpler designs of systems using elastic band gaps specifically for vibration isolation, such as the curve beams with plates shown in Figure 2.14, have also been proposed recently. The studies conducted for elastic metamaterials and phononic crystals specifically for vibration isolation in recent years, instead of just wave guid-

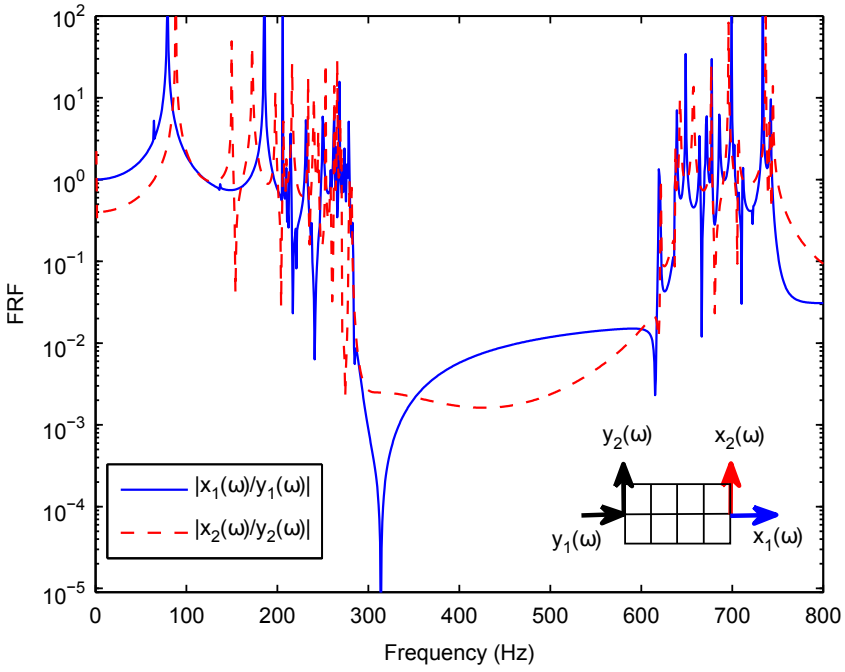



Figure 2.12: FRF of inertia amplification elastic metamaterial. Reprinted from [71] with kind permission from Elsevier.

(a) (b)

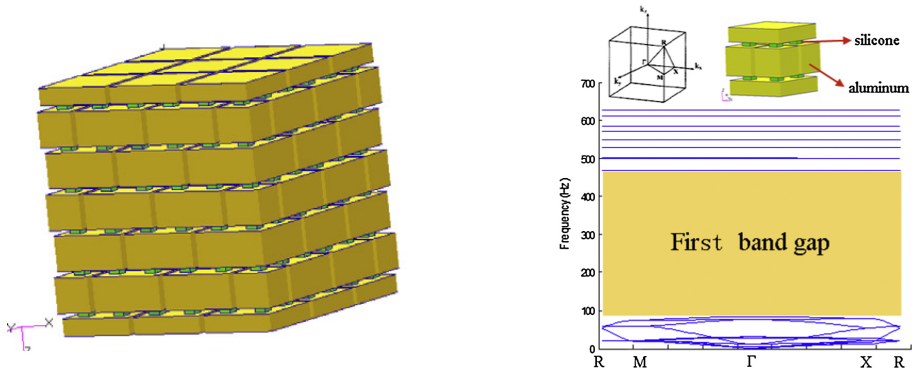



Figure 2.13: (a) Nacreous composite material design (b) Band structure of nacreous composite material. Reprinted from [74] with kind permission from Elsevier.

ing or acoustic cloaking applications, suggest that engineers have started to consider this class of materials as potential solutions for vibration transmission problems. Additionally, with the large amount of development in the field as discussed previously, periodic structures making use of the elastic band gaps for vibration isolation may soon be implemented in practical situations. However, most of the methods developed to analyse these structures, as discussed in the next section, are for theoretical studies and it is imperative to develop analysis methods for these structures and for experimental studies using equipment that are familiar to engineers.

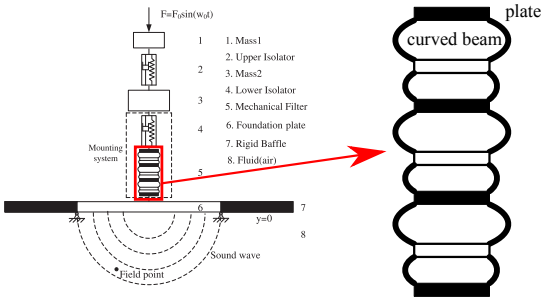



Figure 2.14: Design of vibration isolator using elastic band gap by [75]. Reprinted with kind permission from Elsevier.

### 2.1.3 Band structure analysis techniques

Almost all applications of phononic crystals and elastic metamaterials involve the analysis of the location and width of the band gaps [76]. The accurate prediction of the band gaps is essential in vibration isolation applications with this class of materials. In most studies, the band gaps were determined from the band structure, also known as the dispersion curves, of the periodic structure, for example in Figure 2.16. Prior to discussing the techniques to determine the band structure, several important concepts and assumptions, especially relating to wave propagation in periodic structures, should be introduced here.

In a majority of studies relating to phononic crystals and elastic metamaterials, the material is assumed to be made from an infinite array of discrete points that are arranged in a way where it will appear to be the same regardless of the points in which the array is viewed from. This type of array is known as a *Bravais Lattice* and a two dimensional Bravais lattice is shown in Figure 2.16 (a). The Bravais lattice can be also be defined as a set of points with position vectors $\vec{R}$ in the following form

$$\vec{R} = l\vec{a}_1 + m\vec{a}_2 + n\vec{a}_3 \tag{2.1}$$

where $\vec{a}_1$, $\vec{a}_2$, $\vec{a}_3$ are the *primitive vectors*, while $l$, $m$, and $n$ are integers.

The *primitive vectors* can be any three vectors from one point to another point of

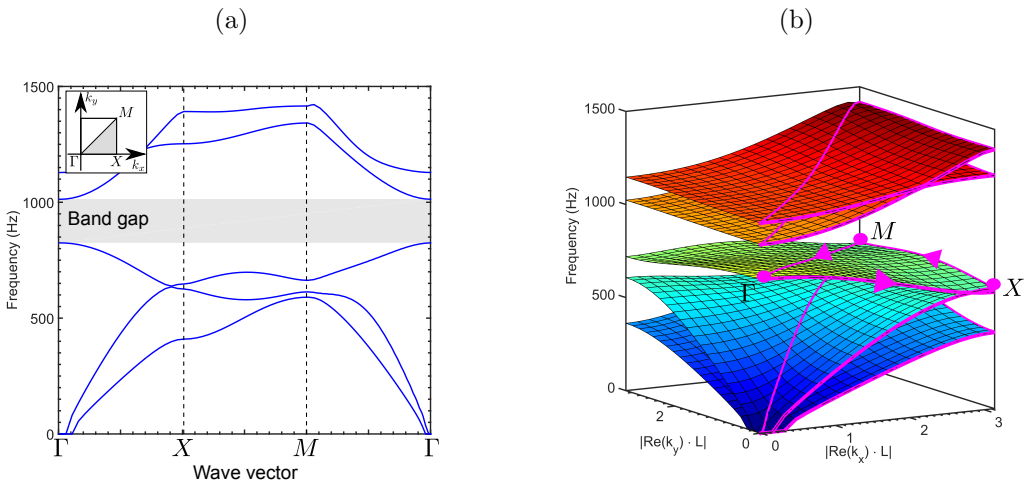



Figure 2.15: Typical band structure of a 2D phononic crystal (a) Common representation (b) Complete surface. Grey regions denote the band gaps.

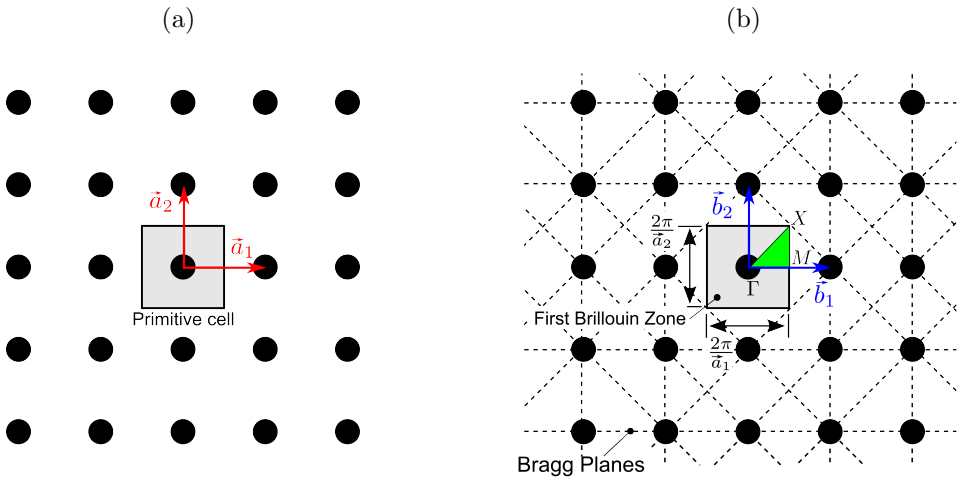



Figure 2.16: (a) Direct lattice (b) Reciprocal lattice.

the lattice provided that all three vectors are not in the same plane. The symmetry of any crystal can be described by a Bravais lattice [77] and a *basis*, which are made from identical units attached to every point of the underlying Bravais lattice. Due to the periodic nature of the Bravais lattice, the phononic crystal or elastic metamaterial can be studied using only the *primitive cell*, which is the volume of space that contains only one lattice point and will not overlap itself or leave voids when translated through all the vectors of a Bravais lattice to fill the entire lattice. An example of the primitive cell is shown in Figure 2.16 (a).

The *reciprocal lattice* is a useful tool in the study of wave propagation and diffraction in periodic media. It can be used to simplify the study the behaviour of the periodic functions in a Bravais lattice [78]. A reciprocal lattice is a lattice with a set of all wave vectors, $\vec{G}$, that will produce periodic plane waves [77] in a Bravais lattice. $\vec{G}$ is defined as follows

$$\vec{G} = l\vec{b_1} + m\vec{b_2} + n\vec{b_3} \tag{2.2}$$

where $\vec{b}_1$, $\vec{b}_2$, $\vec{b}_3$ are the *primitive vectors* for the reciprocal lattice. The reciprocal lattice is shown in Figure 2.16 (b).

The space which the reciprocal lattice occupies is known as the *reciprocal* or *k-space*, while the space of the Bravais lattice of the crystal structure is known as the *direct* or *real space*.

Due to the periodic nature of the waves,

$$\exp\left(i\vec{G}\cdot(\vec{r}+\vec{R})\right) = \exp\left(i\vec{G}\cdot(\vec{R})\right) \tag{2.3}$$

where $\vec{r}$ is a vector for any point in the reciprocal lattice, the reciprocal space has to satisfy the following equation,

$$\exp\left(i\vec{G}\cdot\vec{R}\right) = 1 \tag{2.4}$$

This result suggest that the primitive vectors of the reciprocal lattice can be found from the direct lattice with the following equations,

$$\vec{b_1} = 2\pi\frac{\vec{a}_2\times\vec{a}_3}{\vec{a}_1\cdot(\vec{a}_2\times\vec{a}_3)} \tag{2.5}$$

$$\vec{b_2} = 2\pi\frac{\vec{a}_3\times\vec{a}_1}{\vec{a}_2\cdot(\vec{a}_3\times\vec{a}_1)} \tag{2.6}$$

$$\vec{b_3} = 2\pi\frac{\vec{a}_1\times\vec{a}_2}{\vec{a}_3\cdot(\vec{a}_1\times\vec{a}_2)} \tag{2.7}$$

Due to the periodic nature of the waves, only the *First Brillouin Zone*, denoted by

the grey region in Figure 2.16 (b), of the reciprocal lattice needs to be studied in order to determine all of the possible plane waves that are travelling through the crystal. The First Brillouin Zone can be found by finding the entire space in the reciprocal space that can be reach from the origin without crossing any *Bragg plane*, which are the bisection planes joining a point of the reciprocal lattice with the other points [77]. Additionally, due to symmetry in the First Brillouin Zone, the behaviour of a wave in a crystal can be fully analysed using a section of the First Brillouin Zone, known as the Irreducible Brillouin Zone, as denoted by the green triangle in Figure 2.16 (b).

In short, the modes of all possible elastic waves within an elastic medium can be represented in the reciprocal space, where the reciprocal space represents the wave vector. Since the dynamic stiffness and wavelengths of the elastic waves within a material varies with frequency, the wave vector of the waves will be different for a given mode. Hence, a band structure diagram, which is a frequency versus wave vector plot, $k$, as seen in Figure 2.15 (a) and (b) can be used to determine the wave vectors of all possible propagating waves. There may exist regions of frequencies in which there are no propagating waves as denoted by the grey region in Figure 2.15 (a), these regions are known as the band gaps, which will lead to reduced transmissions of vibrations as no elastic waves are propagating in the material. The techniques to determine the band structure will be discussed later in this chapter.

For a two dimensional system, the band structures are surfaces as shown in Figure 2.15 (b), and the entire region in the Irreducible Brillouin Zone denoted by the region inside the purple boundaries need to be considered while determining the band gaps. However, in many studies only the edges of the Irreducible Brillouin Zone, as seen in Figure 2.15 (a), are used to determine the band gaps. The representation in Figure 2.15 (a) facilitates the presentation of the information and also reduces computational costs as there is no need to calculate the entire surface, but so far there is no proof that the entire surface of the band structure is bounded by the edges of the Irreducible Brillouin Zone, which suggests there is a danger of miscalculating the band gaps when only calculating the band structure at the edges.

Apart from that, some methods of calculating the band structure, such as the transfer matrix method, are able to calculate both the real and imaginary portion of the wave vector, as seen in Figure 2.17, allowing the study of complex waves. Complex waves and waves with imaginary wave vectors are waves that attenuate within the structure. In the methods that can calculate complex waves, the band gaps are determined by the regions where all the waves have imaginary wave vectors.

The wave vector, $k$, can be used to describe the propagation of free waves from one unit cell to the adjacent unit cell of an infinite periodic structure. The real part of the wave vector is known as the propagation constant and it characterises the phase shift, while the imaginary part is known as the attenuation constant and it describes

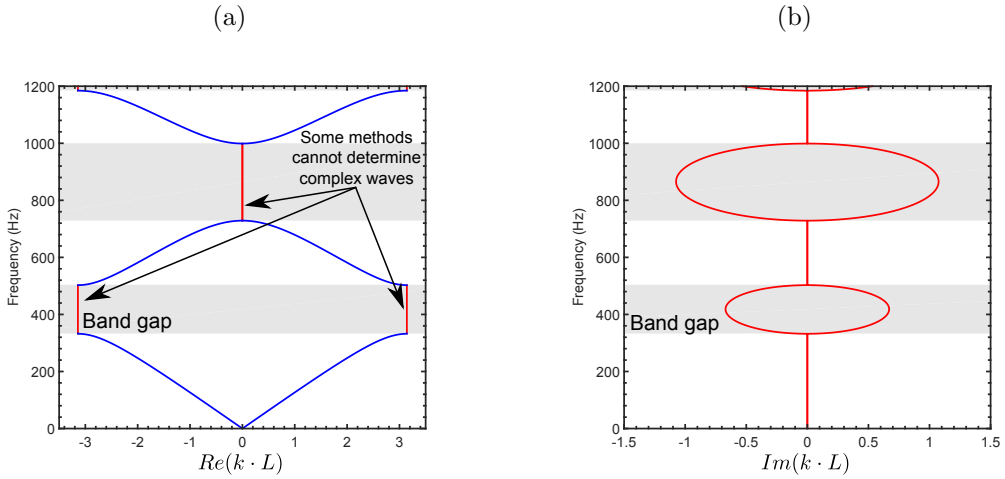



Figure 2.17: Typical band structure of a 1D phononic crystal (a) Real part (b) Imaginary part. Grey regions denote the band gaps.

the attenuation of elastic waves across the unit cell [79].

There is a plethora of methods to calculate the band structure in the literature and since the work in this thesis heavily involves calculating the band structure, this section will summarise a number of common methods used to find the band structure found in the literature. The methods that will be discussed here include, the *plane wave expansion (PWE)* method, the *extended plane wave expansion (EPWE)* method, the *finite element (FE)* method, the *transfer matrix (TM)* method, the *finite difference time domain (FDTD)* method, the *two dimensional Fourier transform* method, the *multiple scattering theory (MST)*, and the *spectral element (SE)* method.

### The plane wave expansion (PWE) method

The plane wave expansion (PWE) method is one of the most widely used techniques to calculate band structures in a periodic medium and a large number of studies, for example [53, 64, 80–96], have implemented PWE. The plane wave expansion method was originally used to solve the Maxwell equations to obtain the photonic band structure in photonic crystals [97] before being implemented in the studies of phononic crystals. Early studies of the band structure for elastic waves with PWE involves the determination of the band gaps of spherical inclusions in a homogeneous material [80–82].

The plane wave expansion method makes use of the Bloch-Floquet theorem that states that all fields in a periodic solid, for example displacements and stresses, can be expanded in an infinite series [86],

$$h(\mathbf{x}, t) = \sum_{\mathbf{G}} \tilde{h}_{\mathbf{G}}(\omega, \mathbf{k}) \ \exp\left[-i(\omega t - \mathbf{k} \cdot \mathbf{x} - \mathbf{G} \cdot \mathbf{x})\right] \tag{2.8}$$

where $\mathbf{x}$ are the coordinates within the unit cell, $\mathbf{G}$ are the vectors of the reciprocal lat-

tice, $h$ is the physical quantity of the field (which can be either stress or displacements), $\tilde{h}_{\mathbf{G}}$ is the amplitude for wave $\mathbf{G}$, $\omega$ is the radial frequency of excitation, $t$ is the time, and $\mathbf{k}$ is the wave vector.

It is important to note that the Eq. (2.8), is quasi periodic as it is a periodic function with a phase shift of $\exp(-i\mathbf{k}\cdot\mathbf{x})$ The expanded values for the stress or displacements fields in Eq. (2.8) are then substituted into the constitutive equation that describes the mechanical behaviour of the periodic medium, which is as follows,

$$\rho(\mathbf{x})\ \ddot{u}_i = \frac{\partial}{\partial x_j}\left(C_{ijkl}(\mathbf{x})\ \varepsilon_{kl}\right) = \frac{\partial}{\partial x_j}\left(C_{ijkl}(\mathbf{x})\ \frac{\partial u_k}{\partial x_l}\right) \tag{2.9}$$

where $\rho(\mathbf{x})$ is the density of the periodic medium, $C_{ijkl}(\mathbf{x})$ a fourth order tensor for the elastic constants, $u$ is the displacement, $\ddot{u}$ is the acceleration, and $\varepsilon_{kl}$ is the strain.

For a medium with inhomogeneous density or elastic constant, $\rho$ and $C_{ijkl}$ will be a function of space, $\mathbf{x}$, and these functions are also commonly written in the expanded form as follows,

$$h(\mathbf{x}) = \sum_{\mathbf{G}} \tilde{h}_{\mathbf{G}}\ \exp\left[i(-\mathbf{G}\cdot\mathbf{x})\right] \tag{2.10}$$

where $h$ is the elastic constant, $C_{ijkl}$, or density $\rho$.

Substituting the expanded form of $\rho$, $C_{ijkl}$, $\sigma_{ij}$, and $u_i$, into Eq. (2.9), will result in an eigenvalue problem to give the values of $\omega$ that will produce the band structure when the values of $\mathbf{k}$ within the first Brillouin zone are used. As an example, the plane wave expansion method will be used to calculate the band structure of a two dimensional phononic crystal with the unit cell shown in Figure 2.18 and with the material properties, shown in Table 2.1.

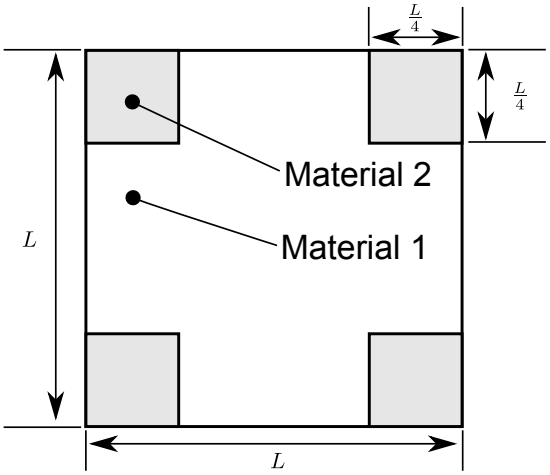



Figure 2.18: Unit cell of phononic crystal.

Firstly, assuming that the material is undergoing harmonic oscillation, the equation

| | Material 1 | Material 2 |
|---|---|---|
| Material | Epoxy | Aluminium |
| Density, $\rho$ (kg m$^{-3}$) | 1200 | 2700 |
| Young's modulus, $E$ (GPa) | 2.4 | 70 |
| Poisson's ratio, $\nu$ | 0.40 | 0.33 |
| Length, $L$ (m) | 1.0 | |

Table 2.1: Properties and geometry of the material in the unit cell.

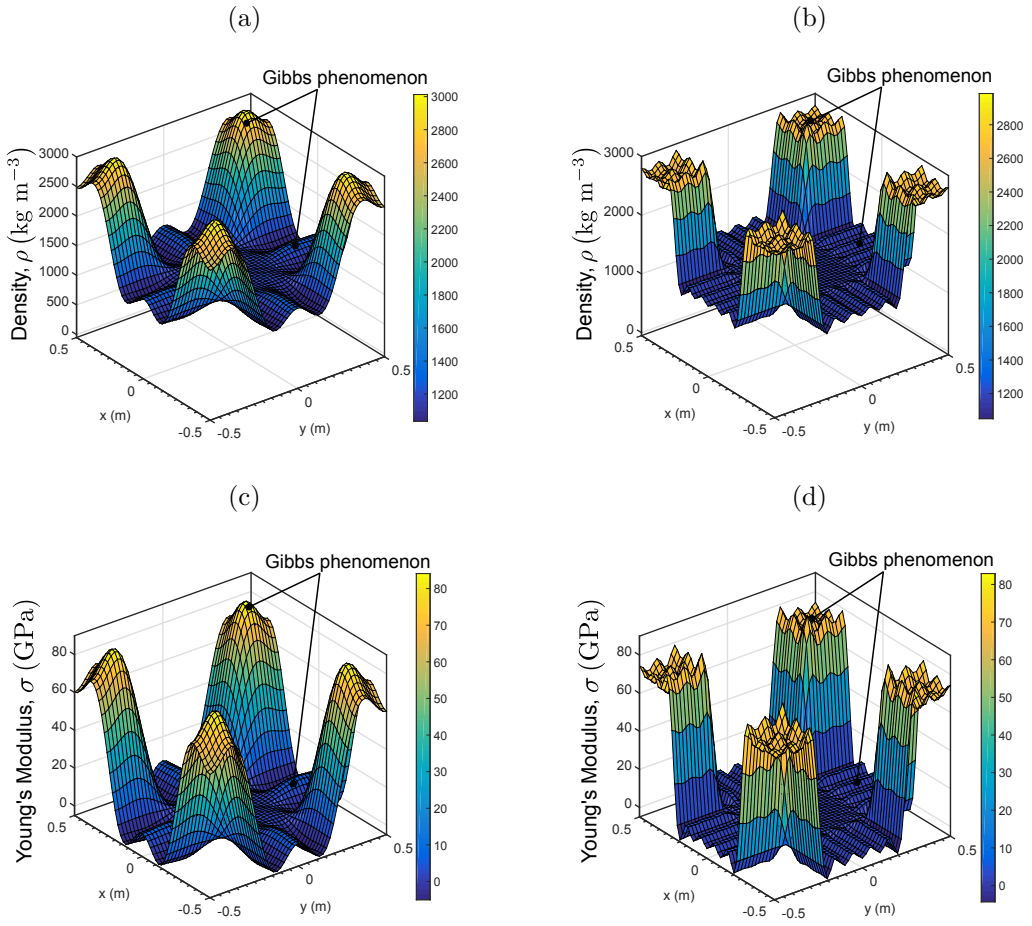



Figure 2.19: Distribution of density and Young's modulus (a) Density with 7 waves (b) Density with 21 waves (c) Young's modulus with 7 waves (d) Young's modulus with 21 waves.

of motion in Eq. (2.8) for plane stress conditions ($\sigma_{33} = \sigma_{13} = \sigma_{23} = 0$), with the time component of the wave being omitted, can be written as follows,

$$-\omega^2 \rho u_1 = \frac{\partial}{\partial x_1}\left(C_1 \frac{\partial u_1}{\partial x_1} + C_2 \frac{\partial u_2}{\partial x_2}\right) + \frac{\partial}{\partial x_2}\left(C_3 \frac{\partial u_1}{\partial x_2} + C_3 \frac{\partial u_2}{\partial x_1}\right) \tag{2.11}$$

$$-\omega^2 \rho u_2 = \frac{\partial}{\partial x_2}\left(C_2 \frac{\partial u_1}{\partial x_1} + C_1 \frac{\partial u_2}{\partial x_2}\right) + \frac{\partial}{\partial x_1}\left(C_3 \frac{\partial u_1}{\partial x_2} + C_3 \frac{\partial u_2}{\partial x_1}\right) \tag{2.12}$$

where the values of $C_1$, $C_2$, and $C_3$ are elastic constants for plane stress conditions shown in Eq. (2.13).

$$\begin{bmatrix} C_1(\mathbf{x}) & C_2(\mathbf{x}) & 0 \\ C_2(\mathbf{x}) & C_1(\mathbf{x}) & 0 \\ 0 & 0 & C_3(\mathbf{x}) \end{bmatrix} \begin{bmatrix} \varepsilon_{11} \\ \varepsilon_{22} \\ \varepsilon_{12} \end{bmatrix} = \begin{bmatrix} \frac{E}{1-\nu^2} & \frac{E\nu}{1-\nu^2} & 0 \\ \frac{E\nu}{1-\nu^2} & \frac{E}{1-\nu^2} & 0 \\ 0 & 0 & \frac{E(1-\nu)}{(1-\nu^2)} \end{bmatrix} \begin{bmatrix} \frac{\partial u_1}{\partial x_1} \\ \frac{\partial u_2}{\partial x_2} \\ \frac{1}{2}\left(\frac{\partial u_1}{\partial x_2} + \frac{\partial u_2}{\partial x_1}\right) \end{bmatrix} \tag{2.13}$$

It is important to note that the variables $\rho$, $C_1$, $C_2$, and $C_3$ are functions of space. A Fourier series expansion was used to represent the values of these variables and for the unit cell shown in Figure 2.18, the series expansion is described by

$$\begin{aligned} h = \sum_{m,n=-\infty}^{\infty} \frac{1}{4\pi^2 mn} [ & -\bar{h}_1(e^{0.5m\pi i}-1)(e^{0.5n\pi i}-1)e^{-i\pi m - i\pi n} \\ & - 2i\bar{h}_2 \sin\left(\frac{1}{2}m\pi\right)(e^{0.5n\pi i}-1)e^{-i\pi n} + \bar{h}_1(e^{0.5\pi mi}-e^{\pi mi})(e^{0.5\pi ni}-1)e^{-\pi ni} \\ & - \bar{h}_2(e^{2\pi mi}-1)(e^{0.5\pi ni}-e^{-0.5\pi ni})e^{-\pi mi} + \bar{h}_1(e^{0.5\pi mi}-1)(e^{0.5\pi ni}-e^{-\pi ni})e^{-\pi mi} \\ & + 2i\bar{h}_2 \sin\left(\frac{1}{2}\pi m\right)(e^{0.5\pi ni}-e^{\pi in}) - \bar{h}_1(e^{0.5\pi mi}-e^{\pi mi})(e^{0.5\pi ni}-e^{\pi ni}) ] \end{aligned} \tag{2.14}$$

where $h$ is the variable for $\rho$, $C_1$, $C_2$, or $C_3$ and $\bar{h}_1$ and $\bar{h}_2$ are the values for Material 1 and Material 2 respectively. $C_1$, $C_2$, and $C_3$ are components of the stiffness tensor, $C_{1111}$, $C_{2222}$, and $C_{1212}$.

Eq. (2.14) is the Fourier series expansion to give the stiffness and density distribution shown in Figure 2.18. Substituting Eqs. (2.8) and (2.14) into Eqs. (2.11) and (2.12),

Eqs. (2.11) and (2.12) can be written as follows:

$$\omega^2 \sum_p \sum_q \sum_m \sum_n e_S \rho_{pq} u_{1mn} =$$
$$\sum_p \sum_q \sum_m \sum_n e_S \left[ \left( \left( \frac{2\pi m}{L} + \frac{2\pi p}{L} + k_1 \right) \left( \frac{2\pi m}{L} + k_1 \right) C_{1pq} + \right.\right.$$
$$\left( \frac{2\pi n}{L} + \frac{2\pi q}{L} + k_2 \right) \left( \frac{2\pi n}{L} + k_2 \right) C_{3pq} \Big) u_{1mn} +$$
$$\left( \left( \frac{2\pi m}{L} + \frac{2\pi p}{L} + k_1 \right) \left( \frac{2\pi n}{L} + k_2 \right) C_{2pq} + \right.$$
$$\left.\left. \left( \frac{2\pi n}{L} + \frac{2\pi q}{L} + k_2 \right) \left( \frac{2\pi m}{L} + k_1 \right) C_{3pq} \right) u_{2mn} \right] \quad (2.15)$$

$$\omega^2 \sum_p \sum_q \sum_m \sum_n e_S \rho_{pq} u_{2mn} =$$
$$\sum_p \sum_q \sum_m \sum_n e_S \left[ \left( \left( \frac{2\pi m}{L} + \frac{2\pi p}{L} + k_1 \right) \left( \frac{2\pi n}{L} + k_2 \right) C_{3pq} + \right.\right.$$
$$\left( \frac{2\pi n}{L} + \frac{2\pi q}{L} + k_2 \right) \left( \frac{2\pi m}{L} + k_1 \right) C_{2pq} \Big) u_{1mn} +$$
$$\left( \left( \frac{2\pi m}{L} + \frac{2\pi p}{L} + k_1 \right) \left( \frac{2\pi m}{L} + k_1 \right) C_{3pq} + \right.$$
$$\left.\left. \left( \frac{2\pi n}{L} + \frac{2\pi q}{L} + k_2 \right) \left( \frac{2\pi n}{L} + k_2 \right) C_{1pq} \right) u_{2mn} \right] \quad (2.16)$$

where $p, q, m$, and $n$ are integers, the first subscript of the terms $C$ and $u$ represents the direction, and

$$e_S = \exp\left( -\frac{2\pi p i x_1}{L} - \frac{2\pi q i x_2}{L} - \frac{2\pi m i x_1}{L} - \frac{2\pi n i x_2}{L} - i k_1 x_1 - i k_2 x_2 \right) \quad (2.17)$$

Eqs. (2.15) and (2.16) can then be simplified by multiplying both sides with an orthogonal function, $\exp\left(\frac{2\pi p i}{L} x\right)$, and integrating them over a unit cell. This will result in the non-trivial solutions being as follows.

$$\omega^2 \sum_p \sum_q \rho_{(p-m)(q-n)} u_{1mn} =$$
$$\sum_p \sum_q \left[ \left( \left( \frac{2\pi m}{L} + \frac{2\pi p}{L} + k_1 \right) \left( \frac{2\pi m}{L} + k_1 \right) C_{1(p-m)(q-n)} + \right. \right.$$
$$\left( \frac{2\pi n}{L} + \frac{2\pi q}{L} + k_2 \right) \left( \frac{2\pi n}{L} + k_2 \right) C_{3(p-m)(q-n)} \Bigg) u_{1mn} +$$
$$\left( \left( \frac{2\pi m}{L} + \frac{2\pi p}{L} + k_1 \right) \left( \frac{2\pi n}{L} + k_2 \right) C_{2(p-m)(q-n)} + \right.$$
$$\left. \left( \frac{2\pi n}{L} + \frac{2\pi q}{L} + k_2 \right) \left( \frac{2\pi m}{L} + k_1 \right) C_{3(p-m)(q-n)} \right) u_{2mn} \Bigg] \quad (2.18)$$

$$\omega^2 \sum_p \sum_q \rho_{(p-m)(q-n)} u_{2mn} =$$
$$\sum_p \sum_q \left[ \left( \left( \frac{2\pi m}{L} + \frac{2\pi p}{L} + k_1 \right) \left( \frac{2\pi n}{L} + k_2 \right) C_{3(p-m)(q-n)} + \right. \right.$$
$$\left( \frac{2\pi n}{L} + \frac{2\pi q}{L} + k_2 \right) \left( \frac{2\pi m}{L} + k_1 \right) C_{2(p-m)(q-n)} \Bigg) u_{1mn} +$$
$$\left( \left( \frac{2\pi m}{L} + \frac{2\pi p}{L} + k_1 \right) \left( \frac{2\pi m}{L} + k_1 \right) C_{3(p-m)(q-n)} + \right.$$
$$\left. \left( \frac{2\pi n}{L} + \frac{2\pi q}{L} + k_2 \right) \left( \frac{2\pi n}{L} + k_2 \right) C_{1(p-m)(q-n)} \right) u_{2mn} \Bigg] \quad (2.19)$$

Eqs. (2.18) and (2.19) can then be rearranged into a matrix form, as seen in Eq. (2.20), which is an eigenvalue problem and it can be solved by replacing the values of $k_1$ and $k_2$ with the wave vectors within the first Brillouin zone to find $\omega$.

$$\omega^2 \mathbf{U} = \left( \rho^{-1} \mathbf{Q} \right) \mathbf{U} \quad (2.20)$$

where $\mathbf{U}$ is the matrix for the magnitude of the waves, $\rho$ is the matrix for the coefficients in the left hand side of Eq. (2.18) and Eq. (2.19), and $\mathbf{Q}$ is the matrix for the coefficients in the right hand side of Eq. (2.18) and Eq. (2.19).

Since the properties and fields of the phononic crystal are described by a Fourier series expansion in the PWE method, the accuracy of the band structure is dependent on the number of waves that are used to represent these values. Figure 2.19 shows the density and Young's modulus of the phononic crystal with different number of waves. Comparing Figure 2.19(a) with Figure 2.19(b) and Figure 2.19(c) with Figure 2.19(d), it was observed that the representation using the Fourier series with more waves is more accurate. This will in turn affect the calculated band structure of the phononic

crystal, as seen in Figure 2.20, in which there is a significant difference between the band structure and the predicted band gap between the calculations made using 7 waves and 21 waves. Hence, it is important that a sufficient number of waves is used when calculating the band structure with the PWE method. However, the computational cost increases with increasing the number of waves with the PWE method and the PWE method might be less efficient compared to other methods available in the literature, such as the finite element method. Another issue with the PWE method is that the Fourier series expansion will lead to the Gibbs phenomenon, as seen in Figure 2.19. The Gibbs phenomenon is the overshooting and undershooting of the predicted function at discontinuities [98]. The Gibbs phenomenon is an artefact of using a series of sine and cosine waves to approximate functions with step discontinuities.

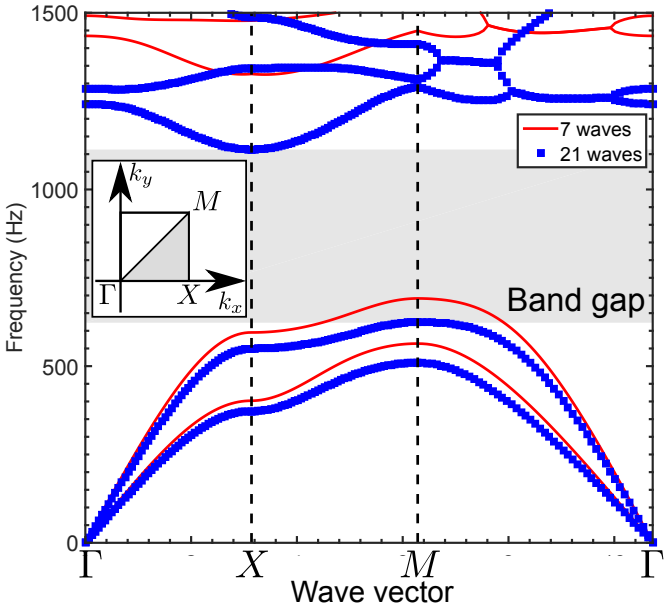



Figure 2.20: Band structure of phononic crystal.

### The extended plane wave expansion (EPWE) method

A limitation of the plane wave expansion method discussed in the previous section is that it cannot calculate complex bands and the imaginary parts of the wave vectors, as the wave vectors were assumed to be real. Therefore, the plane wave expansion method cannot be used to study evanescent waves in phononic crystals or elastic metamaterials with material damping. In order to overcome this limitation, the plane wave expansion method was extended to enable the calculation of complex bands [99–102].

The extended plane wave expansion method (EPWE) has been used in studies to analyse the effects of material loss on the dispersion relationship [99, 101] and also to

study evanescent waves [100, 102].

Similar to the traditional plane wave expansion method, the extended plane wave method also expands the stress and displacement fields with an infinite series, as seen in Eq. (2.8). However, the equations after substituting Eq. (2.8) into the constitutive equations in Eq. (2.9) are arranged using Voigt notation as follows [99, 100].

$$i\boldsymbol{\sigma}_i = \mathbf{C}_{ij}\boldsymbol{\Gamma}_{jk}\mathbf{U}_k \tag{2.21}$$

$$\omega^2\boldsymbol{\rho}_{ij}\mathbf{U}_j = \boldsymbol{\Gamma}_{ij}(i\boldsymbol{\sigma}_j) \tag{2.22}$$

where the material constants, $\boldsymbol{\rho}$ and $\mathbf{C}$, are the same as the traditional plane wave expansion method, while $\boldsymbol{\Gamma}_{ij}$ is a diagonal matrix that contains the wave vector defined in Eq. (2.23) [100].

The Bloch wave vector is then incorporated into the diagonal matrix $\boldsymbol{\Gamma}_{ij}$ as seen below

$$\boldsymbol{\Gamma}_{ij} = \left(k_i + G_i^j\right)\delta_{ji} \tag{2.23}$$

where $G_i^j$ is the reciprocal lattice vector, while $k_i$ is defied as follows [100],

$$\mathbf{k} = \mathbf{k}_0 + k\boldsymbol{\alpha} \tag{2.24}$$

where $\mathbf{k}_0$ is a constant and $\boldsymbol{\alpha}$ is a unit vector to define the direction of the Bloch wave.

Eq. (2.21) and Eq. (2.22), which are Eq. (2.8) and Eq. (2.9) with the wave vector explicitly stated can then be arranged in matrix form as follows [99, 100],

$$\begin{bmatrix} -\mathbf{A}_2 & \mathbf{I}_d \\ \omega^2\boldsymbol{\rho} - \mathbf{B} & \mathbf{0} \end{bmatrix}\begin{bmatrix} \mathbf{U} \\ i\boldsymbol{\sigma}' \end{bmatrix} = k\begin{bmatrix} \mathbf{D} & \mathbf{0} \\ \mathbf{A}_1 & \mathbf{I}_d \end{bmatrix}\begin{bmatrix} \mathbf{U} \\ i\boldsymbol{\sigma}' \end{bmatrix} \tag{2.25}$$

where the matrices in Eq. (2.25) are as follows [99, 100],

$$\mathbf{B} = \mathbf{G}_i\mathbf{C}_{ij}\mathbf{G}_j \tag{2.26}$$

$$\mathbf{A}_1 = \mathbf{G}_i\mathbf{C}_{ij}\boldsymbol{\alpha}_j \tag{2.27}$$

$$\mathbf{A}_2 = \boldsymbol{\alpha}_i\mathbf{C}_{ij}\mathbf{G}_j \tag{2.28}$$

$$\mathbf{D}_2 = \boldsymbol{\alpha}_i\mathbf{C}_{ij}\boldsymbol{\alpha}_j \tag{2.29}$$

Eq. (2.25) is an eigenvalue problem similar to Eq. (2.20) of the traditional plane wave expansion method. However, instead of the substituting $k$ to find $\omega$ in the traditional plane wave expansion method, the excitation frequency $\omega$ is substituted into Eq. (2.25) to find the wave vector $k$ instead. Figure 2.21 shows the band structure of the shear wave of a steel/epoxy phononic crystal shown in Figure 2.22 calculated using both the EPWE and PWE methods in [100]. The material properties of the phononic crystal are

listed in Table 2.2. As seen in the figure, the results for the EPWE and PWE methods are identical for the real waves but the EPWE is capable of calculating the complex bands where the curves with imaginary wave vectors are present.

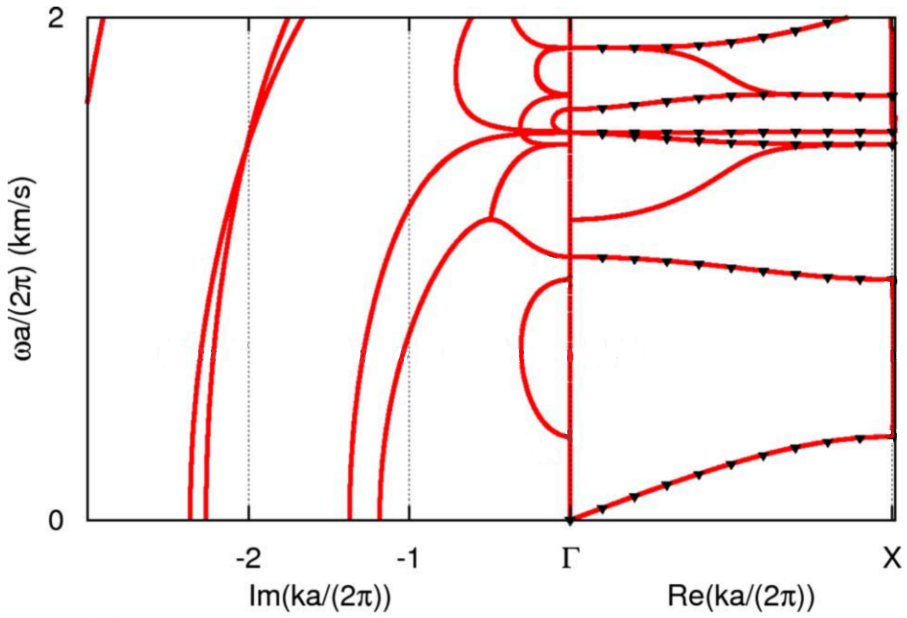



Figure 2.21: Band structure of a phononic crystal. Curves represent bands calculated using EPWE while markers represent band calculated using PWE. Reprinted from [100] with kind permission from APS Publishing.

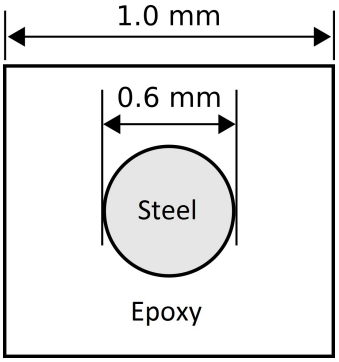



Figure 2.22: Unit cell of phononic crystal studied.

### The finite element (FE) method

The finite element method is the most straightforward and convenient method to calculate the band structure of periodic structures and materials. This is mainly because the many commercial finite element software, such as COMSOL and Abaqus, can output the required mass matrix, $\mathbf{M}$, and stiffness matrix, $\mathbf{K}$, for calculating the band structure.

| Property | Au | Si |
|---|---|---|
| $\rho$ | 19.5 kg m$^{-3}$ | 2.33 kg m$^{-3}$ |
| $C_{11}$ | 3.36 GPa | 8.95 GPa |
| $C_{44}$ | 2.71 GPa | 1.67 GPa |

Table 2.2: Properties and geometry of the materials in steel/epoxy phononic crystal. [100]

The finite element method has been used in many studies from simple structures, such as lattice structures [24, 25, 103], periodic beams [104, 105], simple phononic crystals [54, 106, 107], and plates [108, 109], to two and three dimensional acoustic metamaterials with complex geometry [36, 60, 110–113].

In the conventional finite element method, the Bloch wave boundary conditions,

$$\mathbf{U}(\mathbf{L}) = \mathbf{U}(\mathbf{0})\ e^{i\mathbf{k}\cdot\mathbf{L}} \tag{2.30}$$

$$\mathbf{F}(\mathbf{L}) = \mathbf{F}(\mathbf{0})\ e^{i\mathbf{k}\cdot\mathbf{L}} \tag{2.31}$$

are applied to the boundaries in the finite element solutions for a unit cell, which is as follows,

$$\left[\mathbf{K} - \omega^2\mathbf{M}\right]\mathbf{U} = \mathbf{F} \tag{2.32}$$

This is done by reducing the displacement, $\mathbf{U}$, and force matrix, $\mathbf{F}$, for a single unit cell with a transformation matrix, $\mathbf{Q}$, which describes the boundary conditions and is defined as follows,

$$\mathbf{Q} = \begin{bmatrix} \mathbf{I} & \mathbf{0} \\ \mathbf{0} & \mathbf{I} \\ \mathbf{I}e^{i\mathbf{k}\cdot\mathbf{L}} & \mathbf{0} \end{bmatrix} \tag{2.33}$$

where $\mathbf{I}$ is the identity matrix and $\mathbf{0}$ is a matrix of zeros.

The reduced displacement, $\bar{\mathbf{U}}$, and force matrix, $\bar{\mathbf{F}}$, are defined as follows,

$$\mathbf{U} = \mathbf{Q}\tilde{\mathbf{U}} \tag{2.34}$$

$$\mathbf{F} = \mathbf{Q}\tilde{\mathbf{F}} \tag{2.35}$$

It is important to point out that the reduced matrices, $\tilde{\mathbf{U}}$ and $\tilde{\mathbf{F}}$, are the displacements and forces at the independent nodes that are not restricted by the Bloch wave boundary conditions and Eq. (2.33) requires Eqs. (2.30) to (2.32) to be arranged so that the top rows of $\mathbf{U}$ and $\mathbf{F}$, correspond to the independent boundary nodes, the middle rows correspond to the independent internal node, while the bottom rows correspond to the boundary nodes with the Bloch wave boundary conditions. In order to enforce force

continuity, Eq. (2.33) is again multiplied by the Hermitian of $\mathbf{Q}$ [103] to give,

$$\mathbf{Q}^H \left[\mathbf{K} - \omega^2 \mathbf{M}\right] \mathbf{Q}\mathbf{U} = \mathbf{Q}^H \mathbf{Q}\mathbf{F} \tag{2.36}$$

where the superscript $H$ denotes the Hermitian transpose of the matrix.

Eq. (2.36) can be rearranged as an eigenvalue problem by setting the right hand side to zero and simplifying the equation. The eigenvalue problem is then solved by setting the wave vector, $\mathbf{k}$, and solving for $\omega^2$ which allows one to find the band structure.

$$\left[\tilde{\mathbf{K}} - \omega^2 \tilde{\mathbf{M}}\right] \tilde{\mathbf{U}} = \tilde{\mathbf{F}} = \mathbf{0} \tag{2.37}$$

where,

$$\tilde{\mathbf{K}} = \mathbf{Q}^H \mathbf{K} \mathbf{Q} \tag{2.38}$$

$$\tilde{\mathbf{M}} = \mathbf{Q}^H \mathbf{M} \mathbf{Q} \tag{2.39}$$

The finite element method can be implemented more easily compared to the other methods, like the plane wave expansion method, as commercial finite element software are available to produce the required matrices, while complicated geometries can be meshed easily with finite elements compared to the Fourier series description of the elastic modulus and density required in the plane wave expansion method. However, similar to the plane wave expansion method, in which the accuracy of the band structure depends on the numbers of waves used in the expansion, the finite element method's accuracy is dependent on the mesh and a finer mesh will result in more accurate result but at a cost of computational power. In order to illustrate this, the band structures for the phononic crystal in Figure 2.18 and Table 2.1 are plotted in Figure 2.23 (a) for the FE method calculated using two different mesh sizes of 0.125 m per element (coarse mesh) and 0.0625 m per element (fine mesh). As seen in Figure 2.23 (a), the coarse mesh and fine mesh have identical results for the first two bands but the results differs significantly for the bands at higher frequencies. This results in errors in the band gap predictions, as seen in Figure 2.23 (a), where the band gap predicted using the fine mesh is at 551-598 Hz while the coarse mesh predicts the band gap to be at 617-783 Hz. Therefore, it is essential that a sufficiently fine mesh is used when predicting the band gaps using the finite element method.

Figure 2.23 (b) compares the predictions made using the PWE method with 21 waves and the finite element method with fine mesh. As seen in the figure, the predictions made using the finite element method and the PWE are significantly different, where the predicted band gap with the PWE method is 624-1113 Hz. As seen in Figure 2.23 (b) the finite element method has significantly more modes compared to the PWE method, this is due to the larger matrix in the eigenvalue problem in the finite element method of $578 \times 578$ to the PWE's $42 \times 42$. The finite element in Figure 2.23 (b) with a fine

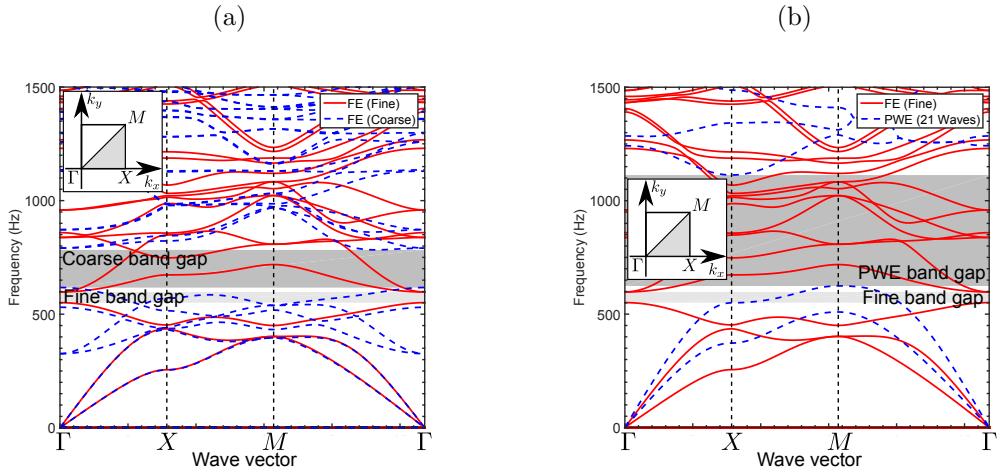



Figure 2.23: Band structure of the 2D phononic crystal in Figure 2.18 (a) Comparison of mesh sizes (b) Comparison between PWE and FE. Grey regions denote the band gaps.

mesh is likely to be more accurate than the PWE method with 21 waves and more waves are required to obtain a more accurate result with the PWE. The key source of error in the FE method is the discretisation of the solution and this error is likely to be less significant compared to the PWE for periodic structures that has step changes in the elastic modulus or the density because of the Fourier series expansion used in the PWE cannot approximate step changes well.

Lastly, like the traditional PWE method, the FE method solves the $\omega(k)$ eigenvalue problem and thus is unable to determine the imaginary part of the band structure. However, this can be overcome by rearranging the matrices and using the transfer matrix method that will be describe next.

### The transfer matrix (TM) method

The transfer matrix method is a popular and versatile technique to calculate band structures of periodic structures. In dynamic calculations, the transfer matrix, $\mathbf{D}$, which is a function of excitation frequency, $\omega$, is commonly used to relate the force and displacements of an "input" part of the component to the "output" part of the component, i.e.

$$\begin{bmatrix} \mathbf{F}_\mathrm{O} \\ \mathbf{U}_\mathrm{O} \end{bmatrix} = \mathbf{D}(\omega) \begin{bmatrix} \mathbf{F}_\mathrm{I} \\ \mathbf{U}_\mathrm{I} \end{bmatrix} \tag{2.40}$$

where $\mathbf{F}$ and $\mathbf{U}$ are the force and displacement matrix, $\mathbf{D}$ is the transfer matrix, and the subscripts O and I denotes the values for the output and inputs respectively.

The Bloch wave boundary conditions can be applied to Eq. (2.40) by substituting Eq. (2.41) into Eq. (2.40) to form the eigenvalue problem,

$$\begin{bmatrix} \mathbf{F}_\mathrm{O} \\ \mathbf{U}_\mathrm{O} \end{bmatrix} = e^{i\mathbf{k}\cdot\mathbf{L}} \begin{bmatrix} \mathbf{F}_\mathrm{I} \\ \mathbf{U}_\mathrm{I} \end{bmatrix} = \lambda \begin{bmatrix} \mathbf{F}_\mathrm{I} \\ \mathbf{U}_\mathrm{I} \end{bmatrix} \tag{2.41}$$

$$[\mathbf{D}(\omega) - \lambda\mathbf{1}] \begin{bmatrix} \mathbf{F}_\mathrm{I} \\ \mathbf{U}_\mathrm{I} \end{bmatrix} = \mathbf{0} \tag{2.42}$$

where $\mathbf{1}$ is the identity matrix.

The transfer matrix formulation in Eq. (2.42) is solved by inputting the $\omega$ values of interest to find $\lambda$. This approach is very similar to the finite element method discussed in the previous section and the finite element method can be rearranged to form the transfer matrix as done in [104, 114–116]. However, there are several differences between the two methods. Firstly, the form shown in Eq. (2.42) will result in what is known as a $k(\omega)$ problem instead of a $\omega(k)$ problem for the finite element method. The form of Eq. (2.42) has an important implication, which is that since $k$ is found from the eigenvalue problem, $k$ can be complex and therefore the transfer matrix method can be used to find complex wave vectors, a useful feature in the study of evanescent waves.

Additionally, the transfer matrix, $\mathbf{D}(\omega)$, is not limited to using finite elements and can be obtained from other formulations, such as analytical solutions of the response of several systems [79, 117, 118] and other more complicated models [73, 119]. Therefore, this allows the transmissibility matrix method to be used with a variety of different methods. Lastly, as seen in Eq. (2.40) and Eq. (2.42), the transfer matrix method is only applicable to cases, which have a single input and output portion. This leads to issues when the band structure for two or three dimensional periodic structures are to be studied, as the band structures of waves propagating in the other directions cannot be calculated easily.

A method to overcome this issue, is to set one of the values for $k_x$, $k_y$, or $k_z$ to be at a given value, which is usually 0, as done in [114]. This is equivalent to studying the wave propagation characteristics in one direction. This means that not the entire band structure in the first Brillouin zone will be found using this solution. However, this allows the transfer matrix and eigenvalue problem in Eq. (2.42) to be formed.

The band structure for the unit cell shown in Figure 2.18 and Table 2.1 will be calculated with this technique to demonstrate the method. Firstly, finite elements are used to discretise the elasticity and inertia of the phononic crystal, and the nodes are arranged and categorised as shown in Figure 2.24.

In order to make use of the transfer matrix method, the finite element solution shown in Eq. (2.32) needs to be converted to the form shown in Eq. (2.42). This is done by applying the appropriate boundary conditions which are as follows [114].

$$\begin{aligned} \mathbf{d}_R &= e^{k_x\cdot L_x}\mathbf{d}_L, & \mathbf{d}_T &= e^{k_y\cdot L_y}\mathbf{d}_B, & \mathbf{d}_{LT} &= e^{k_y\cdot L_y}\mathbf{d}_{LB}, \\ \mathbf{d}_{RB} &= e^{k_x\cdot L_x}\mathbf{d}_{LB}, & \mathbf{d}_{RT} &= e^{k_x\cdot L_x + k_y\cdot L_y}\mathbf{d}_{LB} \end{aligned} \tag{2.43}$$

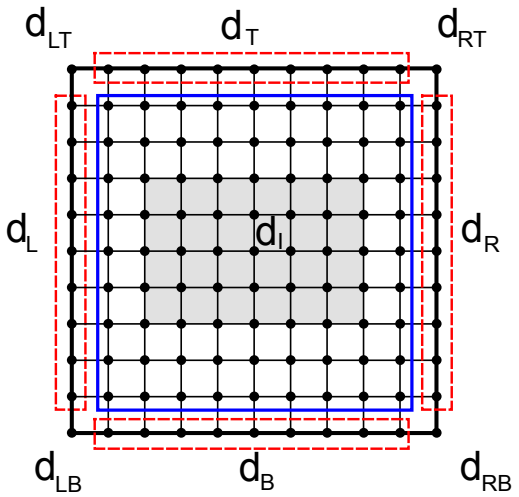



Figure 2.24: (a) Arranged nodes for the phononic crystals.

$$\begin{aligned} \mathbf{f}_R &= -e^{k_x \cdot L_x}\mathbf{f}_L, \qquad \mathbf{f}_T = -e^{k_y \cdot L_y}\mathbf{f}_B, \qquad \mathbf{f}_{LT} = -e^{k_y \cdot L_y}\mathbf{f}_{LB}, \\ \mathbf{f}_{RB} &= -e^{k_x \cdot L_x}\mathbf{f}_{LB}, \quad \mathbf{f}_{RT} = -e^{k_x \cdot L_x + k_y \cdot L_y}\mathbf{f}_{LB} \end{aligned} \tag{2.44}$$

For the case of wave propagation in the x-direction ($k_y = 0$), the finite element equation, Eq. (2.32), can be simplified to Eq. (2.45) [114] and similar equations can be formulated for the case where $k_x = 0$.

$$\mathbf{K_D}\begin{bmatrix} \mathbf{d}_L \\ \mathbf{d}_I \\ \mathbf{d}_R \end{bmatrix} = \begin{bmatrix} \boldsymbol{\alpha}_{LL} & \boldsymbol{\alpha}_{LI} & \boldsymbol{\alpha}_{LR} \\ \boldsymbol{\alpha}_{IL} & \boldsymbol{\alpha}_{II} & \boldsymbol{\alpha}_{IR} \\ \boldsymbol{\alpha}_{RL} & \boldsymbol{\alpha}_{RI} & \boldsymbol{\alpha}_{RR} \end{bmatrix}\begin{bmatrix} \mathbf{d}_L \\ \mathbf{d}_I \\ \mathbf{d}_R \end{bmatrix} = \begin{bmatrix} \mathbf{f}_L \\ \mathbf{0} \\ \mathbf{f}_R \end{bmatrix} \tag{2.45}$$

Eq. (2.45) can then be cast into the transfer matrix form

$$\begin{bmatrix} \mathbf{d}_R \\ \mathbf{f}_R \end{bmatrix} = \mathbf{T}\begin{bmatrix} \mathbf{d}_L \\ \mathbf{f}_L \end{bmatrix} = \lambda\mathbf{1} \tag{2.46}$$

where $\mathbf{T}$ is defined as follows.

$$\mathbf{T} = \begin{bmatrix} -\tilde{\boldsymbol{\alpha}}_{LR}^{-1}\tilde{\boldsymbol{\alpha}}_{LL}^{-1} & \tilde{\boldsymbol{\alpha}}_{LR}^{-1} \\ \tilde{\boldsymbol{\alpha}}_{RR}(\tilde{\boldsymbol{\alpha}}_{LR}^{-1}\tilde{\boldsymbol{\alpha}}_{LL}) - \tilde{\boldsymbol{\alpha}}_{RL} & -\tilde{\boldsymbol{\alpha}}_{RR}^{-1}\tilde{\boldsymbol{\alpha}}_{LR} \end{bmatrix} \tag{2.47}$$

$$\tilde{\boldsymbol{\alpha}}_{LL} = \boldsymbol{\alpha}_{LL} - \boldsymbol{\alpha}_{LI}\boldsymbol{\alpha}_{II}^{-1}\boldsymbol{\alpha}_{IL} \tag{2.48}$$

$$\tilde{\boldsymbol{\alpha}}_{LR} = \boldsymbol{\alpha}_{LL} - \boldsymbol{\alpha}_{LI}\boldsymbol{\alpha}_{II}^{-1}\boldsymbol{\alpha}_{IR} \tag{2.49}$$

$$\tilde{\boldsymbol{\alpha}}_{RL} = \boldsymbol{\alpha}_{RL} - \boldsymbol{\alpha}_{RI}\boldsymbol{\alpha}_{II}^{-1}\boldsymbol{\alpha}_{IL} \tag{2.50}$$

$$\tilde{\boldsymbol{\alpha}}_{RR} = \boldsymbol{\alpha}_{RR} - \boldsymbol{\alpha}_{RI}\boldsymbol{\alpha}_{II}^{-1}\boldsymbol{\alpha}_{IR} \tag{2.51}$$

The band structure of the system can then be obtained by rearranging Eq. (2.46) into the eigenvalue as follows and solving it.

$$\mathbf{T}\begin{bmatrix}\mathbf{d}_L\\ \mathbf{f}_L\end{bmatrix} - \lambda\mathbf{1} = \mathbf{0} \tag{2.52}$$

The calculated band structure is shown in Figure 2.25.

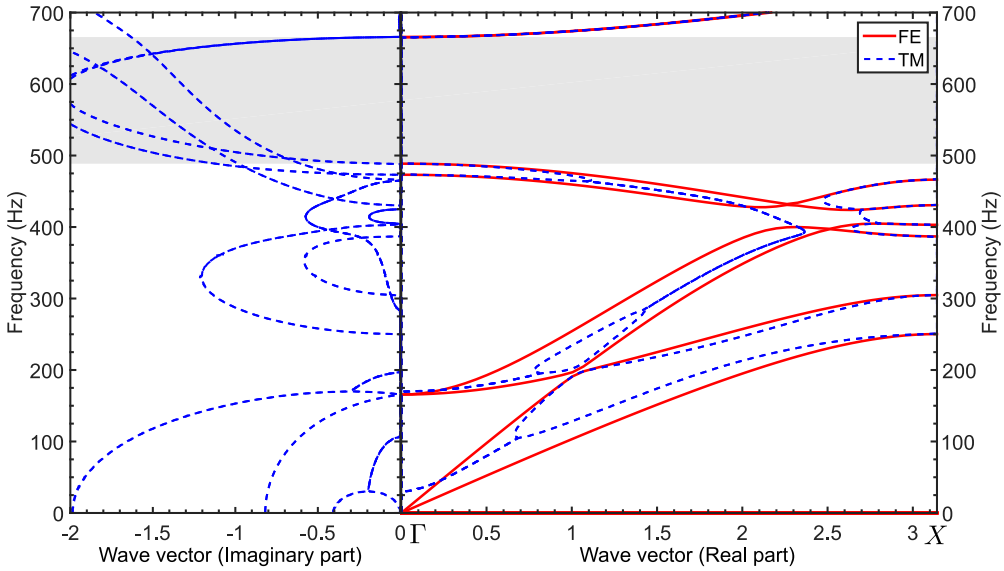



Figure 2.25: Band structure comparison between finite element and transfer matrix method.

A coarse mesh size of 0.25 m per element mesh was used to calculate the band structure in Figure 2.25. The reason for selecting the coarse mesh is due to the badly conditioned matrices for the fine mesh used in the transfer matrix method. The equations used to calculate the band structure for the transfer matrix method here in Eq. (2.47) to Eq. (2.51) requires several portions of the matrices to be inverted, which may result in badly conditioned matrices in Eq. (2.46). Therefore, this is a shortcoming of the method when manipulation of the matrices is required and care should be taken to ensure that the matrices are well conditioned by performing checks on the ranks of the matrices. However, since the purpose of this section is to describe the method, a coarser mesh size that has well conditioned matrices was used instead.

As seen in Figure 2.25, the transfer matrix method is capable of calculating the imaginary part of the wave vector, unlike the finite element method that only manages to calculate the real portion of the wave vector. As seen in Figure 2.25, only the imaginary part of the wave vectors are present at the band gap region. The imaginary parts of the wave vectors characterises the amount of wave attenuation within the band gaps and is important in the studies of the evanescent waves and systems with material damping, such as [99, 100, 102, 120]. Furthermore, the real part of the wave vector for

the transfer matrix and finite element method shown in Figure 2.25 have similar overall shape and are identical at several regions around zero wave vector. Since the same finite element model was used in both methods, the real portion of the wave vectors of the finite element and transfer matrix methods should be identical. The difference between the two methods may be attributed to the errors introduced into the transfer matrix method when the equations are being manipulated in Eq. (2.47) to Eq. (2.51), which can be eliminated with better conditioned matrices. One way to produce better conditioned matrices is to use appropriate units for the stiffness and density properties to prevent the stiffness and mass matrix having a large difference in the order of magnitude, which lead to several columns and rows of the transmission matrix having low or zero values after manipulating the matrix.

Although, the transfer matrix method described here has the benefit of being able to calculate the imaginary parts of the band structure, it has several shortcomings. As seen here, the transfer matrix may have badly conditioned matrices that will give inaccurate results. Another disadvantage is that it can only calculate the wave propagating in a single direction even for two and three dimensional structures. Although the method has issues, it is widely used in many studies, for example in [62, 114, 121–123] to study the wave propagation of piezoelectric patches, [115] for functionally graded material, [104, 124–127] to study periodic beams, and many others [128–130].

### The finite difference time domain (FDTD) method

The finite difference time domain (FDTD) method is another popular technique to calculate the band structure of phononic crystals and can be seen in several studies [131–137]. Unlike the other methods, such as PWE, that calculates the band structure in the frequency domain, the finite difference time domain method calculates the response of the periodic structures in the time domain and frequency spectrum analysis is then performed to find the band structure in the frequency domain. Additionally, the FDTD method does not encounter convergence issues that are associated with the PWE method, when there is a large acoustic mismatch between the constituent materials within the periodic structure [131, 133, 137].

The FDTD method seeks to solve the equation of motion and the constitutive equation for the material described by [131]

$$\boldsymbol{\rho}\ddot{\mathbf{u}}_i = \boldsymbol{\sigma}_{ij,j} + \boldsymbol{\rho}\mathbf{f}_i \tag{2.53}$$

$$\boldsymbol{\sigma}_{ij} = \boldsymbol{C}_{ijkl}\boldsymbol{\varepsilon}_{kl} \tag{2.54}$$

For the finite difference time domain method, a unit cell of material to be studied is first discretised in order for the stress and displacement fields to be calculated. An example of a discretised grid is shown in Figure 2.26.

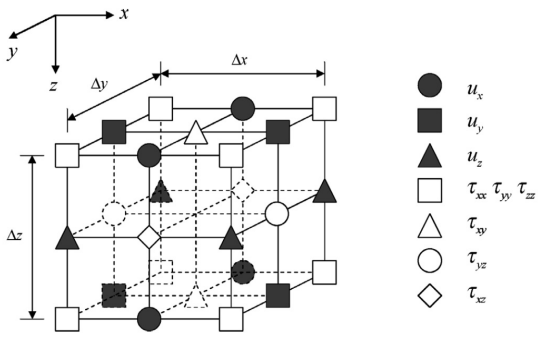



Fig. 1. The unit of the grids in the FDTD method.

Figure 2.26: Example of discretised grid. ©IEEE. Reprinted from [131] with kind permission from IEEE.

Since Eqs. (2.53) and (2.54) have derivatives in them, the FDTD requires the derivatives to be approximated. For a three dimensional material, the approximations using the first order central difference scheme [131] are as follows,

$$D_1\left[M\left(i,j,k,l\right)\right] = \frac{1}{\Delta x_1}\left[M\left(i+\frac{1}{2},j,k,l\right) - M\left(i-\frac{1}{2},j,k,l\right)\right] \tag{2.55}$$

$$D_2\left[M\left(i,j,k,l\right)\right] = \frac{1}{\Delta x_2}\left[M\left(i,j+\frac{1}{2},k,l\right) - M\left(i,j-\frac{1}{2},k,l\right)\right] \tag{2.56}$$

$$D_3\left[M\left(i,j,k,l\right)\right] = \frac{1}{\Delta x_3}\left[M\left(i,j,k+\frac{1}{2},l\right) - M\left(i,j,k-\frac{1}{2},l\right)\right] \tag{2.57}$$

$$\frac{\partial^2}{\partial t^2}\left[M\left(i,j,k,l\right)\right] = \frac{1}{(\Delta t)^2}\left[M\left(i,j,k,l+\frac{1}{2}\right) - 2M\left(i,j,k,l\right) + M\left(i,j,k,l+\frac{1}{2}\right)\right] \tag{2.58}$$

where $D_j$ is the derivative with respect to space where the subscript represent the directions and $M$ is the field that is being evaluated.

The discretised equations that describe the material can be found by substituting Eq. (2.55) to Eq. (2.58) into Eqs. (2.53) and (2.54). In order to analyse the band structure, the Bloch wave theorem is implemented into the equation. There are a few ways that this can be done.

One way is to modify the equations in Eqs. (2.53) and (2.54) to the following

$$\rho(\mathbf{x})\ddot{\mathbf{u}}(\mathbf{x},t) = i\mathbf{k}_j\boldsymbol{\sigma}_{ij}(\mathbf{x},t) + \partial_j\boldsymbol{\sigma}_{ij} \tag{2.59}$$

$$\boldsymbol{\sigma}_{ij} = \mathbf{C}_{ijkl}(\mathbf{x})\ \partial_j\mathbf{u}_i(\mathbf{x},t) \tag{2.60}$$

and then apply periodic boundary conditions,

$$\mathbf{u}_i(\mathbf{x}+\mathbf{a},t) = \mathbf{u}_i(\mathbf{x},t) \tag{2.61}$$

$$\boldsymbol{\sigma}_{ij}(\mathbf{x}+\mathbf{a},t) = \boldsymbol{\sigma}_{ij}(\mathbf{x},t) \tag{2.62}$$

as done in [133]. Alternatively, the Bloch wave boundary conditions can be directly applied using the following equations as done in [131].

$$\mathbf{u}_i(\mathbf{x}+\mathbf{a},t) = e^{i\mathbf{k}\cdot\mathbf{a}}\mathbf{u}_i(\mathbf{x},t) \tag{2.63}$$

$$\boldsymbol{\sigma}_{ij}(\mathbf{x}+\mathbf{a},t) = e^{i\mathbf{k}\cdot\mathbf{a}}\boldsymbol{\sigma}_{ij}(\mathbf{x},t) \tag{2.64}$$

The wave vector, $\mathbf{k}$, in Eqs. (2.63) and (2.64) is restricted to the first Brillouin zone.

After that, the initial conditions at $t = 0$ are then applied to the equations. The initial disturbance is usually a small impulse at a random position, for example,

$$\mathbf{u}_i(x_1, x_2, x_3, t = 0) = \delta(x1)_x\delta(x2)_y\delta(x3)_z \tag{2.65}$$

where $\delta$ is the Dirac delta function defined as follows

$$\delta(x)_i = \frac{1}{a\sqrt{\pi}}\exp\left(-\frac{x^2}{a^2}\right), \text{as } a \to 0 \tag{2.66}$$

where the subscript $i$ denotes the direction.

This allows all possible wave modes to be transported in the phononic crystal. The displacement fields for this initial condition are then calculated over a range of time, $t$. A Fourier transform is then performed on the calculated displacement fields to find the frequency spectrum and the peak values of frequency for a given value of $k$ is taken to be a point in the dispersion curve.

The band structure for the phononic crystal shown in Figure 2.27 (a) is shown in in Figure 2.27 (b). As seen in the figure the calculated value of FDTD is similar to the values calculated using PWE, especially for the lower bands where the results are almost identical, this suggest that the results of the FDTD are accurate or at least comparable to the PWE.

Despite being able to overcome the convergence issue of PWE, being a time domain method, a large number of steps may be require in order to obtain the required time domain response of the system and this has to be performed for the different values of wave vectors. Thus, the computational costs using the FDTD method may be high compared to the other methods, such as the finite element method, that calculates the band structure in the frequency domain. However, a benefit of the FDTD method is that parallel computing may be used to solve the equations as described in [131], which allows computer clusters to be used for the calculations.

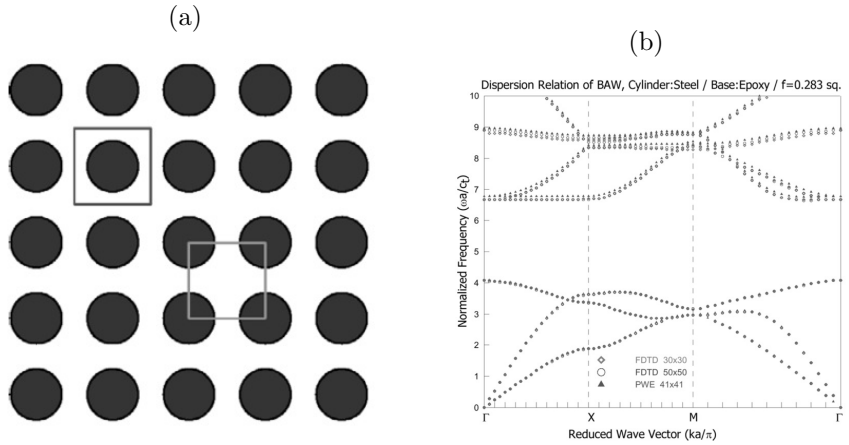



Figure 2.27: (a) 2D phononic crystal made from epoxy and steel cylinder (b) Calculated band structure [131]

### The two dimensional Fourier transform

Apart from analytical methods, the band structure of periodic structures can also be calculated from measured frequency response functions by performing a two dimensional Fourier transform. This method is implemented in [138, 139] and is one of the very few methods available to determine the band structures from the response of the systems available in the literature.

The application of this technique starts by measuring the frequency response across a few periods of the periodic structure and then applying the Fourier transform, $W(k,\omega)$, to the measured response.

$$W(k,\omega) = \int_{-\infty}^{\infty}\int_{-\infty}^{\infty} w(x,t)e^{-i(kx+\omega t)}\ dt\ dx \tag{2.67}$$

where $W$ is the function in the frequency/wavenumber domain and $w$ is the response in the time/space domain.

This technique requires the response measurements to have fine temporal and spatial resolutions in order to properly estimate the frequency and wavenumber content of the wave response [138].

An example of the response obtained in the time-space domain for a periodic beam with piezoelectric patches in Figure 2.28 (a) is plotted in Figure 2.28 (b). Since the beam is finite, the wave will be reflected at the boundary, as seen in Figure 2.28 (b).

The reflected waves will result in the presence of dominant harmonic terms that correspond to the resonant modes of the beam and will result in the band structure being discontinuous with energies concentrated at the frequency/wavenumbers of the resonant modes [138]. Therefore, post-processing of the response is required to remove the reflection.

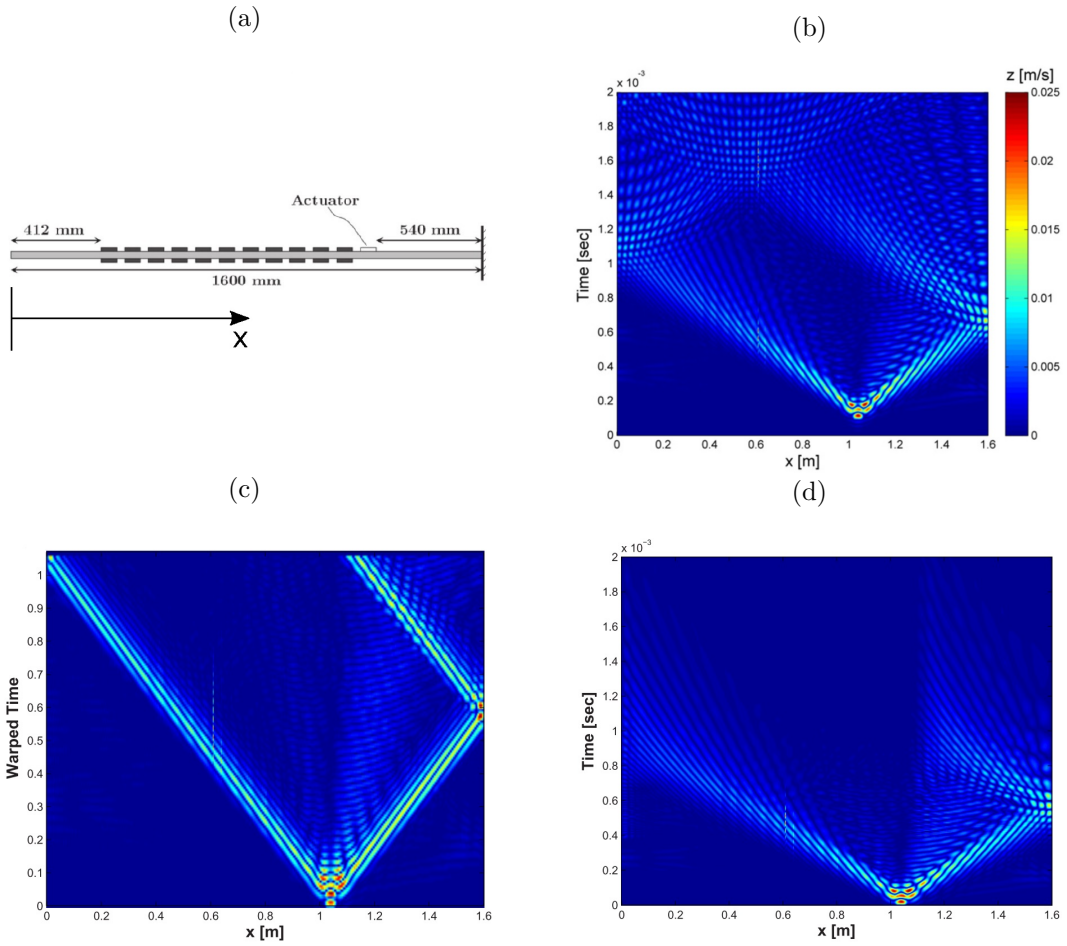



Figure 2.28: (a) Tested periodic beam (b) Measured frequency response, the legend shows the magnitude of the velocity measured in the transverse direction (c) Warped frequency response (d) Frequency response after removing reflection. Reprinted from [138] with kind permission from IOP Publishing.

One method to identify and remove the reflected wave is to first perform a space-warped time domain transformation to compensate the dispersion characteristic as done in [138]. The transformation can be done using a linear transformation known as the warped frequency transform (WFT) proposed in [140].

The WFT is based on the warping of the frequency domain according to the dispersion properties of the medium of interest [138]. This allows the signal to be represented in the warped-time axis where it appears non-dispersive, as seen in Figure 2.28 (c), in which the warped-time axis is restricted to the values prior to the left boundary reflection through appropriate windowing. The signal is then inverted back to the time domain with the reflection being removed, as seen in Figure 2.28 (d).

Lastly, the two dimensional Fourier transform described by Eq. (2.67) is performed on the measured response shown in Figure 2.28 (d).

The Fourier transform will give the amplitudes of the wave vectors and frequencies of the waves that are present in the measured response. The results from the Fourier transform is shown in Figure 2.29, where the coloured contours describes the magnitudes of wave vectors and frequencies. As seen in the figure, the predicted band structure from the 2D Fourier transform denoted by the region with the largest amplitudes overlaps with the band structures predicted from analytical calculations.

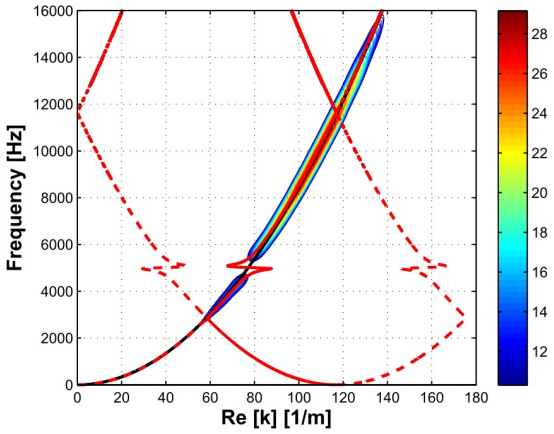



Figure 2.29: Band structure of tested periodic piezopatches. The red lines are the analytical predictions and the coloured contours show the amplitudes calculated using the 2D Fourier transform with the values stated in the legend. Reprinted from [138] with kind permission from IOP Publishing.

Although, performing the two dimensional Fourier transform is one of the very few methods available to calculate the band structure from experimental responses, it has a few shortcomings. Firstly, the method requires the responses to be measured at high temporal and spatial resolutions. This makes it difficult for measurements to be made using other equipment, such as accelerometers, that are much easier to implement. This is one of the key motivations of the work done in this thesis, which is to develop

methods that will facilitate the adoption of elastic metamaterials and phononic crystals into practical applications. Another shortcoming is that it is unable to be calculate the imaginary part of the band structure and complex band structures like the ones seen in the transfer matrix method. Lastly, the two dimensional Fourier transform may require post-processing of the experimental data using various techniques to remove the artefacts of wave reflection.

### The multiple scattering theory (MST)

The multiple scattering theory (MST), sometimes known as the Korringa, Kohn, and Rostoker (KKR) approach, is another popular technique used to calculate the band structure for elastic waves in periodic structures. The MST has been implemented in number of studies [141–144] and was initially used to calculate the band structure of electromagnetic waves in photonic crystals.

One of the key benefits to the MST method is that the method can overcome the convergence issues found in plane wave methods [141] for systems with very high or very low filling ratios. Additionally, it is capable of calculating the band structure for both ordered and disordered systems [141]. Lastly, the multiple scattering theory can also be formulated to calculate the transmission and reflection coefficients of the systems, allowing measurements to be compared with theoretical values.

The MST method presented in this thesis will be in the form used in [141] as the equations were given in modern form and is convenient for numerical calculations. Like the other techniques listed in this work, the MST method attempts to solve the elastic wave equation

$$(\lambda + 2\mu)\nabla(\nabla \cdot \mathbf{u}) - \mu\nabla \times \nabla \times \mathbf{u} + \rho\omega^2\mathbf{u} = 0 \tag{2.68}$$

where $\rho$ is the density while $\lambda$ and $\mu$ are the Lamé constants for the medium.

The general solution for Eq. (2.68) is,

$$\mathbf{u}(\mathbf{r}) = \sum_{lmn} \left[a_{lmn}\mathbf{J}_{lmn}(\mathbf{r}) + b_{lmn}\mathbf{H}_{lmn}(\mathbf{r})\right] \tag{2.69}$$

where $l$ is summed from 0 to $\infty$, $m$ is summed from 0 to $n$, and $n$ describes the modes with 1 being the longitudinal mode and 2-3 being the transverse mode, while $\mathbf{r}$ is the location from the centre of the scatterer, and the terms $\mathbf{J}$ and $\mathbf{H}$ are defined as follows.

$$\mathbf{J}_{lm1}(\mathbf{r}) = \frac{1}{\alpha}\nabla\left[j_l(\alpha r)Y_{lm}(\hat{\mathbf{r}})\right] \tag{2.70}$$

$$\mathbf{J}_{lm2}(\mathbf{r}) = \frac{1}{l(l+1)}\nabla \times \left[\mathbf{r}j_l(\beta r)Y_{lm}(\hat{\mathbf{r}})\right] \tag{2.71}$$

$$\mathbf{J}_{lm3}(\mathbf{r}) = \frac{1}{l(l+1)\beta}\nabla \times \nabla \times [\mathbf{r} j_l(\beta r) Y_{lm}(\hat{\mathbf{r}})] \tag{2.72}$$

$$\mathbf{H}_{lm1}(\mathbf{r}) = \frac{1}{\alpha}\nabla [h_l(\alpha r) Y_{lm}(\hat{\mathbf{r}})] \tag{2.73}$$

$$\mathbf{H}_{lm2}(\mathbf{r}) = \frac{1}{l(l+1)}\nabla \times [\mathbf{r} h_l(\beta r) Y_{lm}(\hat{\mathbf{r}})] \tag{2.74}$$

$$\mathbf{H}_{lm3}(\mathbf{r}) = \frac{1}{l(l+1)\beta}\nabla \times \nabla \times [\mathbf{r} h_l(\beta r) Y_{lm}(\hat{\mathbf{r}})] \tag{2.75}$$

where $\mathbf{r} = \frac{\hat{\mathbf{r}}}{|\mathbf{r}|}$, $\alpha = \omega\sqrt{\frac{\rho}{\lambda} + 2\mu}$, $\beta = \omega\sqrt{\frac{\rho}{\mu}}$, $j_l(x)$ is the spherical Bessel function, $h_l(x)$ is the spherical Hankel function of the first kind, and $Y_{lm}(\hat{\mathbf{r}})$ are the spherical harmonics, which are normalised functions on the surface of the unit sphere and their expressions can be found in [145].

For a medium made from a host matrix with embedded scatterers, the incident wave for the scatterer, $\mathbf{u}_i^{in}$ is expressed as

$$\mathbf{u}_i^{in}(\mathbf{r}_i) = \sum_{lmn} a_{lmn}^i \mathbf{J}_{lmn}^i(\mathbf{r}_i) \tag{2.76}$$

where the subscript $i$ denotes the scatterer and $\mathbf{r}_i$ is measured from the centre of the scatterer. Similarly the wave scatted by the scatterer is defined as follows.

$$\mathbf{u}_i^{sc}(\mathbf{r}_i) = \sum_{lmn} b_{lmn}^i \mathbf{H}_{lmn}^i(\mathbf{r}_i) \tag{2.77}$$

Based on the MST, the wave incident on the scatterer can be split into two parts, the externally incident waves described by Eq. (2.78) and the sum of all scattered wave other than that from the scatterer described by Eq. (2.79).

$$\mathbf{u}_i^{in(0)}(\mathbf{r}_i) = \sum_{lmn} a_{lmn}^{in(0)} \mathbf{J}_{lmn}^i(\mathbf{r}_i) \tag{2.78}$$

$$\mathbf{u}_i^{in}(\mathbf{r}_i) - \mathbf{u}_i^{in(0)}(\mathbf{r}_i) = \sum_{j \neq i} \sum_{l''m''n''} b_{l''m''n''} j \mathbf{H}_{l''m''n''} j(\mathbf{r}_j) \tag{2.79}$$

where $(\mathbf{r}_i)$ and $(\mathbf{r}_j)$ refer to the spatial point measured from scatterers $i$ and $j$ while $\mathbf{R}_{i(j)}$ denoting the position of the scatterer $i(j)$. It has been shown in [141] that $\mathbf{H}_{l''m''n''}j$ can be expressed as follows.

$$\mathbf{H}_{l''m''n''} j(\mathbf{r}_i + \mathbf{R}_i - \mathbf{R}_j) = \sum_{lmn} G_{l''m''n''lmn}(\mathbf{R}_i - \mathbf{R}_j) \mathbf{J}_{lmn}^i(\mathbf{r}_i) \tag{2.80}$$

where $G$ is the "vector structure constant", that is a translation matrix given by Bostrom

[146] and is defined by Eq. (2.81)

$$G_{lmnl'm'n'}(\mathbf{R}) = \begin{cases} X^{\alpha}_{lml'm'}(\mathbf{R}), & n = n' = 1 \\ \sum\limits_{\mu} = c(l1lm-\mu\mu)X^{\beta}_{lm-\mu l'm'-\mu'}(\mathbf{R})c(l'1l'm'-\mu\mu), & n = n' = 2,3 \\ -i\left(\frac{2l'+1}{l'+1}\right)\sum\limits_{\mu} c(l1lm-\mu\mu)X^{\beta}_{lm-\mu l'm'-\mu'}(\mathbf{R})c(l'1l'm'-\mu\mu), & n \neq n'; n, n' \neq 1 \end{cases} \tag{2.81}$$

where $c(l1lm-\mu\mu)$ is the Clebsch-Gordan coefficients, which can be found in tables provided in books like [147], and $X^{\kappa}_{lml'm'}(\mathbf{R})$ is the "structure constant" of scalar waves defined as follows.

$$X^{\kappa}_{lml'm'}(\mathbf{R}) = 4\pi \sum_{l''} i^{l'+l''-l} C^{lm}_{l'm'l''(m-m')} h_{l''}(\kappa R) Y_{l''(m-m')}(\hat{\mathbf{R}}) \tag{2.82}$$

$Clm_{l'm'l''m''}$ is a constant expressed as

$$Clm_{l'm'l''m''} = \int\int_{s} Y_{lm}(\Omega) Y^{*}_{l'm'}(\Omega) Y^{*}_{l''m''}(\Omega) d\Omega \tag{2.83}$$

where $\Omega$ is a dummy variable and $s$ represents the surface of the scatterer.

By defining $G^{ij}_{l''m''n''lmn}$ as $G^{ij}_{l''m''n''lmn}(\mathbf{R}_i - \mathbf{R}_j)$, $\mathbf{H}^{j}_{l''m''n''}(\mathbf{r}_j)$ can be expressed as Eq. (2.84).

$$\mathbf{H}^{j}_{l''m''n''}(\mathbf{r}_j) = \sum_{lmn} G^{ij}_{l''m''n''lmn} \mathbf{J}^{i}_{lmn}(\mathbf{r}_i) \tag{2.84}$$

The scattered displacement field is determined from the incident field through the scattering matrix as shown below.

$$B = TA \tag{2.85}$$

where $A = \{b^{j}_{lmn}\}$, $B = \{a^{j}_{lmn}\}$, and $T = t_{lmnl'm'n'}$ is the scattering matrix that can be obtained using the elastic Mie scattering solution for a scatterer as done in [141, 148].

Substituting Eqs. (2.76), (2.78), (2.84) and (2.85) into Eq. (2.79) will lead to,

$$\sum_{jl'm'n'} \left( \delta_{ij}\delta_{ll'}\delta_{mm'}\delta_{nn'} - \sum_{l''m''n''} t^{j}_{l''m''n''l'm'n'} G^{ij}_{l''m''n''lmn} \right) a^{j}_{l'm'n'} = a^{i(0)}_{lmn} \tag{2.86}$$

where $\delta_{ij}$ is the Kronecker delta function.

Eq. (2.86) is the general form of the scalar MST. For a finite or disordered system, Eq. (2.86) must be solved to determine the system response to external excitations. The normal modes of the system can be found by solving the following equation.

$$\left| \delta_{ij}\delta_{ll'}\delta_{mm'}\delta_{nn'} - \sum_{l''m''n''} t^{j}_{l''m''n''l'm'n'} G^{ij}_{l''m''n''lmn} \right| = 0 \tag{2.87}$$

The Bloch wave boundary conditions can be added to Eq. (2.87) to find the band structure of a periodic system, by replacing $G^{ij}_{l''m''n''lmn}$ with $G^{ss}_{l''m''n''lmn}$ described by Eq. (2.88), which gives,

$$G^{ss'}_{l''m''n''lmn}(\mathbf{k}) = \sum_{\mathbf{R}} G_{l''m''n''lmn}(\mathbf{o}_s - \mathbf{o}_{s'} - \mathbf{R}) \exp\left(i\mathbf{k}\cdot\mathbf{R}\right) \tag{2.88}$$

where $s$ and $s'$ denote the scatterers in the unit cells and $\sum_{\mathbf{R}}$ is the sum for all lattice sites while $\mathbf{o}_s$ and $\mathbf{o}_{s'}$ are position vectors.

$$\left| \delta_{ij}\delta_{ll'}\delta_{mm'}\delta_{nn'} - \sum_{l''m''n''} t^{s}_{l''m''n''l'm'n'} G^{ss'}_{l''m''n''lmn}(\mathbf{k}) \right| = 0 \tag{2.89}$$

An example band structure for an FCC AU/Si composite with a filling fraction of 10 % is shown in Figure 2.30, the properties for the constituent materials are listed in Table 2.3.

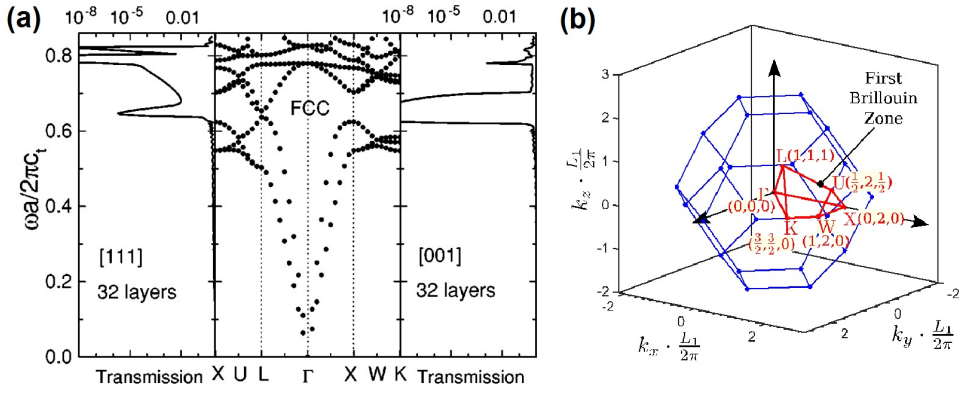



Figure 2.30: (a) Band structure of an FCC Au/Si composite (b) First Brillouin Zone of FCC structure. Reprinted from [141] with kind permission from APS.

| Property | Au | Si |
|---|---|---|
| $\rho$ | 19.5 g cm$^{-3}$ | 2.33 g cm$^{-3}$ |
| $c_l$ | 3.36 km s$^{-1}$ | 8.95 km s$^{-1}$ |
| $\frac{c_l}{c_t}$ | 2.71 | 1.67 |

Table 2.3: Properties and geometry of the materials in FCC composite material. [141]

As seen in Figure 2.30, the MST is capable of calculating the band structure, reflection coefficient, and transmission coefficient for the FCC structure without convergence issues. Additionally, since the waves are described analytically in the MST, the equations provide more insight to the physics of the wave propagation and scattering. However, the MST is mathematically more complicated compared to the other methods, such as FEM and TF, which may not be well suited to be used for engineering applications,

where optimisation and flexibility in the technique is needed.

### The spectral element (SE) method

The spectral element (SE) method is another method that has been implemented in the study of wave propagation, for example in [47, 149–152]. The spectral element method is similar to the finite element method, in which the structure is analysed using separate elements that describe the behaviour of material or component. However, unlike the finite element method that uses simple harmonic solutions to generate the dynamic stiffness matrix, the spectral element method expresses the dynamic response of the structure using spectral representations [153]. Therefore, the spectral element analysis will provide a dynamic stiffness matrix at each frequency component and the matrix is known as the spectral element matrix or spectral dynamic stiffness matrix.

The spectral element method is best used for beams and plates, and arrangements of these components because shape functions in spectral representation of these elements are well known. A simplified system of a rod-joint structure in Figure 2.31 (a) will be used to show the basic principles of the spectral element method.

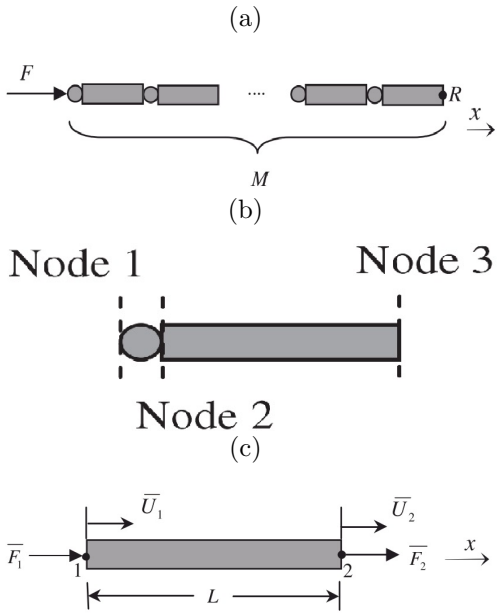



Figure 2.31: (a) Periodic rod-joint structure (b) unit cell of the rod-joint structure (c) rod element [47]

Again, similar to the other methods, the spectral element method seeks to solve the solution describing the dynamic behaviour of the system, the equation for a rod element in Figure 2.31 is

$$\rho \frac{\partial^2 u(x,t)}{\partial t^2} - E \frac{\partial^2 u(x,t)}{\partial x^2} = 0 \tag{2.90}$$

In the spectral element method, the solution of Eq. (2.90) is expressed by the spectral representation, i.e.

$$u(x,t) = \frac{1}{N}\sum_{n=0}^{N-1} U_n(x,\omega_n)e^{i\omega t} \tag{2.91}$$

where $U_n(x,\omega_n)$ is the spectral displacement and $N$ is the number of samples in the time domain. For computing purposes the optimal value for $N$ should be an integer power of 2 [47]. $\omega_n$ is the circular frequency and can be expressed as follows.

$$\omega_n = \frac{2\pi n}{\Delta t\ N} \tag{2.92}$$

Substituting Eq. (2.91) into Eq. (2.91), the equation for each mode can be found.

$$E\frac{\partial^2 U_n}{\partial x^2} + \omega_n \rho U_n = 0 \tag{2.93}$$

Therefore, each spectral displacement has the solution in the form expressed as follows,

$$U_n(x,\omega_n) = A_1 e^{-ik_{Ln}x} + A_4 e^{-ik_{Ln}(L-x)} \tag{2.94}$$

where $k_{Ln}$ is the wave number for a given mode described as follows.

$$k_{Ln} = \omega_n\sqrt{\frac{\rho}{E}} \tag{2.95}$$

For the sake of simplification, the subscript $n$ will be omitted herein. The boundary conditions for the rod, as seen in Figure 2.31, are then defined as follows.

$$\bar{U}_1 = U(x)|_{x=0} \tag{2.96}$$

$$\bar{U}_2 = U(x)|_{x=L} \tag{2.97}$$

where $U(x)$ is the amplitude of the displacement, $u$.

Eq. (2.94), Eq. (2.96), and Eq. (2.97) can then be combined a matrix form:

$$\begin{bmatrix} A_1 \\ A_4 \end{bmatrix} = \frac{1}{1-e^{-i2k_L L}} \begin{bmatrix} 1 & -e^{-ik_L L} \\ -e^{-ik_L L} & 1 \end{bmatrix} \begin{bmatrix} \bar{U}_1 \\ \bar{U}_2 \end{bmatrix} \tag{2.98}$$

This enables the spectral displacement to be expressed as

$$U(x,\omega) = N_{R1}(x,\omega)\bar{U}_1 + N_{R2}(x,\omega)\bar{U}_2 \tag{2.99}$$

where the shape functions $N_{R1}(x,\omega)$ and $N_{R2}(x,\omega)$ are expressed as follows.

$$N_{R1} = \frac{\sin\left(k_L(L-x)\right)}{\sin(k_L L)} \tag{2.100}$$

$$N_{R1} = \frac{\sin\left(k_L x\right)}{\sin(k_L L)} \tag{2.101}$$

It is important to note that the shape function for the spectral element method described here depends on the frequencies instead of just position, as seen in conventional finite element method. Similarly, the force for the rod can be expressed in spectral form.

$$f(x,t) = \frac{1}{N}\sum_{n=0}^{N-1} F(x,\omega_n)e^{i\omega_n t}. \tag{2.102}$$

Using a similar approach as the displacement, the forces can also be expressed in terms of the shape functions.

$$F(x,\omega) = EA\left[\frac{\partial N_{R1}(x,\omega)}{\partial x}\bar{U}_1 + \frac{\partial N_{R2}(x,\omega)}{\partial x}\bar{U}_2\right] \tag{2.103}$$

This allows the force to be related to the displacement described by,

$$\mathbf{S}_R(\omega)\begin{bmatrix}\bar{U}_1\\ \bar{U}_2\end{bmatrix} = \begin{bmatrix}\bar{F}_1\\ \bar{F}_2\end{bmatrix} \tag{2.104}$$

where $\mathbf{S}_R$ is the spectral element stiffness matrix for the rod element defined as follows,

$$\mathbf{S}_R(\omega) = \frac{EA}{L}\frac{ik_L L}{1-e^{-2ik_L L}}\begin{bmatrix}1+e^{-i2k_L L} & -2e^{-ik_L L}\\ -2e^{-ik_L L} & 1+e^{-i2k_L L}\end{bmatrix} \tag{2.105}$$

$$= \frac{EA}{L}\frac{k_L L}{\sin\left(k_L L\right)}\begin{bmatrix}\cos\left(k_L L\right) & -1\\ -1 & \cos\left(k_L L\right)\end{bmatrix} \tag{2.106}$$

The rod element is then combined with the mass for the rod-joint element shown in Figure 2.31 (b), where the joint is treated as a spring-mass element shown in Figure 2.32. They can be combined into a single matrix by enforcing force equilibrium and continuity. This is trivial and will not be described in detail in this thesis. Interested readers may refer to [47].

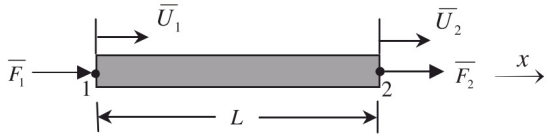



Figure 2.32: Mass spring element for the joint. Reprinted from [141] with kind permission from Elsevier.

The spectral element matrix for the unit cell, $\mathbf{S}_c$, is then expressed as,

$$\mathbf{S}_c(\omega) = \begin{bmatrix} k_{jl} - m_j\omega^2 & -k_{jl} & 0 \\ -k_{jl} & k_{jl} + \frac{EA}{L}\frac{k_L L\cos(k_L L)}{\sin(k_L L)} & -\frac{EA}{L}\frac{k_L L\cos(k_L L)}{\sin(k_L L)} \\ 0 & -\frac{EA}{L}\frac{k_L L\cos(k_L L)}{\sin(k_L L)} & k_{jl} + \frac{EA}{L}\frac{k_L L\cos(k_L L)}{\sin(k_L L)} \end{bmatrix} \tag{2.107}$$

Lastly, the spectral stiffness matrix for $N$ number of unit cells is then combined, as shown schematically in Figure 2.33, to form the global spectral stiffness matrix, which is similar to that for FEM. The matrix dimension is $(2N+1)\times(2N+1)$. The frequency response is obtained by solving the global spectral stiffness matrix.

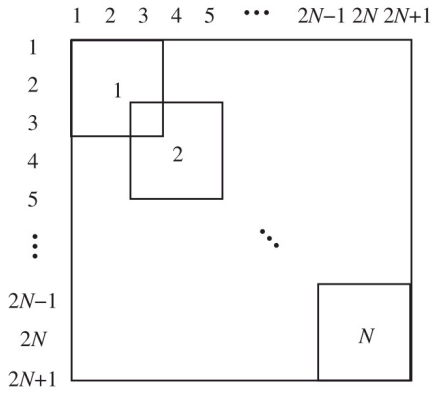



Figure 2.33: Schematic of combining spectral matrices. Reprinted from [141] with kind permission from Elsevier.

The frequency response calculated for the rod-beam structure comparing the spectral element method with finite element method is shown in Figure 2.34.

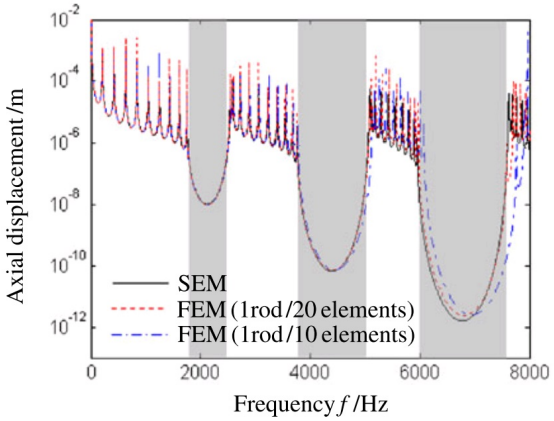



Figure 2.34: Frequency response function of the final node of the system with 10 unit cells. Reprinted from [141] with kind permission from Elsevier.

As seen in Figure 2.34, the calculations made with FEM approaches the SEM results

when more elements per unit rod are used, showing that the SEM with one spectral element is accurate. Additionally, since the SEM only uses a single element per rod, the computational costs of using the finite spectral element is very low, making the SEM method an efficient method to find the response especially for lattice structures made from beams and/or plates. However, a major shortcoming with the SEM is that it is unable to calculate the band structure of the system and the band gaps are determined in the SEM through the frequency response shown in Figure 2.34.

**Summary**

As seen in this chapter, several methods to determine the band structure can be found in the literature. Each of these methods have their strengths and weaknesses and the selection of which method to use is dependent on the type of structure to be studied and the desired information to be obtained from the system. Once of the key considerations while selecting the method is if the complex and evanescent waves are too be studied. If one desires to study the complex and evanescent waves, then one is limited to the transfer matrix (TM) and extended plane wave expansion (EPWE) methods, as these are the only two techniques that can find waves with imaginary wave vectors.

Apart from that, another key consideration is the complexity of the structures. The finite element (FE) and transfer matrix (TM) methods are generally preferable for complicated structures. This is mainly because the stiffness and density for the structure can be represented using finite elements in these methods, which can be easily programmed on a computer. Furthermore, several commercial software are also available construct the required matrices in these methods, which facilitates the analysis. Since the finite element and transfer matrix methods does not require a lot of theoretical background on the subject of wave propagation in periodic medium, they can be used by people who do not have previous experience on this subject. Conversely, methods that require analytical mathematical expressions for the distribution of material or the displacement and stress fields, such as the plane wave expansion (PWE) and multiple scattering theory (MST) are generally not preferable for complicated structures as the required mathematical expression for the fields and material distribution may not be easily found for these structures. Despite not being able to model complicated structures easily, these techniques (PWE and MST) have explicit mathematical expressions for the waves, which gives more insight to the mechanisms on the formation of the band gaps.

Additionally, another consideration is the unique limitations of each method. For example, the PWE method is susceptible to the Gibbs phenomenon if there are step discontinuity in the material properties and is known to have convergence issues for materials with large difference in material properties, while quantisation errors are present in the FE method and may require large number of elements for accurate results. There-

fore, one should avoid using a method for cases where the limitation of the method will significantly reduce the accuracy of the result.

In summary, the selection of the technique one wishes to implement in one's analysis heavily depends on the structure to be studied. Lastly, an important point to note is that among all the methods explored in this section, only the two dimensional Fourier transform can determine the band structure from experimental measurements and this method requires measurements to be taken with high temporal and spatial resolutions, and further post-processing of the data may be required. Thus, one is limited to a single technique if one wishes to find the band structure experimentally from the frequency response functions. Therefore, there is an imperative to devise a simple technique that can measure the band structures from experimental measurements to facilitate the development the field of phononic crystals and elastic metamaterials.

## 2.2 Lightweight periodic lattice materials

### 2.2.1 Introduction

As stated in the previous section, periodic lattice structures can be designed to possess band gaps, which can prevent the transmission of vibrations, as done in [22, 23, 25, 26, 52, 111, 154–157]. In addition to the ability to create band gaps, periodic lattice structure can also be designed to be lightweight structural components, which have high stiffness and strength to density ratios. The benefits of this has been highlighted in [2, 3]. Periodic lattice materials can be used as core materials for sandwich structures and the relevant ratios to be optimised for lightweight structural applications are summarised in Table 2.4. The key requirement of a structural component, such as a beam or plate, is to have either a minimum value of stiffness or strength, which limits the amount of reduction in density that can be achieved. A *strength constrained* component is one where the component is restricted by the requirement to have the strength of component being above a values and a *stiffness constrained* component is one that need to achieve a minimum value of stiffness. As seen in the Ashby charts for stiffness vs density and strength vs density, shown in Figure 2.35 (a) and (b) respectively, lattices made from aluminium possess stiffness and strength parameters that are larger than many classes of materials including alloys, ceramics, and composites. Therefore, lattice materials are ideal to be used as lightweight structural components. Additionally, these lattice structures can be modified by adding local resonators to produce band gaps.

Although metal foams also have high stiffness and strength to density ratios, the stochastic nature of metal foams makes it difficult to design a system with a targeted band gap. Therefore, periodic lattice materials can be designed to possess excellent structural properties and dynamic characteristics enabling them to be used as structural components and vibration isolators. In anticipation of later work in the project to study

| Configuration | Strength Constrained | Stiffness Constrained |
|---|---|---|
| Beam | $\frac{\sigma_f^{\frac{2}{3}}}{\rho}$ | $\frac{E^{\frac{1}{2}}}{\rho}$ |
| Plate | $\frac{\sigma_f^{\frac{1}{2}}}{\rho}$ | $\frac{E^{\frac{1}{3}}}{\rho}$ |

Table 2.4: Ratios to maximise for beam and plate configurations [158].

lightweight components with elastic band gaps, a brief summary of homogenisation techniques used to find the effective properties of this class of material will be given in Section 2.2.2.

There are several common lattice topologies studied in the literature, such as chiral, two dimensional, three dimensional Kagomé, honeycomb, simple cubic, body centre cubic (BCC), face centre cubic (FCC), and octet truss. These lattice topologies are illustrated in Figure 2.36.

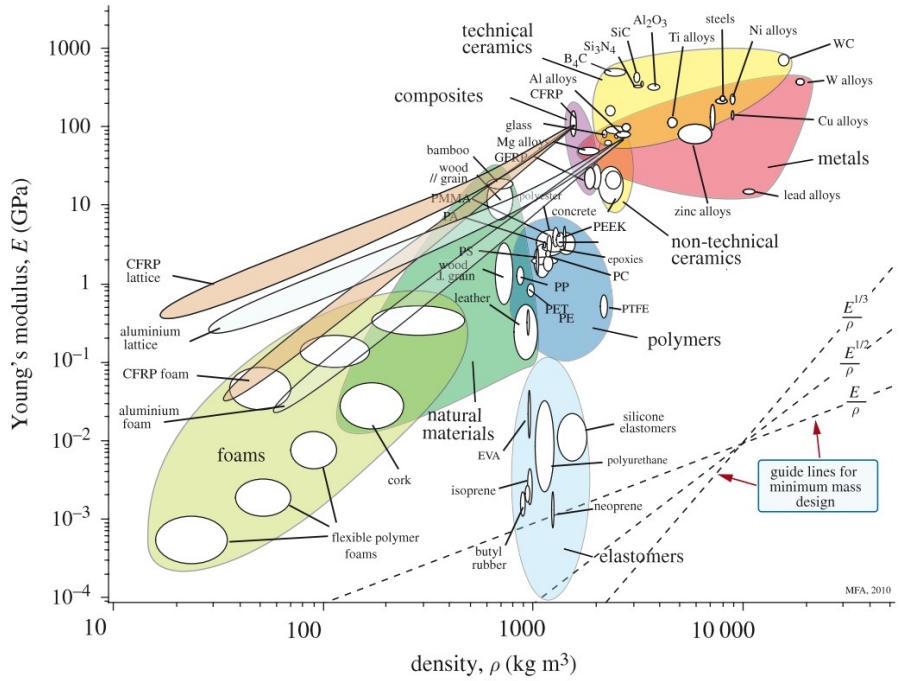
All the lattices shown in Figure 2.36 have significantly high stiffness to density and strength to density ratios, which makes them suitable to be used in sandwich panels and lightweight structure. However, some of the lattices have characteristics that are unique to them. For example, the Kagomé truss lattice is the only known periodic truss structure that have isotropic stiffness [149], while Chiral lattices can be designed to have negative effective Poisson's ratios [52]. Due to the requirement of adding local resonators to produce the band gaps in this project as done in [22], this project will mainly focus on the cubic structures, which are the simple cubic, BCC, FCC, and Octet truss. This is because these structures can be easily manufactured with the 3D printing technology available.

Since one of the key goals of the project is to design lightweight structural components with band gaps, the effective stiffness to density and effective strength to density ratios of the lattice structures are to be evaluated. This can be done using homogenisation techniques.

### 2.2.2 Homogenisation techniques

In general, the characteristic length of a unit cell in a periodic lattice material would be designed to be a few orders of magnitude below the characteristic length of the component, which allows the macroscopic properties of such lattices to be calculated using homogenisation materials. Homogenisation also avoids the need to analyse the entire microstructure of the periodic lattice, which is often impractical [160]. An overview of the homogenisation methods found in the literature will be presented in this section, with emphasis on several notable techniques.

(a)




(b)

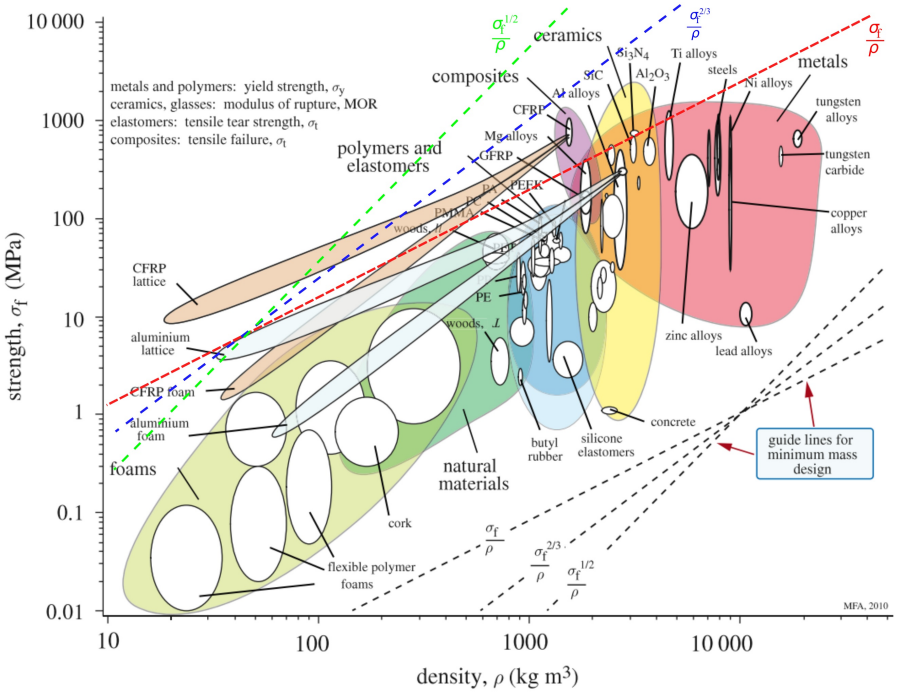



Figure 2.35: Ashby charts (a) Stiffness versus density (b) Strength versus density. Reprinted from [159] with kind permission from the Royal Society Publishing.

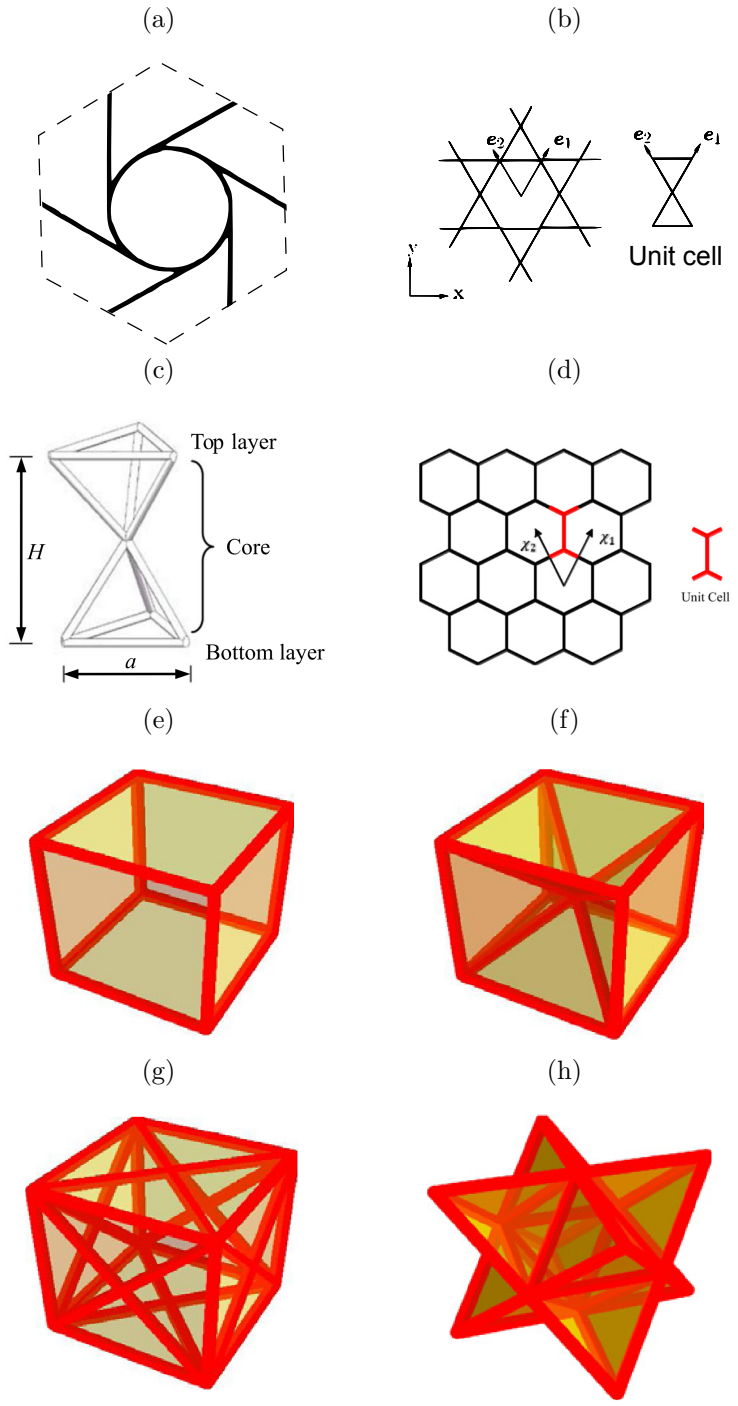



Figure 2.36: Unit cells of common lattice structures (a) Chiral (b) 2D Kagomé (c) 3D Kagomé [149] (d) Honeycomb [23] (e) Simple cubic (f) BCC (g) FCC (h) Octet truss [29]. Reprinted from various sources with kind permission from Elsevier.

### Analytical methods

The simplest form of homogenisation methods are analytical calculations performed by [31, 161–165]. The most basic analytical method is to perform a dimensional analysis using a unit cell as done in [161]. For example, the effective properties of the unit cell shown in Figure 2.37 can be easily calculated by assuming that the unit cells will deform and fail by the same mechanism. Therefore, the effective static density of the lattice material, $\rho^*$, can be calculated by dividing the mass of the total material in the unit cell by the length of the unit cell described by

$$\rho^* = \rho_s t^2 [4l + 2(l - 2t)] \tag{2.108}$$

where $\rho_s$ is the density of the solid material and $l$ and $t$ are dimensions shown in Figure 2.37.

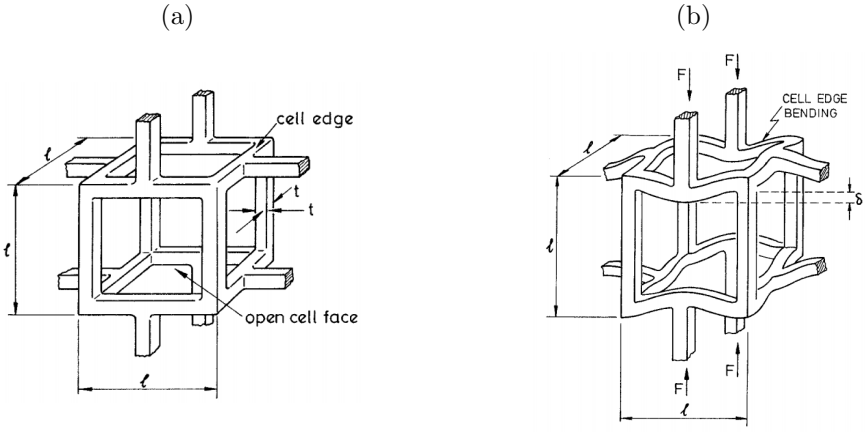



Figure 2.37: (a) Unit cell model (b) Deformed unit cell. Reprinted from [161] with kind permission from Cambridge University Press.

The effective Young's modulus, $E^*$, is then be calculated from the linear-elastic deflection of the beams shown in Figure 2.37. Based on the Timoshenko beam theory that is suitable for both thick and slender beams, the deflection, $\delta$, can be related to the applied uni-axial force, $F$, via the following equation.

$$\delta = \frac{Fl^3}{E_s I} \tag{2.109}$$

where $E_s$ is the Young's modulus of the solid material and $I$ is the second moment of area.

Additionally, the strain, $\varepsilon$, is directly proportional to $\frac{\delta}{l}$ while the stress, $\sigma$, is equal to the force divided by the area of the unit cell. By combining Eq. (2.109) with these relationships, the effective Young's modulus can be expressed as,

$$E^* = \frac{\sigma}{\varepsilon} = \frac{C_1 E_s I}{l^4} \tag{2.110}$$

Using similar analysis, the effective shear modulus, $G^*$, can be expressed as,

$$G^* = \frac{\tau}{\gamma} = \frac{C_2 E_s I}{l^4} \tag{2.111}$$

where $C_1$ and $C_2$ are constants, $\tau$ is the shear stress, and $\gamma$ is the shear strain.

The analytical methods offer a key benefit. The relationships of the effective properties to the geometries are expressed in a closed form solution based on these analyses. Therefore, the properties and their trends can be predicted with very low computational costs. However, several assumptions with the deformation mechanisms were made during the analysis, for example in Eq. (2.109) to Eq. (2.111), the struts were assumed to not buckle and deform like a Timoshenko beam. Some of the assumptions may be simplified and will only be accurate for simple arrangements of the unit cells [160]. Although, more thorough analysis can be performed by taking into account other deformation mechanisms or defects, such as curvature or waviness of the struts as seen in [165], in order to improve the accuracy of the predictions.

### Matrix-based techniques

Another type of homogenisation technique are the matrix-based techniques using the Cauchy-Born hypothesis as done in [166, 167]. The homogenisation technique in [166] will be used as an example for matrix-based techniques in this thesis. The technique in [166] was developed based on the equilibrium matrix analysis methods found in [168].

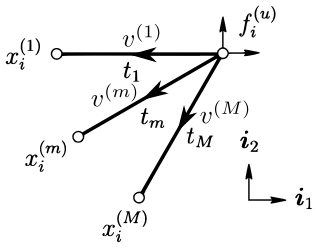



Figure 2.38: Truss structure showing joint equilibrium. Reprinted from [166] with kind permission from Elsevier.

The analysis starts by defining the equilibrium matrix, $\mathbf{A}$, and kinematic matrix, $\mathbf{B}$, for an arbitrary structure. For a structure with $M$ bars and an unconstrained joint $u$ as shown in Figure 2.39, the equilibrium equation is expressed as follows,

$$\sum_{m=1}^{M} \frac{x_i^{(m)} - x_i^{(u)}}{L_m} \cdot T_m = \sum_{m=1}^{M} v^{(m)} \cdot T_m \equiv \sum_{m=1}^{M} C_i^{(m)} \cdot T_m = f_i^u \tag{2.112}$$

where $i$ denotes the joint number, $m$ is the bar number, $L_m$ is the length of the $m^{th}$ bar, $T_m$ is the tension in the $m^{th}$ bar, $v^{(j)}$ is the unit vector describing the direction of the bar, $C_i^{(m)}$ is the $i^{th}$ component of the $m^{th}$ direction cosine vector, and $f_{i^u}$ are the forces at the unconstrained joints.

Eq. (2.112) can be simplified as follows,

$$\mathbf{A} \cdot \mathbf{T} = \mathbf{f} \tag{2.113}$$

Similarly, the elongation of each bar defined in Eq. (2.114) gives rise to the kinematic matrix, $\mathbf{B}$.

$$e_m = \sum_{i=1}^{n} C_i^{(m)} \cdot \left( d_i^{(b)} - d_i^{(u)} \right) \tag{2.114}$$

where $e$ is the elongation of each bar, $b$ is the bar number, and $d$ is the infinitesimal joint displacement.

$$\mathbf{B} \cdot \mathbf{d} = \mathbf{e} \tag{2.115}$$

Eq. (2.115) has been proven in Chapter 3.4 of [169] that $\mathbf{B} = \mathbf{A}^T$, where $T$ denotes the transpose, by applying the virtual work principle. This is known as contragredience [169]. A unit cell, for example the Kagomé lattice, was selected and the Bloch's theorem was applied to these equations for the unit cell to analyse the infinite structure and perform the necessary homogenisation.

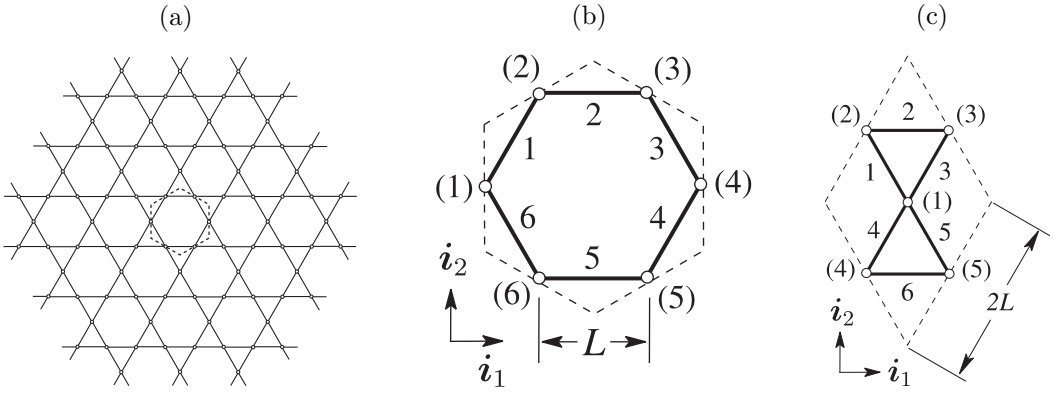



Figure 2.39: (a) Kagomé lattice (b) Primitive unit cell (c) Alternative unit cell. Reprinted from [166] with kind permission from Elsevier.

Prior to implementing the Bloch's theorem, several translation basis and vectors are to be defined. For a primitive cell, for example in Figure 2.39 (b), a *direct translational basis*, $\{\mathbf{a}_k\}$, can be defined and is illustrated in Figure 2.40 (a). The *reciprocal lattice basis*, $\{\mathbf{a}^k\}$, relates the lattice to the reciprocal space and relates to the direct translation basis by $\{\mathbf{a}^j\} \cdot \{\mathbf{a}_k\} = \delta_j^k$, where $\delta_j^k$ is the Kronecker delta. Tessellation of the unit cell

can be made by translating the unit cell by the basis vector, $\{\mathbf{a}_k\}$. Therefore, the neighbouring cells of a reference cells can be reached by performing a translation using a *direct translational vector*, $\mathbf{x}$, defined by

$$\mathbf{x} \equiv x^k \mathbf{a}_k \tag{2.116}$$

where $x^k$ is an integer, i.e. $k = 1, 2, 3$ in three dimensions.

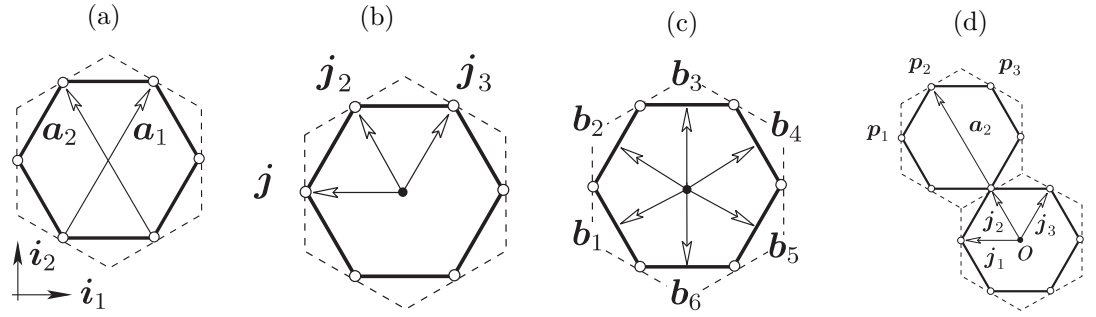



Figure 2.40: Kagomé lattice bases: (a) direct translation vectors (b) joint vectors (c) bar vectors (d) illustration of lattice position vectors. Reprinted from [166] with kind permission from Elsevier.

The *joint basis*, $\{\mathbf{j}_l\}$, as shown in Figure 2.40 (b), is used to define the locations of the independent nodes while the *bar basis*, $\{\mathbf{b}_m\}$, is used to define the location of the mid-points of the independent bars, as shown in Figure 2.40 (c). Lastly, the joint location is defined by $\mathbf{p}_l$, which is illustrated in Figure 2.40 (d) and defined by

$$\mathbf{p}_l = \mathbf{j}_l + \mathbf{x} = \mathbf{j}_l + x^k \mathbf{a}_k. \tag{2.117}$$

With all the definitions for the basis and vectors, the displacements fields of infinite structures can be analysed. This is first done by using Bloch's theorem to define the joint displacement field, $\mathbf{d}$, of the entire lattice via

$$\mathbf{d}\left(\mathbf{p}_l, \mathbf{w}\right) \equiv \mathbf{d}\left(\mathbf{j}_l + \mathbf{x}, \mathbf{w}\right) = \mathbf{d}\left(\mathbf{j}_l, \mathbf{w}\right) \exp\left(2\pi i \mathbf{w} \cdot \mathbf{x}\right) \tag{2.118}$$

where $\mathbf{w}$ is the wave vector defined by

$$\mathbf{w} \equiv w_\alpha \mathbf{a}^\alpha \tag{2.119}$$

where $0 \leq w_\alpha < 1$

The Bloch's theorem is used to form the set of all possible periodic and non-periodic mechanisms across all possible wavelengths that produces macroscopic strains. The Bloch wave theory used in Eq. (2.117) is an extension of Triantafyllidis's work [170] and further details on the background of Bloch's theorem can be found in [171, 172].

For an infinite structure, the kinematic matrix in Eq. (2.115) can be constructed by

assuming that the unit cell has no external kinematic constraints. The kinematic matrix can then be reduced by first imposing periodicity. The periodic joint pairs on the unit cell boundary is then separated by the unit cell translation vectors defined by

$$\hat{\mathbf{x}} = \hat{x}^{\alpha}\mathbf{a}_{\alpha} \tag{2.120}$$

so that the linearly independent joint basis, $\{\mathbf{j}_l\}$, defines the joint basis of the dependent joints, $\{\mathbf{j}_l + \hat{\mathbf{x}}_l\}$.

Applying the joint dependencies on Eq. (2.118) will result in

$$\mathbf{d}\left(\mathbf{j}_l + \mathbf{x}_l, \mathbf{w}\right) = z\left(\mathbf{w}, \hat{\mathbf{x}}_l\right)\mathbf{d}\left(\mathbf{j}_l, \mathbf{w}\right) \tag{2.121}$$

where $z$ is a scalar complex function defined as

$$z\left(\mathbf{w}, \hat{\mathbf{x}}_l\right) = \exp 2\pi i \mathbf{w} \cdot \hat{\mathbf{x}}_l \tag{2.122}$$

Eq. (2.115) can then be reduced by inserting Eq. (2.121) to form,

$$\bar{\mathbf{B}}\left(\mathbf{w}\right) \cdot \bar{\mathbf{d}}\left(\mathbf{w}\right) = \bar{\mathbf{e}}\left(\mathbf{w}\right) \tag{2.123}$$

The calculation of the four fundamental subspaces of $\bar{\mathbf{B}}$ will enable one to analyse the displacement field of an infinite lattice. The null space of $\bar{\mathbf{B}}$ is a linearly independent basis for all $\bar{\mathbf{d}}$ that is compatible with no bar elongations. This suggests that the null vector $\bar{\mathbf{d}}$ describes the *periodic mechanism* of the lattice with wave vector $\mathbf{w}$. The row space of $\bar{\mathbf{B}}$ is a basis spanning all joint displacement vectors $\bar{\mathbf{d}}$ that are compatible when bar elongation occurs, while the column space of $\bar{\mathbf{B}}$ spans all geometrically compatible reduced bar elongation vectors. Lastly, the left null space of $\bar{\mathbf{B}}$ spans all geometrically incompatible bar elongation vectors for each assumed value of $\mathbf{w}$.

A similar approach can be used to reduce Eq. (2.113) to

$$\bar{\mathbf{A}}\left(\mathbf{w}\right) \cdot \bar{\mathbf{T}} = \bar{\mathbf{f}}. \tag{2.124}$$

Again the principle of virtual work implies that $\bar{\mathbf{A}} = \bar{\mathbf{B}}^{H}$ where the superscript $H$ denotes the Hermitian transpose. Since the formulations in Eqs. (2.123) and (2.124) are linear Fourier series representations, joint displacements can be found as follows.

$$\mathbf{d}\left(\mathbf{p}_l\right) = \mathbf{d}\left(\mathbf{j}_l + \mathbf{x}\right) = \sum_{\mathbf{w}\in\mathbb{W}} \mathbf{d}\left(\mathbf{j}_l\right) \exp\left(2\pi i \mathbf{w} \cdot \mathbf{x}\right) \tag{2.125}$$

where $\mathbb{W}$ is the first Brillouin zone in the reciprocal space.

Eq. (2.125) will give all possible displacements for infinite lattice structure. The calculated displacement field describes the periodic mechanisms within the lattice structure. In order to determine the required effective stiffness of the lattice structures the *Cauchy-*

*Born hypothesis* was first implemented to calculate the strain-producing mechanisms as done in [166]. According to the Cauchy-Born hypothesis, "the infinitesimal displacement fields of the periodic truss can be additively decomposed into an affine deformation field of the joints as dictated by the macroscopically homogeneous strain, $\bar{\boldsymbol{\varepsilon}}$, and into a displacement field which repeats from one cell to the next." [166] Therefore, the displacement of any unit cell can be defined by,

$$\mathbf{d}\left(\mathbf{j}_l + \hat{\mathbf{x}}_l\right) = \bar{\boldsymbol{\varepsilon}} \cdot \hat{\mathbf{x}}_l + \mathbf{p}\left(\mathbf{j}_l\right) \tag{2.126}$$

where $\hat{\mathbf{x}}_l$ is calculated from Eq. (2.120) and the vector field $\mathbf{p}\left(\mathbf{j}_l\right)$ is unit cell periodic.

By inserting Eq. (2.126) into Eq. (2.115), a reduced kinematic matrix relationship can be formed

$$\bar{\mathbf{B}} \cdot \bar{\mathbf{d}} = \bar{\mathbf{e}} \tag{2.127}$$

The four fundamental subspaces of $\bar{\mathbf{B}}$ are then calculated as described previously. Additionally, it is important to note that the static boundary conditions for the assumed kinematics in Eq. (2.126) is that the *macroscopic tractions*, $\bar{\boldsymbol{\sigma}} \cdot n$, are equal and opposite on the opposite faces of the unit cell boundary. Therefore, the macroscopic tractions are anti-periodic over the unit cell, which can be expressed as follows for the joints and bars.

$$\mathbf{f}\left(\mathbf{j}_l + \hat{\mathbf{x}}_l\right) + \mathbf{f}\left(\mathbf{j}_l\right) = \mathbf{0} \tag{2.128}$$

$$\mathbf{T}\left(\mathbf{b}_m + \hat{\mathbf{x}}_l\right) - \mathbf{T}\left(\mathbf{b}_m\right) = \mathbf{0} \tag{2.129}$$

The implementation of Eqs. (2.128) and (2.129) into the unit cell equilibrium matrix, Eq. (2.123), gives rise to the states of self-stress.

Lastly, the macroscopic stiffness of the lattice is calculated from the macroscopic strain energy density in [166]. For a periodic structure made from bars, in which the unit cell has an area of $S$ and $b$ bars. The existence of a *macroscopic (or effective)* strain energy density, $W$, is defined as,

$$W\left(\bar{\boldsymbol{\varepsilon}}\right) = \frac{1}{2}\bar{\boldsymbol{\sigma}}(\bar{\boldsymbol{\varepsilon}}) \colon \bar{\boldsymbol{\varepsilon}} = \frac{1}{2S} T_k(\bar{\boldsymbol{\varepsilon}}) e_k(\bar{\boldsymbol{\varepsilon}}) \tag{2.130}$$

Assuming that the bars are deformed axially, i.e.

$$T_k = \frac{EA}{L} e_k \tag{2.131}$$

where $E$ is the Young's modulus of a bar, $A$ is the cross sectional area of the bar, and $L$ is the length of the bar.

Kinematic and constitutive linearity dictates that $W\left(\bar{\boldsymbol{\varepsilon}}\right)$ is quadratic in $\bar{\boldsymbol{\varepsilon}}$. Therefore, the stress is defined as,

$$\bar{\boldsymbol{\sigma}}(\bar{\boldsymbol{\varepsilon}}) = \frac{\partial W(\bar{\boldsymbol{\varepsilon}})}{\partial \bar{\boldsymbol{\varepsilon}}} = \bar{\mathcal{L}} \colon \bar{\boldsymbol{\varepsilon}} = \frac{EA}{LS} e_k(\bar{\boldsymbol{\varepsilon}}) \frac{\partial e_k(\bar{\boldsymbol{\varepsilon}})}{\partial \bar{\boldsymbol{\varepsilon}}} \tag{2.132}$$

where $\bar{\mathcal{L}}$ is a fourth-order, linear elastic, and the *macroscopic stiffness tensor* is defined as,

$$\bar{\mathcal{L}}_{\alpha\beta\gamma\delta} = \frac{\partial^2 W(\bar{\boldsymbol{\varepsilon}})}{\partial \bar{\varepsilon}_{\alpha\beta} \partial \bar{\varepsilon}_{\gamma\delta}} = \frac{EA}{LS} \frac{\partial e_k(\bar{\boldsymbol{\varepsilon}})}{\partial \bar{\varepsilon}_{\alpha\beta}} \frac{\partial e_k(\bar{\boldsymbol{\varepsilon}})}{\partial \bar{\varepsilon}_{\gamma\delta}} \tag{2.133}$$

The macroscopic stiffness tensor is the effective stiffness of the lattice material.

### Generalised matrix method

Apart from the method introduced by R.G. Hutchinson [166] that was just described, Vigliotti and Pasini [29] have developed a generalised matrix method. Their method uses a multiscale approach without making assumptions on the internal nodes of the unit cell. They have also take into account several different modes of failure, including the elastic buckling of the periodic structure. This allows their method to be used to calculate the buckling and plastic yielding stresses in addition to the effective stiffness.

According to [29], a lattice structure material has at least two length scales: the macroscopic length scale, which is the length scale of the component, and the microscopic length scale, which is the length scale of the unit cell. Here, the variation of the strain energy calculated using the constitutive relationship of the material must equate to the variation of the potential energy by the external forces in the virtual work material. For a lattice material this relationship between the macroscopic stress and strains cannot be expressed directly as a functional dependence, so a boundary value problem is formulated to calculate the required lattice strain energy in terms of the macroscopic strain.

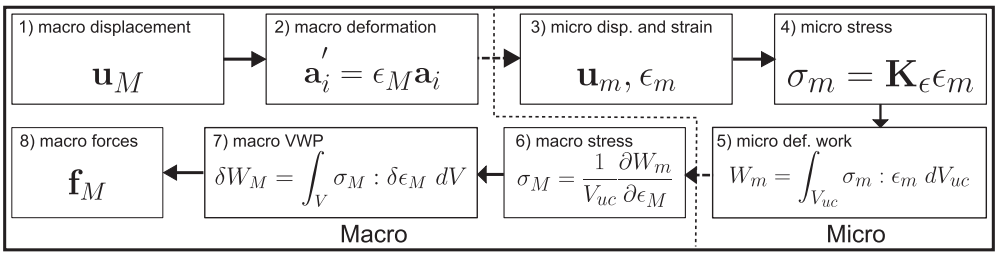



Figure 2.41: Modelling approach [29]. Reprinted with kind permission from Elsevier.

The multiscale approach developed by [29], is summarised as a flow chart in Figure 2.41. In this scheme, the macroscopic forces are to be found based on a given macroscopic displacements and the relationship between macroscopic forces and displacements will allow the effective stiffness of the properties to be determined. The analysis starts by finding a relationship between the microscale deformation from a

known applied macroscopic deformation. In Steps 1 to 3, the Cauchy strain tensor, $\epsilon_M$, and the deformed lattice periodic vectors, $\mathbf{a}_i$, are first determined from the known the macroscopic displacements, $\mathbf{u}_M$. This allows the microscale displacements of the unit cell nodes to be expressed as a function of the macroscopic strain. The microscale stress of the uniform solid material within the members of the lattice is then determined by applying Hooke's law to the microscopic strain field in Step 4 of Figure 2.41. Then in Step 5, the microscopic deformation work is calculated using a finite element model of the unit cell. The macroscopic stress tensor, which is the gradient of the strain energy density with respect to the macroscopic strain, is then determined in Step 6. Lastly, the macroscopic forces are determined by applying the virtual work principle at the macroscopic level.

In order to define the equilibrium problem of the unit cell, a kinematic condition to preserve the periodicity of the unit cell boundaries and a static condition to ensure the equilibrium of the confining cells were imposed. This allows the analysis of any arbitrary lattice. Once the unit cell equilibrium formulation is solved, the deformation work and forces in the cell elements can then be determined as a function of the macroscopic strain tensor.

The macroscopic stress field can be determined from the virtual work principle on the unit cell and assuming that the virtual work at the macroscopic quantities are uniform across the unit cell, i.e.

$$\delta W = \int_{V_{uc}} \boldsymbol{\sigma}_m \colon \delta \boldsymbol{\epsilon}_m dV_{uc} = V_{uv} \boldsymbol{\sigma}_M \colon \delta \boldsymbol{\epsilon}_M \tag{2.134}$$

where $V_{uc}$ is the volume of the unit cell, and the subscripts $m$ and $M$ denote the micro and macro scale properties.

The macroscopic stress tensor, $\boldsymbol{\sigma}_M$, is defined as

$$\boldsymbol{\sigma}_M = \frac{1}{V_{uc}} \frac{\partial W}{\partial \boldsymbol{\epsilon}_M} \tag{2.135}$$

For a linear elastic material, the lattice stiffness matrix, $K_\epsilon$, can be calculated as the Hessian of the deformation work with respect to the components of the macroscopic deformation tensor. The derivation of the required equations for a unit cell of a lattice structure, as shown in Figure 2.42, are described in this section.

Firstly, periodic boundary conditions are applied to a unit cell of an infinite lattice by applying the kinematic constraints to the nodes at the cell boundaries. The position, $\mathbf{r}_k$, within an infinitely periodic cell is linked to the corresponding position of a reference unit cell, $\mathbf{r}_0$, using periodic vectors, $\mathbf{a}_i$. This can be expressed as follows,

$$\mathbf{r}_k = \mathbf{r}_0 + k_i \mathbf{a}_i; \; i = 1, 2, 3 \tag{2.136}$$

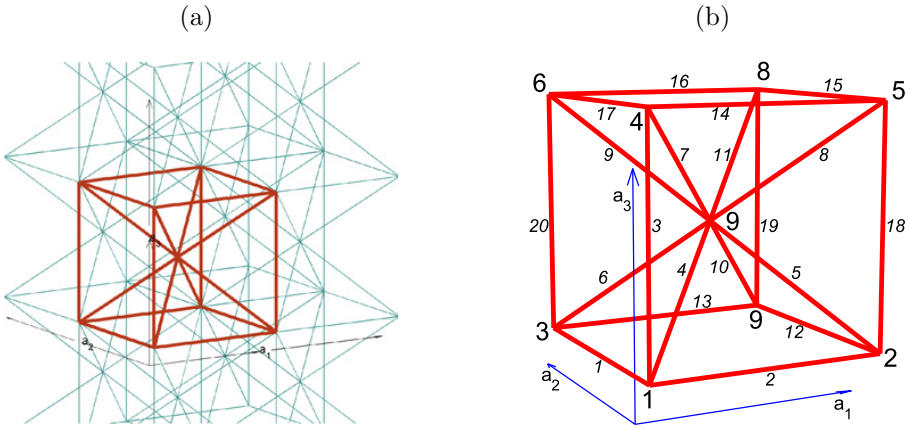



Figure 2.42: (a) Example BCC lattice (b) Unit cell. Reprinted from [29] with kind permission from Elsevier.

where $k$ refers to the unit cell $k$.

Similarly, the deformed position of the lattice can be written as

$$\mathbf{r}'_k = \mathbf{r}'_0 + k_i \mathbf{a}'_i \tag{2.137}$$

The displacements are determined by subtracting Eq. (2.137) from Eq. (2.136).

$$\mathbf{u}'_k = \mathbf{u}'_0 + k_i \Delta\mathbf{a}_i \tag{2.138}$$

There are two types of nodes: the internal nodes that connect the elements in the unit cells and the boundary nodes that connects the element to the adjacent cell. The boundary nodes must correspond along the periodic vectors, therefore only a subset of the unit cell nodes is required to generate all the nodes of the lattice. Hence, the independent nodes will be made from only a selection of boundary nodes. The displacements of all the nodes, $\mathbf{d}$, in the lattice can be expressed as a function of the displacements of the independent nodes, $\mathbf{d}_0$, i.e.

$$\mathbf{d} = \mathbf{B}_0 \mathbf{d}_0 + \mathbf{B}_a \Delta\mathbf{a}_i \tag{2.139}$$

where $\Delta\mathbf{a}_i$ is a matrix of all the $\Delta\mathbf{a}_i$ vectors, $\mathbf{B}_0$ and $\mathbf{B}_a$ are block matrices determined by the lattice topology, details relating to $\mathbf{B}_0$ and $\mathbf{B}_a$ can be found in [29].

For a linear elastic material the forces can be expressed as

$$\mathbf{F} = \mathbf{K}_{uc} \mathbf{d} \tag{2.140}$$

where $\mathbf{K}_{uc}$ is the unit cell stiffness matrix.

In order to satisfy static equilibrium of the infinite lattice for the deformed material, the internal forces must be equal to the external forces, which results in

$$\mathbf{A}_0\mathbf{F} = \mathbf{A}_0\mathbf{K}_{uc}\mathbf{d} = \mathbf{0} \tag{2.141}$$

where $\mathbf{A}_0$ is a block matrix equal to the transpose of $\mathbf{B}_0$.

Proof for the equation Eq. (2.141) can be found in [29] and substituting Eq. (2.141) into Eq. (2.139) gives

$$\mathbf{B}_0^T\mathbf{K}_{uc}\left(\mathbf{B}_0\mathbf{d}_0 + \mathbf{B}_a\Delta\mathbf{a}\right) = \mathbf{0} \tag{2.142}$$

Rearranging Eq. (2.142), the following equation for the independent degrees of freedom can be found.

$$\mathbf{B}_0^T\mathbf{K}_{uc}\mathbf{B}_0\mathbf{d}_0 = -\mathbf{B}_0^T\mathbf{K}_{uc}\mathbf{B}_a\Delta\mathbf{a} \tag{2.143}$$

The left side of Eq. (2.143) represents the unbalance forces due to $\mathbf{d}_0$ to preserve the periodic vectors, while the right hand side represents the unbalance forces that causes the variation of the periodic vectors if the independent degrees of freedom, $\mathbf{d}_0$, is set to 0. Hence, the solution of this equation is an array of independent degree of freedoms of the unit cells that equilibrates the forces from the surrounding cells to that originated by the lattice deformation. The matrix $\mathbf{B}_0^T\mathbf{K}_{uc}\mathbf{B}_0$ represents the constrained stiffness matrix of the unit cell, which is the effective stiffness when the constrains imposed on the unit cell by the surrounding cells are taken into account.

There is a non-trivial but not unique solution to Eq. (2.143). The solution represents an affine space [29] and is given by

$$\mathbf{d}_0 = -\left(\mathbf{B}_0^T\mathbf{K}_{uc}\mathbf{B}_0\right)^+\mathbf{B}_0^T\mathbf{K}_{uc}\mathbf{B}_a\Delta\mathbf{a} = \mathbf{D}_0\Delta\mathbf{a} \tag{2.144}$$

where the superscript + denotes the Moore-Penrose pseudo-inverse. Combining Eqs. (2.139) and (2.144) the generalised displacement fields of the unit cell can be found.

$$\mathbf{d} = (\mathbf{B}_0\mathbf{D}_0 + \mathbf{B}_a)\Delta\mathbf{a} = \mathbf{D}_a\Delta\mathbf{a} \tag{2.145}$$

Eq. (2.145) is then used to evaluate the deformation work of the unit cell, which will allow the expression of the lattice stiffness to be determined.

$$W = \frac{1}{2V}\mathbf{d}^T\mathbf{K}_{uc}\mathbf{d} = \frac{1}{2V}\Delta\mathbf{a}^T\mathbf{D}_a^T\mathbf{K}_{uc}\mathbf{D}_a\Delta\mathbf{a} = \frac{1}{2V}\Delta\mathbf{a}^T\mathbf{K}_{\Delta a}\Delta\mathbf{a} \tag{2.146}$$

where $V$ is the volume of the unit cell.

In order to determine the lattice macroscopic stiffness, the deformation work in terms of the uniform macroscopic strain field acting on the lattice must be found. The Cauchy strain tensor allows the periodic vectors to be related to the macroscopic strain field.

$$\mathbf{a}' = (\mathbf{I} + \boldsymbol{\epsilon}_M)\mathbf{a} \Rightarrow \Delta\mathbf{a} = \boldsymbol{\epsilon}_M \mathbf{a} \tag{2.147}$$

where $\boldsymbol{\epsilon}_M$ is the Cauchy strain tensor and $\Delta\mathbf{a}$ is defined as

$$\Delta\mathbf{a} = \mathbf{B}_\epsilon \epsilon_M \tag{2.148}$$

where $\mathbf{B}_\epsilon$ is a matrix relating the lattice lengths to the strains and is analogous to shape functions.

Substituting Eq. (2.148) into the deformation work in Eqs. (2.145) and (2.146). The unit cell nodal degrees of freedom and the deformation work can be expressed as a function of the macroscopic strain field components as follows.

$$\mathbf{d} = \mathbf{D}_a \mathbf{B}_\epsilon \epsilon_M = \mathbf{D}_\epsilon \epsilon_M \tag{2.149}$$

$$W = \frac{1}{2V} \epsilon_M^T \mathbf{B}_\epsilon^T \mathbf{K}_{\Delta a} \mathbf{B}_\epsilon \boldsymbol{\epsilon}_M \tag{2.150}$$

The macroscopic stiffness is the Hessian of the strain energy defined by

$$K_{ijkl} = \frac{\partial^2 W}{\partial \epsilon_{ij} \partial \epsilon_{kl}} \tag{2.151}$$

which means that the lattice stiffness can be expressed as

$$\mathbf{K}_\epsilon = \frac{1}{V} \mathbf{B}_\epsilon^T \mathbf{K}_{\Delta a} \mathbf{B}_\epsilon \tag{2.152}$$

In order to assess the yield strength of the lattice structure, the deformation of the individual struts with respect to the macroscopic stress is first calculated for a given loading condition via

$$\mathbf{d} = \mathbf{D}_\epsilon \mathbf{C}_\epsilon \boldsymbol{\sigma}_M \tag{2.153}$$

where $\mathbf{C}_\epsilon = \mathbf{K}_\epsilon^{-1}$ is the lattice compliance matrix.

Then, the microscopic stresses of each strut are calculated from the microscopic displacements determined from the previous equations over a range of magnitudes. The lattice is thought to have failed when the microscopic stress at any point of the member reaches the yield stress of the material. In short, the entire lattice is considered to have failed when any part of it fails. The macroscopic yield stress when this occurs is set to be the failure stress for the yielding of the lattice structure.

Apart from material yielding, the periodic lattice structures may fail by local buckling. According to [173], buckling of structural components occurs when the membrane forces, which are the forces acting along the axis of the component, reaches a critical condition that results in the conversion of the membrane strain energy into the bending strain

energy with no addition externally applied load. The critical conditions for buckling can be found by introducing a stress stiffness matrix, also known as the geometric stiffness matrix, $\mathbf{K}_\sigma$, and solving the following eigenvalue problem

$$(\mathbf{K} + \lambda \mathbf{K}_\sigma)\,\mathbf{x} = 0 \tag{2.154}$$

where $\mathbf{K}$ are the stiffness matrix of the structure.

The geometric stiffness matrix, $\mathbf{K}_\sigma$, represents the increase in bending stiffness due to the membrane forces and the component buckles when $\lambda$ reaches a critical value of 1 or higher in Eq. (2.154), which suggests that buckling occurs when the compressive membrane forces are sufficiently large to overcome the stiffness of the component. Further details on the buckling of structures can be found in Chapter 14 of [173].

Eq. (2.154) is an common method to determine buckling with finite element analysis and is used in [29] and this thesis to determine the bucking strength, the buckling loads, and the buckling modes of the lattice structure.

For a periodic structure, the global critical loads are calculated by first considering the effective loads on a single cell and its constraints induced by the surrounding cells. For a given macroscopic loading condition, the stress stiffness matrix is obtained by imposing node displacements. Additionally, the periodic boundary conditions in Eq. (2.154) represent the constrained stiffness matrix of the unit cell. Therefore, the buckling loads for the lattice can be found by solving the following equation.

$$\left(\mathbf{B}_0^T \mathbf{K}_{uc} \mathbf{B}_0 + \lambda \mathbf{B}_0^T \mathbf{K}_{Uc\sigma} \mathbf{B}_0\right) \mathbf{d}_0 = 0 \tag{2.155}$$

where $\mathbf{K}_{Uc}$ is the unconstrained stress stiffness matrix of the unit cell.

In order to obtain the buckling loads and modes, the stress stiffness matrix is first calculated for a given macroscopic stress field, followed by the calculation of the eigenvalues and eigenvectors for Eq. (2.155). The lattice is assumed to buckle if the eigenvector $\lambda$ reaches a critical value of $\lambda_{cr} = 1$.

The generalised method described in [29], has several benefits, firstly since the required matrices can be obtained via finite element, this technique can be easily implemented with stiffness matrices extracted from finite element software. Additionally, as seen in [29], the member struts can be described using analytical solutions of beams allowing analytical solutions to be found. Lastly, the method allows the calculation of the macroscopic failure stress and all the components of the stiffness matrix.

#### Asymptotic homogenisation (AH)

Apart from the matrix-based methods, asymptotic homogenisation (AH) is also a method to obtain the effective properties of the lattice materials, as done in [160, 174–176]. In the AH method, any field quantity, for example stress, can be expressed as an asymp-

totic expansion. The asymptotic expansion then replaces the equilibrium equations to determine the effective properties of the material [160]. A unique advantage of AH is that it can accurately calculate the stress distribution in the unit cell, which can be used to performed a detailed analysis of the strength and damage of heterogeneous periodic materials [160, 177, 178]. The AH method can also be applied to periodic lattices with any relative density [160].

The AH method obtains the effective properties using representative volume element (RVE) analysis, which represents a representative portion of the material as illustrated in Figure 2.43. The periodic microstructure, $\Omega^{\varepsilon}$, is assumed to be a homogeneous body $\Omega$ with no internal geometrical details and voids, in which the external and traction boundaries are applied to $\Omega^{\varepsilon}$. The periodic microstucture is assumed to be subjected to the traction $T$ at the traction boundary $\Gamma_t$, a displacement $d$ at the displacement boundary $\Gamma_d$, and a body force $f$ across the material, as shown in Figure 2.43.

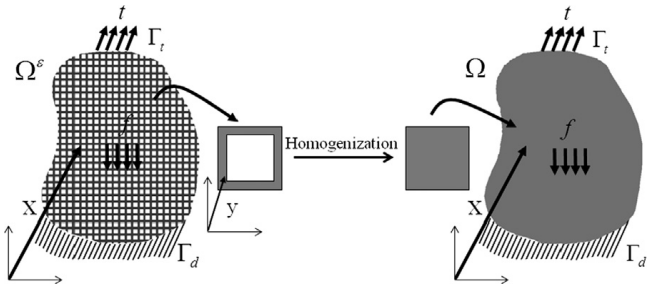



Figure 2.43: RVE analysis concept. Reprinted from [160] with kind permission from Elsevier.

The key assumption of the AH method is that each field quantity depends on two different scales, which are the macroscopic level $x$ and on the microscopic level $y = \frac{x}{\epsilon}$, where $\epsilon$ is a magnification factor that scales the dimensions of the RVE, generally known as the periodic or unit cell, to the macroscale material dimensions [160]. Another assumption is that field quantities vary smoothly at the macroscopic level and are periodic at the microscale [160].

This allows the field, such as the displacement field, $u$, to be expanded into a power series with respect to a small parameter, $\epsilon$, i.e.

$$u^{\epsilon}(x) = u_0(x, y) + \epsilon u_1(x, y) + \epsilon^2 u_2(x, y) + \cdots \tag{2.156}$$

where the functions $u_n$ are Y-periodic with respect to local coordinate $y$.

The small deformation strain tensor, $\varepsilon(u)$, is found by taking the derivative of the asymptotic expansion of the displacement field with respect to $x$ and using the chain rule.

$$\varepsilon(u) = \frac{1}{2}\left[(\nabla u_0^T + \nabla u_0)_x + (\nabla u_1^T + \nabla u_1)_y\right] + O(\varepsilon). \tag{2.157}$$

Eq. (2.156) is simplified after neglecting the higher order terms, $O(\varepsilon)$, as

$$\varepsilon(u) = \bar{\varepsilon} + \varepsilon^*(u) \tag{2.158}$$

where $\bar{\varepsilon}$ and $\varepsilon^*$ are the macroscopic strain and the periodically varying fluctuating strain at the microscale level respectively. They are defined as follows

$$\bar{\varepsilon}(u) = \frac{1}{2}\left(\nabla u_0^T + \nabla u_0\right)_x, \tag{2.159}$$

$$\varepsilon^*(u) = \frac{1}{2}\left(\nabla u_1^T + \nabla u_1\right)_y. \tag{2.160}$$

Substituting Eq. (2.158) into the standard weak form of the equilibrium equations for the cellular body $\Omega^\varepsilon$ gives

$$\int_{\Omega^\varepsilon} \left(\varepsilon^0(v) + \varepsilon^1(v)\right)^T E\left(\bar{\varepsilon}(u) + \varepsilon^*(u)\right)^T d\Omega^\varepsilon = \int_{\Lambda_T} T^T v d\Gamma \tag{2.161}$$

where $E$ is the local elasticity tensor, $\varepsilon^0$ and $\varepsilon^1$ are the virtual macroscopic and microscopic strains, and $v$ is the virtual displacement.

Assuming that virtual displacements only vary on the microscopic level, the microscopic equilibrium can then be written as

$$\int_{\Omega^\varepsilon} \left(\varepsilon^1(v)\right)^T E\left(\bar{\varepsilon}(u) + \varepsilon^*(u)\right)^T d\Omega^\varepsilon = 0. \tag{2.162}$$

By taking the integral over the RVE volume, Eq. (2.162) can then be rewritten as

$$\int_{V_{\mathrm{RVE}}} \left(\varepsilon^1(v)\right)^T E\left(\varepsilon^*(u)\right)^T dV_{\mathrm{RVE}} = -\int_{V_{\mathrm{RVE}}} \left(\varepsilon^1(v)\right)^T E\left(\bar{\varepsilon}(u)\right) dV_{\mathrm{RVE}}. \tag{2.163}$$

Eq. (2.163) is a local problem defined on the RVE and can be discretised using finite element analysis. The material can be characterised for a given applied macroscopic strain if the fluctuating strain, $\varepsilon^*$, is known. Periodic boundary conditions as shown in Figure 2.44, are then imposed on the boundaries to ensure the strain field is also periodic.

The discretised solution is expressed as follows,

$$\mathbf{Kd} = \mathbf{f} \tag{2.164}$$

where $\mathbf{K}$ is the stiffness matrix, $\mathbf{d}$ is the microscopic displacement field, and $\mathbf{f}$ is the

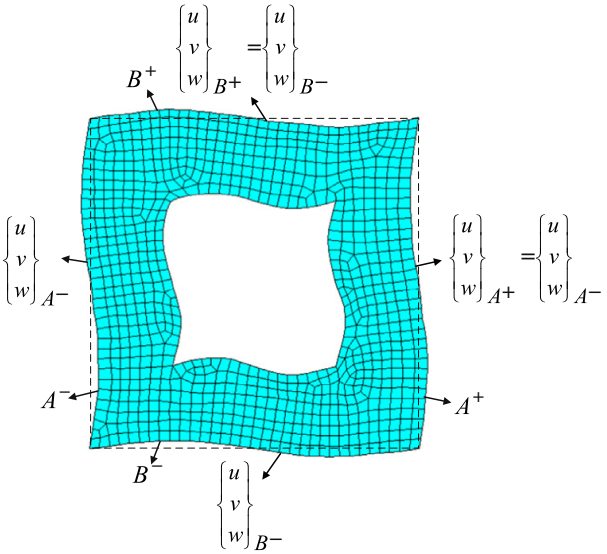



Figure 2.44: Periodic boundary conditions on the opposite edges of the RVE. Reprinted from [160] with kind permission from Elsevier.

force vector. **K** and **f** are defined as follows.

$$\mathbf{K} = \sum_{e=1}^{m} k^e, \;\; k^e = \int_{Y^e} \mathbf{B}^T \mathbf{E} \mathbf{B} dY^e \tag{2.165}$$

$$\mathbf{f} = \sum_{e=1}^{m} f^e, \;\; f^e = \int_{Y^e} \mathbf{B}^T \mathbf{E} \bar{\varepsilon}(u) dY^e \tag{2.166}$$

where $m$ is the number of elements, **B** is the strain-displacement matrix, and $Y^e$ is the element volume.

Eq. (2.166) can be used for both the linear elastic and non-linear elasto-plastic deformation analysis for the unit cell. This allows the yield strength and ultimate strength of the material to be analysed.

By assuming small deformation and elastic material behaviour, Eq. (2.164) leads to a linear relationship between the macroscopic $\bar{\varepsilon}(u)$ and microscopic $\varepsilon(u)$ strains, described by the following equation.

$$\varepsilon(u) = M \bar{\varepsilon}(u) \tag{2.167}$$

where $M$ is the local structural tensor.

The force vector used to calculate the microscopic displacements are found using Eq. (2.164) by applying the relevant macroscopic strains to Eq. (2.166). $\varepsilon^*$ is then determined using **B**, which is then used to calculate $\varepsilon$ via Eqs. (2.160) and (2.161). The local structural tensor **M** at the centroid of the element can then be found by solving

the matrix equations once $\bar{\varepsilon}$ and $\varepsilon$ are known. By considering independent unit strains, each column of $\mathbf{M}$ represents the microscopic strain tensor. Hence, the effective stiffness matrix can be derived by integrating the microscopic stress over the RVE and dividing by the RVE volume as follows,

$$\bar{\sigma} = \frac{1}{|V_{\mathrm{RVE}}|} \left( \int_{V_{\mathrm{RVE}}} EM \; dV_{\mathrm{RVE}} \right) \; \bar{\varepsilon} \tag{2.168}$$

$$\bar{E} = \frac{1}{|V_{\mathrm{RVE}}|} \int_{V_{\mathrm{RVE}}} EM \; dV_{\mathrm{RVE}} \tag{2.169}$$

The homogenised stiffness matrix, $\bar{E}$, can then be used to relate the macroscopic strains to the macroscopic stresses. This allows the AH method to find the macroscopic stress that will cause yield and fracture within the microstructure. This is important as the yield strength of the unit cell can be calculated using this information.

The yield strength of the unit cell is first calculated by determining the microscopic stress distribution, $\sigma$, that corresponds to a given multiaxial macroscopic stress, $\bar{\sigma}$,

$$\sigma = EM\bar{E}^{-1}\bar{\sigma} \tag{2.170}$$

The yield surface can then be captured by taking the von Mises stress distribution at the microstructure via,

$$\bar{\sigma}^{\mathrm{y}} = \frac{\sigma_{\mathrm{ys}}}{\max\left\{\sigma_{\mathrm{vM}(\bar{\sigma})}\right\}}\bar{\sigma} \tag{2.171}$$

where $\bar{\sigma}^{\mathrm{y}}$ is the yield surface of the unit cell, $\sigma_{\mathrm{ys}}$ is the yield strength of the bulk material, and $\sigma_{\mathrm{vM}}$ is the von Mises stress distribution within the microstructure.

Hence, the yield surface can be determined by calculating the yield strength over a range of multiaxial stresses. Although, the effective properties calculated using the AH homogenisation method assumes periodic boundary conditions, which allows it to only capture the average macroscopic field quantities, it can be integrated with finite element mesh superposition method or adaptive multiscale methodology to calculate local stress heterogeneities [160].

Despite the benefits of AH having no limitation on cell topology and having accurate results, the computational costs of AH are very high, especially if the problem is complex [160].

### Discrete homogenisation

Another type of homogenisation method is the discrete homogenisation technique, as seen in [178–182]. In discrete homogenisation, the lattice strut members are modelled

with discrete elements, such as beam elements, and Taylor's expansion of the nodal displacement and internal forces are then derived and substituted into the equilibrium equations. Lastly, the homogenised properties are calculated by converting the discrete sum of equilibrium equations into a continuous relation of stress and strain [160].

Here, the discrete homogenisation by [179] is used as an example to demonstrate the discrete homogenisation technique. The first step of the discrete homogenisation method by [179] is to formulate the equilibrium equations in terms of the stress vector, $\mathbf{S}^i$. The weak form of the equilibrium over the domain of the structure, $\Omega$, in terms of Cauchy stress, $\boldsymbol{\sigma}$, shown in Eq. (2.172) is expressed in curvilinear coordinates, $\lambda = (\lambda^1, \lambda^2, \lambda^3)$.

$$\int_{\Omega} \boldsymbol{\sigma} : \nabla_x \boldsymbol{v} dx = 0. \tag{2.172}$$

The relationship between the Cartesian coordinates to the curvilinear coordinates are expressed by the following equations.

$$\mathbf{x} = \mathbf{R}(\lambda^1, \lambda^2, \lambda^3) = x^i \mathbf{e}_i \tag{2.173}$$

Here, the covariant basis vectors, $\mathbf{e}_k^{\lambda}$, and the contravariant, $\mathbf{e}_{\lambda}^i$, basis vector of the curvilinear coordinate system can be defined as follows.

$$\mathbf{e}_k^{\lambda} = \frac{\partial x^i}{\partial \lambda^i} \mathbf{e}_i \tag{2.174}$$

$$\mathbf{e}_{\lambda}^i \cdot \mathbf{e}_j^{\lambda} = \delta_j^i \tag{2.175}$$

The virtual velocity field in the curvilinear coordinate system can be related to the Cartesian coordinate system via,

$$\nabla_x \mathbf{v} = \frac{\partial \mathbf{v}}{\partial \lambda^i} \otimes \mathbf{e}_{\lambda}^i \tag{2.176}$$

Therefore, Eq. (2.172) can be expressed as follows,

$$\int_{\Omega} \boldsymbol{\sigma} : \left(\nabla_x \mathbf{v}\right) dx = \int_{\Omega} \boldsymbol{\sigma} : \left( \frac{\partial \mathbf{v}}{\partial \lambda^i} \otimes \mathbf{e}_{\lambda}^i \right) \, g \, d\lambda = \int_{\Omega} \left( \boldsymbol{\sigma} \cdot \mathbf{e}_{\lambda}^i \right) \cdot \frac{\partial \mathbf{v}}{\partial \lambda^i} \, g \, d\lambda = 0 \tag{2.177}$$

where $g$ is the Jacobian after the transformation $dx = g \, d\lambda$.

The stress vector, $\mathbf{S}^i$, can be defined as follows.

$$\mathbf{S}^i = g \boldsymbol{\sigma} \cdot \mathbf{e}_{\lambda}^i \tag{2.178}$$

Inserting Eq. (2.178) into Eq. (2.177).

$$\int_{\Omega} \mathbf{S}^i \frac{\partial \mathbf{v}}{\partial \lambda^i} \, d\lambda = 0 \tag{2.179}$$

The force-stress tensor can then be expressed as follows.

$$\boldsymbol{\sigma} = \frac{1}{g}\mathbf{S}^i \otimes \mathbf{e}_i^{\lambda} = \frac{1}{g}\mathbf{S}^i \otimes \frac{\partial \mathbf{R}}{\partial \lambda^i} \tag{2.180}$$

where $\frac{\partial \mathbf{R}}{\partial \lambda^i}$ is the position gradient.

Prior to performing the homogenisation process for a lattice structure, the nodes and beams must be numbered and a unit direction for the beams must be designated. Additionally, several sets are defined and summarised in Table 2.5 and the notations are illustrated in Figure 2.45.

| Set | Definition |
|---|---|
| $\mathscr{B}(\bar{b})$ | Set of beams numbered $\bar{b}$ |
| $\mathscr{N}(\bar{n})$ | Set of nodes numbered $\bar{n}$ |
| $\mathscr{O}(\bar{n})$ | Set of nodes at the origins of beams |
| $\mathscr{E}(\bar{n})$ | Set of nodes at the ends of beams |
| $\bar{\mathscr{E}}(\bar{n})$ | Set of nodes at the sides of beams |

Table 2.5: Definition of sets used in analysis.

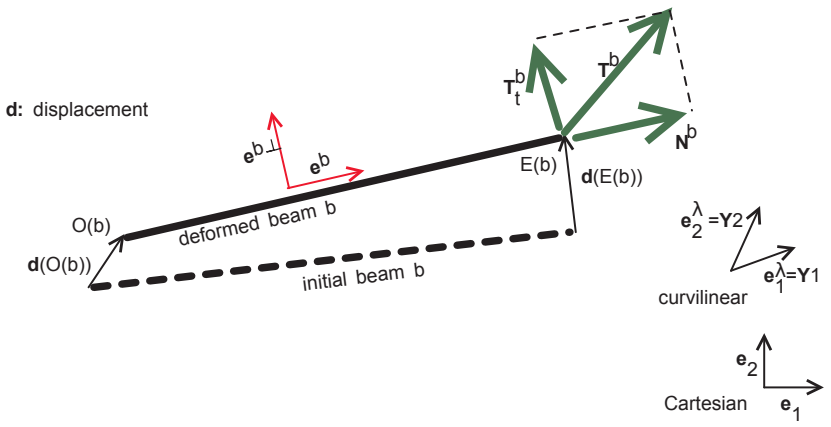



Figure 2.45: Illustration of beam element. Reprinted from [179] with kind permission from Otto-von-Guericke-University Magdeburg.

The equilibrium of the forces within a lattice composing of beams can be described as follows,

$$\sum_{\bar{b}\in\mathscr{O}(\bar{n})} \mathbf{T}^{\bar{b}} - \sum_{\bar{b}\in\mathscr{E}(\bar{n})} \mathbf{T}^{\bar{b}} + \sum_{\bar{b}\in\bar{\mathscr{E}}(\bar{n})} \mathbf{f}^{\bar{b}} = \mathbf{0} \tag{2.181}$$

where $\mathbf{T}^{\bar{b}}$ are the forces at the origin and end nodes while $\mathbf{f}^{\bar{b}}$ are the forces along the

edges of the beam.

Assuming that there are no rotation at the lattice nodes, which leads to no coupling stresses at the lattice edges, Eq. (2.181) is simplified to a virtual power form as follows,

$$\sum_{\bar{b}\in\mathscr{B}(\bar{b})} \mathbf{T}^{\bar{b}} \cdot \left[\mathbf{v}\left(O(\bar{b})\right) - \mathbf{v}\left(E(\bar{b})\right)\right] = \mathbf{0} \tag{2.182}$$

Due to difficulty in calculating the entire lattice in Eq. (2.182), a simplifying assumption that the lattice is made up of a reference unit cell, $\mathbb{Z}^3$, and that the deformed state of the lattice is periodic. This allows the beam and node sets to be simplified and they are denoted as $\mathscr{N}_R$ and $\mathscr{B}_R$ respectively. Here, any vector $v^i = (v^1, v^2, v^3) \in \mathbb{Z}^3$ can be used to associate the basic cell, therefore the nodes of the lattice is described by $\bar{n} = (n, v^1, v^2, v^3)$ in $\mathscr{N}_R \times \mathbb{Z}^3$ and the beams of the whole lattice is described by $\bar{b} = (b, v^1, v^2, v^3)$ in $\mathscr{B}_R \times \mathbb{Z}^3$.

This allows Eq. (2.182) to be written as,

$$\sum_{v^i\in\mathbb{Z}^3} \sum_{b^i\in\mathbb{B}^3} \mathbf{T}^b \cdot [\mathbf{v}(O(b)) - \mathbf{v}(E(b))] = 0 \tag{2.183}$$

$\mathbf{T}^b$ is then decomposed into a normal and transverse force, and the principle of virtual power can be described as follows.

$$\sum_{v^i\in\mathbb{Z}^3} \sum_{b^i\in\mathbb{B}^3} (\mathbf{N}^b + \mathbf{T}_t^b) \cdot [\mathbf{v}(O(b)) - \mathbf{v}(E(b))] = 0 \tag{2.184}$$

The discrete homogenisation method here follows the homogenisation of periodic media, which is based on asymptotic expansion of the kinematic and static variables versus a small parameter $\varepsilon$ ratio of a typical length characteristic of an elementary cell to a structural length. Therefore, the parameters are used to characterise the entire structure for homogenisation and setting the Lagrangian curvilinear coordinates as $\lambda^\varepsilon = \varepsilon v^i$.

The position of the nodes, node displacement, and lengths are defined by the vectorial functions as follows.

$$\mathbf{R}^\varepsilon(\bar{n}) = \mathbf{R}^0(\lambda^\varepsilon) + \varepsilon\mathbf{R}^{n1}(\lambda^\varepsilon) + \cdots \tag{2.185}$$

$$\mathbf{d}^\varepsilon(\bar{n}) = \mathbf{d}^0(\lambda^\varepsilon) + \varepsilon\mathbf{d}^{n1}(\lambda^\varepsilon) + \cdots \tag{2.186}$$

$$l^{\varepsilon b} = \varepsilon l^{\varepsilon b0} + \varepsilon^2 l^{\varepsilon b1} + \cdots \tag{2.187}$$

where the supercript 0 is the initial value.

Only the dominant term is retained in the analysis. The virtual velocity $\mathbf{v}^\varepsilon$ can be written as a Taylor series expansion.

$$\mathbf{v}^{\varepsilon}(O(\bar{b})) - \mathbf{v}^{\varepsilon}(E(\bar{b})) = \mathbf{v}(\lambda^{\varepsilon}) - \mathbf{v}(\lambda^{\varepsilon} + \varepsilon\delta^{ib}) = -\varepsilon\frac{\partial \mathbf{v}(\lambda^{\varepsilon})}{\partial \lambda^{i}}\delta^{ib} + \cdots \tag{2.188}$$

Here, asymptotic expansion is then performed for the forces using a suitable model for the beam such as the Euler-Bernoulli model. Let $\mathbf{e}^{b\perp}$ be the unit transversal vector for beam $b$ as follows,

$$\mathbf{e}^{b\perp} = e_3 \wedge e^{b} \tag{2.189}$$

The force exerted on beam $b$,

$$\mathbf{T}^{\varepsilon b} = N^{\varepsilon b}\mathbf{e}^{b} + N_t^{\varepsilon b}\mathbf{e}^{b\perp} \tag{2.190}$$

can then be decomposed into the normal and transverse forces as follows,

$$N^{\varepsilon b}\mathbf{e}^{b} = \frac{E_s S^{\varepsilon b}}{l^{\varepsilon b}}\left[\mathbf{d}^{\varepsilon}(E(b)) - \mathbf{d}^{\varepsilon}(O(b)) \cdot \mathbf{e}^{b}\right] \cdot \mathbf{e}^{b} \tag{2.191}$$

$$T_t^{\varepsilon b}\mathbf{e}^{b\perp} = \frac{12E_s I_z^{\varepsilon}}{\left(l^{\varepsilon b}\right)^3}\left[\mathbf{d}^{\varepsilon}(E(b)) - \mathbf{d}^{\varepsilon}(O(b)) \cdot \mathbf{e}^{b}\right] \cdot \mathbf{e}^{b\perp} \tag{2.192}$$

where $E_s$ represents the Young's modulus, $S^{\varepsilon b} = t^{\varepsilon b}$ is the beam section, and $I_z$ is the quadratic moment of the beam.

The order in $\varepsilon$ for $t^{\varepsilon}$ is obtained from the density $\rho^*$ of the lattice based on the following scales.

$$\rho^* \propto \frac{t^{\varepsilon b}}{l^{\varepsilon b}} \Rightarrow t^{\varepsilon b} \propto l^{\varepsilon b} \tag{2.193}$$

Eq. (2.193) is then expanded as follows.

$$t^{\varepsilon b} = \varepsilon t^{b0} + \varepsilon^2 t^{b1} + \cdots \tag{2.194}$$

By taking only the first term, the moment for a rectangular beam can be written as,

$$I_z^{\varepsilon} = \frac{(\varepsilon t^{b0})^3}{12} \tag{2.195}$$

Lastly, a Taylor series expansion is used to express the displacement difference as follows.

$$\mathbf{d}^{\varepsilon}(O(b)) = \mathbf{d}^{0}(\lambda^{\varepsilon}) + \varepsilon\mathbf{d}^{O_R(b)1}(\lambda^{\varepsilon}) + \cdots \tag{2.196}$$

$$\mathbf{d}^{\varepsilon}(E(b)) = \mathbf{d}^{0}(\lambda^{\varepsilon} + \varepsilon\delta^{ib}) + \varepsilon\mathbf{d}^{E_R(b)1}(\lambda^{\varepsilon} + \varepsilon\delta^{ib}) + \cdots \tag{2.197}$$

$$= \mathbf{d}^{0}(\lambda^{\varepsilon}) + \varepsilon\frac{\partial\mathbf{d}^{0}(\lambda^{\varepsilon})}{\partial\lambda^{i}}\delta^{ib} + \varepsilon\mathbf{d}^{E_R(b)1}(\lambda^{\varepsilon}) + \varepsilon^{2}\frac{\partial\mathbf{d}^{E_R(b)1}(\lambda^{\varepsilon})}{\partial\lambda^{i}}\delta^{ib} + \cdots \tag{2.198}$$

$$= \mathbf{d}^{0}(\lambda^{\varepsilon}) + \varepsilon\left(\frac{\partial\mathbf{d}^{0}(\lambda^{\varepsilon})}{\partial\lambda^{i}}\delta^{ib} + \mathbf{d}^{E_R(b)1}(\lambda^{\varepsilon})\right) + \cdots \tag{2.199}$$

$$\mathbf{d}^{\varepsilon}(E(b)) - \mathbf{d}^{\varepsilon}(O(b)) = \varepsilon\left(\mathbf{d}^{E_R(b)1}(\lambda^{\varepsilon}) - \mathbf{d}^{O_R(b)1}(\lambda^{\varepsilon}) + \frac{\partial\mathbf{d}(\lambda^{\varepsilon})}{\partial\lambda^{i}}\delta^{ib}\right) + \cdots \tag{2.200}$$

where $\mathbf{d}^{E_R(b)1}(\lambda^{\varepsilon})$ and $\mathbf{d}^{O_R(b)1}(\lambda^{\varepsilon})$ are the unknown displacements of the reference nodes within the unit cell.

Eq. (2.200) is then simplified further to,

$$d\mathbf{D}^{\varepsilon}_{EO} = \mathbf{d}^{\varepsilon}(E(b)) - \mathbf{d}^{\varepsilon}(O(b)) \tag{2.201}$$

$$= \varepsilon\left(\mathbf{d}^{E_R(b)1}(\lambda^{\varepsilon}) - \mathbf{d}^{O_R(b)1}(\lambda^{\varepsilon}) + \frac{\partial\mathbf{d}(\lambda^{\varepsilon})}{\partial\lambda^{i}}\delta^{ib}\right) + \cdots \tag{2.202}$$

The following equations are found by inserting Eq. (2.195) and Eq. (2.200) into Eq. (2.192) and Eq. (2.193), the normal and transverse forces are as follows.

$$N^{\varepsilon b}\mathbf{e}^{b} = \frac{E_s t^{b}}{l^{b}} d\mathbf{D}^{\varepsilon}_{EO} \cdot \mathbf{e}^{b}\delta^{ib} \cdot \mathbf{e}^{b} \tag{2.203}$$

$$T_t^{\varepsilon b}\mathbf{e}^{b\perp} = \frac{E_s t^{b}}{(l^{b})^{3}} d\mathbf{D}^{\varepsilon}_{EO} \cdot \mathbf{e}^{b\perp}\delta^{ib} \cdot \mathbf{e}^{b\perp} \tag{2.204}$$

Inserting Eq. (2.203) and Eq. (2.204) into Eq. (2.190).

$$\mathbf{T}^{\varepsilon b} = \frac{E_s t^{b}}{l^{b}} d\mathbf{D}^{\varepsilon}_{EO} \cdot \mathbf{e}^{b}\delta^{ib} \cdot \mathbf{e}^{b} + \frac{E_s t^{b}}{(l^{b})^{3}} d\mathbf{D}^{\varepsilon}_{EO} \cdot \mathbf{e}^{b\perp}\delta^{ib} \cdot \mathbf{e}^{b\perp} \tag{2.205}$$

Substituting Eq. (2.205) into Eq. (2.188).

$$\sum_{v^i\in\mathbb{Z}^3}\sum_{b\in\mathscr{B}_R}\left(\frac{E_s t^{b}}{l^{b}} d\mathbf{D}^{\varepsilon}_{EO} \cdot \mathbf{e}^{b}\delta^{ib} \cdot \mathbf{e}^{b} + \frac{E_s t^{b}}{(l^{b})^{3}} d\mathbf{D}^{\varepsilon}_{EO} \cdot \mathbf{e}^{b\perp}\delta^{ib} \cdot \mathbf{e}^{b\perp}\right) \cdot \left[\varepsilon\frac{\partial\mathbf{v}(\lambda^{\varepsilon})}{\partial\lambda^{i}}\delta^{ib}\right]$$

$$= \sum_{v^i\in\mathbb{Z}^3}\varepsilon^{2}\sum_{i\in\{1,2\}}\mathbf{S}^{i}\left[\frac{\partial\mathbf{v}(\lambda^{\varepsilon})}{\partial\lambda^{i}}\right] = 0 \tag{2.206}$$

where the vector $\mathbf{S}^{i}$ is defined as follows.

$$\mathbf{S}^i = \sum_{b\in\mathscr{B}} \left( \frac{E_s t^b}{l^b} d\mathbf{D}^{\varepsilon}_{EO} \cdot \mathbf{e}^b \delta^{ib} \cdot \mathbf{e}^b + \frac{E_s t^b}{(l^b)^3} d\mathbf{D}^{\varepsilon}_{EO} \cdot \mathbf{e}^{b\perp} \delta^{ib} \cdot \mathbf{e}^{b\perp} \right) \delta^{ib} \tag{2.207}$$

$$= \sum_{b\in\mathscr{B}} (\mathbf{N}^b + \mathbf{T}^b_t) \delta^{ib} \tag{2.208}$$

Using the procedure from [179], Eq. (2.206) can be transformed from the discrete to continuous form, written as,

$$\int_{\Omega} \mathbf{S}^i \cdot \frac{\partial \mathbf{v}(\lambda^{\varepsilon})}{\partial \lambda^i} d\lambda \tag{2.209}$$

The stress tensor, $\sigma$, is then determined from the stress vectors as follows.

$$\sigma = \frac{1}{g} \mathbf{S}^i \otimes \frac{\partial \mathbf{R}}{\partial \lambda^i} \tag{2.210}$$

In the discrete homogenisation technique, there is no need to average of the microscopic fields to determine the macroscopic fields as the macroscopic variables naturally follow from the homogenization technique [179].

### Micromechanics theories for homogenisation

Micromechanics theories for homogenisation can also be used to determine the effective modulus (or stiffness) of heterogeneous materials. Micromechanical theories have been used in a number of studies, for example in [183] where the effective elastic properties of a metal/ceramic composite was calculated using micromechanical modelling and finite elements.

Here an overall framework for the micromechanics homogenisation theory developed by Hori and Nemat-Nasser is presented. In micromechanics homogenisation, an elastic body, as shown in Figure 2.46, can be split into a macroscopic length scale, $D$, that is the dimension of the material that is being measured, and a microscopic length scale, $d$.

Here, a small scale relative length scale parameter, $\epsilon$, is defined as follows.

$$\epsilon = \frac{d}{D} \ll 1 \tag{2.211}$$

Since the microstructure of the material as seen in Figure 2.46 is inhomogeneous, the elasticity tensor, $\mathbf{C}^{\epsilon}$, displacement, $\mathbf{u}^{\epsilon}$, strain, $\boldsymbol{\varepsilon}^{\epsilon}$, and stress, $\boldsymbol{\sigma}^{\epsilon}$, are all functions of $\mathbf{X}$, which is the location of a point in the material. The superscript $\epsilon$ in these terms is used to emphasize that the variation in these fields are calculated at the relative scale of $\epsilon$, which is for a representative volume element (RVE) as shown by the microstructure

of the material in Figure 2.46. These terms are related to each other in the following equations.

$$\boldsymbol{\varepsilon}^{\epsilon}\mathbf{X} = \nabla \otimes \mathbf{u}^{\epsilon}(\mathbf{X}) \tag{2.212}$$

$$\nabla \cdot \boldsymbol{\sigma}^{\epsilon}(\mathbf{X}) = 0 \tag{2.213}$$

$$\boldsymbol{\sigma}^{\epsilon}(\mathbf{X}) = \mathbf{C}^{\epsilon}(\mathbf{X}) \colon \boldsymbol{\varepsilon} \tag{2.214}$$

where $\nabla$ is the del operator and $\otimes$ is the tensor product.

Substituting Eqs. (2.212) and (2.213) into Eq. (2.214) gives the following relationship.

$$\begin{array}{ll} \nabla \cdot (\mathbf{C}^{\epsilon}(\mathbf{X}) \colon (\nabla \otimes \mathbf{u}^{\epsilon}(\mathbf{X}))) = 0 & \text{within the material,} \\ \mathbf{u}^{\epsilon}(\mathbf{X}) = \mathbf{u}^{0}(\mathbf{X}) & \text{on the RVE boundary.} \end{array} \tag{2.215}$$

In the micromechanics homogenisation method, the elasticity tensor at the macroscale is then approximated by the microscale elasticity tensor.

$$\mathbf{C}(\mathbf{x}) \approx \mathbf{C}^{\epsilon}(\mathbf{X}) \tag{2.216}$$

where $\mathbf{x} = \epsilon^{-1}\mathbf{X}$.

$\mathbf{C}$ is generally assumed to be periodic, which allows the displacement fields to be represented as follows.

$$\mathbf{u}^{\epsilon}(\mathbf{X}) \approx \sum_{n=0} \epsilon^{n} \mathbf{u}^{n}(\mathbf{X}, \mathbf{x}) \tag{2.217}$$

where each $\mathbf{u}^{n}$ has the same periodicity as $\mathbf{C}$ with respect to $\mathbf{x}$.

Replacing $\nabla$ with $\nabla_{\mathbf{X}} + \epsilon^{-1}\nabla_{\mathbf{x}}$ and substituting Eq. (2.217) into Eq. (2.215) gives

$$\begin{aligned} &\epsilon^{-2} \left\{ \nabla_{\mathbf{x}} \cdot (\mathbf{C}(\mathbf{x}) \colon (\nabla_{\mathbf{x}} \otimes \mathbf{u}^{0}(\mathbf{X}, \mathbf{x}))) \right\} \\ &\quad + \epsilon^{-1} \left\{ \nabla_{\mathbf{X}} \cdot (\mathbf{C}(\mathbf{x}) \colon (\nabla_{\mathbf{x}} \otimes \mathbf{u}^{0}(\mathbf{X}, \mathbf{x}))) \right. \\ &\quad \left. + \nabla_{\mathbf{x}} \cdot \mathbf{C}(\mathbf{x}) \colon (\nabla_{\mathbf{x}} \otimes \mathbf{u}^{0}(\mathbf{X}, \mathbf{x}) + (\nabla_{\mathbf{x}} \otimes \mathbf{u}^{1}(\mathbf{X}, \mathbf{x}) \right\} \\ &\quad + \sum_{n=0} \epsilon^{n} \left\{ \nabla_{\mathbf{X}} \cdot (\mathbf{C}(\mathbf{x}) \colon (\nabla_{\mathbf{X}} \otimes \mathbf{u}^{n}(\mathbf{X}, \mathbf{x}) + (\nabla_{\mathbf{x}} \otimes \mathbf{u}^{n+1}(\mathbf{X}, \mathbf{x}))) \right. \\ &\quad \left. + \nabla_{\mathbf{x}} \cdot (\mathbf{C}(\mathbf{X}) \colon (\nabla_{\mathbf{X}} \otimes \mathbf{u}^{n+1}(\mathbf{X}, \mathbf{x}) + (\nabla_{\mathbf{x}} \otimes \mathbf{u}^{n+2}(\mathbf{X}, \mathbf{x}))) \right\} = 0 \end{aligned} \tag{2.218}$$

In order to simplify presentation, $O(\epsilon^{n})$ will be used to define the terms in Eq. (2.218) with the $n^{\text{th}}$ order of $\epsilon$. In order to solve Eq. (2.218) up the order of $O(\epsilon^{0})$, the homogenisation theory assumes that $\mathbf{u}^{0}$ is a function of only $\mathbf{X}$ and that $\mathbf{u}^{1}$ can be represented as follows.

$$\mathbf{u}^1(\mathbf{X},\mathbf{x}) = \boldsymbol{\chi}^1(\mathbf{x}) \colon (\nabla_{\mathbf{X}} \otimes \mathbf{u}^0(\mathbf{X})) \tag{2.219}$$

where $\boldsymbol{\chi}^1$ is a third-order tensor that is periodic with respect to $\mathbf{x}$.

This will cause the terms of $O(\epsilon^{-2})$ to vanish and the terms in $O(\epsilon^{-1})$ to become

$$\left\{\nabla_{\mathbf{x}} \cdot (\mathbf{C}(\mathbf{x}) \colon (\nabla_{\mathbf{x}} \otimes \boldsymbol{\chi}^1(\mathbf{x}) + \mathbf{1}))\right\} : (\nabla_{\mathbf{X}} \otimes \mathbf{u}^0(\mathbf{X})) \tag{2.220}$$

where $\mathbf{1}$ is the symmetric fourth-order identity tensor.

In order for Eq. (2.220) to vanish identically for both $\mathbf{X}$ and $\mathbf{x}$, $\boldsymbol{\chi}^1$ must satisfy the following equation.

$$\nabla_{\mathbf{x}} \cdot (\mathbf{C}(\mathbf{x}) \colon (\nabla_{\mathbf{x}} \otimes \boldsymbol{\chi}^1(\mathbf{x}) + \mathbf{1})) = 0 \tag{2.221}$$

Here, the term $\boldsymbol{\chi}^1 \colon (\nabla_{\mathbf{X}} \otimes \mathbf{u}^0)$ is viewed as the microscopic displacement field when a stress field of $\boldsymbol{\sigma}^1 \colon (\nabla_{\mathbf{X}} \otimes \mathbf{u}^0)$ is present. This stress field does not satisfy equilibrium resulting in oscillating microstrains and associated stresses being produced. Therefore, $\boldsymbol{\chi}^1$ corresponds to the microscale response that accommodates the strain field $(\nabla_{\mathbf{X}} \otimes \mathbf{u}^0)$ that causes the non-equilibrium stresses.

Once $\boldsymbol{\chi}^1$ is found, the terms in $O(\epsilon^0)$ from Eq. (2.218) can be expressed as follows

$$\begin{aligned}\left\{\nabla_{\mathbf{x}} \cdot (\mathbf{C}(\mathbf{x}) \colon (\nabla_{\mathbf{x}} \otimes \boldsymbol{\chi}^1(\mathbf{x}) + \mathbf{1}))\right\} : (\nabla_{\mathbf{X}} \otimes \mathbf{u}^0(\mathbf{X})) \\ + \nabla_{\mathbf{x}} \cdot \left\{\mathbf{C}(\mathbf{x}) \colon ((\nabla_{\mathbf{X}} \otimes \mathbf{u}^1(\mathbf{X},\mathbf{x})) + \nabla_{\mathbf{x}} \otimes \mathbf{u}^2(\mathbf{X},\mathbf{x}))\right\}\end{aligned} \tag{2.222}$$

The effective elastic tensor, $\bar{\mathbf{C}}^0$ can be found by taking the volume average of the unit cell, so that the terms varying with $\mathbf{x}$ are eliminated and the governing equation for $\mathbf{u}^0$ becomes

$$\nabla_{\mathbf{X}} \cdot (\bar{\mathbf{C}}^0 \colon (\nabla_{\mathbf{X}} \otimes \mathbf{u}^0(\mathbf{X}))) = 0 \tag{2.223}$$

where the effective elastic tensor, $\bar{\mathbf{C}}^0$, is as follows

$$\bar{\mathbf{C}}^0 = \frac{1}{V} \int_V \nabla_{\mathbf{x}} \cdot (\mathbf{C}(\mathbf{x}) \colon (\nabla_{\mathbf{x}} \otimes \boldsymbol{\chi}^1(\mathbf{x}) + \mathbf{1}))\, dV \tag{2.224}$$

where $V$ is the volume of the RVE.

The micromechanical homogenisation method described here can determine all the components of the elastic tensor, $\bar{\mathbf{C}}^0$, which is a useful tool for systems in which the different components of the elastic tensor is of interest. Additionally, the micromechanical homogenisation method uses a periodic microstructure and is widely used for modelling composite materials with regularly arranged microstructures [184]. However, this tech-

nique is not commonly use in the study of lattice structure materials, and this may be because the elastic stiffness tensor for beams that the lattice structure materials are made of with different orientation cannot be easily expressed as a continuous function required in the previous equations.

### Concluding remarks

As seen in this section, there are a variety of methods for homogenisation of lattice structures and the effective properties of lattice structures can be found using any of these methods. In this thesis, the method by Vigliotti and Pasini [29] was selected to find the effective properties, mainly because it can be used with finite element method, which was also used to determine the band structure. Additionally, the Vigliotti and Pasini [29] technique is simpler to be implemented and requires less computational costs compared to the other methods.

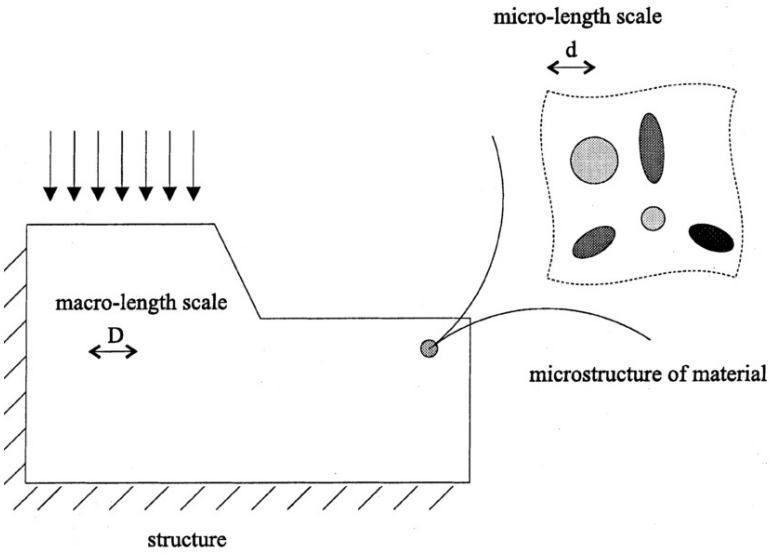



Figure 2.46: A material with microstructure under load. Reprinted from [184] with kind permission from Elsevier.

# 3 An inverse method to determine the dispersion curves of periodic structures based on wave superposition

## 3.1 Introduction

As described in the previous chapter, many studies of phononic crystals and acoustic metamaterials use the Brillouin approach [13]. Significant pioneering work on wave propagation in periodic structures was done by Mead and his co-workers [14]. In order to reduce computation time, many models in the literature exploit the Floquet-Bloch theorem, as it allows the behaviour of periodic structures to be analysed using only a single unit cell. The Bloch wave theorem is described as follows [185],

$$\begin{aligned}\mathbf{u}(\mathbf{x},t) &= \tilde{\mathbf{u}}(\mathbf{x})e^{i\mathbf{k}\cdot\mathbf{x}}e^{-i\omega t} \\ &= \sum_{\mathbf{G}} \overline{\mathbf{u}}_{\mathbf{G}} e^{i\mathbf{G}\cdot\mathbf{x}} e^{i\mathbf{k}\cdot\mathbf{x}} e^{-i\omega t}\end{aligned} \tag{3.1}$$

where $\mathbf{u}$ is the displacement, $\tilde{\mathbf{u}}$ is a periodic wave function describing the displacements, $\overline{\mathbf{u}}$ is the magnitude of the wave, $\mathbf{G}$ is the reciprocal lattice constants, $\mathbf{x}$ is the position, $\mathbf{k}$ is the wave vector, $\omega$ is the forcing frequency and $t$ is time.

Eq. (3.1) implies that the displacement at one end of a unit cell is a factor of $e^{-i\mathbf{k}\cdot\mathbf{x}}$ times the displacement at the other end of the unit cell in an infinitely repeating structure. Additionally, the wave vector, $\mathbf{k}$, which may be complex, also describes how the wave propagates from one unit cell to the adjacent unit cell. The real part of the wave vector is known as the propagation constant and it characterises the phase shift, while the imaginary part is known as the attenuation constant and it describes the attenuation of elastic waves across the unit cell.

In a large number of studies, for example [23, 25, 72, 109, 110, 185–191], the wave vector, $\mathbf{k}$, was utilised to determine the location and width of band gaps. This is commonly done by calculating the band structure, also known as the dispersion curve, which is the relationship between frequency and the wave vector. The imaginary parts

of the wave vectors were also calculated in several studies, such as [99, 109, 120, 130]. When material damping is present, all wave vectors will become complex as energy will be dissipated and the wave will always attenuate.

Despite the abundance of methods available, no method have been developed to use experimental results to predict the band gap properties of inhomogeneous materials in a direct manner. So far, only a small number of studies, in which the dispersion curves were determined from experimental measurements, have been conducted, for example in [138, 139]. The ability to measure the dispersion curve from experimental data is useful in studies of phononic crystals and elastic metamaterials for several reasons. In many experimental studies using periodic structures with band gaps for vibration isolation [110, 124], the existence of band gaps are verified by measuring the frequency response of the structure and comparing the frequencies that have low amplitudes with the frequencies predicted by the band gaps. However, in practice, the finiteness of the structure may result in peaks occurring within the band gaps as reported in [124, 192] for several reasons, such as the accelerations at the excitation end having low amplitudes or the presence of surface modes. The low vibration regions found in frequency response measurements may also be a result of other mechanisms, such as anti-resonance. Furthermore, the materials used in practice may have different mechanical properties from the values used in the model, especially damping that is hard to characterise. Therefore, the ability to measure the dispersion curves directly from a structure is important to the study of vibrations in periodic structures.

In the studies that measure the band structure experimentally [138, 139], laser doppler vibrometry (LDV) was used to measure the velocity from an excitation and two-dimensional Fourier transformation, described in Section 2.1.3, was then applied to the data to calculate the dispersion curve. In these studies, laser doppler vibrometers with high temporal and spatial resolution were required. Additionally, further post processing of the data may be required to remove the effects of the reflected wave as seen in [138].

In this chapter, a method to determine the dispersion curves from the frequency response in a limited number of unit cells in a one dimensional periodic structure is introduced. The method introduced here is based on the superposition of waves and does not require specific information about the material or structure. Hence, the band structure can be found using frequency response functions from experiments or models that can be used to predict the frequency response functions, which are referred to as analytical models herein. However, other methods in the literature are likely to be more efficient for calculating the dispersion curves if the analytical models are used to calculate the band structure. The key benefit of the proposed method is that it only requires the frequency response at a small number of points, which can be easily achieved with simple experimental equipment, e.g. a shaker or an impact hammer and accelerometers. Furthermore, the proposed method can be extended to calculate the

response of finite periodic structures using the band structure and the components of the eigenvectors. An attempt has also been made to extend the method to two and three dimensional systems. The method is capable of measuring a portion of the dispersion surface of the band structure in two dimensional system but it has some limitations on systems with more then one dimension. However, acoustic metamaterials and phononic crystals that are one dimensional or can be approximated as one dimensional are still widely studied in recent years, for example in [3, 104, 105, 192–194], and studies on these one dimensional systems can benefit from the method.

This chapter is organised as follows. The theory of this method will be presented in the next section along with the derivation of the relevant equations. The method proposed in this chapter will be referred to as the *wave superposition method* (WSM), because it was derived using the superposition of elastic waves. This is then followed by a numerical example using a bi-material beam to act as a proof of concept. The band structures of the bi-material beams in the example were determined using the magnitudes and phase shifts of various points calculated from the analytical solution of Timoshenko beams. The band structure of the system was also found using the transfer matrix method for comparison. The setup for the numerical example will be presented in Section 3.3, followed by the results for the band structures in Section 3.4. Additionally, the transmissibilities calculated using the band structure and components of the eigenvectors for the finite periodic bi-material beam with different number of unit cells will also be presented in Section 3.4. Furthermore, some observations relating to the transmissibilities and the number of unit cells will be discussed. Lastly, the steps taken to extend the method for two and three dimensional systems will be discussed, before concluding the chapter.

## 3.2 Theory

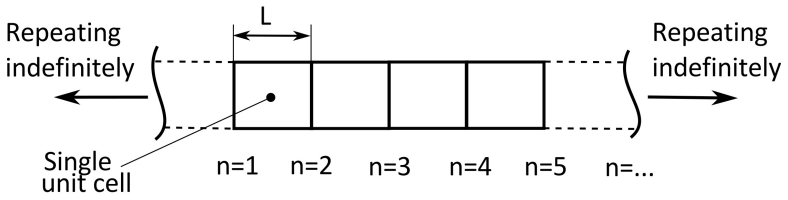
### 3.2.1 Superposition of elastic waves

The development of the wave superposition method (WSM) begins by considering an infinitely repeating structure in one dimension as shown in Figure 3.1(a). For a structure vibrating with a frequency of $\omega$, the Bloch wave theory in Eq. (3.1) can be applied to the displacement functions at the boundary nodes of each unit cell, which gives the following relationship at each node,

$$\mathbf{U}_{n+N} = \mathbf{U}_n \; e^{N(ik\cdot L)} \tag{3.2}$$

where $\mathbf{U}_n$ is a wave function, $\mathbf{L}$ is the lattice constant that is a vector describing the lengths of the unit cell, the subscript $n$ is the node number, $N$ is the number of nodes adjacent to node $n$, and $k$ is the wave vector.

(a)




(b)

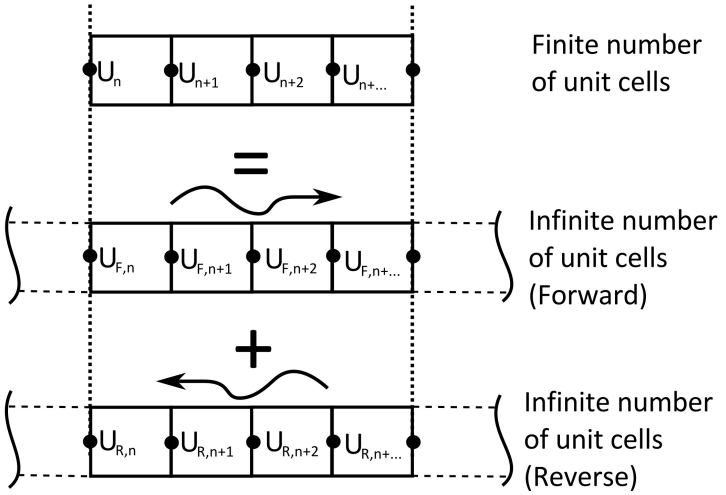



Figure 3.1: (a) A structure with infinitely repeating unit cells (b) Superposition of two infinite structures.

Eq. (3.2) is similar to a wave solution propagating through a material in a single direction, i.e. from left to right according to Eq. (3.1). The relationship in Eq. (3.2) also implies that the displacements at a point in any unit cell of a periodic structure can be found if the displacements in one unit cell are known. However, the relationship in Eq. (3.2) does not apply to finite structures, because elastic waves are reflected at the boundaries of finite structures and this is not accounted for in Eq. (3.2). The reflection of elastic waves even for common components, such as Timoshenko beams, are not straightforward as it depends on the boundary conditions and the different elastic waves will interact at the boundaries except at a specific frequency [195].

Assuming the equations of motion describing the dynamic behaviour of the structure are linear, the displacements of the vibrations can be summed up linearly using the superposition principle [1]. The superposition principle allows the dynamic behaviour of a structure with finite repetitions of unit cells to be described using two infinitely repeating structures as shown in Figure 3.1(b), where one represents a forward moving wave and the other represents a backward moving wave. This is analogous to a wave that is travelling due to an external excitation at one end, with a reflected wave. Thus, the displacements at different points can be described by

$$\mathbf{U}_n = \mathbf{U}_{F,n} + \mathbf{U}_{R,n} \tag{3.3}$$

where $\mathbf{U}_n$ is the wave function of the displacement of the finite structure at the boundary node $n$, $\mathbf{U}_{F,n}$ is the wave function of the displacement of the forward wave in the infinite structure and $\mathbf{U}_{R,n}$ is the wave function of the displacement of the reverse wave in the infinite structure.

The displacements of the finite structure, $\mathbf{U}_n$, can be found using conventional vibration analysis, such as the finite element method or experimental measurements. On the other hand, the displacements of the infinite structure, $\mathbf{U}_{F,n}$ and $\mathbf{U}_{R,n}$, are unknowns to be found along with $e^{N(i\mathbf{k}\cdot\mathbf{L})}$ to determine the wave vector, $\mathbf{k}$. Eq. (3.2) can then be used to describe the behaviour of $\mathbf{U}_{F,n}$ and $\mathbf{U}_{R,n}$, where $e^{N(i\mathbf{k}\cdot\mathbf{L})}$ is the same for both the forward and backward waves as this is a property of the structure.

A relationship describing the function $e^{N(i\mathbf{k}\cdot\mathbf{L})}$ and the wave function at various points of the finite structure, $\mathbf{U}_n$, can then be found by combining Eqs. (3.2) and (3.3) and eliminating the wave functions of the infinite structure, $\mathbf{U}_{F,n}$ and $\mathbf{U}_{R,n}$, at various points to find the band structure of the system. The number of points required is dependent on the number of degrees of freedom measured and the presence of coupled waves, such that the number of equations and unknowns are equal.

Since the equations to find the wave vector, $\mathbf{k}$, in Eq. (3.2) and Eq. (3.3) do not explicitly include the terms related to the material properties, such as Young's Modulus, damping ratios, or the geometry with the exception of the lattice constant, $\mathbf{L}$, the wave superposition method proposed here does not require a model to determine the band

structure. Therefore, this method can be considered to be an inverse method, in which the band structure is determined from the response of the system instead of using a model as done in the direct methods that constitute a majority of the methods in the literature.

The procedure to calculate the band structure for a single uncoupled wave with a single degree of freedom will be presented next. The calculations for two coupled waves will be presented after that. The steps taken in the two cases will then be generalised for systems with arbitrary numbers of degrees of freedom and waves.

### 3.2.2 Single wave

For a system with a single degree of freedom, such as axial displacements of a bar, there is only a single wave. Thus, the displacement vector is in a single direction, $U_n$. Similarly, the wave vector is also in a single direction, $k$. The first step in calculating the dispersion curve is to determine the number of nodes required in the analysis.

Applying Eq. (3.3) to the finite structure will result in two additional unknowns and one additional equation for each node. Furthermore, Eq. (3.2) will contribute two additional equations for each unit cell, where the number of unit cells is one less than the number of nodes. Lastly, the variable, $e^{ikL}$, is an additional unknown in the system.

Therefore, the number of equations and unknowns for vibrations with a single wave can be summarised as shown in Table 3.1.

| Relationship | Number of equations | Number of unknowns |
|---|---|---|
| Displacement relationships, Eq. (3.3) | $n$ | $2n$ |
| Bloch wave conditions, Eq. (3.2) | $2(n-1)$ | 0 |
| $\lambda$ | 0 | 1 |
| Total | $3n-2$ | $2n+1$ |

Table 3.1: Number of equations for a system with a single wave; where $n$ is the number of nodes.

By equating the final row in Table 3.1 and solving for $n$, the required number of nodes, $n$ for a single degree of freedom system is 3. This will result in 7 equations and 7 unknowns. The required equations are as follows.

From displacement relationships, Eq. (3.3):

$$U_1 = U_{F,1} + U_{R,1} \tag{3.4}$$

$$U_2 = U_{F,2} + U_{R,2} \tag{3.5}$$

$$U_3 = U_{F,3} + U_{R,3} \tag{3.6}$$

From Bloch wave conditions, Eq. (3.2):

$$U_{F,2} = \lambda U_{F,1} \tag{3.7}$$

$$U_{F,3} = \lambda U_{F,2} \tag{3.8}$$

$$U_{R,2} = \lambda U_{R,3} \tag{3.9}$$

$$U_{R,1} = \lambda U_{R,2} \tag{3.10}$$

where,

$$\lambda = e^{ikL} \tag{3.11}$$

By substituting Eqs. (3.7) to (3.10) into Eqs. (3.4) to (3.6) and then eliminating all other terms except for $U_1, U_2, U_3$, and $\lambda$, a quadratic equation for $\lambda$ in terms of the displacements of the finite structure can be found.

$$\lambda^2 - \left(\frac{U_1 + U_3}{U_2}\right)\lambda + 1 = 0 \tag{3.12}$$

Eq. (3.12) can be easily solved to give two solutions, $\lambda_1$ and $\lambda_2$. The wave vector, $k$, can then be found from the following equation.

$$k_{1,2} = -\frac{i}{L} \cdot \ln\left(\lambda_{1,2}\right) \tag{3.13}$$

where the subscripts 1 and 2 refers to the first and second wave vectors.

### 3.2.3 Two coupled waves

Many systems, such as plates, possess more than one elastic wave and a similar approach can be applied to these systems. The number of elastic waves in a system can be determined based on a priori knowledge of the system. Using beam theory as an example, the number of waves can be determined by considering the general form of the solutions for a beam as follows,

$$W(x,t) = e^{-i\omega t}\left[a_1\ e^{-iK_1 x} + b_1\ e^{iK_1 x} + a_2\ e^{-K_2 x} + b_2\ e^{K_2 x}\right] \tag{3.14}$$

where, $W$ is the transverse displacement, $K_1$ and $K_2$ are the wave numbers, and $a_1$, $b_1$, $a_2$ and $b_2$ are the constants that depend on the boundary conditions.

As seen in Eq. (3.14), the transverse displacement in a beam is caused by two sets of elastic waves with different wave numbers, $K_1$ and $K_2$. Each set of elastic waves consists of a forward moving wave and a reverse (or reflected) wave. In a majority of methods available in the literature, a model, such as the Timoshenko beam or Euler-Bernoulli beam, is needed to find the wave numbers, $K_1$ and $K_2$, in order to define the behaviour of the beam. The beam theories used are as follows.

For Timoshenko beams,

$$\phi(x,t) = e^{-i\omega t}\left[iPa_1\ e^{-iK_1x} - iPb_1\ e^{iK_1x} + Qa_2\ e^{-K_2x} - Qb_2\ e^{K_2x}\right] \tag{3.15}$$

$$P = \frac{GK_1^2\kappa - \omega^2\rho}{GK_1\kappa} \tag{3.16}$$

$$Q = \frac{GK_2^2\kappa + \omega^2\rho}{GK_2\kappa} \tag{3.17}$$

$$K_1 = \frac{1}{2}\sqrt{2\left(\frac{1}{E}+\frac{1}{\kappa G}\right)\rho\omega^2 + 2\sqrt{\left(I-\frac{EI}{\kappa G}\right)^2\left(\frac{\rho\omega^2}{EI}\right)^2 + \frac{4\rho A\omega^2}{EI}}} \tag{3.18}$$

$$K_2 = \frac{1}{2}\sqrt{-2\left(\frac{1}{E}+\frac{1}{\kappa G}\right)\rho\omega^2 + 2\sqrt{\left(I-\frac{EI}{\kappa G}\right)^2\left(\frac{\rho\omega^2}{EI}\right)^2 + \frac{4\rho A\omega^2}{EI}}} \tag{3.19}$$

$$F_B = GA\kappa\left(\frac{\partial W(x,t)}{\partial x} - \phi(x,t)\right) \tag{3.20}$$

$$M = EI\frac{\partial\phi(x,t)}{\partial x} \tag{3.21}$$

where $\phi$ is the angle of rotation, $K_1$ and $K_2$ are the wave numbers for the elastic waves, $E$ is the elastic modulus, $G$ is the shear modulus, $A$ is the cross sectional area, $\kappa$ is the shear coefficient for Timoshenko beams, $I$ is the second moment of area, $F_B$ is the force and $M$ is the bending moment.

For Euler-Bernoulli beams,

$$\theta(x,t) = \frac{\partial W}{\partial x} \tag{3.22}$$

$$K_1 = K_2 = \left(\frac{\rho A\omega^2}{EI}\right) \tag{3.23}$$

$$F_B = -\frac{\partial M}{\partial x} \tag{3.24}$$

$$M = EI\frac{\partial^2 W}{\partial x^2} \tag{3.25}$$

where the $\theta(x,t)$ is the gradient of $W$ and the other symbols have the same definitions as in Timoshenko beam theory.

Direct methods, such as the finite element method and the transfer matrix method, require models such as this in the calculation of the band structure, and when shear effects are significant, the Euler-Bernoulli and Timoshenko beam theories will give different results. However, in the wave superposition method, the wave numbers, $K_1$ and $K_2$, *do not need to be modelled*. Thus, the band structure found will be that of the physical system, unless an analytical model was used to find the response.

As seen in Eqs. (3.14), (3.15) and (3.22), for beams with two elastic waves as studied

here, there are two degrees of freedom that can measured or calculated. However, in practice, only the transverse response can be measured with ease. Due to the linear elastic assumption, the displacement, velocity and acceleration can be related using,

$$W = \frac{\dot{W}}{i\omega} = -\frac{\ddot{W}}{\omega^2} \tag{3.26}$$

and the required displacements can be deduced from the acceleration measurements. The number of degrees of freedom available for calculations in the wave superposition method can influence the minimum number of nodes required to find the band structure.

Using the same approach as the single wave case, the equations relating the displacement at each point are as follows, where the two sets of waves are denoted as Wave A and Wave B. For the Euler-Bernoulli case, $\phi$ is replaced with $\theta$.

$$W_n = W_{FA,n} + W_{FB,n} + W_{RA,n} + W_{RB,n} \tag{3.27}$$

$$\phi_n = \phi_{FA,n} + \phi_{FB,n} + \phi_{RA,n} + \phi_{RB,n} \tag{3.28}$$

where the subscripts $F$ and $R$ refer to the forward and reverse wave, respectively, while the subscripts $A$ and $B$ refer to waves A and B.

Applying the response equations, Eqs. (3.27) and (3.28) to each node, each degree of freedom will contribute to an additional equation and 4 additional unknowns, which are the individual contributions of the amplitude of each wave. The displacements, $W$, and rotations, $\phi$, are known from measurements. Additionally, applying the Bloch wave relationship to each of the individual wave amplitudes for the beam, the following equations are found.

$$W_{FA,n+1} = \lambda_A W_{FA,n} \tag{3.29}$$

$$W_{FB,n+1} = \lambda_B W_{FB,n} \tag{3.30}$$

$$W_{RA,n} = \lambda_A W_{RA,n+1} \tag{3.31}$$

$$W_{RB,n} = \lambda_B W_{RB,n+1} \tag{3.32}$$

$$\phi_{FA,n+1} = \lambda_A \phi_{FA,n} \tag{3.33}$$

$$\phi_{FB,n+1} = \lambda_B \phi_{FB,n} \tag{3.34}$$

$$\phi_{RA,n} = \lambda_A \phi_{RA,n+1} \tag{3.35}$$

$$\phi_{RB,n} = \lambda_B \phi_{RB,n+1} \tag{3.36}$$

An important point to note here is that, the waves were assumed to originate from the two ends of the structure being investigated in the wave superposition method. Since elastic waves are introduced at the nodes that are externally excited or constrained, the

wave superposition method can be used for finite structures with arbitrary boundary conditions provided the internal nodes are not externally excited or constrained. This is not a problem in practice as structures are generally unconstrained in experiments to measure the frequency response functions. Another exception with the method is that only one of the sets of the waves will be detected if the boundary conditions at the two ends are exactly the same as one of the eigenvectors, because the other mode is not excited. However, this problem is unlikely to occur in practice and can be easily avoided by measuring the band structure with different boundary conditions. Therefore, dispersion curves calculated using the wave superposition method are generally independent of the boundary conditions at the two ends of the structure.

Eqs. (3.29) to (3.36) show that each degree of freedom will contribute to 4 additional equations for each unit cell and no additional unknowns as the unknowns have already appeared in the displacement relationships. Furthermore, the number of unit cells in the system is one less than that of the total number of nodes. Eqs. (3.33) to (3.36) are unavailable if only the transverse displacements are measured.

Finally, the two wave vectors contribute to the two final unknowns.

$$\lambda_A = e^{ik_A L} \tag{3.37}$$

$$\lambda_B = e^{ik_B L} \tag{3.38}$$

where $k_A$ and $k_B$ are the wave vectors to be determined for waves A and B respectively.

Based on the analyses made in this section, the number of equations from each relationship can be summarised in Table 3.2. Using the equations summarised in Table 3.2, the number of nodes required to find the wave vectors for a periodic structure with two waves can be found using Eq. (3.39).

| Relationship | Number of equations | Number of unknowns |
|---|---|---|
| Displacement relationships | $dn$ | $4dn$ |
| Bloch wave conditions | $4d(n-1)$ | 0 |
| $\lambda_A, \lambda_B$ | 0 | 2 |
| Total | $5dn - 4d$ | $4dn + 2$ |

Table 3.2: Number of equations required for a periodic system with two waves; where $d$ is the number of degrees of freedom and $n$ is the number of nodes required.

$$n = \frac{4d+2}{d} \tag{3.39}$$

The number of nodes required for the case where both $W$ and $\phi$ can be measured is 5; while if only $W$ is measured, the number of nodes required is 6. The low number of nodes needed to be measured for the wave superposition method of 6 is significantly lower than the 645 spatial points measured in [138]. For a continuous beam, the wave vector

measured is equal to the wave number of the beam, $K_1$ and $K_2$, in Eq. (3.14) which allows the complex moduli of the material to be estimated using the wave superposition method, if the density and geometry of the beam are known.

Using similar steps as the single wave case, the relationships defined in Eqs. (3.29) to (3.39) and eliminating the unknowns, the solution for the wave vectors, when two degrees of freedom can be measured, is a fourth order polynomial described by Eq. (3.40). The solutions for the case when only the transverse displacements are measured are listed in Appendix A.

$$\begin{aligned}(-W_2\phi_3 + W_3\phi_2 + W_3\phi_4 - W_4\phi_3)\lambda^4 + (W_1\phi_3 - W_3\phi_1 - W_3\phi_5 + W_5\phi_3)\lambda^3 + \\ (-W_5\phi_4 - W_1\phi_2 - W_1\phi_4 + W_2\phi_1 + W_2\phi_5 + W_4\phi_1 + W_4\phi_5 - W_5\phi_2)\lambda^2 + \\ (W_1\phi_3 - W_3\phi_1 - W_3\phi_5 + W_5\phi_3)\lambda + (-W_2\phi_3 + W_3\phi_2 + W_3\phi_4 - W_4\phi_3) = 0 \end{aligned} \tag{3.40}$$

$$\lambda = \lambda_A = \lambda_B \tag{3.41}$$

$$k_{1,2,3,4} = -\frac{i}{L} \cdot \ln\left(\lambda_{1,2,3,4}\right) \tag{3.42}$$

Eqs. (3.40) and (A.3) have analytical solutions, where the inputs are the displacements. Hence, the band structure can be found using only the response of the system.

### 3.2.4 Generalising to systems with multiple degrees of freedom or waves

The procedure to obtain the solution for the wave vector in terms of displacements described for the single degree of freedom system and two coupled waves can be generalised to cases with multiple waves and degrees of freedom. The procedure is summarised as follows,

1. Determine the number of coupled waves and degrees of freedom.
2. Determine the number of nodes required.
3. Generate the appropriate equations describing displacement relations and Bloch wave conditions.
4. Eliminate unknowns using the equations to obtain solutions in polynomial form.
5. Calculate or measure displacements and phase difference at the required points.
6. Solve the polynomial equation to obtain wave vectors.

As stated previously, the number of coupled waves and number of degrees of freedom can be determined with a priori knowledge of the system. Waves that are not coupled can be solved separately. The key equations that form the final solution for the

wave superposition method are the wave dispersion relationships and the Bloch wave relationships at the nodes. These equations are generalised as

$$W_{n,d} = \sum_{q=1}^{\mathrm{w}} W^{\mathrm{F}}_{q,d,n} + W^{\mathrm{R}}_{q,d,n} \tag{3.43}$$

$$W^{\mathrm{FR}}_{\mathrm{q},d,n} = \begin{cases} \lambda_{\mathrm{q}} W^{\mathrm{F}}_{\mathrm{q},d,n-1} & \text{, for Forward waves} \\ \lambda_{\mathrm{q}} W^{\mathrm{R}}_{\mathrm{q},d,n+1} & \text{, for Reverse waves} \end{cases} \tag{3.44}$$

where the superscript F or R denotes the direction of the wave, $q$ denotes the $n^{\mathrm{th}}$ wave, and $W^{FR}_{q,d,n}$ is the individual amplitude of the component waves.

The displacement relationship in Eq. (3.43) shows that the displacement for a given degree of freedom measured at each node will contribute to an additional equation and 2w additional unknowns, which are the components of each of the forward and reverse waves for a single set of waves at the node. The displacements at the nodes, $W_{n,d}$, are found from measurements. Hence, for $n$ nodes, the number of equations from the displacement relationship is $d\mathrm{w}n$, while the number of unknowns is $2d\mathrm{w}n$, where $d$ here refers to the number of the degrees of freedom.

The Bloch wave relationships in Eq. (3.44) are then used to relate the amplitude of a wave component at a node to its adjacent node for every unit cell. No new unknowns were introduced in the Bloch wave relationships and each unit cell considered will contribute to an additional $2d\mathrm{w}$ equations. As the total number of unit cells is one less than the total number of nodes, the total number of equations from the Bloch wave relationships will contribute to $2d\mathrm{w}(n-1)$ equations. Lastly, each wave will have an individual $\lambda_{\mathrm{w}}$, and will contribute to a total of w unknowns. The total number of equations and unknowns are summarised in Table 3.3.

| Relationship | Number of equations | Number of unknowns |
|---|---|---|
| Displacement relationships | $dn$ | $2d\mathrm{w}n$ |
| Bloch wave conditions | $2d\mathrm{w}(n-1)$ | 0 |
| $\lambda_{\mathrm{w}}$ | 0 | w |
| Total | $(d+2d\mathrm{w})n - 2d\mathrm{w}$ | $2d\mathrm{w}n + \mathrm{w}$ |

Table 3.3: Number of equations required for a periodic system with arbitrary number of degrees of freedom; where $d$ is the number of degrees of freedom and w is the number of waves.

Based on the summary in Table 3.3, the number of nodes required for one dimensional phononic crystals or meta-materials is described by

$$n = \frac{(1+2d)\mathrm{w}}{d} \tag{3.45}$$

Once the number of required waves and nodes are calculated, the equations that relate the displacements to the individual waves, Eq. (3.43), and the equations for the Bloch wave conditions at the boundaries, Eq. (3.44), are then determined for all the required nodes. After that, the unknowns are eliminated to find the solutions in terms of $\lambda$. Lastly, the displacements at the different nodes are either measured or calculated, which will be substituted into the solutions to find the wave vectors.

The assumption of the displacements of system being made up of superposition of elastic waves described by Eq. (3.43) is not unique to the wave superposition method, for example the method introduced in [196] also incorporate this assumption. Despite this similarity, the general concept in deriving the equations to find the band structure are significantly different. In [196], the Bloch wave expansion method was used to generate the matrices to form an eigenvalue problem in order to find the band structure. The superposition of waves assumption was then applied to the matrices to reduce them to smaller matrices by only retaining a selected number of modes. This results in a reduced Bloch wave expansion with smaller matrices, which is still an eigenvalue problem and a model to describe the structure is required. However, for the method described in this chapter, the wave superposition assumption and the Bloch wave boundary conditions were applied to the displacements at the boundary nodes of consecutive unit cells instead and plane wave expansion was not implemented. Hence, the responses of a finite structure are expressed as equations in terms of the wave vectors, $k$, when only the two ends of the finite structure are externally excited or constrained. The equations were then combined via substitution to form a single equation in terms of the response of the structure, that can be solved to find the band structure. This method does not require a model for the structure and hence the Bloch wave expansion was not implemented and the stiffness or mass matrices, as seen in [196], were not calculated with the wave superposition method described here.

The steps described here can be directly applied to more complicated structures, like the ones introduced in [26, 36, 43, 70, 112, 124], for transmission in a single direction (i.e. arranged in a line). Although, there are many studies performed on two or three dimensional phononic crystals, one dimensional phononic crystals have many potential applications especially in vibration isolation in structural components and there is an abundance of studies in one dimensional phononic crystals, for example [50, 104, 105, 118, 126, 127, 138, 193, 197–200]. The wave superposition method will greatly benefit future studies of these one dimensional periodic structures as it allows the comparison of experimental results to models especially if the periodic structures contains oscillators with complicated geometry or materials that cannot be easily characterised. In order to increase the capability of the wave superposition method, an attempt has been made to extend the method to be applicable for two and three dimensional structures. The steps taken to extend the method for structures with more dimensions and its analysis

are presented in Section 3.5.

### 3.2.5 Calculating the eigenvectors and predicting response of periodic structures with different numbers of unit cells

Apart from the band structure, the eigenvectors are also of interest in the study of elastic waves in periodic materials as they represent the mode shapes of the infinite periodic structures. The wave superposition method can also be used to calculate the components of the eigenvectors provided the relevant physical quantities, such as forces, $F$, moments, $M$, and shear rotations, $\phi$, are measured. Furthermore, the eigenvector components when combined with the band structure enables the calculation of the frequency response of the finite structure with arbitrary boundary conditions.

In this work, the eigenvectors for beam bending were calculated. The eigenvectors, $v$, were scaled, so that the transverse displacements, $W$, are equal to unity, i.e.

$$Wv = \begin{bmatrix} W \\ \phi \\ F \\ M \end{bmatrix} = W \begin{bmatrix} 1 \\ v_\phi \\ v_F \\ v_M \end{bmatrix} \tag{3.46}$$

Based on the theory discussed previously, the transverse displacements at the $n^{\text{th}}$ node, $W_n$, of a finite structure that is only constrained or excited at the boundaries can be described as follows,

$$W_n = \lambda_A^n W_{FA0} + \lambda_A^{-n} W_{FA0} + \lambda_B^n W_{FB0} + \lambda_B^{-n} W_{RB0} \tag{3.47}$$

The eigenvalue equation in Eq. (3.46) implies that the other physical quantities can be related to the wave equations via the following equation.

$$\begin{aligned} P_n &= \lambda_A^n P_{FA0} + \lambda_A^{-n} P_{RA0} + \lambda_B^n P_{FB0} + \lambda_B^{-n} P_{RB0} \\ &= \lambda_A^n v_{P,FA} W_{FA0} + v_{P,RA} \lambda_A^{-n} W_{RA0} + v_{P,FB} \lambda_B^n W_{FB0} + v_{P,RB} \lambda_B^{-n} W_{RB0} \end{aligned} \tag{3.48}$$

where $P$ is a physical quantity to represent $F$, $M$ or $\phi$.

Given that the values of $W_{FA0}$, $W_{FB0}$, $W_{RA0}$ and $W_{RB0}$ are known from the measurements taken to determine the band structure and Eq. (3.47), there are only 4 unknowns, which are the components of the eigenvectors, $v_{P,FA}$, $v_{P,RA}$, $v_{P,FB}$, $v_{P,RB}$, in Eq. (3.48). Therefore, by measuring the physical quantity, $P$, at any 4 nodes and substituting the values into Eq. (3.48), there are sufficient equations to solve for the eigenvectors.

In practice, the physical quantities can be measured from the two ends of the beam using transducers; for example, load cells can be placed at the ends of the beams to

measure the forces. However, there is no straightforward method to measure these quantities at the internal nodes without significantly influencing the behaviour of the structure. This problem can be resolved by taking measurements with different boundary conditions and substituting the values into Eq. (3.48). If these physical quantities are measured at both ends, each set of boundary conditions will give 2 equations. An example of the calculation of the eigenvector components using this method is described in Appendix B.

On the other hand, when the eigenvector components are known, Eq. (3.48) can then be used to predict the response of a finite periodic structure with any boundary conditions. This is done by setting the boundary equations in Eq. (3.48) to find the values of $W_{FA0}$, $W_{FB0}$, $W_{RA0}$ and $W_{RB0}$, and the desired response at any node can then be calculated by substituting the values of $W_{FA0}$, $W_{FB0}$, $W_{RA0}$ and $W_{RB0}$ in Eq. (3.48) and setting the value of $n$ to the node number. This is similar to the procedure of solving for the vibrations of the beam using the analytical solution. Based on this analysis, the response of a finite periodic structure with any number of unit cells and boundary conditions can be easily calculated requiring only simple linear algebra. This will reduce the amount of computational time required for studies of finite structures, especially when the unit cell is complicated, because the response of finite structures can now be calculated using the band structure and the relevant components of the eigenvectors; simulation of the entire finite structure is unnecessary. Furthermore, the band structures and eigenvectors needed to calculate the response can be obtained using other methods, such as the transfer matrix method.

## 3.3 Virtual experiment: demonstration and validation of the method

A periodic bi-material beam, modelled using sections of Timoshenko beams, was used to validate the proposed method and serves as a proof of concept. The full benefits of the wave superposition method will be realised in an actual experiment, especially in cases where a simple model of the structure is unavailable. The numerical example was selected over a physical experiment to demonstrate that the proposed method is accurate under ideal conditions. This is to ensure that any inaccuracies observed can be directly attributed to the proposed method instead of experimental error. Experimental aspects of the wave superposition method will be addressed in Chapter 4.

The wave superposition method is validated in this section by comparing the band structure and eigenvectors to those predicted by the transfer matrix method. Additionally, the transmissibility of a finite periodic material with a varying number of unit cells is presented, calculated using only the eigenvectors and band structure.

### 3.3.1 Structure

The structure used in the virtual experiment was made of two materials, steel and lead. These materials were selected as they have a large difference in axial wave speed, 5063.7 m $s^{-1}$ and 1072.6 m $s^{-1}$ for steel and lead respectively, to produce large and easily observable band gaps. The unit cell of the structure is shown in Figure 3.2 (a). The geometry was arbitrarily selected. As described previously in Section 3.2, the number of nodes required for the single axial wave is 3, while for the bending waves 5 unit cells are required if both $W$ and $\phi$ are measured, and 6 unit cells are required if only $W$ is measured. Therefore, the structure used in this analysis was made up of 5 unit cells and 6 nodes as shown in Figure 3.2 (b). The properties and dimensions used for the steel and lead beams in this study are listed in Table 3.4. A case with material damping was also studied to demonstrate that the wave superposition method is also capable of determining the band gaps when damping is present. In this work, material damping was introduced by using the complex modulus, $E_r$,

$$E_r = E(1 + i\eta) \tag{3.49}$$

where $E_r$ is the effective Young's modulus.

Representing the stiffness as complex is a common treatment for material damping and can be found in several textbooks [1, 201, 202]. The mechanical loss modulus, $\eta$, used for the materials are stated in Table 3.4, which are within the known ranges for these materials listed in [203].

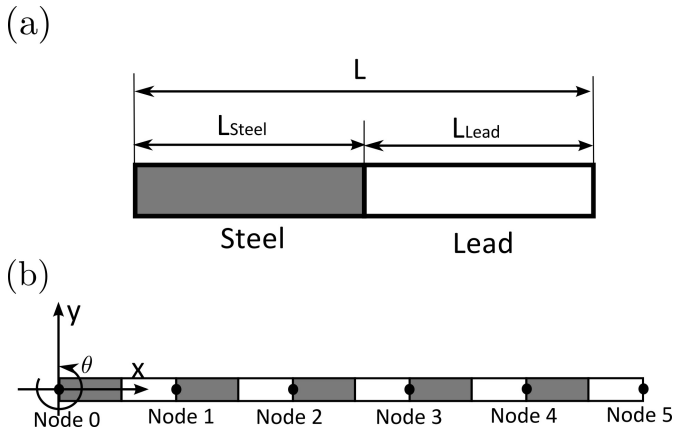



Figure 3.2: (a) Unit cell of structure (b) Five unit cell structures used in the numerical example.

| | Steel | Lead |
|---|---|---|
| Density, $\rho$ (kg m$^{-3}$) | 7800 | 11300 |
| Young's modulus, $E$ (GPa) | 200 | 13 |
| Poisson's ratio, $\nu$ | 0.33 | 0.44 |
| Shear coefficient, $\kappa$ | 0.89 | 0.89 |
| Cross-sectional area, $A$ (m$^2$) | 0.7854 | 0.7854 |
| Second moment of area, $I$ (m$^4$) | 0.0491 | 0.0491 |
| Length, $L$ (m) | 1.0 | 1.0 |
| Mechanical loss coefficient, $\eta$ | $1 \times 10^{-4}$ | 0.05 |

Table 3.4: Properties and geometry of the beams in the unit cell.

### 3.3.2 Calculation of band structure using the wave superposition method

The band structure of the system was calculated using Eq. (3.12) for the longitudinal vibrations and for the transverse direction; both Eq. (3.40) and Eq. (A.3) were used. These equations require only the response, which are displacements at the boundary nodes of the unit cells. In this work, the material properties and geometries were only used to simulate the response of the system for demonstration and validation purposes. The response would in reality be measured experimentally.

In this example, the analytical solutions, Eqs. (3.14) to (3.21), were used to determine the response of the system. Two different boundary conditions were used to demonstrate that the boundary conditions do not affect the band structure calculated using the wave superposition method. The two boundary conditions in this study were the free-free and free-fixed boundary conditions summarised in Table 3.5. The boundary conditions at both ends of the structure do not have to be as stated in Table 3.5. The values in Table 3.5 are not required for the wave superposition method, and any values of forces or displacements can be used, provided that the values at one of the ends are non-zero. Otherwise, there will be no excitation.

| Free-Free | Free-Fixed |
|---|---|
| $F_{x,0} = 1$ N | $F_{x,0} = 1$ N |
| $F_{y,0} = 1$ N | $F_{y,0} = 1$ N |
| $M_0 = 1$ Nm | $M_0 = 0$ Nm |
| $F_{x,5} = 0$ N | $U_{x,5} = 0$ N |
| $F_{y,5} = 0$ N | $W_{y,5} = 0$ N |
| $M_5 = 0$ Nm | $\phi_5 = 0$ Nm |

Table 3.5: Boundary conditions of beams in the virtual experiment.

**Displacement calculations using the analytical solution**

The wave equations for the bending of Timoshenko beams are Eqs. (3.14) and (3.23) stated previously, while the wave equations for axial vibrations are as follows.

$$U = e^{i\omega t}(a_3 e^{-iK_3 x} + b_3 e^{iK_3 x}) \tag{3.50}$$

$$K_3 = \sqrt{\frac{\rho\omega^2}{E}} \tag{3.51}$$

$$\begin{aligned} F &= EA\frac{\partial U}{\partial x} \\ &= EAe^{i\omega t}(-ia_3 K_3 e^{-iK_3 x} + ib_3 K_3 e^{iK_3 x}) \end{aligned} \tag{3.52}$$

The calculations were performed by using the wave equations for each section of the beam and applying the appropriate boundary conditions. Force equilibrium and continuity were enforced for the internal nodes. The relevant equations were then organised into a matrix using commercial software Maple and Matlab. The equations were solved to find the displacements and relevant constants, $a_1$, $a_2$, $a_3$, $b_1$, $b_2$, $b_3$, $c_1$, $c_2$, $d_1$ and $d_2$ for each section of the beam in Eqs. (3.14) and (3.15), and Eqs. (3.50) and (3.51).

### 3.3.3 Transfer Matrix Method

An established method was used to calculate the band structure in order to validate the wave superposition method. In this work, the transfer matrix method [126, 204, 205] was selected because the transfer matrix, $\tilde{\mathbf{D}}$, can be constructed using the analytical solutions of beam theory.

In the transfer matrix method, the eigenvalue problem in Eq. (3.53) is formulated and solved. The eigenvalues found using the transfer matrix method are equivalent to $\lambda = e^{ikL}$, as stated throughout this work:

$$\tilde{\mathbf{D}}(\omega)\tilde{\mathbf{X}}_{\mathbf{0}} = e^{ikL}\tilde{\mathbf{X}}_{\mathbf{0}} = \tilde{\mathbf{X}}_{\mathbf{L}} \tag{3.53}$$

where $e^{ikL}$ are the eigenvalues, $\mathbf{X_0}$ are the forces and displacements at one end of the unit cell and $\mathbf{X_L}$ are the forces and displacements at the other end of the unit cell, defined in Eq. (3.54) and Eq. (3.55) respectively.

$$\tilde{\mathbf{X}}_{\mathbf{0}} = [U(0)\ W(0)\ \phi(0)\ F_x(0)\ F_{y(0)}\ M(0)]^T \tag{3.54}$$

$$\tilde{\mathbf{X}}_{\mathbf{L}} = [U(L)\ W(L)\ \phi(L)\ F_x(L)\ F_y(L)\ M(L)]^T \tag{3.55}$$

The unit cell of the periodic bi-material beam is shown in Figure 3.2(a). The two different materials are treated as separate beams and the boundary conditions at both

ends of the beams were applied using Eqs. (3.14) to (3.21), where continuity and force balance are enforced at the interface. Arranging the equations in matrix form gives

$$\mathbf{D}(\omega)\mathbf{X_0} = \mathbf{X_L} \tag{3.56}$$

where $\mathbf{D}(\omega)$ is a 30 $\times$ 30 matrix, and $\mathbf{X}_0$ and $\mathbf{X}_L$ are 30 $\times$ 1 matricies defined by Eq. (3.57) and Eq. (3.58) respectively.

$$\begin{aligned}\mathbf{X_0} = [&U_{\text{Steel}}(0)\ W_{\text{Steel}}(0)\ \phi_{\text{Steel}}(0)\ F_{x,\text{Steel}}(0)\ F_{y,\text{Steel}}(0)\ M_{\text{Steel}}(0)\\ &U_{\text{Steel}}(L)\ W_{\text{Steel}}(L)\ \phi_{\text{Steel}}(L)\ F_{x,\text{Steel}}(L)\ F_{y,\text{Steel}}(L)\ M_{\text{Steel}}(L)\\ &U_{\text{Lead}}(0)\ W_{\text{Lead}}(0)\ \phi_{\text{Lead}}(0)\ F_{x,\text{Lead}}(0)\ F_{y,\text{Lead}}(0)\ M_{\text{Lead}}(0)\\ &a_{1,\text{Steel}}\ a_{2,\text{Steel}}\ a_{3,\text{Steel}}\ b_{1,\text{Steel}}\ b_{2,\text{Steel}}\ b_{3,\text{Steel}}\\ &a_{1,\text{Lead}}\ a_{2,\text{Lead}}\ a_{3,\text{Lead}}\ b_{1,\text{Lead}}\ b_{2,\text{Lead}}\ b_{3,\text{Lead}}]^T\end{aligned} \tag{3.57}$$

$$\mathbf{X_L} = [U_{\text{Lead}}(L)\ W_{\text{Lead}}(L)\ \phi_{\text{Lead}}(L)\ F_{x,\text{Lead}}(L)\ F_{y,\text{Lead}}(L)\ M_{\text{Lead}}(L)\ \mathbf{0}]^T \tag{3.58}$$

where $\mathbf{0}$ is a 1 $\times$ 24 matrix of zeros.

The matrix $\mathbf{D}$ in Eq. (3.56) was simplified to the form required in Eq. (3.53) by performing the following matrix operation.

$$\tilde{\mathbf{D}} = \mathbf{D}_{p,p} - \mathbf{D}_{p,q}(\mathbf{D}_{q,q}^{-1}\mathbf{D}_{q,p}) \tag{3.59}$$

where $p$ ranges from 1 to 6 and $q$ from 7 to 42.

The eigenvalue problem in Eq. (3.53) was solved using the *eig* function in Matlab. Since the analytical wave solutions were used in the transfer matrix in this section instead of the finite element, the predicted band gaps will be more accurate compared to the finite element method as the analytical solutions do not have quantisation errors.

## 3.4 Results and discussion on band structure

### 3.4.1 Response functions

The frequency response functions for the transverse displacement, $W$, at the nodes for the free-free and free-fixed cases of the bi-material beam studied are shown in Figure 3.3. For the sake of brevity, the frequency responses for the vibrations in the longitudinal directions are not shown.

As seen in Figure 3.3, the frequency response of the bi-material beam studied for both the free-free boundary conditions and free-fixed boundary conditions are similar.

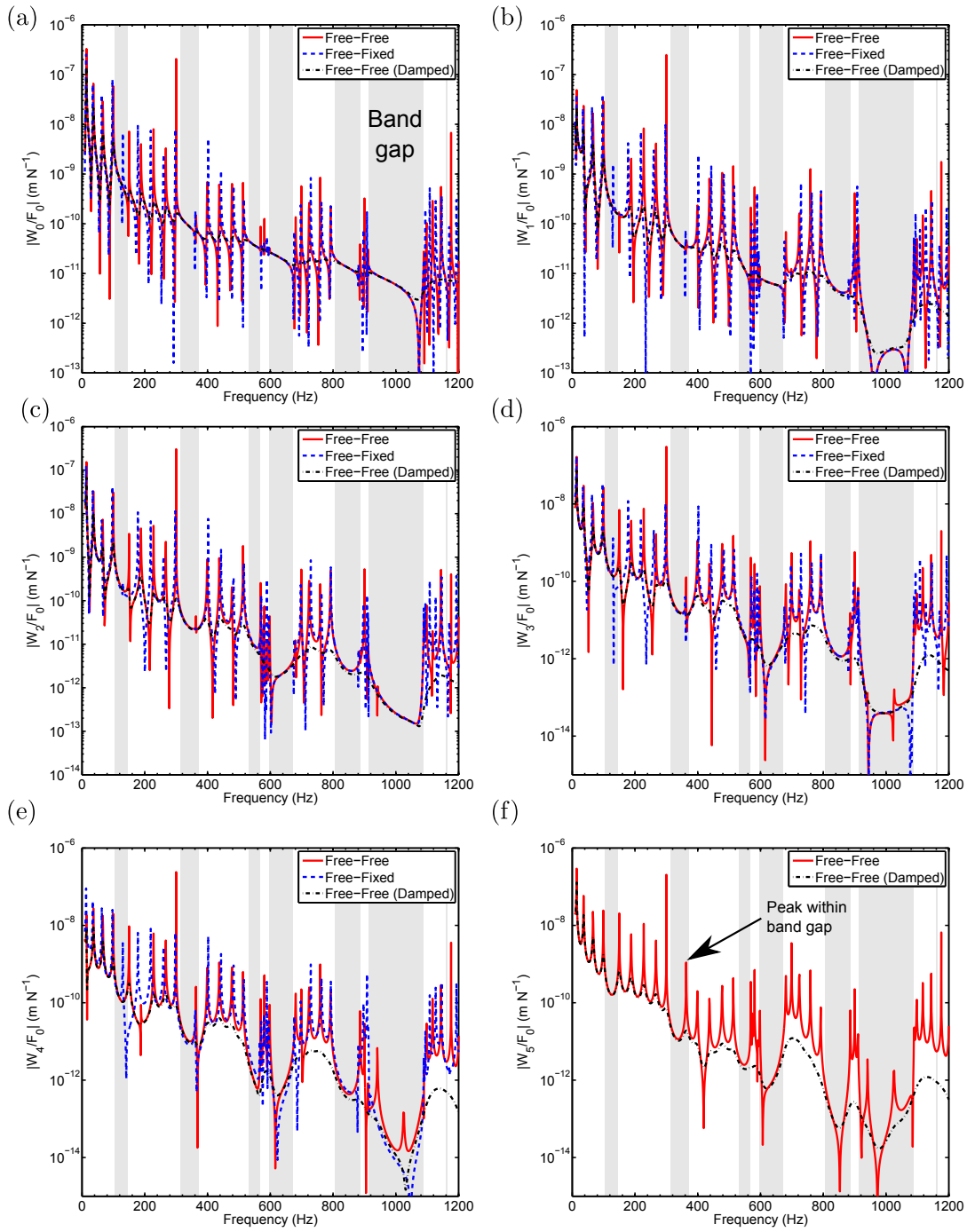



Figure 3.3: Frequency response of bi-material beam at various locations (a) Node 0 (b) Node 1 (c) Node 2 (d) Node 3 (e) Node 4 (f) Node 5 (Free-Fixed is 0 and not plotted). The band gaps calculated from the TM method are highlighted in grey.

Despite the similarities, the frequency response of both cases are not identical. One notable difference is the different peaks observed around 100 to 200 Hz for all nodes in Figure 3.3, suggesting different modes of vibrations. Additionally, there are significant differences in the frequency responses at Node 3 and 4 in between 900 to 1100 Hz, suggesting that the mode shape for the vibration modes at these frequencies are different.

The frequency response for the free-free case with damping is also plotted in Figure 3.3. At lower frequencies of below 400 Hz, material damping reduces the amplitudes of vibrations at resonances for all nodes. It is important to point out that the high damping values used for lead in this study is to ensure that the damping effects are sufficiently large to be observed and many materials will not have large damping values used here. Therefore, this reduction in amplitudes are unlikely to be observed in actual experiments. However, the amplitude at the anti-resonances are higher for the damped case compared to the undamped case. Material damping has a larger effect on the response at higher frequencies with a significant decrease in amplitude at the resonances, and some vibration modes in Figure 3.3 appear to be eliminated.

The band gaps found using the dispersion curves presented later have also been highlighted in Figure 3.3. In theory, the amplitude of vibrations within the band gaps should be low and this is generally observed in the frequency response for the bi-material beam in Figure 3.3 with the exception of the response at the first node because the first note was excited and the wave have not undergo any attenuation. However, contrary to the analysis in [206], several resonant peaks were observed within the band gap, for example the resonant peaks for the bi-material beam with the free-free boundary condition has a peak at the final node of around 350 Hz as shown in Figure 3.3 (f). Similarly, for the fixed-fixed case, there is a clear resonance peak at around 100 Hz, which is within the band gap and this occurs at all nodes. Another observation is that the peak for the free-free boundary condition at about 350 Hz for the final node has a higher amplitude than the amplitudes at previous nodes. This observation appears to be inconsistent with the theory as the waves should be decreasing in magnitude. The reason for this observation is the finiteness of the bi-material beam studied; similar observations was made in a study by Xiao [116]. In [116], the peaks are a result of the first node having a significantly lower amplitude than the final node. As will be explained later, the peaks and higher amplitudes at the band gaps for finite structures are a result of the waves being reflected at the end instead of being propagated further. The conclusion by Hussein [206] that resonant peaks should not appear in the band gap was made based on observations of finite periodic structures with the ends connected to an elastic medium, so that the waves can pass through at the end instead of being reflected, which is not the case in this study. The frequency response at these nodes was used in the wave superposition method to determine the band structure.

### 3.4.2 Dispersion curves

The dispersion curves calculated using the transfer matrix method and wave superposition method are shown in Figs. 3.5 to 3.8 for both the transverse and longitudinal directions, without and with material damping. The results found using the wave superposition method for the free-free and free-fixed conditions are identical. Similarly, the results found using one ($W$) and two ($W$ and $\phi$) degrees of freedom for the transverse vibrations were also identical. Thus, the results for the wave superposition method calculated using frequency response with different boundary conditions are only plotted once in Figs. 3.5 to 3.8 as square markers. The number of markers was chosen for clarity. Identical results for the different boundary conditions is expected, as discussed in Section 3.2.3. As seen in Figs. 3.5 to 3.8, the results calculated using the transfer matrix method (the solid lines), are identical to the results from the WSM. This observation indicates that the wave superposition method is accurate.

The band gaps were determined from the dispersion curves, where the band gaps are regions of frequencies for which the imaginary parts of all wave vectors are non-zero. This is because the imaginary parts of the wave vectors represent the attenuation of the waves and a non-zero value for the imaginary part means that the wave is reducing in amplitude after each unit cell. A positive imaginary part is considered to be an attenuating wave in the reverse direction. The band gaps in the bi-material beam studied are highlighted in Figs. 3.5 and 3.6.

In some simple finite element methods, as seen in [186], only the real part of the wave vector was found, although more sophisticated finite element methods [99, 120] can provide the imaginary parts of the wave vectors. Generally, in the simple finite element methods, the lines and markers in the band gap regions will not be found, and in such cases the band gaps are determined by the regions where there are no real wave vectors. These observations are consistent with most of the results shown in Figs. 3.5 and 3.6 as all the band gaps, with the exception of the band gaps at 595 to 635 Hz and 914 to 1088 Hz for the transverse vibrations, have normalised wave vectors of either 0 or $\pm\pi$ (corresponding to the reverse wave), which is the same as having no real part. However, the existence of the real parts at frequencies of 595 to 635 Hz and 914 to 1088 Hz suggests that waves can propagate through the system and may lead one to believe that these regions are not band gaps, even though the non-zero imaginary parts indicate that the wave will attenuate with each unit cell.

In order to explain the difference between the band gaps at 595 to 635 Hz and 914 to 1088 Hz and the other band gaps, the wave profiles for the infinite beam were investigated. Generally for a beam with two sets of waves, at the pass band they consist of a set of propagating waves and a set of evanescent waves. The propagating waves will have a real wave vector, for example Point A in Figure 3.5 (a) and (b) at 9 Hz. The wave profile for this wave at different normalised times, $\tau = \omega t$, which represent the

phase of the wave for an infinite periodic structure, is shown in Figure 3.4 (a). As seen in Figure 3.4 (a), the waves will move forward with time, $t$, with the same magnitude. Conversely, the evanescent wave, denoted by Point B in Figure 3.5 (a) and (b), is a standing wave due to the wave vector being purely imaginary and this can be seen in the wave profile in Figure 3.4 (b). The decreasing magnitude is a result of the imaginary part being non-zero. Based on this observation, the presence of the propagating wave as seen in Figure 3.4 (a) will cause vibrations to pass through even for an infinite periodic structure provided no damping is present.

On the other hand, for the other band gaps, such as the one at 806 to 887 Hz, the two sets of waves are both evanescent waves or standing waves with reducing magnitude. An example are the waves at 855 Hz denoted by points C and D in Figure 3.5 (a) and (b), in which their wave profiles are shown in Figure 3.4 (c) and (d) respectively. The reducing magnitude for both waves indicates that the vibrations will reduce with increasing distance and hence the vibrations will approach asymptotically to zero.

For the band gaps with complex wave vectors, such as the band gaps for the transverse direction at 595 to 635 Hz and 914 to 1088 Hz in Figure 3.5, the waves can propagate through the medium but the magnitude of the waves decreases with increasing distance. The wave profiles for these waves at 625 Hz and 855 Hz, denoted by Points E and F in Figure 3.5 (a) and (b), are shown in Figure 3.4 (d) and (e). As seen in Figure 3.4 (d) and (e), these waves travel through the structure, unlike the standing waves in Figure 3.4 (c) and (d). The reducing magnitude with distance will cause the wave to be extinguished eventually and therefore this frequency band can be considered to be a band gap. Some simple methods in literature that only calculate the real parts of the wave vectors may not be able to distinguished between these two types of band gaps since these regions will not be present in those analysis. A key difference in the band gaps at these frequency bands is that the solution to the eigenvalue problem (for transfer matrix and finite element methods) or the polynomial equation (for the wave superposition method) are two pairs of complex conjugates (i.e. Point F), while the solution for a pass band is a pair of complex conjugates and a pair of real values (i.e. Point A and B), and the solution for the other type of band gap is two pairs of imaginary values (i.e. Point C and D).

For the cases with material damping, the wave superposition method will also yield accurate results as seen in Figs. 3.7 and 3.8, where the results of the wave superposition method and the transfer matrix method, which is an established method in the literature, are identical, thus validating the wave superposition method for use with material damping. As seen in Figs. 3.7 and 3.8, the general shape of the band structures are similar to the undamped cases in Figs. 3.5 and 3.6, especially at lower frequencies. Additionally, the band gaps are less distinct for the cases with material damping as the imaginary part are present across all frequencies. This is expected as material damping

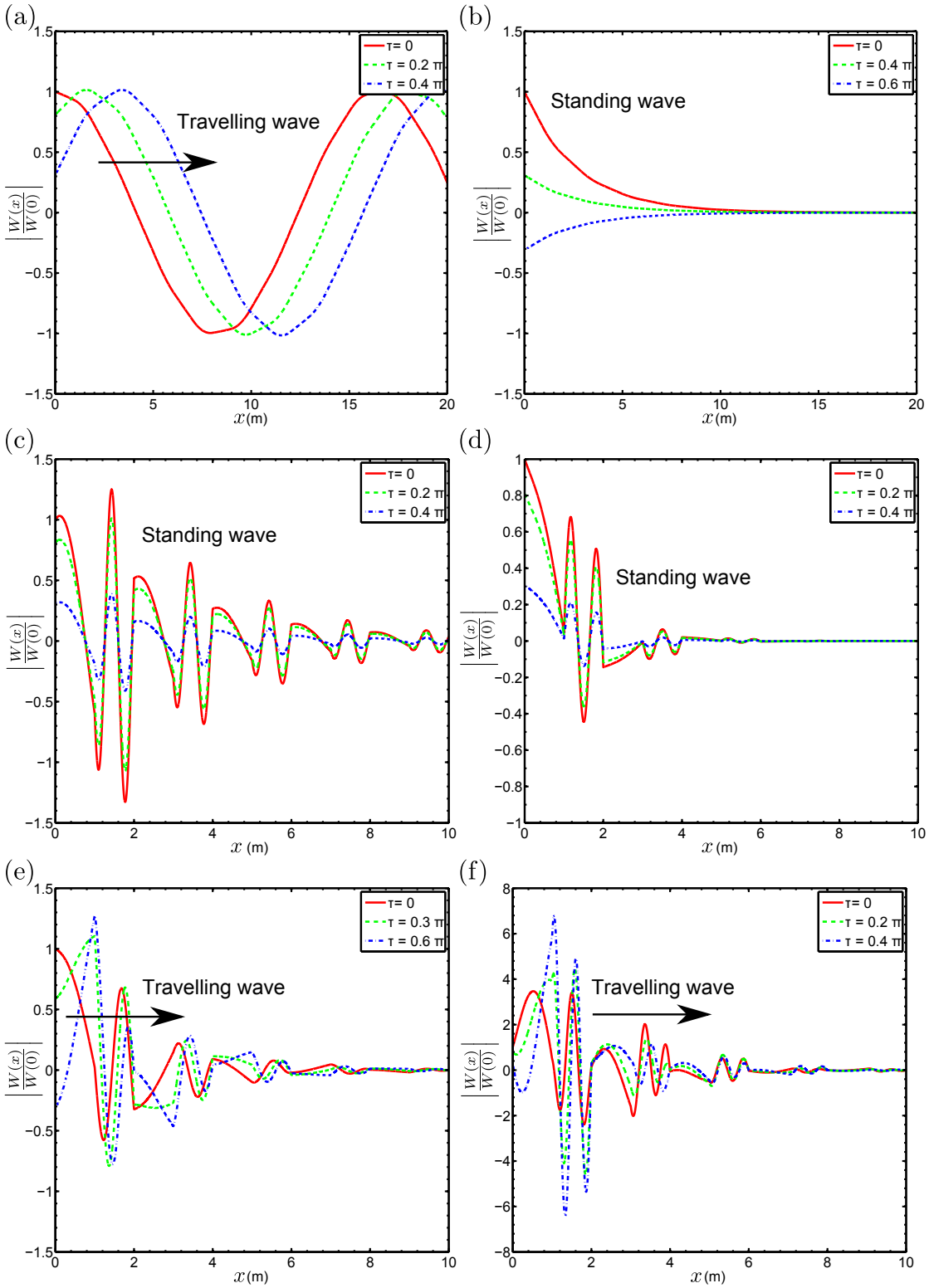



Figure 3.4: Wave profiles for infinite structures at different frequencies and waves where the values are normalised, each unit cell is 2 metres (a) Point A - 9 Hz (b) Point B - 9 Hz (c) Point C - 855 Hz (d) Point D - 855 Hz (e) Point E - 625 Hz (f) Point F - 1063 Hz

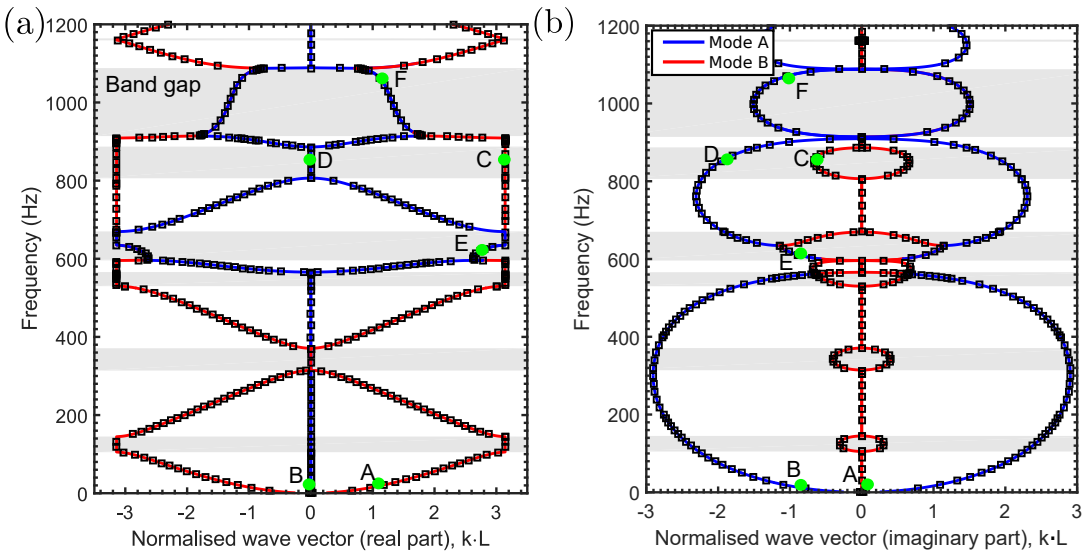



Figure 3.5: Dispersion curves for the undamped bi-material beam in the transverse direction (a) Real part (b) Imaginary part. Solid lines (–) denote results using transfer matrix method while square markers (□) denote results using the wave superposition method. The band gaps are highlighted in grey.

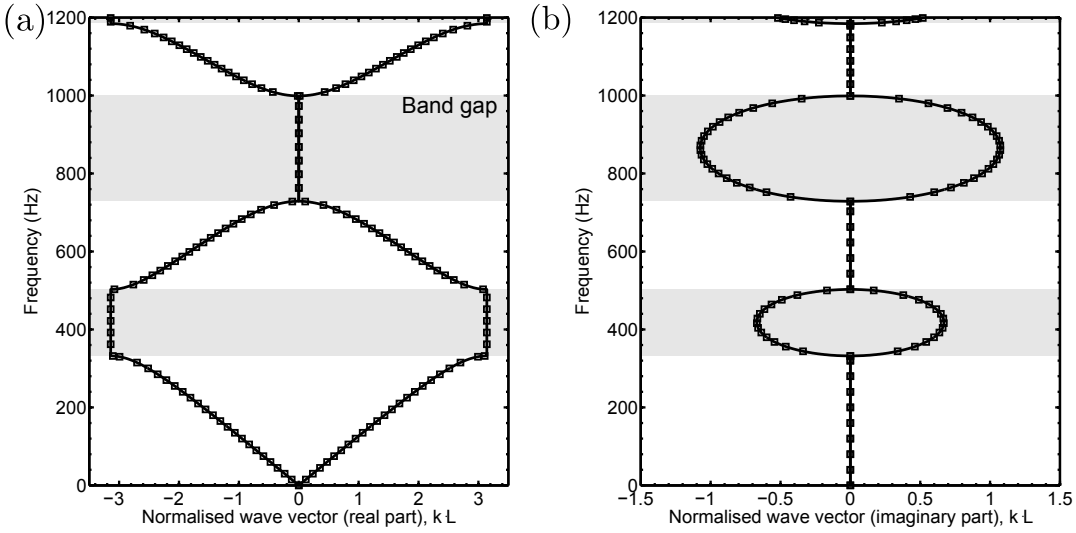



Figure 3.6: Dispersion curves for the undamped bi-material beam in the longitudinal direction (a) Real part (b) Imaginary part. Solid lines (–) denote results using transfer matrix method while square markers (□) denote results using the wave superposition method. The band gaps are highlighted in grey.

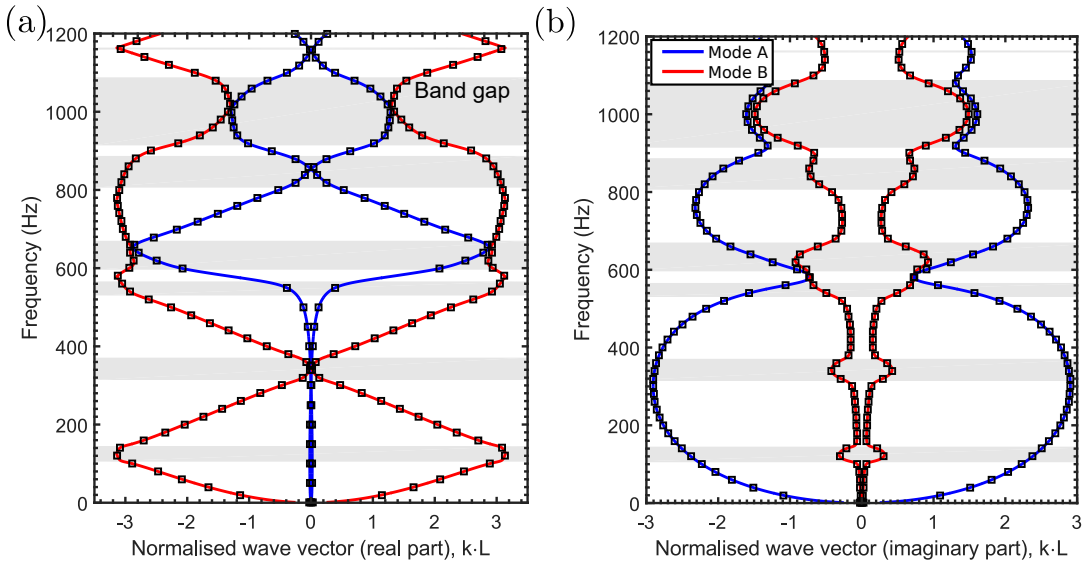



Figure 3.7: Dispersion curves for the damped bi-material beam in the transverse direction (a) Real part (b) Imaginary part. Solid lines (–) denote results using transfer matrix method while square markers (□) denote results using the wave superposition method. Band gaps of the undamped case are highlighted in grey.

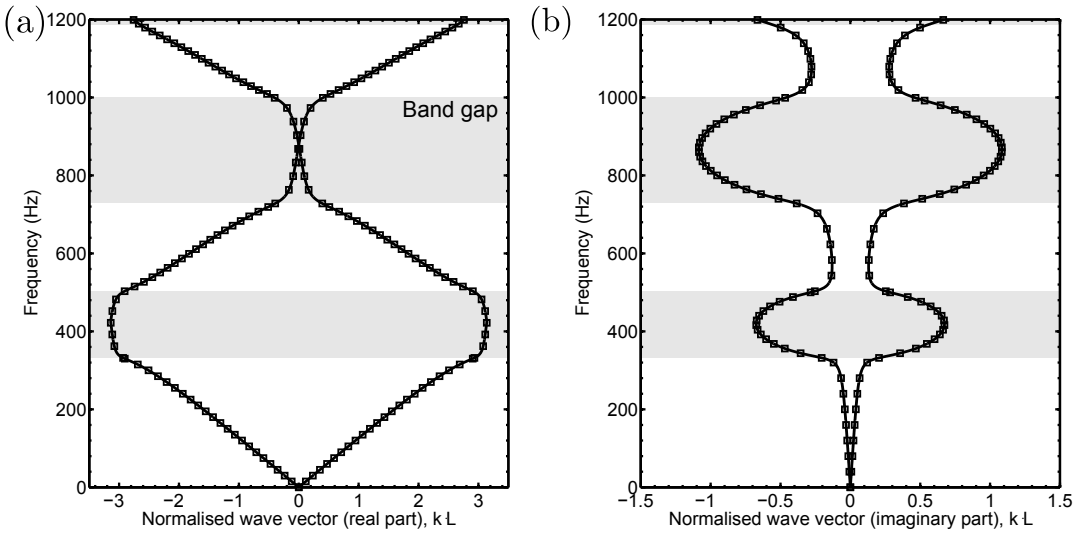



Figure 3.8: Dispersion curves for the damped bi-material beam in the longitudinal direction (a) Real part (b) Imaginary part. Solid lines (–) denote results using transfer matrix method while square markers (□) denote results using the wave superposition method. Band gaps of the undamped case are highlighted in grey.

will result in energy being dissipated. Lastly, as the wave vectors at all frequencies also possess non-zero real parts, all waves can propagate including within the band gaps of the undamped case, highlighted in Figs. 3.7 and 3.8. The effects of material damping will not be discussed in detail here as the purpose of this section is to demonstrate the validity of the wave superposition method. Details on the effects of damping on dispersion curves can be found in other studies, such as [99, 185, 188].

### 3.4.3 Components of the eigenvectors

The components of the eigenvectors, $v_\phi$, $v_F$ and $v_M$ in Eq. (3.46), calculated in this study were based on the wave superposition method described in Section 3.2.5, using the known wave vectors and the boundary conditions of both the free-free and free-fixed cases. Although the eigenvector, $v$, in Eq. (3.46), is a vector, its components, $v_\phi$, $v_F$ and $v_M$, are scalars. Furthermore, the components of eigenvectors, $v_\phi$, $v_F$ and $v_M$, are functions of space, $x$, but the values calculated in this study is for the case where $x = 0$ as the measurements of the responses are taken at that point. In order to calculate the components of the eigenvector at different values of $x$ or for the entire range of $x$, the responses at other points should also be measured with the same boundary conditions and the calculated values at these points should be scaled with respect to $v_w(x = 0)$. For the eigenvector components for the forces, $v_F$, the boundary conditions used were the transverse displacement and the forces at both ends of the beam. In practice, the forces can be measured using load cells but transducers for moments and rotations are less common.

The magnitudes of the eigenvector components calculated using the transfer matrix method and wave superposition method are shown in Figure 3.9, where the values for the transfer matrix method are shown using solid lines and the values using the wave superposition method are denoted by square markers. For the transverse vibrations, there are two set of waves resulting in 4 eigenvector components and for longitudinal vibrations, there is only one set of waves resulting in 2 eigenvector components. The eigenvector components are distinguished in Figure 3.9 with different colours and markers; they were sorted to ensure that they are continuous with respect to frequency. There are a total of four waves for the bending of beams and each wave has an individual wave vector and eigenvector. Each different colour in Figure 3.9 represent the component of eigenvector for a given wave. The band gaps for the undamped case are also highlighted in Eq. (3.7). The results of the transfer matrix method and wave superposition method are identical for both the damped and undamped cases. Therefore, the results calculated using the method described in Section 3.2.5 are accurate. Similar to the wave vectors, the eigenvector components of the damped and undamped cases have similar shapes but the eigenvector components for the damped case can be distinguished more easily. The eigenvector components are useful in the analysis of periodic structures because it

allows the frequency response for finite structures with any number of unit cells and boundary conditions to be calculated with minimal computational effort. This is done by substituting the appropriate boundary conditions in Eq. (3.48).

Additionally, comparing the solutions for the axial vibrations and beam equations with the eigenvector components, the eigenvalues and wave vectors can be used to provide an equivalent stiffness that represents the overall stiffness of the periodic beam as if it is a homogeneous material. Taking the uni-axial case as an example, the product of a representative Young's modulus and cross-sectional area for the wave, $\overline{EA}$, can be related to the eigenvector components for the uni-axial bars as follows.

$$\overline{EA} = \pm \frac{v_F}{ik} \tag{3.60}$$

where the sign changes depending on the direction of the wave.

### 3.4.4 Transmissibilities

The transmissibilities, defined as the magnitude of the vibrations at the final node to the magnitude of vibrations at the first node, for the free-free cases in the transverse and longitudinal directions were calculated using the band structures and eigenvector components for different numbers of unit cells. The frequency responses for the transverse direction were calculated using Eq. (3.48), while the frequency responses for the longitudinal directions were calculated using Eqs. (3.61) to (3.63), using only the frequency response at the first three nodes. The analytical solutions were used to determine the transmissibilities as comparison.

$$U_0 = U_F + U_R \tag{3.61}$$

$$U_N = \lambda^N U_F + \lambda^{W-N} U_R \tag{3.62}$$

$$F_N = \lambda^N v_F^{\text{Forward}} U_F + \lambda^{-N} v_F^{\text{Reverse}} U_R \tag{3.63}$$

The values of $\lambda$ were obtained from the band structures seen in Figs. 3.5 and 3.6, while the eigenvector components were as seen in Figure 3.9. An important point to note is that the eigenvector components used in Figure 3.9 must match with their respective values of $\lambda$ in the calculations.

The results in Figure 3.10 show that the transmissibility and frequency response calculated using the wave superposition method are the same as the analytical solution. The eigenvalues and eigenvector components used to calculate the transmissibility is not limited to the wave superposition method and can also be obtained using a majority of methods available in literature, such as the transfer matrix method. This is advantageous as it allows the transmissibilities of a finite periodic structure with any arbitrary number of unit cells to be calculated using information that can be easily ob-

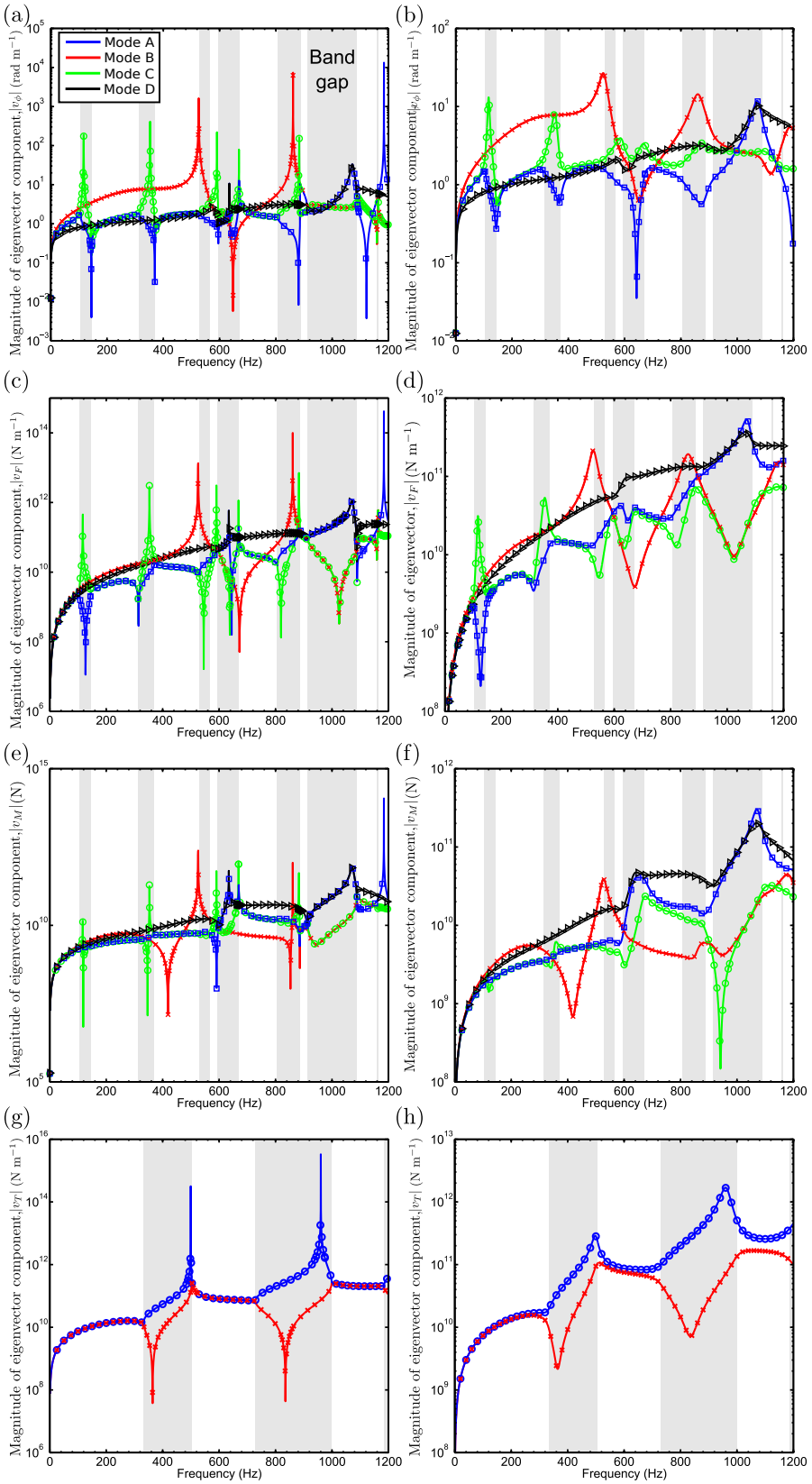



Figure 3.9: Magnitudes of eigenvectors components (a) $v_\phi$ Undamped (b) $v_\phi$ Damped (c) $v_F$ Undamped (d) $v_F$ Damped (e) $v_M$ Undamped (f) $v_M$ Damped (g) $v_T$ Undamped (h) $v_T$ Damped. Band gaps for the undamped cases are highlighted in grey and each colour corresponds to the values for a given wave.

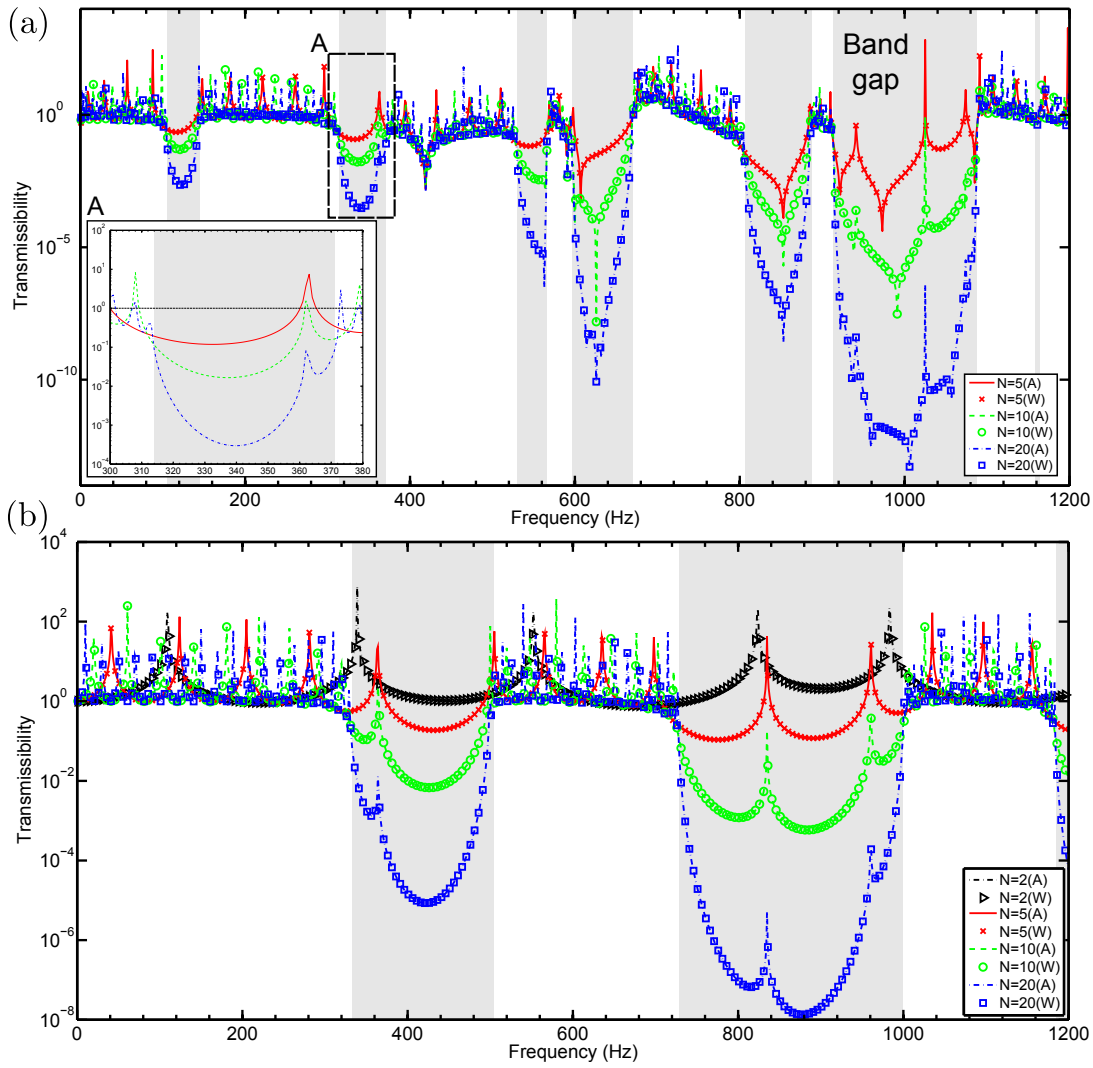



Figure 3.10: Transmissibility for the bi-material beam structure for the free-free case (a) Transverse direction (b) Longitudinal direction. Legend: (A) analytical solution; (W) Wave superposition method; N represents the number of unit cells. The band gaps are highlighted in grey.

tained from the analysis of a single unit cell or experimental measurement. A limitation of this method is that the transmissibilities can only be calculated for the nodes at the boundaries of the unit cell. A model is required for the unit cells if the responses of internal portions of the unit cells are to be determined.

As seen in Figure 3.10, the transmissibilities at the band gaps are generally low with the amplitude decreasing with the number of unit cells in the finite structure. However, as discussed in the previous section, resonant peaks within the band gaps may occur for periodic structures with finite numbers of unit cells. For example, in this study, resonant peaks were observed at 361, 941, 1025 and 1074 Hz for the free-free case in Figure 3.10 (a), which are within the band gaps for the transverse vibrations. Similarly, for the free-free case in the longitudinal direction in Eq. (3.9) (b), resonant peaks were observed at 364, 835 and 961 Hz for the structure with 5, 10 and 20 unit cells, while resonant peaks occur at 339, 824 and 983 Hz for the case with 2 unit cells. Despite the magnitudes of the peaks being lower with larger numbers of unit cells, for example the magnitude of the transmissibility of the 835 Hz peak in Figure 3.10 (b) is lower than $10^{-5}$, there is still a distinct peak in transmissibilities within the band gap. The existence of the peaks within the band gaps is mainly due to the reflected or reverse wave that is produced in order to meet the boundary conditions. This will be explained further using the wave profiles at the resonant peak for the longitudinal vibrations at 835 Hz.

The elastic waves for the longitudinal vibrations at 835 Hz for 2, 5 and 10 unit cells at, $t$=0 are decomposed in Figure 3.11 (a), (c) and (d) respectively. As seen in Figure 3.11 (a) and (c), for a low number of unit-cells, the elastic waves in the finite structure are mainly composed of the reverse wave so that the boundary condition at the end of, $F_N = 0$, is met. Since the reverse wave decreases exponentially from the final node to the first node, the transmissibility will be higher at the final node, resulting in a higher transmissibility. For larger number of unit cells, the magnitude of the reflected wave will be lower compared to the forward wave as seen in Figure 3.11 (c), where with 10 unit cells, the elastic wave is mainly composed of the forward wave.

The magnitude of the eigenvector components as seen in Eq. (3.7) may be used as an indicator to determine if the reverse wave will be sufficiently large to cause a peak in the transmissibility within the band gap. For example, in the longitudinal direction, peaks and troughs in the magnitude of eigenvector components can be found to be at 364, 500, 835 and 961 Hz in Figure 3.9 (g). Since the components of the eigenvectors for this case indicate the ratio of force over displacement amplitude, a peak or trough in the eigenvector components means that a small magnitude of displacement at the boundaries will lead to large magnitude forces, and vice versa. This increases the likelihood of a resonance or anti-resonance occurring around these frequencies, especially when the boundary has end conditions (either force or displacements) that are close to 0. This is

consistent with the observation in which resonant peaks for the axial vibrations at 364, 835 and 961 Hz were observed for the beam studied in Figure 3.10 (b) with 5, 10 and 20 unit cells.

Although resonant peaks within the band gap around frequencies where the magnitude of the components of the eigenvectors experiences a trough or peak were observed, this effect is not universal. For example, for the axial vibrations with 2 unit cells, the transmissibility peaks within the band gaps occur at 339, 824 and 983 Hz, and this was caused by the phase differences between the forward and reverse waves that cause the displacements at the first node to be small despite the magnitudes of both constituent waves being large as seen in Figure 3.11 (b). Additionally, for systems with more than a single set of waves with multiple degrees of freedom, such as transverse bending, the wave reflection characteristics are more complicated and resonances or anti-resonances within the band gaps may not occur at the frequencies where the magnitude of eigenvector components experiences peaks or troughs. However, an important conclusion that can be drawn here is that for a finite periodic structure with a small number of unit cells, the boundary conditions may have wave reflections that cause resonant peaks to occur within band gaps, and that peaks are likely to occur around frequencies where the magnitudes of eigenvector components experience peaks or troughs.

### 3.4.5 Effects of finiteness of the periodic structure

In order to study the effects of the finiteness of the periodic structure, the longitudinal transmissibilities at 835 Hz, which is within the band gap, of the bi-material beam connected to a massless spring of different stiffness, as shown in Figure 3.12, were studied. The transmissibilities of the bi-material beam for different numbers of unit cells are shown in Figure 3.13 (a). One notable observation in Figure 3.13 is that regardless of the spring stiffness, with sufficient number of unit cells (6 in this case), the transmissibility follows the trend described by,

$$T = \frac{U_N}{U_0} = C\ \tilde{\lambda}^N \tag{3.64}$$

where $C$ is a constant.

The trends predicted with Eq. (3.64) are indicated by the dasbyhed lines in Figure 3.13(a). In this case, $\tilde{\lambda}$ in Eq. (3.64) is equal to $e^{i[im(k)]L}$ with the wave vector, $k$, of the forward wave, while $C$ is a constant that is affected by the end boundary condition.

For an infinite periodic structure, the constant $C$ in Eq. (3.64) will be equal to unity according to the Bloch wave theory stated in Eq. (3.1), and this is the same as the case where the spring stiffness, $K$, was set to be equal to the eigenvector component, $v_F$, as seen in Figure 3.13 (a), in which the points lie on the dashed line. The spring with a stiffness equal to the eigenvector component will have an identical response to the

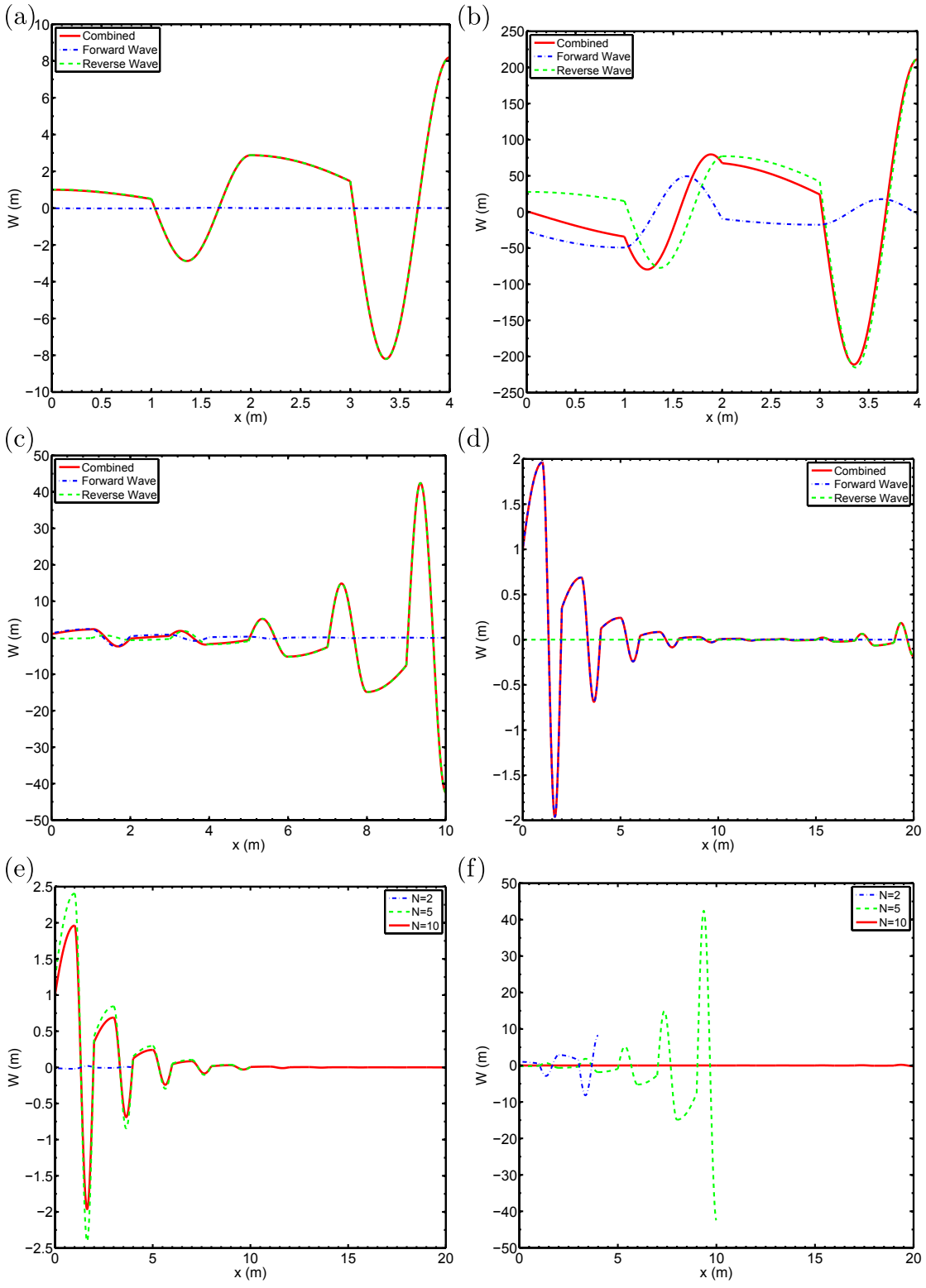



Figure 3.11: Decomposition of elastic waves for free-free axial vibration (a) 835 Hz, N=2 (b) 824 Hz, N=2 (c) 835 Hz, N=5 (d) 835 Hz, N=10 (e) 835 Hz, forward waves (f) 835 Hz, reverse waves. Each unit cell is 2 m long. N represents the number of unit cells.

infinite structure because only one wave will be present in the periodic structure.

However, when the spring stiffness is not equal to the eigenvector component, a reverse or reflected wave will be produced in order for the boundary conditions to be met. This is similar to the cases seen in Figure 3.11 and discussed in Section 3.4.4. At a larger number of unit cells, the effects of the reverse or reflected waves are less pronounced and hence the transmissibility follows the general trend described by Eq. (3.64), where the effects of the reverse wave is described using the constant, $C$. This suggests that the magnitude at the final node caused by the reverse wave is directly proportional to the magnitude of the forward wave at the final node.

Comparing the transmissibilities of different spring stiffnesses in Figure 3.13 (a), the overall transmissibility and $C$ decrease with increasing spring stiffnesses. This result is expected as the displacement will be lower for ends with a higher stiffness but a higher spring stiffness may lead to larger forces being transmitted. For stiffnesses lower than the eigenvalues, the transmissibility increases with decreasing stiffness until the stiffness is equal to zero, which corresponds to the free-free case. Additionally, the minimum number of unit cells required for the bar to follow the trend described in Eq. (3.64) increases with decreasing stiffness. The deviation at a low number of unit cells is a result of the reverse wave contributing a large proportion of the vibrations as described in Section 3.4.4. Within this region, the transmissibility follows the trend where $\tilde{\lambda}$ is that for the reverse wave as shown by the dashed-dot line in Figure 3.13(a).

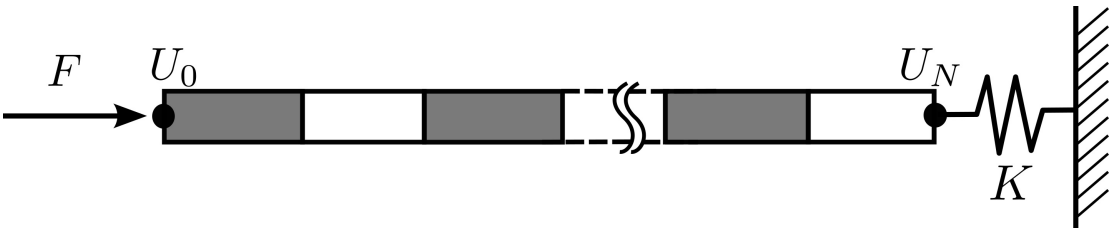



Figure 3.12: Periodic bar with massless spring at the end.

Similar trends were observed for cases with more than a single wave and also with waves that have complex wave vectors, as seen in Figure 3.13 (b), which shows the transmissibilities for the transverse vibrations of the free-free case at different frequencies. Firstly, no attenuation was observed at 9 Hz, which is within the pass band for the pass band in Eq. (3.12). Conversely, within the band gaps, the transmissibility generally follows the trend outlined in Eq. (3.64), but for multiple waves the value of $\tilde{\lambda}$ is that of the wave vector with the smallest imaginary part. However, unlike simple longitudinal vibrations, there are several deviations from the trends in Eq. (3.64). For example, there is significant scatter for the transmissibilities at 624 and 1063 Hz with significant deviations at 9 and 18 unit cells for the 624 Hz case. The scatter is a result of the presence of the real part of the wave vector that causes a phase shift and more

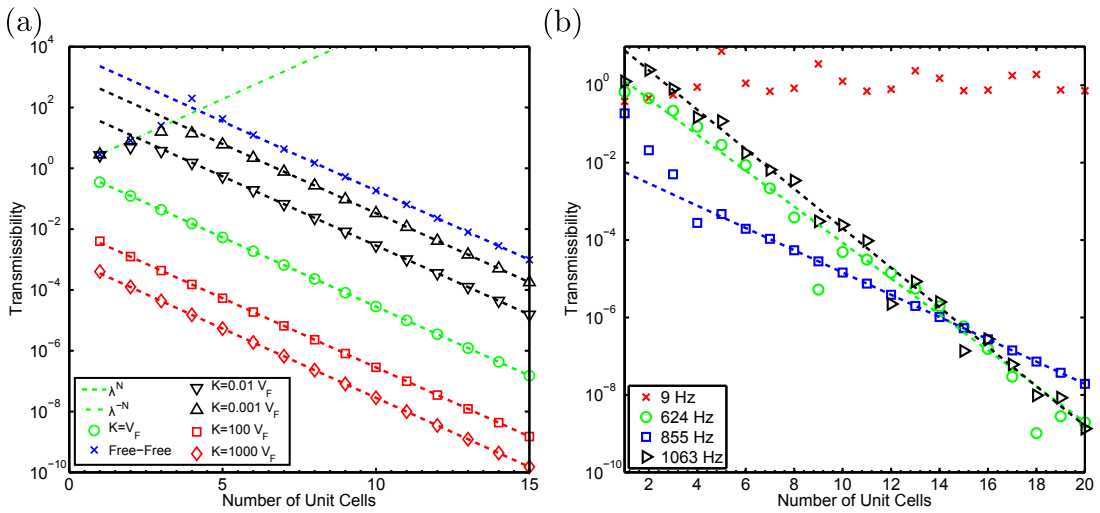



Figure 3.13: Transmissibility vs number of unit cells (a) Axial vibration with different values of spring stiffness at 835 Hz (b) Transverse vibration at free-free condition at different frequencies

complicated wave interactions. At band gaps where the imaginary part of the wave vector for one set of the waves is significantly larger than the other, the wave with the larger imaginary part of the wave vector will be negligible compared to the other wave, especially for the cases with larger numbers of unit cells. Hence, the transmissibilities will follow Eq. (3.64) as in the case for the longitudinal case at 855 Hz in Figure 3.13 (b).

Two important conclusions can be drawn from these observation. Firstly, since the transmissibility follows the trend in Eq. (3.64), the imaginary part of the wave vector should be maximised in order to reduce the number of unit cells required to achieve a given level of attenuation. Secondly, the boundary conditions at the end should have dynamic stiffnesses that are similar to the eigenvector component of the periodic structure within the band gap, so that the periodic structure will have a similar response to the infinite case. Since the analysis on transmissibilities here is based on a one dimension periodic structures, the findings of this analysis is applicable to one dimensional systems and further studies are required to determine if this is also the case for systems with more than a single dimension.

## 3.5 Extending method to 2D and 3D structures: Potential and limitations

Since two and three dimensional phononic crystals and acoustic metamaterials are widely studied, the capability of extending the method to two and three dimensional systems will significantly increase the efficacy of the method. In this section, an at-

tempt will be made to generalise the wave superposition method for periodic structures with more than one dimension. This is done by deriving the relevant equations from the general wave equation. The capabilities and limitations of the method will be discussed during the derivation and by comparing the band structure of a two dimensional phononic crystal calculated using the wave superposition method and that found using conventional methods.

### 3.5.1 Generalising equations for 2D and 3D structures

The first step in extending the theory is to make use of the general form of the Bloch-Floquet theory in Eq. (3.1). By assuming that the excitation and response are harmonic, the time dependent component can be eliminated and Eq. (3.1) can be simplified as

$$\mathbf{u}(\mathbf{x}) = \sum_{\mathbf{G}} \overline{\mathbf{u}}_{\mathbf{G}} e^{i\mathbf{G}\cdot\mathbf{x}} e^{i\mathbf{k}\cdot\mathbf{x}} \tag{3.65}$$

Based on the theory of the wave superposition method, the responses at the boundaries of neighbouring unit cells are known either through measurements or calculations. In the two or three dimensional case, the responses are taken at positions $\mathbf{x} = n\mathbf{L}$, where $n$ is an integer, so that $\mathbf{L}\cdot\mathbf{G} = 2\pi$, for cubic cells. Therefore, the most suitable values for $\mathbf{x}$ are $\mathbf{x} = [L_x, 0, 0]^T, [0, L_y, 0]^T$ and $[0, 0, L_z]^T$.

Unfortunately, these values of $\mathbf{x}$ can only determine one component of the wave vector, $\mathbf{k}$, which are $k_x$, $k_y$ or $k_z$. An important point to note is that, the wave vectors of the other components will still be present when these values of $\mathbf{x}$ are used but it will not be found using this method as these components will be eliminated from the equations during the calculation.

The responses at $\mathbf{x} = n\mathbf{L}$ when $\mathbf{L}\cdot\mathbf{G} = 2\pi$, can be written as,

$$\mathbf{u}(\mathbf{x} = n\mathbf{L}) = \sum_{\mathbf{G}} \overline{\mathbf{u}}_{\mathbf{G}} e^{i2\pi n} e^{in\mathbf{k}\cdot\mathbf{L}} \tag{3.66}$$

Further inspection of Eq. (3.66) shows that it is periodic. Making use of the periodicity at the points, in which the responses are taken and also that Eq. (3.66) is a series representation of a function, Eq. (3.66) can be simplified as,

$$\mathbf{u}(\mathbf{x} = n\mathbf{L}) = \tilde{\mathbf{u}}\lambda^n \tag{3.67}$$

where $\lambda^n = e^{in\mathbf{k}\cdot\mathbf{L}}$.

Eq. (3.67) is the generalised form of Eq. (3.44), which represent one of the many Bloch waves that are present in the system. Since the response of the periodic structure at a given frequency is the sum of all the Bloch waves that are present, the response at $\mathbf{x} = n\mathbf{L}$, $\mathbf{U}(\mathbf{x} = n\mathbf{L})$ can be written as,

$$\mathbf{U}(n\mathbf{L}) = \sum_{\mathrm{W}} \tilde{\mathbf{u}}_{\mathrm{W}} \lambda_{\mathrm{W}}^{n} \tag{3.68}$$

Here, it is important to clarify that the number of waves, W, in Eq. (3.68) is not the same as the number of harmonics (the number of $\mathbf{G}$ in Eq. (3.1) and Eq. (3.65)). The number of harmonics, $n_G$, is the number of waves that are used in the series expansion of the arbitrary function $\tilde{\mathbf{u}}$. Therefore, for the plane wave expansion and extended plane wave expansion methods, it is essential that a sufficiently large number of harmonics are used in order to approximate the arbitrary function, $\tilde{\mathbf{u}}$, accurately. Since the function $\tilde{\mathbf{u}}$ in the wave superposition method is not represented by a series expansion, it is not subjected to the accuracy problems associated with using a low number of harmonics, $n_G$, which are present in plane wave expansion methods, that uses series expansions to approximate the density, stiffness, stresses and displacements.

On the other hand, the number of waves, W, is the number of different waves that are present within the periodic structure. Generally, this number refers to the total number of Bloch waves with unique values of wave vectors or eigenvalues. Several studies [100, 102] have discovered that there are an infinite number of evanescent Bloch waves present in two and three dimensional phononic crystals. An infinite number of waves will result in an infinite number of unknowns, which cannot be calculated using the wave superposition method. Since these waves are evanescent and a majority of them have large attenuation constants, the problem of the infinite evanescent waves can be resolved by using the responses at locations away from the boundaries and sources of excitations. If the displacements or forces at the boundaries are finite, the evanescent waves will attenuate exponentially with each unit cell and can be considered negligible after a few unit cells. Mathematically, the evanescent waves are present in finite structures to fulfil the boundary conditions, which are expected to have higher magnitudes of displacements or forces. Unfortunately, this introduces a shortcoming of the wave superposition method, where the evanescent waves with larger attenuation constants will not be detected. However, methods like the traditional plane wave expansion method and the traditional finite element methods are unable to obtain the complex band structures.

Furthermore, for a two or three dimensional phononic crystal or elastic metamaterial, the wave vectors will have multiple components, $k_x$, $k_y$, and $k_z$, and the bands will be a surface or volume, for example the dispersion surface of a two dimensional phononic crystal is shown in Figure 3.14(a). Therefore, at a given excitation frequency, there will be an infinite number of waves since the surfaces or volume, as seen in the contour plot of the band structure shown in Figure 3.14(b), have an infinite number of possible $\mathbf{k}$ values at a given frequency. Each contour in Figure 3.14(b) shows all the possible propagating waves that can be present at a given frequency, highlighting the importance

of considering the entire surface or volume of first Brillouin zone when determining the band gaps of periodic structures that have more than one dimension.

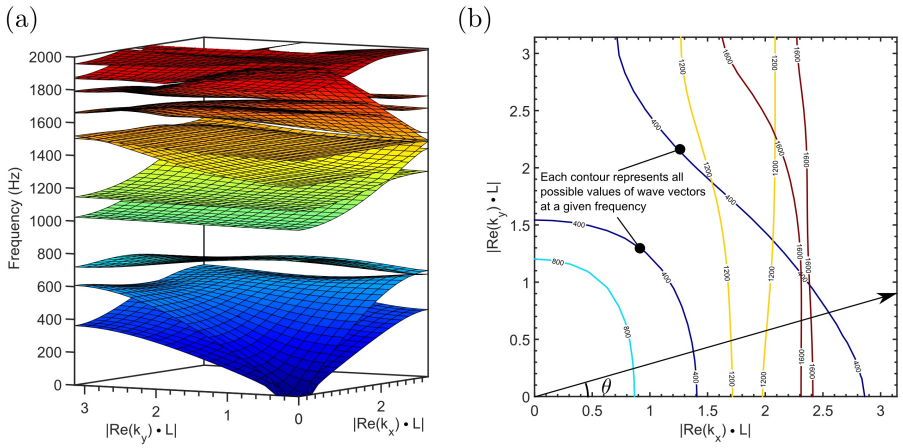



Figure 3.14: (a) Real portion of band structure of 2D phononic crystal shown in Section 3.5.3 (b) Contour plot of real portion of band structure of 2D phononic crystal shown in Section 3.5.3, the numbers on the contour denote the frequency.

In traditional plane wave expansion methods and finite element methods, the real portion of the band structure, as shown in Figure 3.14, was found by calculating the eigenvalues, that represents the radial frequency, $\omega$, squared. For the extended plane wave expansion method, the surfaces can be found by first constraining the wave vectors, $\mathbf{k}$,

$$\mathbf{k} = k\boldsymbol{\alpha} \tag{3.69}$$

where $\boldsymbol{\alpha}$ is a unit vector that can be defined using Eq. (3.70) for two dimensional phononic crystals.

Then, the eigenvalue problem is solved with different values of $\theta$,

$$\boldsymbol{\alpha} = \begin{bmatrix} \cos(\theta) \\ \sin(\theta) \end{bmatrix} \tag{3.70}$$

where $\theta$ is as shown in Figure 3.14 (b).

Unlike these methods, the wave superposition method is unable to calculate the band structure by setting values of $\mathbf{k}$ or imposing constrains on $\mathbf{k}$ as done in Eq. (3.70) in a practical 2D or 3D phononic crystal. This is because the response of these systems at a given frequency may include all possible waves along a contour as shown in Figure 3.14(b). This is the key limitation of the wave superposition method for 2D and 3D phononic crystals.

Despite this limitation, the method is capable of determining the band structure of a

2D or 3D phononic crystals for the cases when only one component of the wave vector is present. This corresponds to $\theta$ in Eq. (3.70) being equal to 0 or $\frac{\pi}{4}$, by constraining the boundaries. Upon inspection of Eq. (3.66), when only a single component of $\mathbf{k}$, which are either $k_x$, $k_y$ or $k_z$, is non-zero, the responses and stresses of the phononic crystals are periodic in the other directions for a phononic crystal measured along its length. For example, in a two dimensional system, when $\theta$ in Eq. (3.70) is zero, $e^{ik_y L_y}$ will be equal to unity resulting in the responses to be periodic across $L_y$. Therefore, by setting the relevant boundaries to be periodic, for example the two dimensional case, and taking the responses at periodic intervals along a single line, as seen in Figure 3.15(a) and (b), the wave superposition method can be used to determine the band structure for 2D or 3D structures along the axis of the dispersion plot. The required periodic boundary conditions can be implemented if the responses are calculated using models, for example using a finite element model, but these periodic boundary conditions cannot be easily implemented in an experiment. Hence, in this study the band structure of a 2D periodic structure with the sides being free, as seen in Figure 3.15(c), will also be calculated in order to assess the errors introduced by the free boundaries.

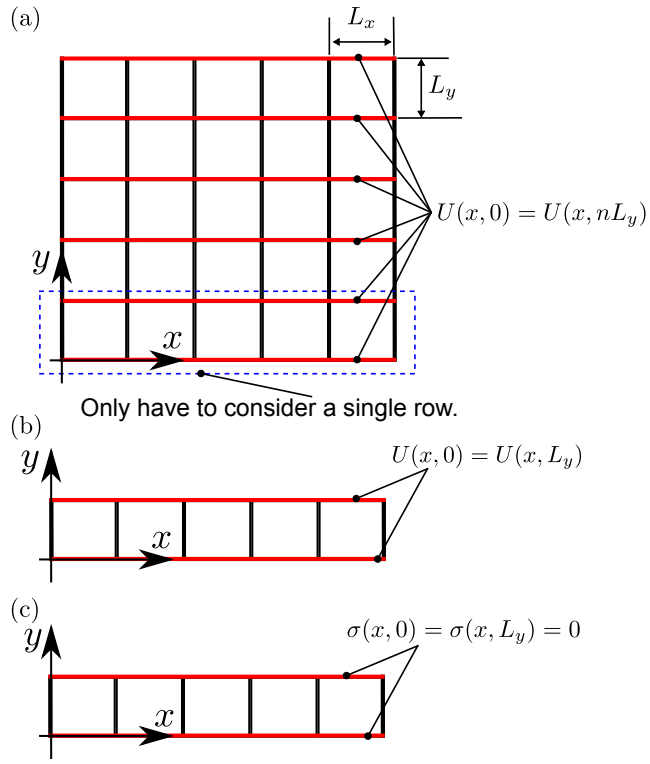



Figure 3.15: (a) A two dimensional phononic crystal in with periodic boundary conditions in the y direction (b) Single row of two dimensional phononic crystal (c) Single row of two dimensional phononic crystal with free boundary conditions.

For the cases in which the waves are only travelling in a single direction, for example in the 2D cases shown in Figure 3.15(b) and (c), by splitting the waves into a forward travelling wave and a backward travelling wave, Eq. (3.68) can be written as,

$$\mathbf{U}(n\mathbf{L}) = \sum_{\mathrm{w}} \tilde{\mathbf{u}}_{\mathrm{w,F}} \lambda_{\mathrm{w}}^{n} + \tilde{\mathbf{u}}_{\mathrm{w,R}} \lambda_{\mathrm{w}}^{-n} \tag{3.71}$$

where the subscripts $F$ and $R$ denote the forward and reverse wave respectively.

This simplification halves the number of unknowns and hence the number of measurements required for the wave superposition method. According to Eq. (3.71), each wave in the system will result in $(2d+1)$w unknowns ($\tilde{u}_{\mathrm{w,F}}$,$\tilde{u}_{\mathrm{w,F}}$ and $\lambda_{\mathrm{w,F}}$), where $d$ is the number of degrees of freedoms measured. Since $\mathbf{U}(n\mathbf{L})$ are known values, the total number of equations is equal to $dn$. This is an important result as this suggests that by knowing the responses at $n = \frac{(2d+1)w}{d}$ points in the periodic structure, there will be sufficient equations to determine $\lambda_w$ and then the wave vectors from the responses of the system. Based on the discussion in this section, the wave superposition method is able to determine the band structure of 2D and 3D phononic crystals for cases when only one component of $\mathbf{k}$ is present and when appropriate periodic boundary conditions are applied. This is a result of the infinite number of propagating waves present across the entire band structure as seen in Figure 3.14(b). In this study, a 2D phononic crystal will be used as an example to assess the ability of the wave superposition method to determine the band structure of periodic structures with more than a single dimension and the errors introduced by neglecting the evanescent waves and propagating waves in other directions. The next section will describe the phononic crystal used in this study followed by the results and discussion.

### 3.5.2 Numerical example of 2D phononic crystal

The unit cell of the phononic crystal used in this study is shown in Figure 3.16 (a) and the properties of the material properties are summarised in Table 3.6. The phononic crystals were assumed to be undergoing plane stress. In this study, the responses required for the wave superposition method were calculated using finite element analysis. Plane stress elements (CPS4R in Abaqus) were used to simulate the individual materials and the mesh of a unit cell is as shown in Figure 3.16 (b), in which each unit cell contains 100 elements. As discussed previously, the wave superposition is only able to obtain the band structure of the 2D phononic crystal for a wave travelling in a single direction. Therefore, the simulation is set up so that the unit cell shown in Figure 3.16 (a) is arranged in a single row similar to the configuration shown in Figure 3.15 (b) with a finite number of unit cells and the displacements of the top nodes set to be equal to the displacements at the bottom nodes. This is so that the calculated band structure is equivalent to the cases, where $k_y$ is set to zero in the extended plane wave expansion

and transfer matrix methods. The boundary conditions on right end is set to be free while each of the 8 middle nodes of the left end of the row as shown in Figure 3.16 (b) is excited by a unit load in both the x and y directions. The load was applied in both the x and y directions, so that the shear mode will also be excited. The band structures were calculated for the cases with 10 and 20 unit cells to demonstrate that the errors caused by the infinite number of complex waves for a two dimensional structure can be reduced by taking measurements at points that are far away from the boundaries. The horizontal and vertical displacements across a frequency range of 1 to 2000 Hz were calculated for both cases. Since only a maximum of two real waves were expected for this 2D phononic crystal, the band structure was calculated for the wave superposition method by assuming only two sets of waves are present and solving Eq. (3.40) but replacing $\phi$ with the vertical displacements. For the case with 10 unit cells, the responses of the central node, as seen in Figure 3.16 (b), at the third to seventh unit cells were used to calculate the band structure while for the case with 20 unit cells, the responses of the central node at the ninth to thirteenth unit cells were used. These points were selected because they are the unit cells in the middle of the row and are furthest from both ends.

The band structure for the row with 20 unit cells was also calculated for the case, in which the unit cell were rotated 90 degrees to demonstrate that the wave superposition method is capable of calculating the band structure of anisotropic structures. Additionally, the band structure of the row with 20 unit cells were also calculated for the case, in which the top and bottom nodes at each unit cells were set to be free, as seen in Figure 3.15(c). This is because setting up an experiment with the displacements of the top and bottom surface of a row being equal is difficult if not impossible.

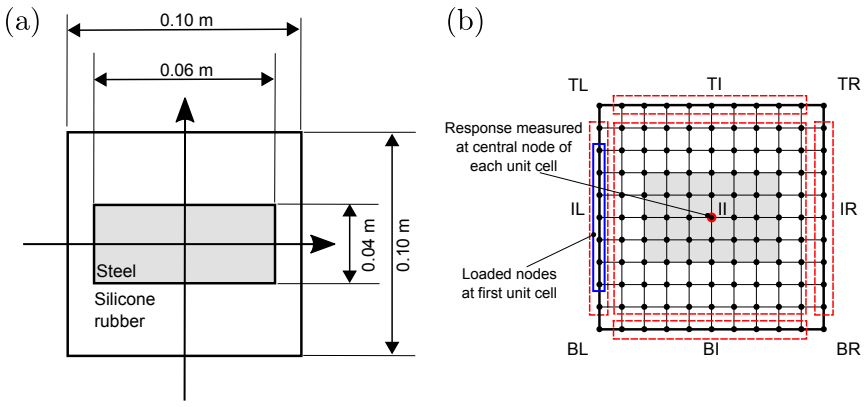



Figure 3.16: (a) Dimensions of a unit cell of the 2D phononic crystal studied (b) Mesh of a unit cell used in the finite element analysis.

The cases that were studied are summarised in Table 3.7 and the band structures calculated with the wave superposition method were compared with the band structure calculated using conventional methods. The conventional methods that were used in this

| Property | Silicon rubber | Steel |
|---|---|---|
| Young's modulus, $E$ (GPa) | $5 \times 10^{-2}$ | 200 |
| Poisson's ratio, $\nu$ | 0.33 | 0.33 |
| Density, $E$ (kg m$^{-3}$) | 1100 | 7800 |

Table 3.6: Material properties for 2D phononic crystal

| Case | Unit cells | Orientation | Boundaries |
|---|---|---|---|
| A | 10 | Original | Top and bottom displacements are equal. |
| B | 20 | Original | Top and bottom displacements are equal. |
| C | 20 | Rotated 90° | Top and bottom displacements are equal. |
| D | 20 | Original | Top and bottom displacements are free. |

Table 3.7: Summary of cases studied for 2D phononic crystals

study are the traditional finite element method and transfer matrix method. Although the transfer matrix method is capable of calculating both the real and complex waves, the band structure of the real waves shown in the results were calculated using the traditional finite element method because it is significantly more convenient to sort the band structures found using the traditional finite element method.

Only a single unit cell as seen in Figure 3.15(b) was used to calculate the band structure in both the traditional finite element and transfer matrix method. The stiffness matrix, $\mathbf{K}$, and mass matrix, $\mathbf{M}$, were extracted from a commercial finite element software, Abaqus, using the substructure generation function. The conventional finite element method and the transfer matrix method used in this study are similar to the ones used in [207] and [114] respectively but the stiffness and mass matrix were obtained using the appropriate elements.

### 3.5.3 Results for two dimensional phononic structures

The dispersion surfaces of the real waves for the two dimensional phononic crystal studied in between 0 to 2000 Hz are shown in Figure 3.14. From the dispersion curve there is only one full band gap within this frequency range. The full band gap was found to be from 825 to 1013 Hz. The dispersion curve for Case A and Case B in Table 3.7, corresponding to the case when $k_y = 0$ with the band structure calculated by the wave superposition method using responses taken from a finite structure from 10 and 20 unit cells respectively, are shown in Figure 3.17 (a) and (b). All complex waves that have imaginary parts of the wave vectors with magnitudes larger than 7 have been omitted for clarity and because these waves are negligible even after a single unit cell.

As seen in Figure 3.17 (a) for the case with 10 unit cells, the wave superposition method is able to accurately predict the wave vectors of the two waves with the smallest imaginary part up to a frequency of approximately 920 Hz. For frequencies lower than

920 Hz, the magnitude of the imaginary parts, referred to as attenuation constants herein, of the other complex waves are significantly larger than the attenuation constants of the first two waves. Therefore, for a row of these phononic crystals, the magnitude of the complex waves will be negligible compared to the first two waves after a few unit cells, which results in these complex waves not being detected and the band structure of the first two waves being detected accurately by the wave superposition method assuming that only two sets of waves exist.

On the other hand, at higher frequencies, the number of waves with lower attenuation constants increases above two, which is the number of waves assumed in this analysis. This will result in errors in the results as seen in Figure 3.17 (a) for frequencies above 920 Hz. The main cause of these errors is the presence of the additional waves that have significantly affected the response of the phononic crystal, as indicated by more than two waves with similar attenuation constants in Figure 3.17 (a). Despite these errors, the wave superposition method is still capable of determining the general shape of the propagating waves (waves that have attenuation constants of 0), even though there is scatter in the prediction and some incorrect bands being predicted. This is because the magnitudes of the response caused by the propagating waves will still be larger than the complex wave after a few unit cells. This issue can be resolved by increasing the number of waves considered in the wave superposition method but this will result in additional measurements and more complicated equations to be solved. The minimum number of waves to be considered should be equal to the sum of the real and complex waves, which can be estimated by calculating the band structures using other methods. Alternatively, the predictions made by the wave superposition method can be improved by using a finite phononic crystal with more unit cells, which allows the measurements to be taken further away from the boundaries. This is so that the magnitude of complex waves, including the waves with low attenuation constants, will be negligible compared to the propagating waves so that only the propagating waves are present. Figure 3.17 (b), compares the results of the 2D phononic crystals with 20 unit cells calculated using the wave superposition method with the finite element and transfer matrix methods. As seen in Figure 3.17 (b), by increasing the number of unit cells and measuring the responses further away from the boundaries will result in improved predictions of the real waves and some of the incorrectly predicted bands in Figure 3.17 (a) are no longer present. Additionally, the dispersion curves at higher frequencies for the case with 20 unit cells appear to be more accurate compared to the case with 10 unit cells, as the shapes of the curves match the values from the traditional methods more closely. Furthermore, as seen in Figure 3.17 (b) the complex waves at higher frequencies are no longer detected as the magnitude of these waves have attenuated to very low values due to the large number of unit cells present but since the evanescent waves will still affect the response of the system, there will still be errors and scatter at higher frequencies as

seen in Figure 3.17 (b).

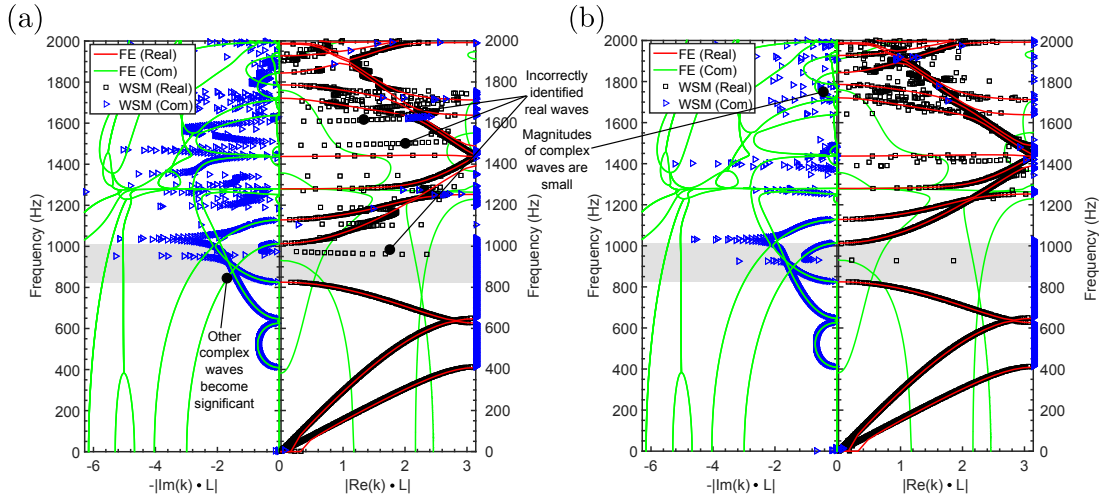



Figure 3.17: Band structure of 2D phononic crystal $k_y = 0$ (a) 10 Unit cells (b) 20 Unit cells. Real and Com in the legend denotes real waves and complex waves respectively, full band gaps are highlighted by grey regions.

Figure 3.18 (a) compares the result of the 2D phononic crystal with 20 unit cells when $k_x = 0$ to demonstrate that the wave superposition is capable of measuring the band structure for these cases provided that the appropriate boundary conditions are used. The results calculated by the wave superposition method were found to be accurate up to frequencies before the magnitudes of more than two waves become significant as seen in Figure 3.18 (a). This observation is similar to the case shown in Figure 3.17 (b).

Since setting the boundary conditions for the top and bottom surfaces of the phononic crystals to be equal will be difficult in practice, the band structure of the phononic crystal with 20 unit cells was also calculated using the wave superposition method by using the response when the top and bottom surfaces are free. This configuration can be set up easily for experiments. Figure 3.18 (b) compares the result from the wave superposition method with conventional methods for this case. One of the first observations in Figure 3.18 (b) is that the dispersion curves calculated with the wave superposition method at lower frequencies (under 800 Hz) appear to have low amounts of scatter but deviates from the results calculated using the conventional methods. This is because the waves that are excited and measured by the wave superposition method correspond to the section of the dispersion surface as shown in Figure 3.14 that will fulfil the free top and bottom surface boundary conditions. Therefore, the values calculated by the wave superposition method at the lower frequencies agrees with the results from the conventional methods, when the top and bottom boundaries were set to be free as denoted by the cyan curve in Figure 3.18 (b). Only the first three bands of the conventional method with the free top and bottom surface boundary conditions

are shown in Figure 3.18 (b) to prevent congestion within the figure. Since the wave superposition method can only measure the waves that are present in the phononic crystals, which is subjected to the boundary conditions, the method is unable to measure the entire dispersion surface, as seen in Figure 3.16, and this the major limitation of the method. However, this result also highlight the importance of considering the entire first Brillouin zone when determining the band gap of two or three dimensional periodic structures because elastic waves may still propagate in a given direction as long as there is a real wave with a non-zero component wave vector in that direction.

The general shape of the dispersion curve calculated using the wave superposition method is similar to the shape predicted by the conventional methods but with a significant amount of scatter at high frequencies and the method have also incorrectly identified several bands as seen in Figure 3.18. The causes of these errors are the same as discussed previously.

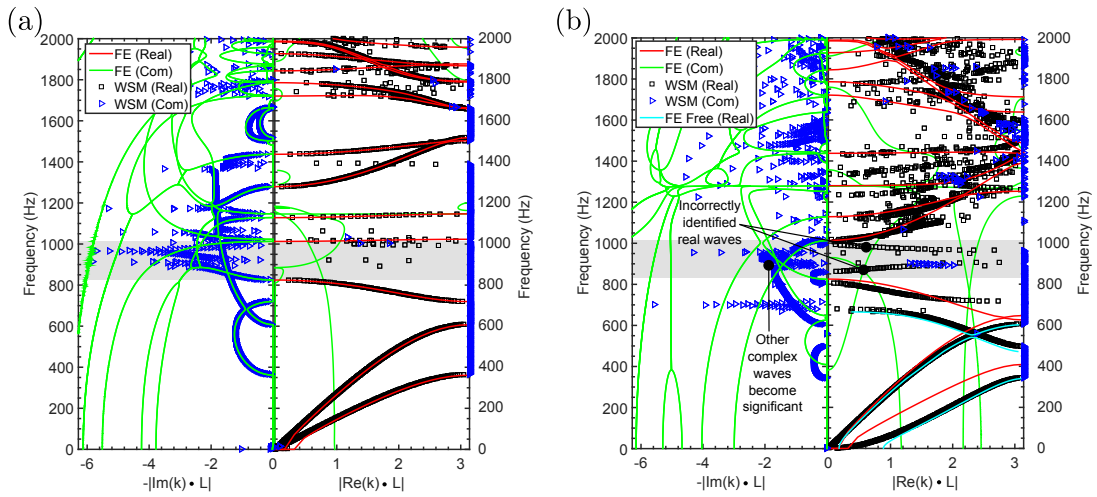



Figure 3.18: Band structure of 2D phononic crystal (a) $k_x = 0$, 20 Unit cells (b) $k_y = 0$, 20 Unit cells free boundaries. Real and Com in the legend denotes real waves and complex waves respectively, full band gaps are highlighted by grey regions.

In short, the wave superposition method is capable of measuring the band structure of two dimensional periodic crystals at given boundary conditions. Although there are an infinite number of waves in a two or three dimensional phononic crystals, most of them are evanescent, which will have very low magnitudes at locations away from the boundaries. This enables the wave superposition method to measure the band structures fairly accurately especially for the lower bands, where the evanescent waves have large attenuation constants. Additionally, these issues can be resolved by taking measurements away from the boundaries or by using more waves in the calculations. The key limitation of the method is that it can only measure a section of the dispersion

curve and this is dictated by the boundary conditions.

## 3.6 Summary and conclusion

The wave superposition method, which is a method to determine the band structure of periodic structures using only the responses at different points without knowledge of the material properties was introduced in this chapter. This method does not require a model to determine the band structure of a periodic material and can be used for system identification purposes. The low number of data points required will also benefit experimental studies in this field, compared to the only other method by [138] that used 645 points.

The wave superposition method was derived by first assuming that the response of the periodic structure is linear and the vibrations are a result of two sets of elastic waves propagating in an infinitely repeating structure, in which one set of waves are forward moving waves while the other set are backward moving waves. The two sets of waves can also be thought of as a set of elastic waves caused by an excitation, with the other set being the reflected waves. Using the superposition principle and the Bloch wave boundary conditions, the relationship between the displacements at adjacent nodes was determined. The equations required to determine the band structure of the periodic structure were found by eliminating the unknowns using these relationships. In this study, the equations to find the band structure of beams in the axial and bending directions were derived. The derived solutions are analytical functions of displacements, allowing the band structure to be found from experiments conducted using simple equipment like a shaker and accelerometers.

A virtual experiment was used in this study to validate the wave superposition method and act as a proof of concept. The band structure of a bi-material beam using the wave superposition method was calculated with displacements obtained from the analytical Timoshenko beam equations for both the free-free and free-fixed cases. The band structures calculated using the responses for the free-free and free-fixed cases were found to be identical indicating that the boundary conditions will not cause errors in the band structure calculations. The results were then compared with the results from the transfer matrix method. The results using both methods were found to be in agreement, validating the method.

Additionally, the components of the eigenvectors of the bi-material beams were also calculated and were found to be accurate after comparing them to the results from the transfer matrix method. The components of the eigenvectors provide useful information for the calculation of the responses and transmissibilities of the periodic material with arbitrary number of unit cells under different boundary conditions. The calculations of the responses using this information were demonstrated in this chapter and may

provide computational savings in the study of finite periodic materials because the required values can be measured easily or calculated using a single unit cell.

The transmissibilities of the structures for different numbers of unit-cells were also studied. Based on the analysis, the transmissibilities are generally directly proportional to the number of unit cells and can be described using Eq. (3.64) when there are sufficient numbers of unit cells. Additionally, the analysis also showed that the response of the structures will be similar to the infinite structure within the band gap if the dynamic stiffness at the boundary is similar to the eigenvalues of the periodic structure. Hence, in order to maximise the attenuation, the periodic structure should be designed to maximise the magnitude of the imaginary parts of the wave vector and have boundaries that have similar dynamic stiffness to the eigenvalues within the band gaps.

An attempt was made to extend the wave superposition method to be used in structures with more than one dimension. The wave superposition method was found to be able to measure a portion of the dispersion surface when measurements are taken from a single row of a two or three dimensional phononic crystal. The results were fairly accurate at the lower bands but due to the larger number of waves being significant at higher frequencies there is some scatter and errors in the results. These errors can be alleviated by either taking measurements further away from the boundaries of the phononic crystals or increasing the number of waves in the calculation. The key limitation of the method is that it can only measure a portion of the dispersion surface and this is dictated by the boundary conditions. Despite the limitations with two and three dimensional phononic crystals, the method is one of the only methods which can measure dispersion curves from responses using simple equipment. Furthermore, the behaviour of one dimensional periodic structures, such as beams, can be accurately predicted by the wave superposition method and there are an abundant studies being conducted in one dimensional structures in recent years, for example in [50, 104, 105, 118, 126, 127, 138, 193, 197–200], and these types of studies will greatly benefit from the method introduced in this chapter. Lastly, since the WSM is developed mainly to facilitate the experiment process of measuring the band structure, an experimental study was conducted in order to assess the validity of the method and this will be discussed in the next chapter.

# 4 Measuring the band structures of periodic beams using the wave superposition method

## 4.1 Introduction

The wave superposition method (WSM) to obtain the band structure from experimental measurements was developed in the previous section. The theory of the WSM was presented and validated using a numerical example in Chapter 3. However, in practice the measured response of a system will contain noise and errors, for example the noise in the accelerometer, manufacturing tolerances, and the accelerometers and force gauge having a finite area rather than a point. Therefore, in this chapter, a physical experiment has been performed in order to validate the WSM experimentally and discuss the issues while implementing WSM in a physical experiment. This is done by taking the required frequency response measurements of a beam and performing the calculations described previously.

The frequency response functions of two different beams, a bi-material beam made from aluminium and polycarbonate (PC), and a beam with periodic variation in geometry, were measured with an accelerometer. The WSM was then used to determine the band structure from the frequency response function. Additionally, the WSM was also used to predict the frequency response at the other nodes using only the measured band structure and the frequency response function at two of the nodes.

Since the theory of the WSM is described in the Chapter 3, it will not be repeated here and this chapter is organised as follows. Firstly, the experimental setup and properties of the beams studied will be described. Then, the results will be presented and discussed with emphasis on the issues related to this method. Finally, the frequency response calculated from the measured band structure is discussed.

## 4.2 Experimental setup

### 4.2.1 Beam properties

In this study, the band structure of the bending of two finite beams, one with a change in material properties and one with a change in geometry, were measured experimentally. The beam with a change in material property is a bi-material beam (designated as Beam 1), while the beam with a change in geometry (designated as Beam 2) is a single material beam. Beam 1 was manufactured by using adhesives to attach beams of different materials together. Beam 2 was manufactured by milling a beam to the required dimensions. The material properties and dimensions of the two beams are listed in Table 4.1, where the damping within the material is accounted for with a loss coefficient as seen in Eq. (3.49). Figure 4.1 is an illustration of the dimensions of the beams used in Table 4.1.

| | | Beam 1 | Beam 2 |
|---|---|---|---|
| Material 1 | Material | Poly-Carbonate | Aluminium |
| | Young's modulus, $E_1$ (GPa) | 2.38 | 70.00 |
| | Poisson's ratio, $\nu_1$ | 0.399 | 0.330 |
| | Shear modulus, $G_1$ (GPa) | 0.85 | 27.00 |
| | Density, $\rho_1$ (kg m$^{-3}$) | 2710 | 2700 |
| | Loss coefficient, $\eta_1$ $\times 10^{-3}$ | 16.80 | 1.05 |
| | Length, $L_1$ (mm) | 17 | 50 |
| | Width, $b_2$ (mm) | 20 | 20 |
| Material 2 | Material | Aluminium | Aluminium |
| | Young's modulus, $E_2$ (GPa) | 70.00 | 70.00 |
| | Poisson's ratio, $\nu_2$ | 0.330 | 0.330 |
| | Shear modulus, $G_2$ (GPa) | 27.00 | 27.00 |
| | Density, $\rho_2$ (kg m$^{-3}$) | 2700 | 2700 |
| | Loss coefficient, $\eta_2$ $\times 10^{-3}$ | 1.05 | 1.05 |
| | Length, $L_2$ (mm) | 63 | 20 |
| | Width, $b_2$ (mm) | 20 | 5 |
| Both | Thickness, $h$ (mm) | 3 | 5 |
| | Unit cells, $N$ | 7 | 10 |
| | Shear coefficient, $\kappa$ | 0.85 | 0.85 |

Table 4.1: Properties and geometry of the beams in the unit cell.

The materials and dimensions of the beams were selected in order to produce band gaps at frequencies lower than 3000 Hz. The lowest band gaps for Beam 1 and Beam 2 are 300-905 Hz and 1930-2230 Hz respectively, as shown in the analytical band structures plotted in Figure 4.2 and Figure 4.3. The dispersion curves were calculated based on the transfer matrix method with analytical Timoshenko beams, as done in Section 3.3.

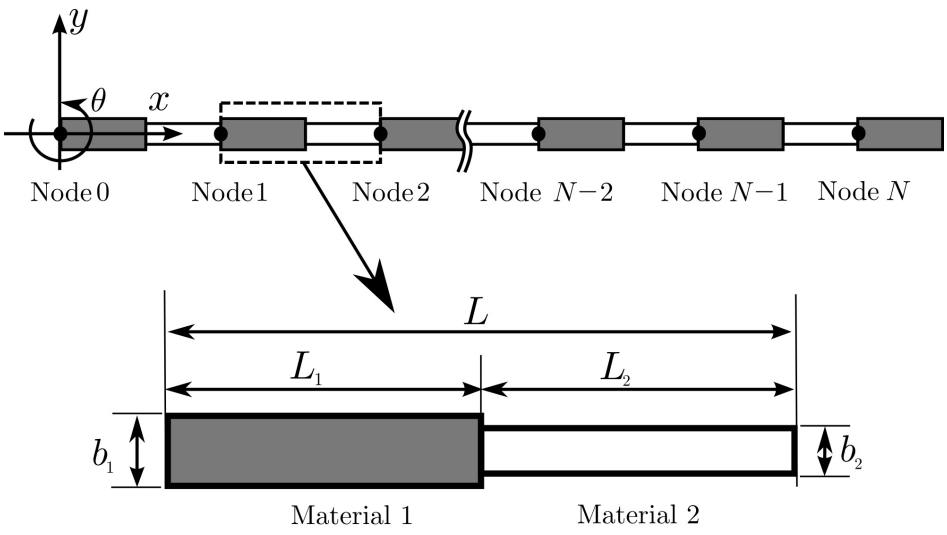



Figure 4.1: Illustration of beam dimensions.

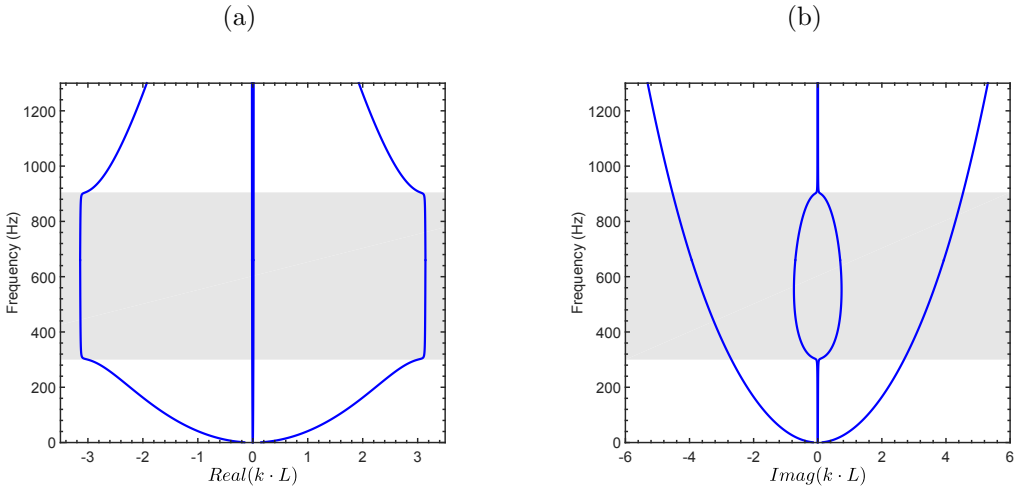



Figure 4.2: Dispersion curve for Beam 1 (a) Real part (b) Imaginary part.

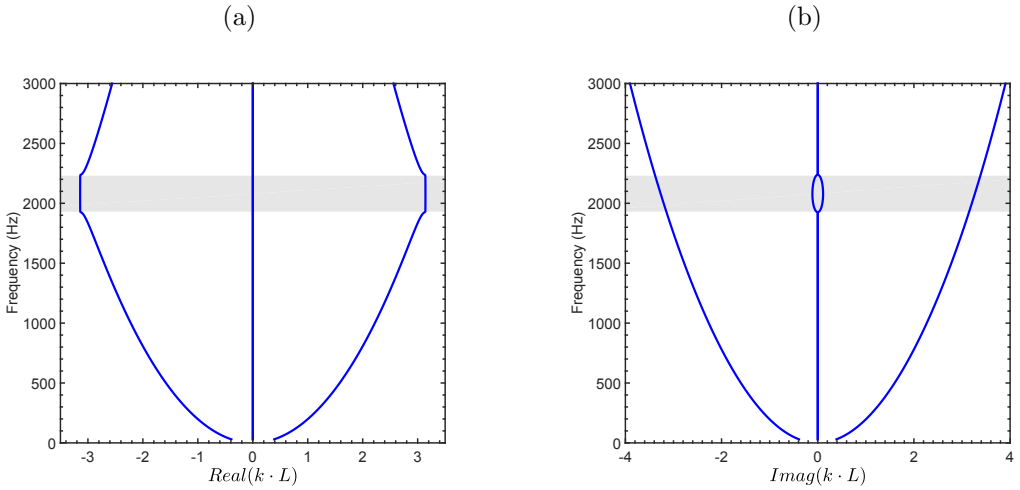



Figure 4.3: Dispersion curve for Beam 2 (a) Real part (b) Imaginary part.

### 4.2.2 Experimental procedure

The experimental setup is shown in Figure 4.4. The beams were hung freely from the support frame using a fishing line. A stinger with a force gauge was then attached to the shaker that is also hanging freely from the support frame. The stinger with a load cell at the end was then attached to the beam at the first point of the first unit cell, as shown in Figure 4.4 and Figure 4.5, while the accelerometer was attached to the beam at the face opposite of the stinger. The accelerometer, load cell and shaker were connected to a data acquisition unit to perform a frequency sweep using a sinusoidal signal.

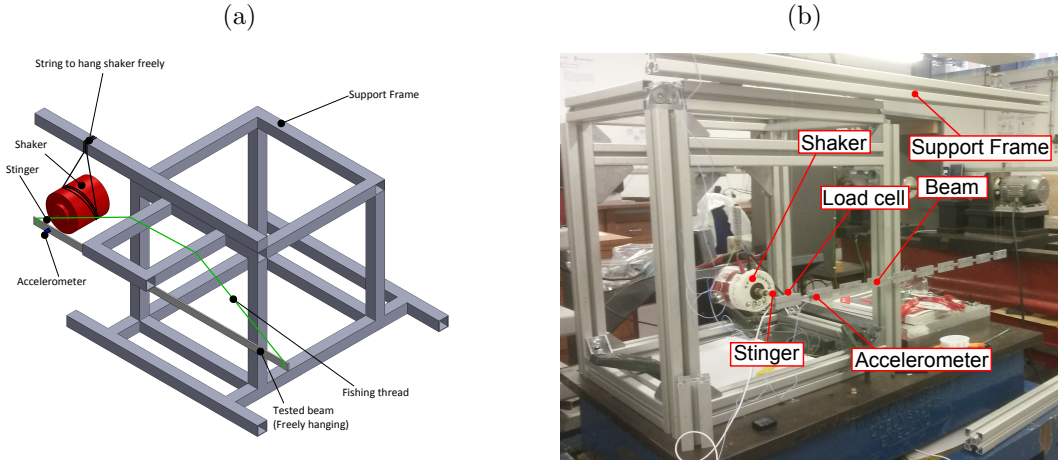



Figure 4.4: Experimental setup. (a) Schematic (b) Photo of experiment.

The frequency sweep was first done for the case where the accelerometer was placed right after the interface between the first and second unit cell as shown in Figure 4.5. The frequency range of the sweep was 10-1200 Hz for Beam 1 and 50-3000 Hz for Beam

2. The frequency response (acceleration per unit force) was measured and recorded. The procedure was then repeated with the accelerometer placed at the next unit cell until the end of the beam. The measured frequency response was then used to calculate the band structure of the beams as described in Section 3.2.3 by solving Eqs. (3.40) and (A.3).

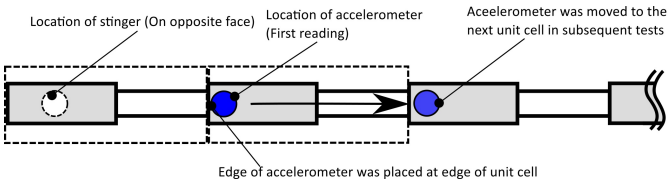



Figure 4.5: Placement of accelerometer and stinger on beam.

Additionally, the frequency response functions at all the nodes for Beam 2 were also predicted using the band structure and the frequency responses at two nodes using the method described in Section 3.2.5. The equations to be solved can be simplified to,

$$\begin{bmatrix} W_{F,A} \\ W_{R,A} \\ W_{F,B} \\ W_{R,A} \end{bmatrix} = \begin{bmatrix} \lambda_A^{N1-1} & \lambda_A^{N1-1} & \lambda_B^{N1-1} & \lambda_B^{N1-1} \\ \lambda_A^{N2-1} & \lambda_A^{N2-1} & \lambda_B^{N2-1} & \lambda_B^{N2-1} \\ \lambda_A^{N3-1} & \lambda_A^{N3-1} & \lambda_B^{N3-1} & \lambda_B^{N3-1} \\ \lambda_A^{N4-1} & \lambda_A^{N4-1} & \lambda_B^{N4-1} & \lambda_B^{N4-1} \end{bmatrix}^{-1} \begin{bmatrix} W_{N1} \\ W_{N2} \\ W_{N3} \\ W_{N4} \end{bmatrix} \tag{4.1}$$

where the subscripts $N1$, $N2$, $N3$, and $N4$ denote the node numbers relative to a reference node, while the subscripts $F$ and $R$ denote the forward and reflected waves and the subscripts $A$ and $B$ denote the waves for Set A and Set B respectively.

## 4.3 Results and discussions

### 4.3.1 Frequency response function

The measured and predicted frequency response for Beam 1 and Beam 2 are plotted in Figure 4.6 and Figure 4.7 respectively. The values in these plots were normalised with the frequency response at the first node to give the transmissibility as the load cell was not calibrated and the damping in the beams are low as expected as the peaks in Figure 4.6 and Figure 4.7 are relatively high. As seen in Figure 4.6, the measured response has very good agreement with the predictions made using the analytical Timoshenko beam at all points with the exception of the responses around 350 Hz, in which an additional mode at 333 Hz is present. This error is a result of the torsional mode that has a calculated natural frequency of 363.4 Hz, which was not taken into account while calculating the response as only the transverse response is of interest. However, the accelerometer picked up the effects of this mode. It is very difficult to place the shaker and accelerometer at the exact mid-point of the beam in practice, which makes

this issue hard to eliminate.

Similarly, the frequency response of Beam 2, as seen in Figure 4.7, also agree well with the predictions made using the analytical Timoshenko beam, although there are some discrepancies at several regions, for example the frequency response at 250 to 395 Hz and additional modes of vibrations at 2280 and 2730 Hz. These modes correspond to the calculated torsion modes at 2492.7 and 3036.4 Hz. Furthermore, the discrepancies between the analytical and experimental values around 2250 to 2500 Hz for the all the nodes in Figure 4.7 are large. The likely cause of the discrepancy is that the analytical modes fail to predict some vibration modes at these frequencies as the analytical model only accounts for the transverse displacements and the simplicity of the model where the displacement across the entire width are assumed to be equal.

Apart from that, the band gaps that are present in Beam 1 can be inferred from the frequency response functions in Figure 4.6 especially in (e), where there are low transmissibilities at the band gap region of 300-905 Hz with the exception of the peak caused by the torsional mode. Conversely, for Beam 2 the transmissibilities at the band gaps appear to be high and there are no obvious band gaps in the frequency response function. This is due to the very low attenuation constant at the band gap, as seen in Figure 4.3 (b), of less than 0.1 and the magnitude of the wave is still large when it is reflected at the end of the finite beam. Therefore, for systems that have band gaps with low attenuation constants, it is important to consider the band structure when demonstrating the presence of the band gaps experimentally.

### 4.3.2 Dispersion curves

The dispersion curve for Beam 1 calculated using the measured frequency response function from all six nodes (Nodes 1 to 6) and the wave superposition method is shown in Figure 4.8. Since there are two sets of waves, Wave A and Wave B, the measured points in the band structure were sorted so that one set of waves (Wave A) are shown in Figure 4.8 (a) and (b), while the measured points for the other waves (Wave B) are shown in Figure 4.8 (c) and (d) for clarity. As seen in Figure 4.8 (a) and (b), the measured points agree well with the analytical predictions of the band structure albeit the presence of some scatter. There are some discrepancies around 300 Hz in Figure 4.8 (a) and (b), which are likely caused by the torsional mode. Another interesting observation that can be made in Figure 4.8 (b) is that the measured imaginary part of the wave vector at the band gap is fairly accurate with values close to the predictions made by the analytical solutions. This demonstrates that the wave superposition method is able to measure the imaginary part of the wave vector with adequate accuracy. This is a capability that is unique to the wave superposition method and have proved that there are complex or imaginary waves present within the band gap.

On the other hand, the results of Wave B for Beam 1, shown in Figure 4.8 (c) and

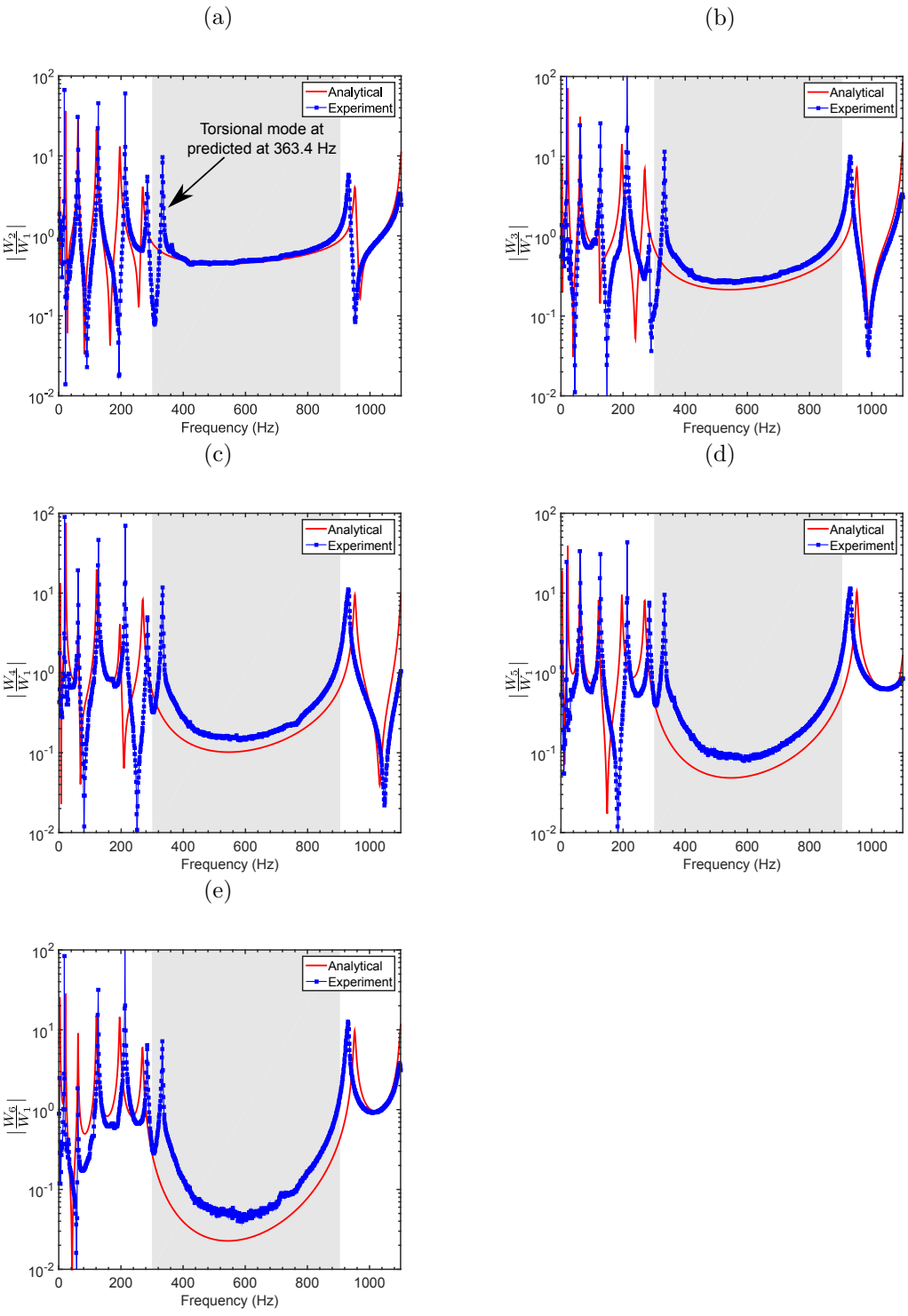



Figure 4.6: Frequency response function of polycarbonate and aluminium bi-material beam (Beam 1). (a) Point 2 (b) Point 3 (c) Point 4 (d) Point 5 (e) Point 6. Analytical band gaps using the transfer matrix method are highlighted in grey.

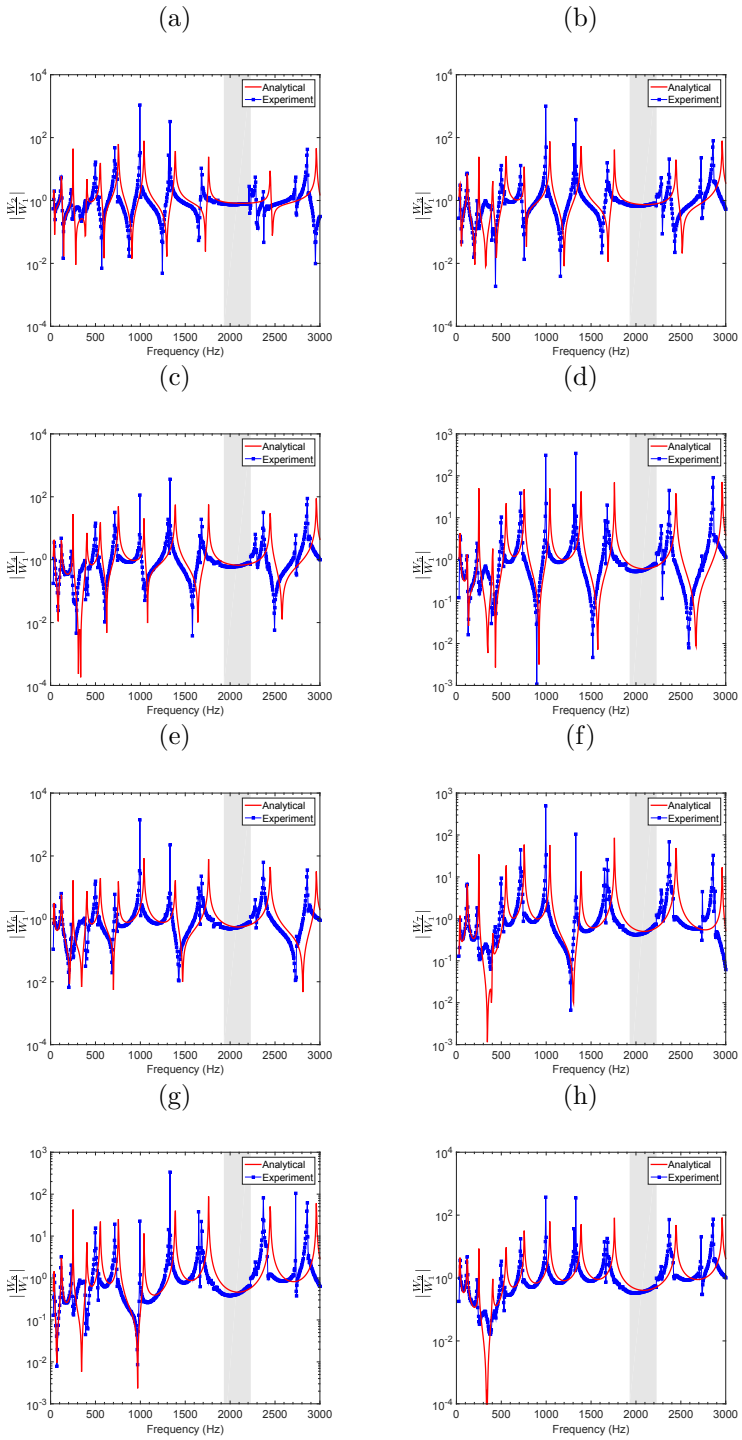



Figure 4.7: Frequency response function of aluminium beam with varying geometry (Beam 2). (a) Point 2 (b) Point 3 (c) Point 4 (d) Point 5 (e) Point 6 (f) Point 7 (g) Point 8 (h) Point 9. Analytical band gaps predicted using the transfer matrix method are highlighted in grey.

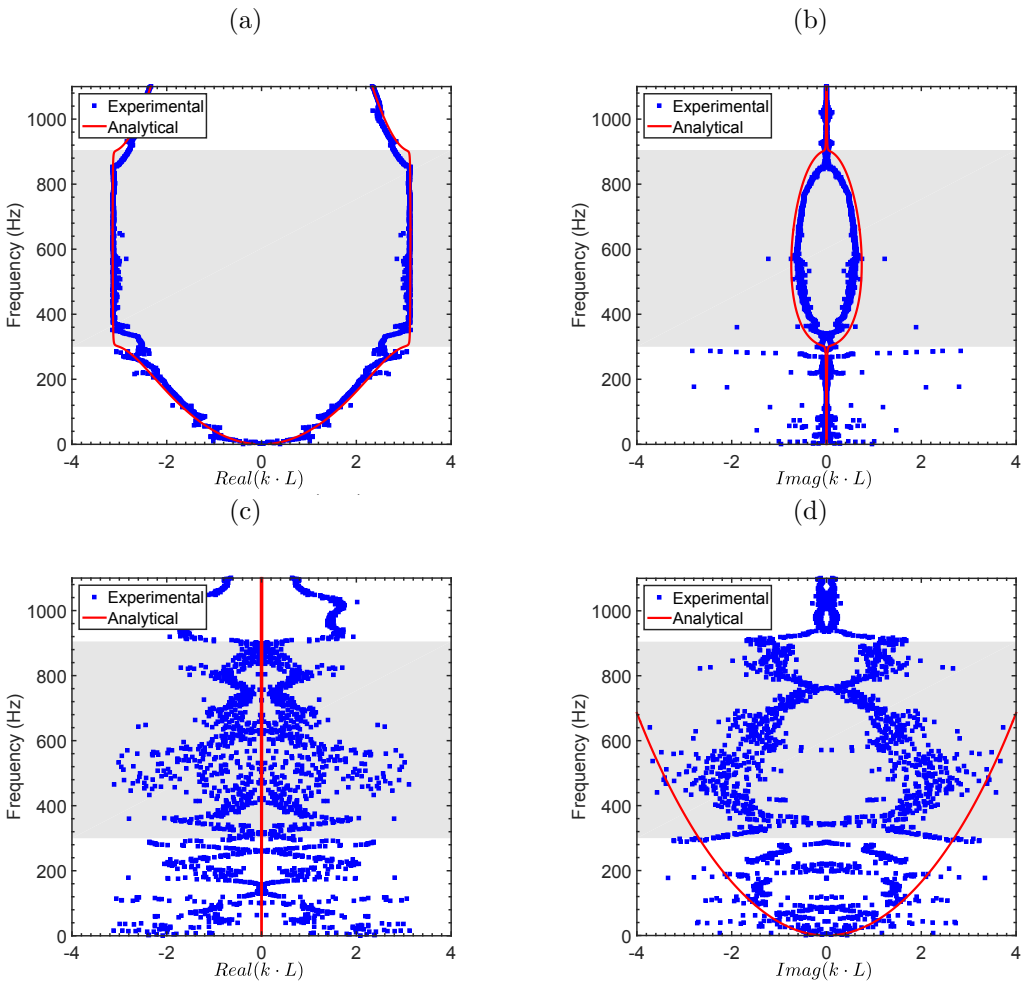



Figure 4.8: Dispersion curve for Beam 1. (a) Wave A (real part) (b) Wave A (imaginary part) (c) Wave B (real part) (d) Wave B (imaginary part). Analytical band gaps are highlighted in grey.

(d), agrees poorly with the predictions made using the analytical solutions and has a large amount of scatter. This is caused by the errors in the measurement in the second set of waves. Wave B consists of evanescent waves in the beams, which attenuate across each unit cell. As seen in Figure 4.8 (c) and (d), the imaginary part of the wave vector of the evanescent waves (Wave B) is very large, which suggest that the attenuation of the evanescent waves are much larger than the propagating wave even at the band gap. This leads to the measurement of the band structure of the evanescent waves being very sensitive to errors in the measured response as the amplitude of these waves will be very low even after the first unit cell. Thus, any noise or 'contamination' by other modes will result in very large errors in the band structure calculations for the evanescent waves.

As the evanescent waves attenuate very rapidly, they could be neglected when analysing phononic crystals or acoustic metamaterials, especially for vibration isolation applications, as the band gap that needs to be considered is that of the propagating waves (Wave A) in Figure 4.8 (a) and (b). Furthermore, some methods used to calculate the band structure, such as the one in [186], that determines the band structure by applying the Bloch wave boundary conditions and then finding the eigenvalues across the first Brillouin zone, are unable to obtain the band structure for the evanescent waves. Hence, in terms of analysing the location of band gaps for phononic crystals and acoustic metamaterials, the evanescent waves can be omitted from the analysis. Unfortunately, the inability of the WSM to predict the evanescent waves accurately in actual situations reduces the utility of the method. The measurement technique used in [138] was also unable to measure the band structure of the waves that correspond to Wave B.

The errors found in the measured data also highlight the fact that the wave superposition method described here and in [79] has the key issue of being unable to reject measurement errors. As discussed in the previous section, the wave superposition method have equal numbers of equations and unknowns. Therefore, the system is fully determined and any error at any point of the measurements of the frequency response will result in large errors in the calculated band structure. Additionally, other factors, such as the size of the load cell and the accelerometer being of a finite radius instead of an infinitesimal point, the placement of the accelerometer not being at the exactly one unit cell distance, and manufacturing tolerances may result in minor difference in the experimental data compared to the analytical solution. This might lead to large errors in the measured dispersion curve. Hence, a key improvement for the wave superposition method is to enable it to reject errors. A possible method to achieve this is to perform regression analysis. However, the solutions for the WSM are very complicated, making the steps required to perform the regression analysis non-trivial and difficult. Therefore, the development of the WSM to reject errors is a topic for future work.

Since the frequency response function of Beam 2 was measured at 9 points, the dispersion curve can be calculated with the wave superposition method using any of the

following 6 points: Points 1-6, Points 2-7, Points 3-8, and Points 4-9. The measured points of the band structure using all four sets of frequency response functions are plotted in Figure 4.9. As seen in Figure 4.9 (a) and (b), the measured band structure of all four sets of data for Wave A are almost identical with the points overlapping each other. This should be the case as the band structure is a characteristic of the wave in the structure and should be identical throughout. Although the overall real parts of the wave vector in Figure 4.9 (a) are almost identical, there appears to be significant differences between the imaginary part of the wave vectors especially near the band gap region as seen in Figure 4.9 (b). Again, the likely cause of the problem near the band gap is the presence of a torsional mode at 1904.8 and 2492.7 Hz.

Despite the agreement for the dispersion curves of Wave A calculated using different datasets in Figure 4.9 (a) and (b), the dispersion curves of Wave B, as seen in Figure 4.9 (c) and (d), was found to be very noisy and the values calculated from each dataset differ significantly from each other. This is likely caused by the errors in the measured frequency response functions explained previously. Fortunately, Wave B is always attenuating with large imaginary wave vectors and the wave attenuation property of the structure will be determined by the band gaps in Wave A.

The dispersion curve with the dataset that gives the best result, defined as the results with the lowest sum of the squares of the difference between the experimental data points and the predictions made using the transfer matrix method for the propagating wave, for Beam 2 (Point 2-7) is shown in Figure 4.10. The observations made for the dispersion curves for Beam 2 is similar to that for the observations made for Beam 1. Firstly, for Wave A the experimental results agree well with the analytical solution as seen in Figure 4.10 (a) and (b). However, the measured band gap appears to be at a lower frequency than the predictions made by the analytical solution. The importance of being able to predict the band gap from the band structure is demonstrated here as the presence of the band gap is not obvious from the frequency response function, shown in Figure 4.7, due to the low values of the imaginary part of the wave vector for this structure. The dispersion curve of Wave B in Figure 4.10 (c) and (d) for Beam 2 does not agree well with the analytical predictions, similar to the case with Beam 1 shown in Figure 4.8 (c) and (d). The causes of the discrepancies of Wave B have been discussed previously.

### 4.3.3 Frequency response predictions

As discussed in Sections 3.2.5 and 4.2.2, the measured band structure and the frequency response of 4 nodes can be used to predict the response of the other nodes of a finite structure using Eq. (4.1). In order to demonstrate this, the predictions of the frequency response of Beam 2 will be shown in this section. The best band structure was the one calculated using the frequency response from Points 2-7 (Figure 4.10). This mea-

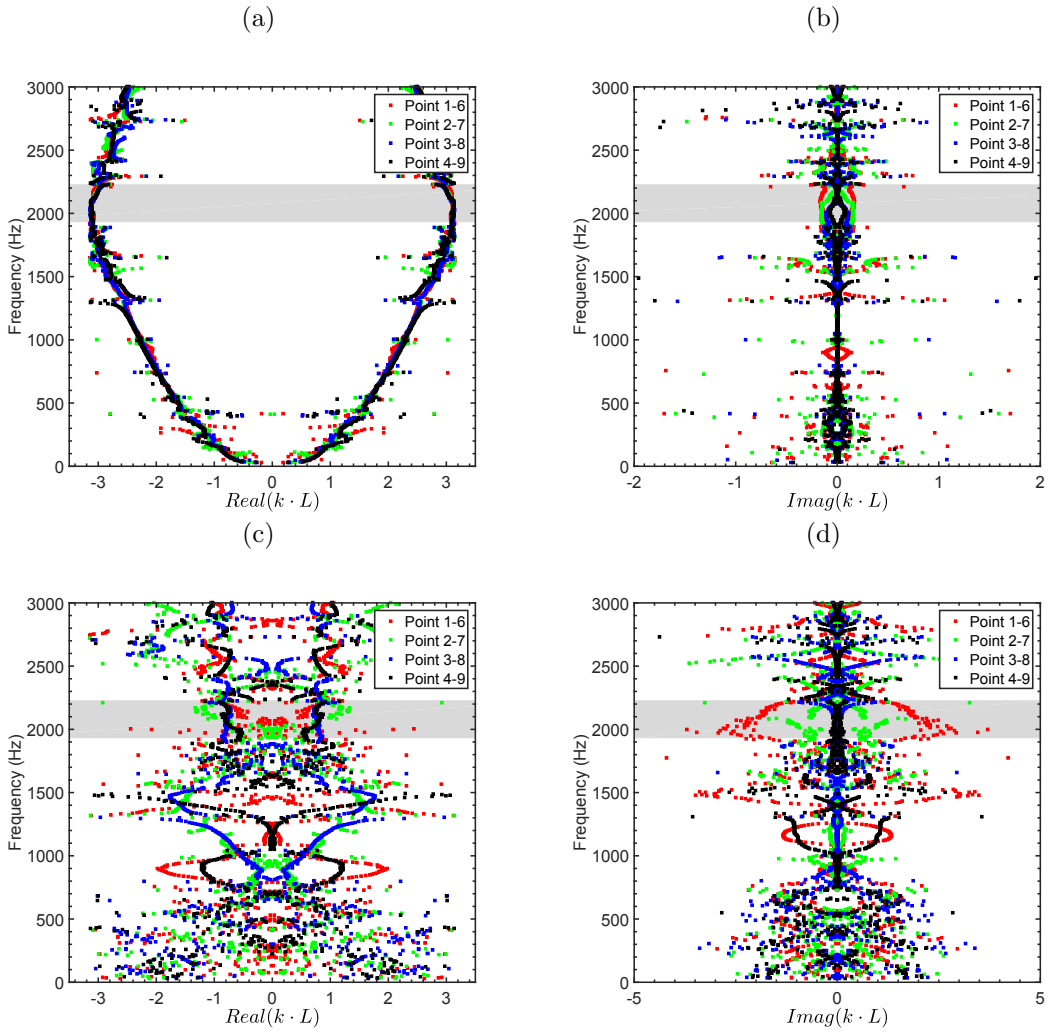



Figure 4.9: Dispersion curve for Beam 2 (combined). (a) Wave A (real part) (b) Wave A (imaginary part) (c) Wave B (real part) (d) Wave B (imaginary part). Analytical band gaps are highlighted in grey.

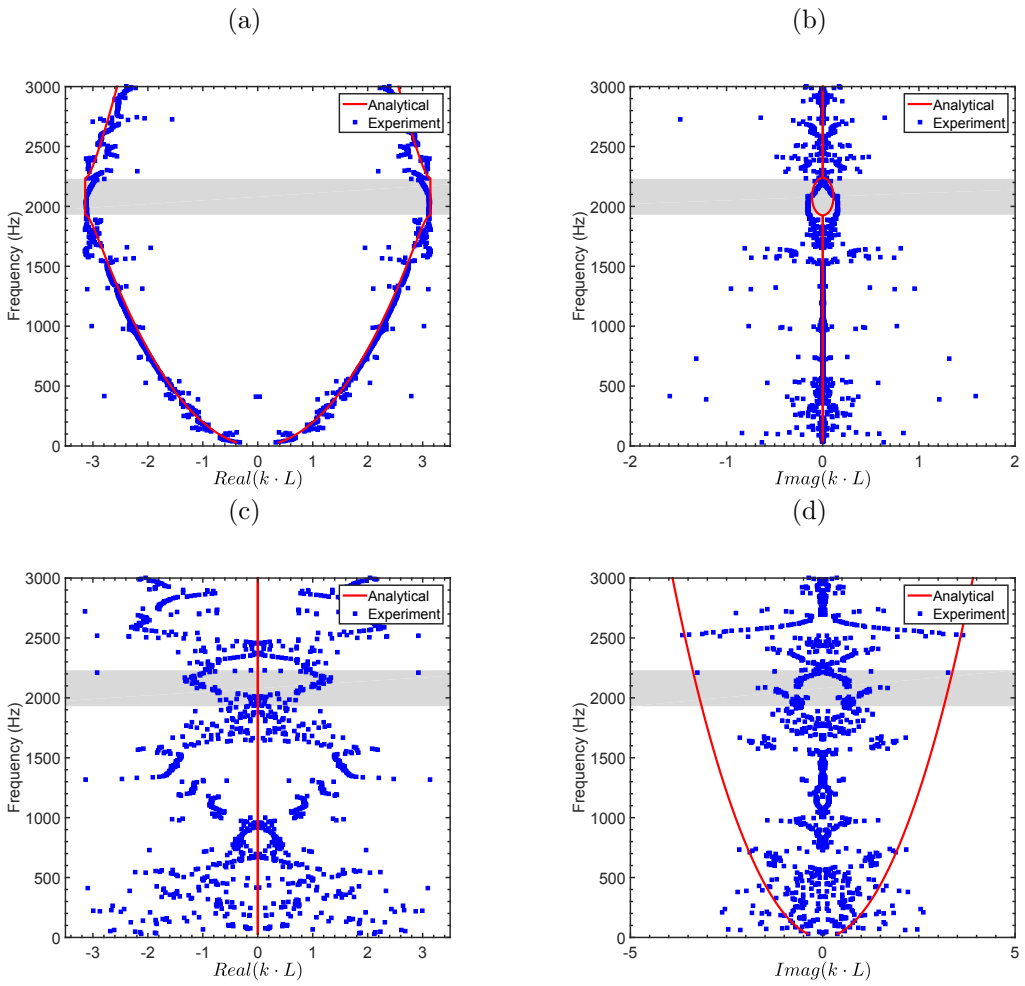



Figure 4.10: Dispersion curve for Beam 2 from points 2-7. (a) Wave A (real part) (b) Wave A (imaginary part) (c) Wave B (real part) (d) Wave B (imaginary part). Analytical band gaps are highlighted in grey.

sured band structure and the frequency response at Points 2-5 were used in Eq. (4.1) to determine the values of $W_{F,A}, W_{R,A}, W_{F,B}$, and $W_{R,A}$ for each of the excitation frequencies and then to calculate the frequency response of the beam at all of the nodes within the beam. Since the band structure was calculated using the frequency response of Points 2-7, the predicted frequency response using the measured band structure at these points will be identical to the measured values. Therefore, only the frequency response at Points 8 and 9 for the measured and predicted response are compared in Figure 4.11 (a) and (b).

The overall predicted response using the measured band structure calculations, shown in Figure 4.11 (a) and (b), agrees well with the measured frequency response. In Figure 4.11 the predicted response for a large portion of the frequencies measured is similar to the measured response, especially for the frequency response at Point 8. The only significant discrepancy there is the additional natural frequency at approximately 2500 Hz.

Although the predicted response for Point 9 agrees fairly well with the measured response, the predictions are less accurate compared to that of Point 8. This is likely to be due to Point 9 being further away from the points in which the band structure was measured. There are some qualitative difference for the predicted and experimental values at frequencies 255-480 Hz and 1595-1640 Hz, while the additional mode at 2500 Hz is also present in the frequency response of Point 9. The errors around the frequencies 255-480 Hz and 1595-1640 Hz can either be attributed to the errors in the measured frequency response function, shown in Figure 4.7, at these regions or errors in the analytical predictions where several modes at these regions were not predicted due to the simplicity of the beam model.

Despite these errors, the method shown in this section appears to able to predict the frequency response of an "entire" finite system using the measured band structure with fair accuracy. This is a valuable tool as it means that calculating the entire transmissibility curve for a finite structure is no longer necessary. However, it is important to point out that these points are close to the measured points and errors are likely to be larger for points that are further away. Additionally, for a band structure calculated from an analytical model, this method allows the frequency response of finite structures to be calculated once the band structure and eigenvectors are known, as discussed in Chapter 3.

## 4.4 Conclusion

A study on the band structure and band gaps of beams with variations in geometry and material property was conducted. In this study, the wave superposition method introduced in Chapter 3 was used to determine the band structure of a one dimensional

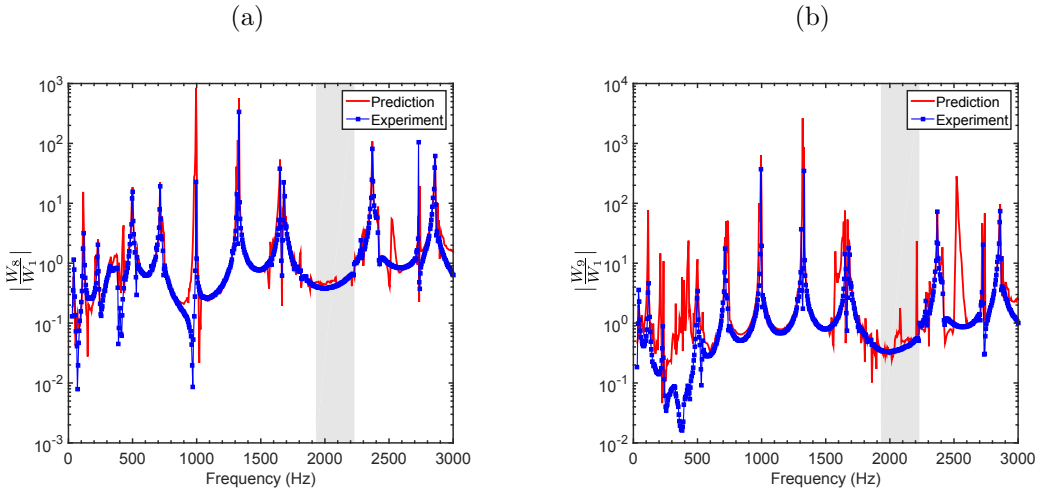



Figure 4.11: Frequency response function predictions of aluminium beam with different widths. (a) Point 8 (b) Point 9. Analytical band gaps are highlighted in grey.

periodic structure with two wave types from experimental measurements. The wave superposition method also allows predictions to be made for the response of other points in a finite periodic structures for a given boundary condition using information from the band structure and a few response measurements.

Experiments were conducted to measure the band structure of two different beams, one consisting of 7 unit cells made from aluminium and polycarbonate sections and the other beam being an aluminium beam consisting of 9 unit cells with varying widths. The band structures of the beams studied were calculated using the wave superposition method. The bi-material beam was constructed by attaching the individual sections using an epoxy based adhesive, while the beam with varying geometry was milled using a CNC machine. The beams were then hung freely from a frame using fishing threads and the beams are excited at one end using a shaker, while the acceleration at different unit-cells for a range of frequencies were measured using an accelerometer. The transmissibilities of the beams measured from the experiments were found to agree with the analytical solution. However, some discrepancies were observed and they were attributed to various factors, such as the effects of the torsional modes. The band structure was determined from the measured acceleration and then compared with the analytical band structure.

In general, similar observations can be made for the measured band structures for both of the beams. Firstly, the measured band structure was found to be noisy but a distinct pattern resembling one set of the waves can be found in the measured values. The scatter in the measured band structure was caused by the measurement of one set of waves (the evanescent waves) being sensitive to noise and the effects of the torsional modes being measured by the accelerometer. As the evanescent waves will experience

large amounts of attenuation across all frequencies, the band gaps of the beams are determined by the band structure of the propagating waves (Wave A), which was found to agree with the analytical solution.

However, several discrepancies were observed around the natural frequencies of the torsional modes that were not considered in the analysis. This result highlights a disadvantage of the proposed method, which is the sensitivity to unaccounted modes of vibrations. This problem can be alleviated in future studies by careful placements of the shaker and the accelerometer to avoid exciting and picking up the accelerations of the torsional modes. Furthermore, a key shortcoming of the method is that it is unable to reject errors and a further development of the method that make use of some form of regression analysis will greatly improve the technique.

Lastly, the measured band structure was used to predict the transmissibility of the final two unit cells (the eighth and ninth unit cells) of Beam 2 in order to further validate the method to determine the frequency response from the measured band structure. The transmissibility was then calculated by using the measured transmissibility at the second to fourth unit cells and the band structure measured from the transmissibility of the second to seventh unit cells. The predicted transmissibility for the eighth and ninth unit cells were then compared with the measured transmissibility and the results were found to be in agreement except at the frequencies where the torsional modes affected the measured result of the band structure and regions with inaccurate frequency response measurements. The frequency response can be determined using the band structure provided that it is measured accurately. This allows the frequency response of finite periodic structures to be determined directly from the band structure and reduce computational costs.

# 5 A parametric study on the mechanical and dispersion properties of cubic lattice structures

## 5.1 Introduction

As discussed in Chapter 2, periodic lattice materials can be engineered to have several unique properties, such as high strength to density ratio [31, 159], high stiffness to density ratio [31, 159], low thermal coefficient with high stiffness [208–210], and elastic band gaps [23–25]. Thus, they have huge potential to be used in multifunctional applications, including ultralight structures, impact absorbers, heat dissipation, vibration control, and many others.

The multi-functionality of lattice materials enables them to overcome several issues that cannot be resolved with conventional bulk materials. Among these issues is the conflicting requirements of stiffness and vibration control of structural components. In order to sustain huge loads without large static displacements or compromising structural integrity, structural components generally require high stiffness [2, 211]. However, structures with high stiffness are also sensitive to vibrations, which may threaten the structural integrity of the system. One of the objectives of this thesis is to explore the possibility of exploiting the high stiffness and strength to density ratios present in selected lattice structures [158, 212] and embedding local resonators, as seen in several studies [2, 3, 22, 36], to produce band gaps that will attenuate vibrations, to minimise the trade-off between vibration attenuation and stiffness in structural components. With current three-dimensional printing technology, lattice structures with embedded local resonators can be manufactured, allowing the potential of the multi-functionality of lattice structures to be realised.

Currently, a large number of studies have been conducted on the analysis of the static mechanical (stiffness and strength) [27–34] and dispersion properties of lattice materials [21–26]. However, only a few studies [2, 3, 35, 36] have investigated these two types of properties in tandem or the design of a stiff structural material with desirable dynamic characteristics. Therefore, the work performed in this chapter aims to contribute to the design of elastic metamaterials with desirable dynamic properties, while having other qualities, like high stiffness, so that it can be implemented in practical situations. This

is an important feature of elastic metamaterials as highlighted in [37]. The parametric study of the effects of the geometry on the static mechanical and dispersion properties will serve as a guide for future designs of multifunctional components and encourage future research in this type of materials.

In this study, the mechanical and dispersion properties of four cubic lattice topologies with internal resonators, similar to the designs seen in [22], were studied. Firstly, a parametric study on the lattice geometry, which are the lengths and radii of the lattice struts, was performed to determine the combination of geometric parameters that give the optimal mechanical properties, which are the bending stiffness and strength per unit density of the structure in this study. Local resonators consisting of struts with a point mass at one of its ends will then be attached to the lattices with the optimal mechanical properties to produce the local resonant band gaps. The width and location of the band gaps resulting from the addition of local resonators of different sizes and masses will be investigated. Lastly, the increase in density was also calculated to determine the penalty of adding the resonators and to assess if this strategy is viable.

## 5.2 Selected Topologies And Analysis Procedures

### 5.2.1 Selected topologies and resonators

Four cubic lattice topologies, which are the simple cubic, body centred cubic (BCC), face centre cubic (FCC), and octet truss structures, to be used as core materials in sandwich structures were studied. The unit cells of these topologies including the local resonators are shown in Figure 5.1. Several of the beams at the edges of the unit cells were omitted to avoid overestimating the strength and stiffness through duplication. The lattice structures will consist of the *base* lattice structures and the added local resonators, which are beams with a point mass, for example a ball bearing, at the end.

There are several reasons for the selection of these topologies. Firstly, the addition of the resonators to these lattices are straightforward and since the resonators do not contribute to the strength or stiffness of the material, the mechanical properties and dispersion properties can be investigated independently. Additionally, cubic lattice structures can be easily manufactured using currently available three-dimensional printing technologies. The natural frequencies of the local resonators, and the location of the band gap, can also be easily tuned without making any changes to the base structure.

Although other methods to create LR band gaps, such as adding masses at the nodes [26] or manipulating the connectivity of the struts as discussed in [155] can be used to introduced band gaps, the key reason that the topologies in Figure 5.1 were selected over other architectures is because the natural frequencies of the resonators can be found easily. This facilitates the selection of the geometric parameters and mass of the resonators to achieve the required tuned frequencies. The calculations for the target

frequencies by adding masses at the nodes are less straightforward than the resonators in the selected designs, which can be treated as a simple cantilever beam with a point mass at the end. Furthermore, the lattice structure studied here is intended to be used as a lightweight structural component, with high stiffness and low mass, suggesting that the struts are likely to be stiff. Since the natural frequency increases with increasing stiffness and reducing mass, the strategy of adding masses at the nodes may lead to large masses being required for a given target frequency. Conversely, the resonators that do not take any load can be designed to have low stiffness and a lower mass can be used to achieve the same natural frequency. This provides more design flexibility. Similarly, the manipulation of the strut connectivity will result in significant changes in the static mechanical properties, which complicates the analysis significantly.

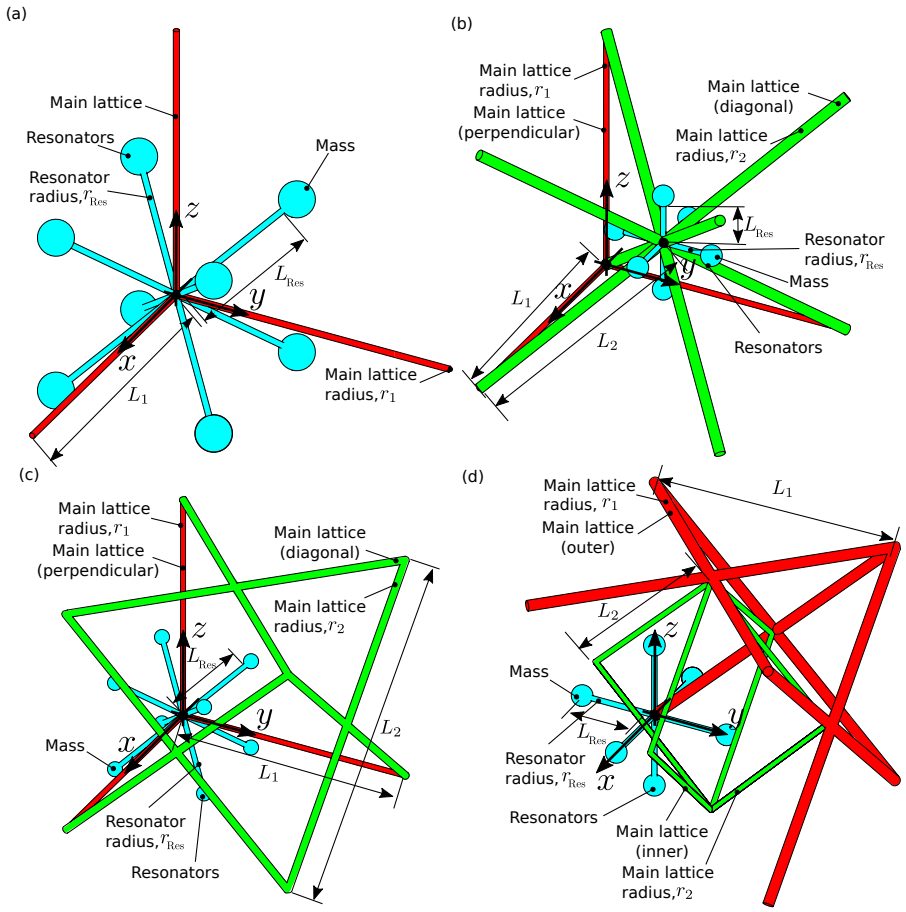



Figure 5.1: Selected topologies and the added resonators (a) Simple Cubic (b) BCC (c) FCC (d) Octet truss.

The ratios characterising the structural performance of lightweight panels and beams according to [158] are summarised in Section 5.3.5. The ratios in the table were obtained using the analysis from [213], which will be described briefly. The mass of a beam or

panel, $m$, can be defined as follows,

$$m = \rho(WHL) \tag{5.1}$$

where $\rho$ is the density of the material and $W, H$, and $L$ are with width, height, and thickness of the beam as shown in Figure 5.2.

For a beam or panel being loaded as shown in Figure 5.2 to be used in lightweight applications, the mass of the beam or panel, $m$, defined in Eq. (5.1) must be minimised. Since the beam has a constrained on the its width, the $W$, and height, $H$, are set to be equal while the height and width are assumed to be independent for the panel.

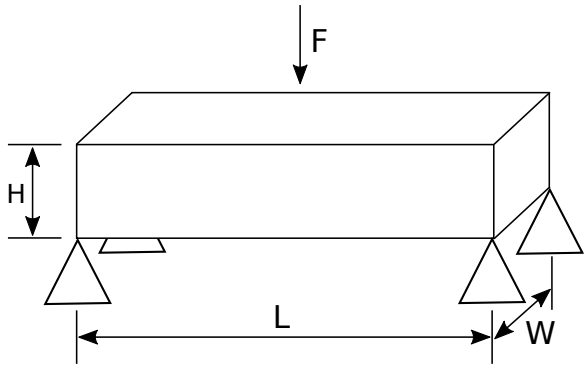



Figure 5.2: Beam and panel being loaded.

According to Eq. (5.1), the mass can be minimised by reducing $W, H$, or $L$. However, as a structural bearing component, the beam or panel must be able to either have a sufficient amount of stiffness (stiffness constrained) to minimise deflection or sufficient strength (strength constrained) to prevent failure. Therefore, the component should achieve a minimum bending $S_E$ and strength, $S_\sigma$ defined as follows,

$$S_E \leq \left(\frac{F}{\delta}\right) = \left(\frac{CWH^3}{12L^3}\right) E \tag{5.2}$$

$$S_\sigma \leq \left(\frac{F}{WH}\right) = \left(\frac{CWH^2}{6L}\right) \sigma_f \tag{5.3}$$

where $S_E$ and $S_\sigma$ are the stiffness and strength constraints, $F$ is the force, $\delta$ is the deflection, $E$ is the Young's modulus, and $\sigma_f$ is the failure stress.

These equations were easily derived based on the Euler-Bernoulli beam theory and although Figure 5.2 shows a point load condition, the equations for other loading conditions can be found by varying the variable $C$. Interested readers can refer to [213] for the derivations of the equations and values of $C$. According to [213], the values of $H$ and $W$ for the beam, and $H$ for the panel can be varied freely. Therefore, the mass should be minimised with the restrictions of the stiffness and strength constraints imposed.

This is done by substituting Eqs. (5.2) and (5.3) into Eq. (5.1) to eliminate $H = W$ for the beam, or $H$ for the panel. Therefore, the mass that needs to be minimised for the different conditions can be written as follows.

For the beam (stiffness constrained) condition,

$$m \geq \left(\frac{12 S_E L^3}{C}\right)^{\frac{1}{2}} L \left(\frac{\rho}{E^{\frac{1}{2}}}\right) \tag{5.4}$$

For the beam (strength constrained) condition,

$$m \geq \left(\frac{6 S_\sigma L}{C}\right)^{\frac{2}{3}} L \left(\frac{\rho}{\sigma_f^{\frac{2}{3}}}\right) \tag{5.5}$$

For the panel (stiffness constrained) condition,

$$m \geq \left(\frac{12 S_E L^3}{CW}\right)^{\frac{1}{3}} WL \left(\frac{\rho}{E^{\frac{1}{3}}}\right) \tag{5.6}$$

For the panel (strength constrained) condition,

$$m \geq \left(\frac{6 S_\sigma L}{CW}\right)^{\frac{1}{2}} WL \left(\frac{\rho}{\sigma_f^{\frac{1}{2}}}\right) \tag{5.7}$$

The important ratios to be minimised relating to material selection can be determined from these equations, and their inverses that are to be maximised are listed in Section 5.3.5. These ratios will be referred to as the strength and stiffness parameters.

| Configuration | Strength Constrained | Stiffness Constrained |
|---|---|---|
| Beam | $\frac{\sigma_f^{\frac{2}{3}}}{\rho}$ | $\frac{E^{\frac{1}{2}}}{\rho}$ |
| Plate | $\frac{\sigma_f^{\frac{1}{2}}}{\rho}$ | $\frac{E^{\frac{1}{3}}}{\rho}$ |

where $\sigma_f$ is the failure stress, $E$ is the Young's modulus, and $\rho$ is the density.

Table 5.1: Ratios to maximise for achieving minimum mass while fulfilling the stiffness and strength requirements for beam and plate configurations [158].

In this chapter, a parametric study is performed by setting the length of the unit cell, $L_1$, to 50 mm and studying the stiffness parameter, strength parameter, and band gap width with varying geometries. The range of the normalised geometry parameters studied are summarised in Table 5.2. Additionally, the material selected to construct the lattice structures was acrylonitrile butadiene styrene (ABS) and its mechanical properties are listed in Table 5.3. The dimension ranges in Table 5.2 were selected based

on restrictions in common three dimensional printing technology and selected material can be typically produced using common three dimensional printing technologies, so that the results of this study can serve as a reference for future studies with 3D printed parts. An important point to note is that 3D printing has been known to introduce anisotropy and reduce the stiffness and strength of the materials [214, 215]. Anisotropy in 3D printed materials is a result of the material being deposited directionally and this is likely to affect the predicted lattice behaviour, where the material was assumed to be isotropic in this study. Since this study mainly focuses on the trends and properties of the lattice structures, the effects of the anisotropy will not be studied. Additionally, other improvements have been made in 3D printing technology to reduce the effects of anisotropy, for example in [214], while other lattice production techniques, such as weaving [216] may result in better material behaviour. Hence, the results in this study can serve as a reference for an initial design and further work should be done to account for the anisotropy of 3D printed parts.

| Ratios | Minimum value | Maximum value |
|---|---|---|
| $\frac{r_1}{L_1}$ | 0.01 | 0.20 |
| $\frac{r_2}{r_1}$ | 0.50 | 1.50 |
| $\frac{L_{\text{Res}}}{L_1}$ | 0.05 | 0.25 |
| $\frac{r_{\text{Res}}}{r_1}$ | 0.30 | 1.50 |

Table 5.2: Dimensions of the selected topologies shown in Figure 5.1 that were investigated in this study.

| Property | Value | Units |
|---|---|---|
| Young's modulus, $E$ | 3.29 | GPa |
| Shear modulus, $G$ | 1.18 | GPa |
| Density, $\rho$ | 1200 | kg m$^3$ |
| Yield strength, $\sigma_y$ | 53 | MPa |

Table 5.3: Mechanical properties of ABS [217].

In addition to the static mechanical properties of the lattice, resonators that are tuned to the target frequency will be introduced into the main lattice, as seen in Figure 5.1. The resonators are similar to dynamic absorbers and are used to introduce local resonant band gaps seen in [16, 20]. In this study, the resonance frequency was set to be 500 Hz for a cantilever configuration, that is within the same order of magnitude for the forcing frequency of typical machinery. The local resonators used in this study have a number of combinations of radii, lengths, and mass that can be tuned to a given target frequency. Therefore, in order to study the effects of these different combinations on the band gaps, the band structure of a range of normalised radii and lengths were studied, while the mass will be varied based on the radii and lengths to give the target natural

frequency.

### 5.2.2 Analysis of mechanical properties

As described previously, the addition of the resonators does not affect the structural performance of the lattices and hence they were omitted in the analysis of the static properties. When a large number of unit cells are present in the system, homogenisation techniques can be used to find the effective properties of the lattice structures. There are several homogenisation methods for lattice and cellular materials that have been published, for example [31, 33, 218, 219]. In this thesis, the generalised matrix method described in Section 2.2.2 (pages 61-66) and introduced in [218], was selected mainly because this method can be used with the finite element method, which is convenient as the band gap analysis also makes use of the finite element method and the struts are modelled as Timoshenko beams, which are more accurate then Euler-Bernoulli beams. Additionally, the method in [218] is capable of calculating all components of the homogenised stiffness matrix, $\mathbf{K}$, described by Eq. (5.8), the yield surface, and buckling surface under different loading conditions.

$$\mathbf{K} = \begin{bmatrix} \alpha & \beta & \beta & 0 & 0 & 0 \\ \beta & \alpha & \beta & 0 & 0 & 0 \\ \beta & \beta & \alpha & 0 & 0 & 0 \\ 0 & 0 & 0 & \gamma & 0 & 0 \\ 0 & 0 & 0 & 0 & \gamma & 0 \\ 0 & 0 & 0 & 0 & 0 & \gamma \end{bmatrix} \tag{5.8}$$

The method in [29] uses a multiscale approach to determine the macroscopic mechanical properties. Firstly, the macroscale displacements and deformation were applied to the lattice, in which the boundary nodes are assumed to have periodic displacements. The microscale stresses are then obtained from the displacements and the microscale deformation is then calculated by using a finite element model of the unit cell. The macroscale stresses were then calculated by treating it as the gradient of the strain energy density with respect to the macroscopic strains, which allows the stiffness matrix to be determined. Lastly, the macroscopic forces can be found by applying the virtual work principle. For the sake of brevity, the homogenisation method will not be described here and interested readers should refer to the section or [29]. The homogenised stiffness matrix, $\mathbf{K}$, in Eq. (5.8) is the Voigt notation of the stiffness tensor, where $\alpha$, $\beta$, and $\gamma$ correspond to $\mathbf{C}_{1111}$, $\mathbf{C}_{1122}$, and $\mathbf{C}_{2323}$ respectively, in which $\mathbf{C}$ is the full stiffness tensor. The stiffness matrix in Eq. (5.8) suggests that the material has several symmetries.

The stiffness component, $\alpha$, in Eq. (5.8) was used to find the stiffness parameters listed in Section 5.3.5 by treating it as equivalent to the Young's modulus, $E$, under plane

strain conditions. This is mainly because the Euler-Bernoulli beam theory was used to derived the required parameters that characterise lattice structure in Section 5.3.5, and $\alpha$ corresponds to the stiffness in the axial direction, which was assumed to be the loading conditions at the top and bottom of the beam under plane strain. The Euler-Bernoulli beam theory was used here as it provides a straightforward method to find the required parameters and is well established [213]. It is important to point out that the structure as a whole is treated as an Euler-Bernoulli beam and not the struts of the lattice, which are modelled as Timoshenko beams as stated previously. The plane strain condition was selected as the cells within the component are likely to be constrained by their surrounding cells and are better model with a plain strain model. The same analysis can be repeated for plane stress conditions to find the results for it.

Similarly, the Generalised matrix method described in Section 2.2.2 (pages 61-66) was also used to find the failure stresses. The failure stresses were determined by assuming that an axial stress is acting on the material. The failure stress for yielding is taken to be the macroscopic stress when the stress at any point of the struts is equal to the yield stress of the bulk material. This means the beam and panel structure is considered to have failed by yielding when any part of the material have yielded. Since the material will buckle when any of the eigenvalues $\lambda$ in Eq. (2.155) reaches unity, and the smallest of stress under the uniaxial loading condition for $\lambda = 1$ is set to be the buckling strength of the structure. The detailed procedure for determining the buckling stresses is explained in [29] and in Section 2.2.2 (pages 61-66).

### 5.2.3 Dispersion analysis

Once the optimal geometries for the parameters listed in Section 5.3.5 were found, local resonators, as seen in Figure 5.1, were then introduced to these lattices to produce the desired elastic band gaps. The resonators were modelled as a cantilever beam with a mass at the free end. The resonance frequency of the resonator was tuned to the desired frequency by varying the point mass and the length and radii of the resonator. The resonant frequency will result in band gaps to be formed around the tuned frequency via the local resonance mechanism. A dispersion analysis was then performed in order to determine the location and width of the band gaps. The dispersion curves in the periodic lattices were determined by applying Bloch wave boundary conditions on the appropriate boundary nodes and calculating the eigenvalues. This technique is commonly used in many studies, such as [24, 109, 113, 124]. Since the finite element method was used, the equations of motion can be written as

$$\left(\mathbf{K} - \omega^2 \mathbf{M}\right) \mathbf{u} = \mathbf{F} \tag{5.9}$$

where $\mathbf{u}$ and $\mathbf{F}$ are the displacements and external forces of the nodes.

The required stiffness matrix, $\mathbf{K}$, and mass matrix, $\mathbf{M}$, in Eq. (5.9) were found using the finite element method, in which the lattice struts were modelled using Timoshenko beams [220], which will give more accurate results when the excitation frequency is high, and the mass being modelled as a point mass.

The Bloch wave boundary conditions, described by Eqs. (5.10) and (5.11), at the required nodes were then applied to the displacements and forces at the boundary nodes. Since the reference node in the unit cells, shown in Figure 5.1, is at the origin, $\mathbf{x}$ in the following equations was set to $[0, 0, 0]^T$.

$$\mathbf{u}_{\mathbf{x}+\mathbf{L}} = \left(e^{i\mathbf{k}\cdot\mathbf{L}}\right)\ \mathbf{u}_{\mathbf{x}} \tag{5.10}$$

$$\mathbf{F}_{\mathbf{x}+\mathbf{L}} = \left(e^{i\mathbf{k}\cdot\mathbf{L}}\right)\ \mathbf{F}_{\mathbf{x}} \tag{5.11}$$

where $\mathbf{x}$ is the coordinate of the nodes, $\mathbf{L}$ is the lattice constant which is equal to the lengths of the lattice structure $L_1$ at the directions corresponding to the boundary nodes, and $\mathbf{k}$ is the wave vector.

A matrix $\mathbf{Q}$ was then used to express the displacements and forces in terms of the independent nodes, i.e.

$$\mathbf{u} = \mathbf{Q}\ \tilde{\mathbf{u}} \tag{5.12}$$

$$\mathbf{F} = \mathbf{Q}\ \tilde{\mathbf{F}} \tag{5.13}$$

where $\tilde{\mathbf{u}}$ and $\tilde{\mathbf{F}}$ are the displacement and force vectors for the independent nodes.

This allows the Eq. (5.9) to be simplified to

$$\left(\mathbf{Q}^H\mathbf{K}\mathbf{Q} - \omega^2\mathbf{Q}^H\mathbf{M}\mathbf{Q}\right)\tilde{\mathbf{u}} = \mathbf{Q}^H\mathbf{Q}\tilde{\mathbf{F}} \tag{5.14}$$

where the superscript $H$ denotes the Hermitian transpose.

This will result in the eigenvalue problem described as,

$$\left(\tilde{\mathbf{K}} - \omega^2\tilde{\mathbf{M}}\right)\tilde{\mathbf{u}} = 0 \tag{5.15}$$

The band structure was then found by solving the eigenvalue problem in Eq. (5.15) for different values of wave vectors, $\mathbf{k}$. Due to symmetry, only the wave vectors, $\mathbf{k}$, within the First Brillouin Zone need to be considered [13] in order to determine the location of the band gaps. The First Brillouin Zones for the lattice structures considered in this study are shown in Figure 5.3. The results and discussions of the dispersion analysis will be presented in Section 5.4.

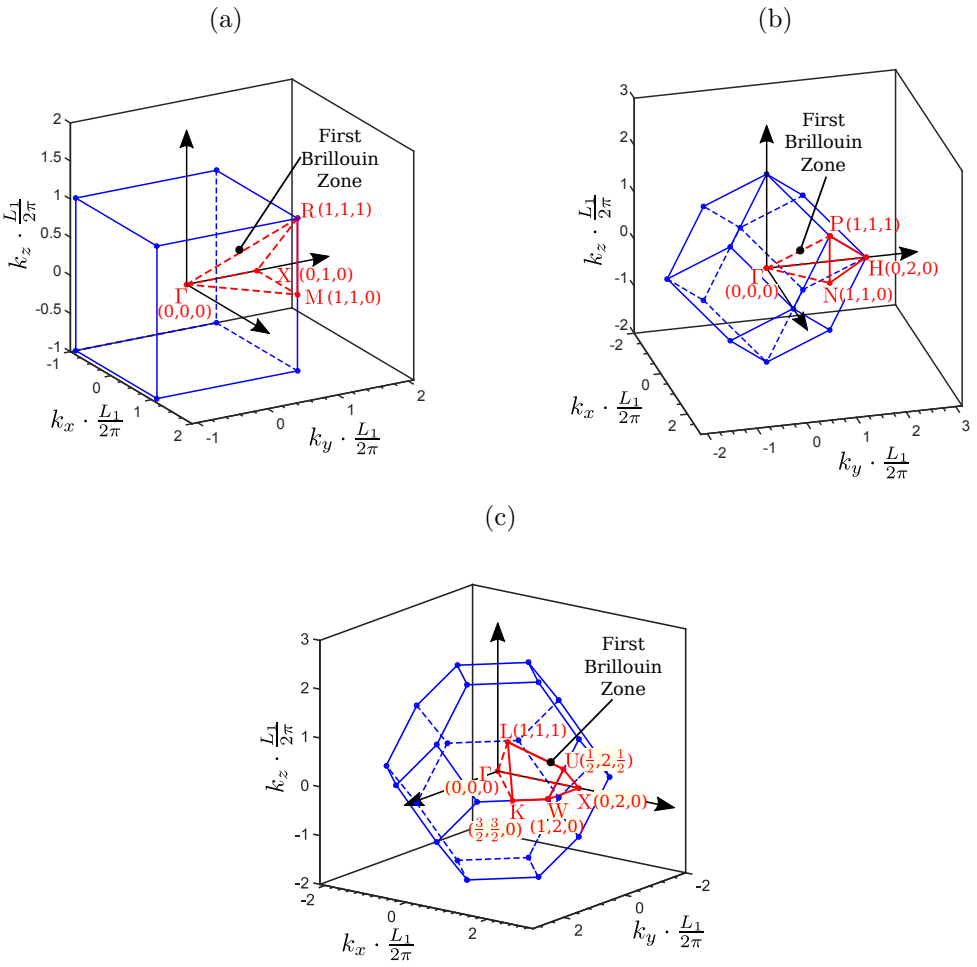



Figure 5.3: First Brillouin Zone of (a) Simple Cubic Lattice (b) BCC Lattice (c) FCC and Octet Lattice

## 5.3 Stiffness and strength properties of lattice materials

The stiffness and strength properties that characterise the performance of the lattice structures as panels or beams for the four topologies will be presented in this section. The stiffness and strength properties were calculated using the procedure described in Section 5.2.2 for each of the topologies over a range of $r_1$, $r_2$, and $L_1$. This is in order to determine the optimal geometry for the lattice prior to the introduction of the local resonators that generates the band gaps.

### 5.3.1 Simple cubic lattice

The stiffness and strength parameters for the lattice structures that have been calculated were normalised with respect to that for the bulk material. Therefore, a normalised parameter with a value greater than one indicates that the lattice structure is superior to the bulk material. These parameters for the simple cubic lattice in the panel and beam configurations are shown in Figure 5.4 and Figure 5.5 respectively. The normalised parameters were found to be independent of the length of the unit cells, $L_1$. Therefore, the only geometric parameter that can affect the static properties for the simple cubic structure is the radius to length ratio, $\frac{r_1}{L_1}$.

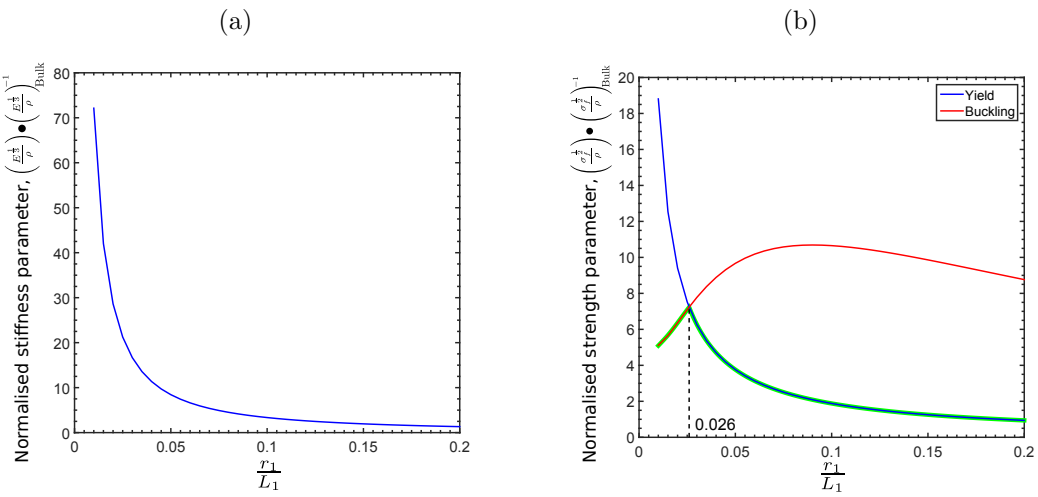



Figure 5.4: Static properties of the simple cubic structure with different radii for panel configurations (a) Normalised stiffness parameter (b) Normalised strength parameter.

As seen in Figure 5.4 (a) and Figure 5.5 (a), the normalised stiffness parameter reduces exponentially with increasing values of $\frac{r_1}{L_1}$. This result suggests that smaller radii are preferred for the simple cubic lattice in beam and panel configurations. Therefore, the lowest value of $\frac{r_1}{L_1}$ should be selected for the simple cubic lattice and the minimum radii will be limited by either the strength of the lattice or manufacturing capabilities.

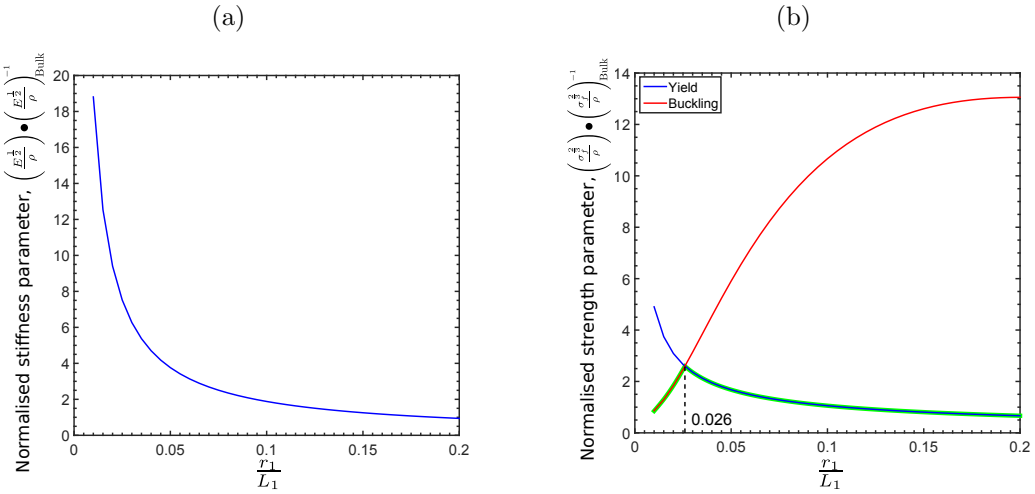



Figure 5.5: Static properties of the simple cubic structure with different radii for beam configurations (a) Normalised stiffness parameter (b) Normalised strength parameter.

On the other hand, the normalised strength parameter for the two failure mechanisms, which are yielding and buckling, for the panel and beam configurations are shown in Figure 5.4 (b) and Figure 5.5 (b) respectively. As seen in these figures, the normalised strength parameter for yielding, reduces exponentially with increasing $\frac{r_1}{L_1}$, like the normalised stiffness parameters. Conversely, the normalised strength parameter for buckling increases initially with increasing $\frac{r_1}{L_1}$ for both the panel and beam configurations. For the panel configuration, the normalised strength parameter for buckling will increase to a maximum value before decreasing again while for the beam configuration, the normalised strength parameter for buckling will continue to increase asymptotically. This trend is expected as the propensity for buckling decreases with decreasing slenderness of the member struts. The decrease in the buckling strength parameter at higher $\frac{r_1}{L_1}$ values is a result of the increase of the buckling strength being lower than the increase in density caused by extra material when the increasing $r_1$.

Since the strength constrained simple cubic lattice panel and beam will fail once the stress reaches the value for either yielding or buckling, the optimal value of $\frac{r_1}{L_1}$ is when the normalised strength parameter for both failure modes are equal. The optimal value is shown in Figure 5.4 (b) and Figure 5.5 (b), and the normalised values of $\frac{r_1}{L_1}$ for both configurations are 0.026. The relatively low value of $\frac{r_1}{L_1} = 0.026$ will also produce relatively stiff simple cubic lattice panels and beams as the normalised stiffness parameter, seen in Figure 5.4 (a) and Figure 5.5 (a), are relatively high at this value.

### 5.3.2 Body-centred cubic (BCC) lattice

The normalised stiffness and strength parameters for the BCC lattice in the panel and beam configurations are shown in Figure 5.6 and Figure 5.7 respectively. Similar to the simple cubic lattice, the static properties for the BCC lattice were also found to be independent of the length of the unit cells, $L_1$. However, as seen in Figure 5.1 (b), there are two sets of beams with different radii that were considered for the BCC structure. Thus, the two geometric parameters that will be analysed are $\frac{r_1}{L_1}$ and $\frac{r_2}{r_1}$.

As seen in Figure 5.6 (a) and Figure 5.7 (a), the normalised stiffness parameter reduces exponentially with increasing values of $\frac{r_1}{L_1}$, while increasing the values of $\frac{r_2}{r_1}$ will only increase this parameter slightly. Therefore, the optimal configuration of the BCC structure is to minimise $\frac{r_1}{L_1}$ and maximise $\frac{r_2}{r_1}$, but increasing $\frac{r_1}{L_1}$ will have a larger overall effect.

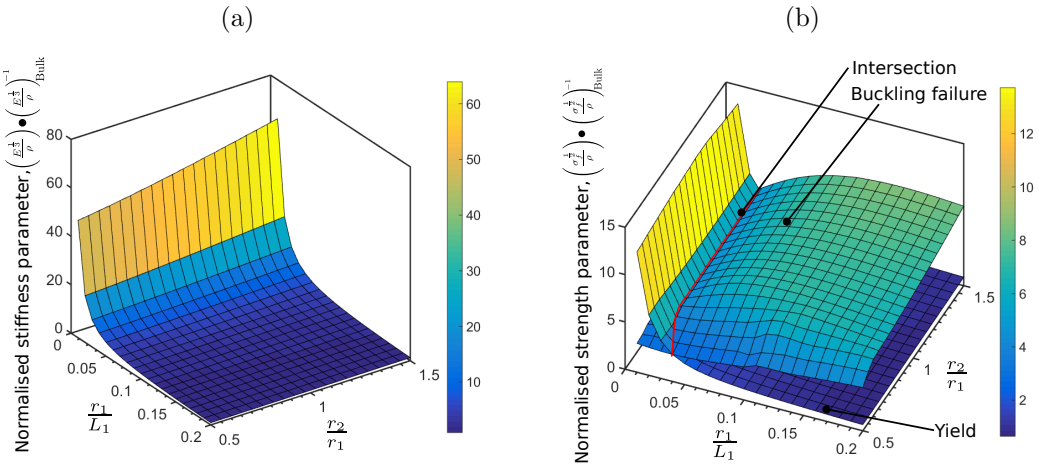



Figure 5.6: Static properties of the BCC lattice structure with different radii for panel configurations (a) Normalised stiffness parameter (b) Normalised strength parameter.

The normalised strength parameters for both the beam and panel configuration are shown in Figure 5.6 (b) and Figure 5.7 (b) respectively. The normalised strength parameters for yielding in both cases were found to decrease exponentially with increasing $\frac{r_1}{L_1}$, but they increase slightly with increasing $\frac{r_2}{r_1}$. Additionally, the normalised strength parameter for buckling, increases with both $\frac{r_1}{L_1}$ and $\frac{r_2}{r_1}$. This result is also expected as the propensity for the lattice to buckle decreases when the slenderness of the struts decreases.

The optimal configuration for the strength constrained panels and beams for the BCC lattice material is the region where the buckling and yielding parameters intersect, as highlighted by the red line in Figure 5.6 (b) and Figure 5.7 (b). As seen in Figure 5.6 (b) and Figure 5.7 (b), the optimal strength parameters appear to be insensitive to the

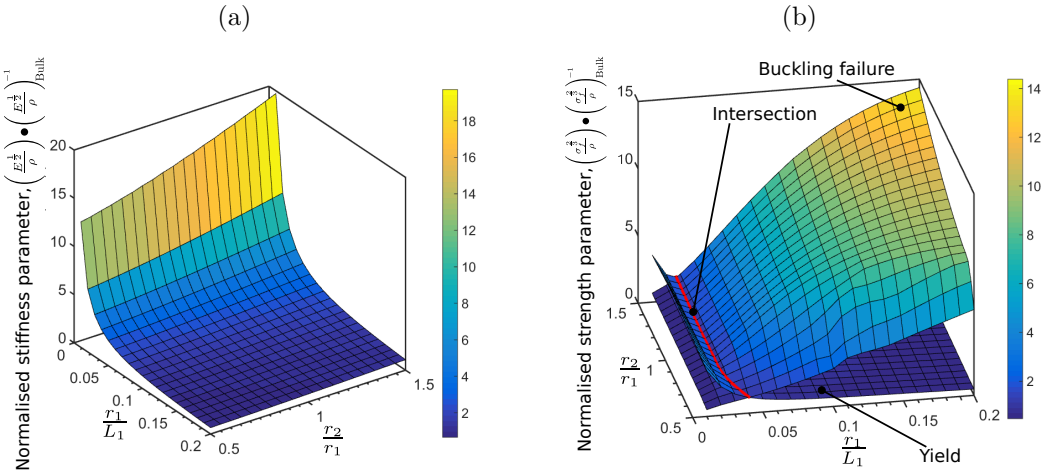



Figure 5.7: Static properties of the BCC lattice structure with different radii for beam configurations (a) Normalised stiffness parameter (b) Normalised strength parameter.

values of $\frac{r_1}{L_1}$, in which the red line is always in between 0.0260 and 0.0398 for both the panel and beam configurations. However, as seen in both Figure 5.6 (b) and Figure 5.7 (b), the normalised strength parameter appears to increase with $\frac{r_2}{r_1}$ until a value and becomes constant after that. In order to investigate this further, the normalised strength parameter versus $\frac{r_2}{r_1}$ curves at the optimal $\frac{r_1}{L_1}$ values (the red line in Figure 5.6 (b) and Figure 5.7 (b)) are plotted in Figure 5.8. As seen in Figure 5.8, the normalised strength parameter will increase with $\frac{r_2}{r_1}$ until a local optimal value of 0.744 and 0.740 for the panel and beam configuration respectively. This result suggests that the inner beams seen in Figure 5.1 for the BCC are the main cause of buckling failure for $\frac{r_2}{r_1}$ values that are lower than the peaks shown in Figure 5.8. Hence, the value of $\frac{r_2}{r_1}$ should be maximised for the BCC lattice. However, since the increase in strength after the peak values are relatively small and increasing the values of $\frac{r_2}{r_1}$ may require more material, the optimal configuration for the BCC lattice in this study is set to be at the peak in Figure 5.8, which are $\frac{r_1}{L_1} = 0.027, \frac{r_2}{r_1} = 0.740$, (giving the normalised strength parameter of 4.374) for the panel and $\frac{r_1}{L_1} = 0.027, \frac{r_2}{r_1} = 0.744$, (giving the normalised strength parameter of 1.618) for the beam configuration.

### 5.3.3 Face-centred cubic (FCC)

Figure 5.9 and Figure 5.10 show the normalised stiffness and strength parameters for the FCC lattice for the panel and beam configurations respectively. The overall trends for the FCC observed in Figure 5.9 and Figure 5.10 appear to be identical to the trends for the BCC lattice structure observed in Figure 5.6 and Figure 5.7. The only exception is that the normalised strength parameter for buckling of the FCC lattice being less

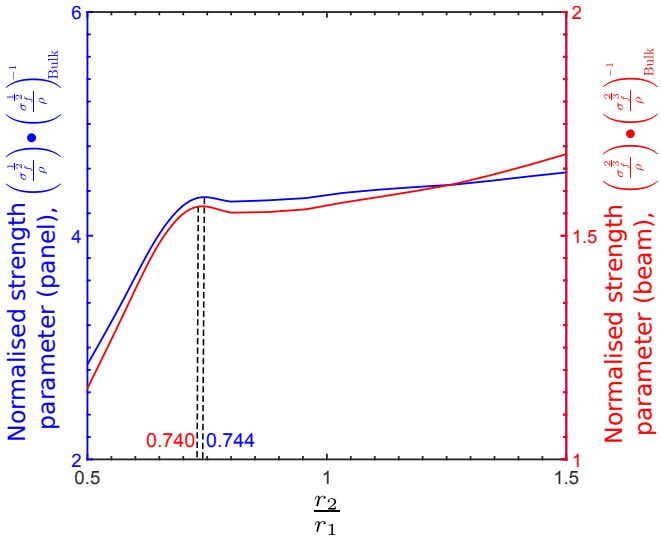



Figure 5.8: Normalised strength parameter versus $\frac{r_2}{r_1}$ for the BCC lattice.

sensitive to the values of $\frac{r_2}{r_1}$, especially for low values of $\frac{r_2}{r_1}$ compared to the BCC lattice.

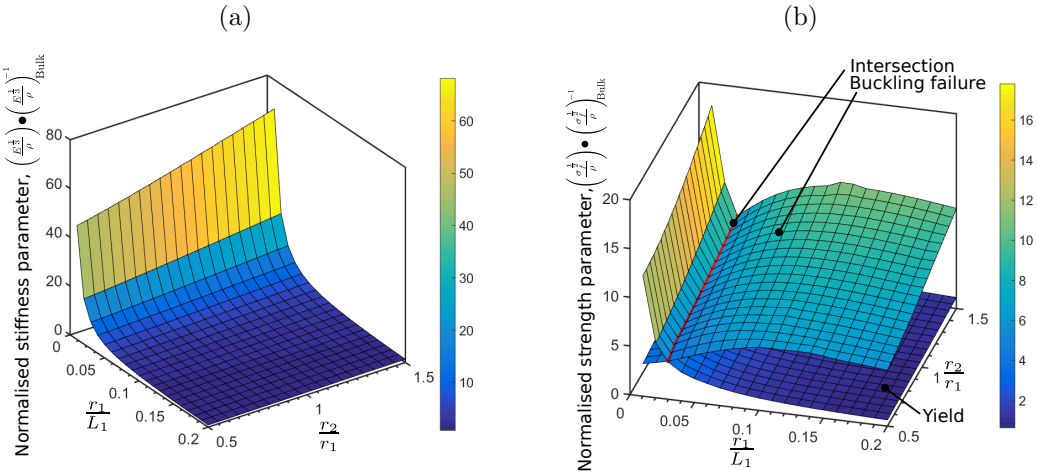



Figure 5.9: Static properties of the FCC structure with different radii for panel configurations (a) Normalised stiffness parameter (b) Normalised strength parameter.

Therefore, the intersection between the surfaces for yielding and buckling is also less sensitive to both $\frac{r_2}{r_1}$ and $\frac{r_1}{L_1}$, where the range of $\frac{r_1}{L_1}$ at the intersection, highlighted by the red line in Figure 5.9 (b) and Figure 5.10 (b), is in between 0.02788 and 0.03000. There were no peaks observed in the normalised strength parameter for both the panel and beam configurations of the FCC structure in Figure 5.11, unlike the case for the BCC lattice. The normalised strength parameter in Figure 5.11 was found to increase with

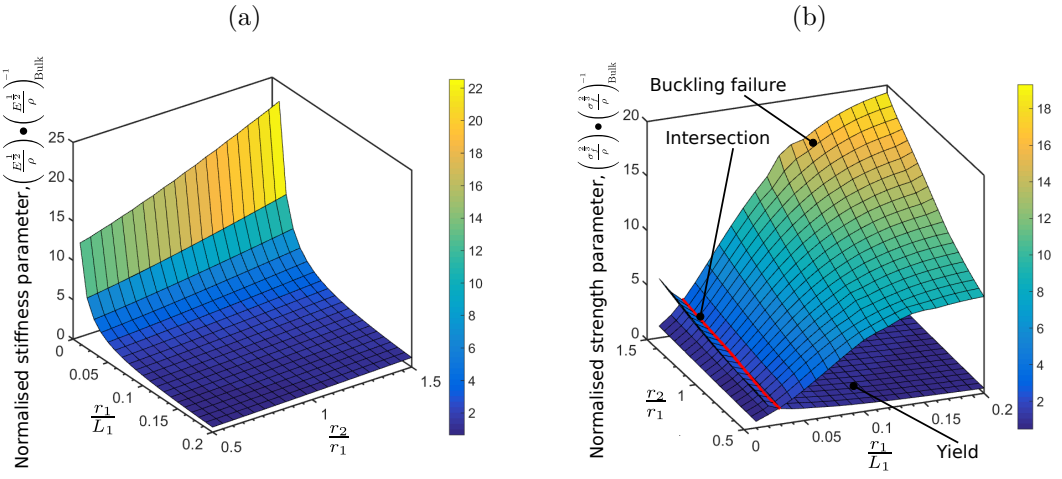



Figure 5.10: Static properties of the FCC with different radii for beam configurations (a) Normalised stiffness parameter (b) Normalised strength parameter.

$\frac{r_2}{r_1}$ throughout the entire range that was studied. Therefore, $\frac{r_2}{r_1}$ should be maximised in order to obtain the optimal strength constrained panel and beams with the FCC structure.

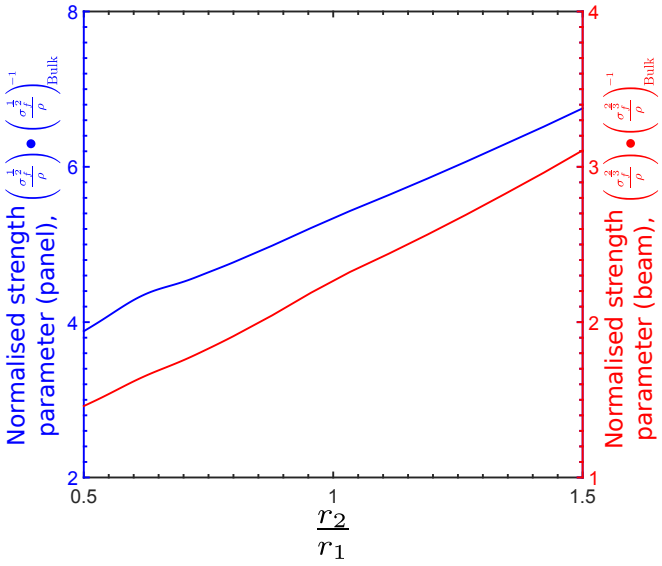



Figure 5.11: Normalised strength parameter versus $\frac{r_2}{r_1}$ for FCC lattice.

### 5.3.4 Regular Octet

The normalised stiffness and strength parameters for the octet lattice are shown in Figure 5.12 and Figure 5.13 for the panel and beam configurations respectively. As seen in Figure 5.12 (a) and Figure 5.13 (a), the stiffness parameters for the panel and

beam configurations showed identical trends to the BCC and FCC lattice structures described earlier. Conversely, the regular octet lattices' normalised strength parameter for buckling is significantly larger than that for yielding over the entire range of geometric parameters studied. Therefore, the normalised strength parameter for buckling was not plotted in Figure 5.12 (b) and Figure 5.13 (b). This result suggests that the octet truss will only fail by yielding and not through buckling. Based on these observations, the optimal regular octet truss geometries in both panel and beam configurations with strength constraints is to minimise $\frac{r_1}{L_1}$ and maximise $\frac{r_2}{r_1}$, with decreasing $\frac{r_1}{L_1}$ having a larger effect.

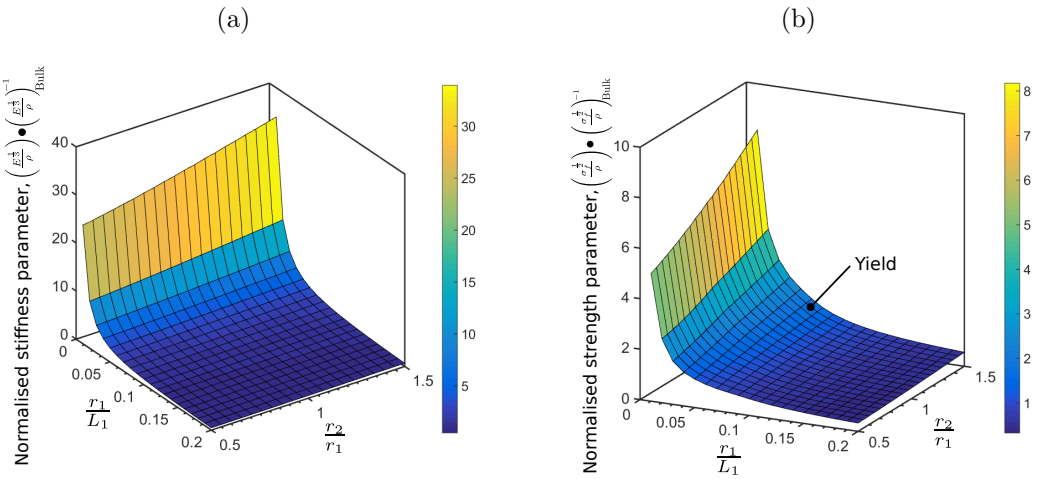



Figure 5.12: Static properties of the regular octet structure with different radii for panel configurations (a) Normalised stiffness parameter (b) Normalised strength parameter.

### 5.3.5 General discussion of the static properties of the lattice structures

The mechanical properties of the cubic topologies have been presented in this section. The normalised stiffness and strength parameters for each cases were then compared in order to determine the best topology that gives the highest values of static parameters shown in for each case. Table 5.4 and Table 5.5 summarise the values and optimal geometric parameters for each topology.

The optimal geometries of all four cubic topologies for the panel and beam configurations are listed in Table 5.4 and Table 5.5 respectively, in which the best topology for a given configuration are bold in the tables. Additionally, for cases in which the parameters for $\frac{r_1}{L_1}$ is to be minimised, this value have been set to 0.01, which will give $r_1 = 1$ mm when $L_1 = 50$ mm. This value is a typical limit based on the resolutions of 3D printers. On the other hand, for values of $\frac{r_2}{r_1}$ that needs to be maximised, these

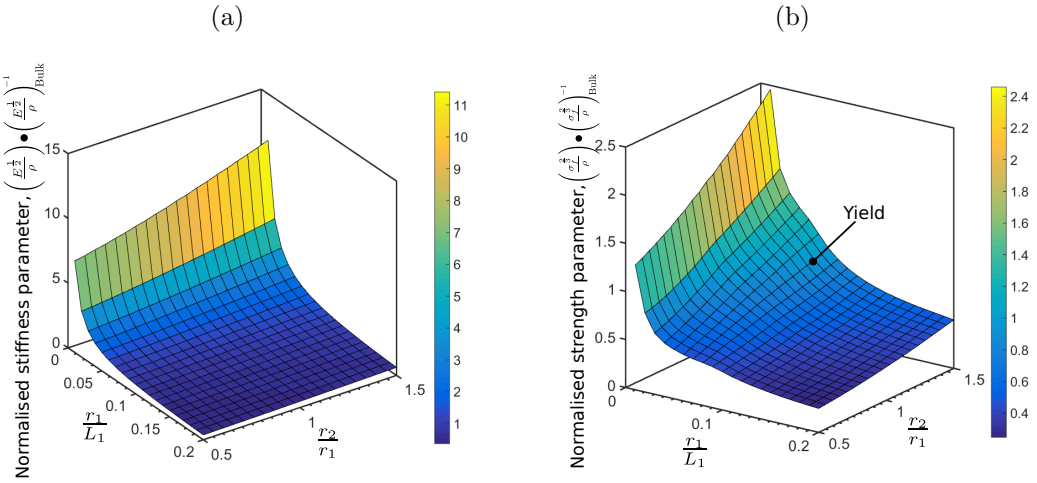



Figure 5.13: Static properties of the regular octet structure with different radii for beam configurations (a) Normalised stiffness parameter (b) Normalised strength parameter.

values have been set to 1.5, which is the maximum value studied in this work.

According to the findings in Table 5.4 and Table 5.5, the optimal topology for the panel with stiffness and strength constraints are the simple cubic and octet truss respectively, while the FCC structure is the optimal topology for the beam configuration with both stiffness and strength constrains. An important point to note here is that the analysis done for these topologies are for the uniaxial loading conditions only as the stresses in a beam and panel bending conditions were assumed to be purely axial similar to an Euler-Bernoulli beam or a plate. The analysis with other loading conditions is a subject of future work.

| Topology | Stiffness Constrained | | | Strength Constrained | | |
|---|---|---|---|---|---|---|
| | $\frac{r_1}{L_1}$ | $\frac{r_2}{r_1}$ | Normalised Parameter | $\frac{r_1}{L_1}$ | $\frac{r_2}{r_1}$ | Normalised Parameter |
| Simple | **0.010** | **N.A.** | **72.13** | 0.026 | N.A. | 7.23 |
| BCC | 0.010 | 1.50 | 63.95 | 0.0269 | 0.744 | 4.345 |
| FCC | 0.010 | 1.50 | 68.10 | 0.02992 | 1.50 | 6.774 |
| Octet | 0.010 | 1.50 | 33.93 | **0.010** | **1.50** | **8.172** |

Table 5.4: Optimal normalised parameters for cubic topologies studied (Panel Configuration).

## 5.4 Band gaps in optimal lattice structure

Resonators were then introduced to the optimal lattice topologies for each configuration from the previous section to produce elastic band gaps. In this study, the target frequency was set to 500 Hz and resonators of different configurations were studied.

| Topology | Stiffness Constrained | | | Strength Constrained | | |
|---|---|---|---|---|---|---|
| | $\frac{r_1}{L_1}$ | $\frac{r_2}{r_1}$ | Normalised Parameter | $\frac{r_1}{L_1}$ | $\frac{r_2}{r_1}$ | Normalised Parameter |
| Simple | 0.010 | N.A. | 18.81 | 0.026 | N.A. | 2.591 |
| BCC | 0.010 | 1.50 | 19.72 | 0.0269 | 0.740 | 1.566 |
| FCC | **0.010** | **1.50** | **22.54** | **0.02992** | **1.50** | **3.11** |
| Octet | 0.010 | 1.50 | 11.41 | 0.010 | 1.50 | 2.459 |

Table 5.5: Optimal normalised parameters for cubic topologies studied (Beam Configuration).

The effects of $L_{\text{Res}}$ and $r_{\text{Res}}$ and band gap width will be studied and the mass of the point mass was varied based on $L_{\text{Res}}$ and $r_{\text{Res}}$ to achieve the target frequency of the resonant frequency. The width of the band gap will be used as the primary criterion for evaluating the vibration isolation performance. Although the attenuation coefficient of the wave as discussed in the previous chapters characterises how quickly the wave attenuates, it is not studied in this chapter as the lattice structures in this section are treated as being repeated infinitely and the waves within the band gap reduced to very low values in such cases.

Due to the large number of oscillator configurations that were evaluated, a low number of 10 elements per unit strut was used in the band gap calculations to conserve computing resources. Despite the low number of elements, there are no significant differences between the band structure of the case with 22 elements and 10 elements per strut at the range of frequencies of interest, as shown in Figure 5.14. Since this is a three dimensional structure, the x-axis of the band structure shown in Figure 5.14 refers to the position within the first Brillouin zone as shown in Figure 5.3. Therefore, the errors associated with reducing the mesh fineness will not significantly affect the analysis. The band gaps for the different configurations of every optimal lattice structure will be examined in turn.

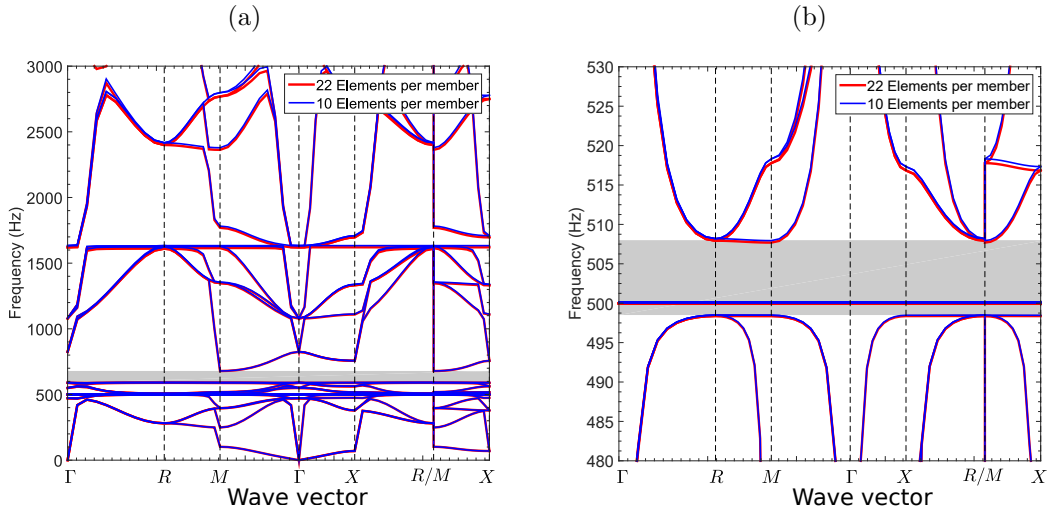



Figure 5.14: Band structure comparing different mesh density at (a) 0 to 3000 Hz (b) 480 to 530 Hz for the simple cubic lattice with a resonator.

### 5.4.1 Optimal lattice for stiffness constrained panel structure (simple cubic lattice)

The optimal lattice topology for the stiffness constrained plate structure is a simple cubic structure. The band structures with and without resonators are shown in Figure 5.15. As seen in Figure 5.15 (a), the introduction of the resonators tuned at 500 Hz generated band gaps at 495.2 to 560.9 Hz and 591.0 to 754.8 Hz, which were not present in the case without the resonators. Additionally, a pass band within the band gap region at the tuned frequency of 500 Hz was also observed in Figure 5.15 (b). The pass band at the tuned frequency of the local resonators are typical for band gaps produced via the local resonance (LR) phenomenon.

The boundaries of the first band gap for this topology are plotted in Figure 5.16 (a) for different values of lengths and radii of the resonators. Only the first band gap will be investigated because it is the only band gap that is directly associated with the tuned frequencies of the resonators. As seen in the figure, the pass band at the tuned frequency of 500 Hz will always be present across all values of lengths and radii. Further observations can be made from Figure 5.16 (a). Firstly, the upper bound of the frequency increases with increasing $\frac{r_{\text{Res}}}{r_1}$ and decreasing $\frac{L_{\text{Res}}}{L_1}$. On the other hand, the lower bound of the frequency decreases steeply with increasing $\frac{r_{\text{Res}}}{r_1}$ and decreasing $\frac{L_{\text{Res}}}{L_1}$. Hence, as illustrated by Figure 5.16 (b) that shows the width of the band gaps, the width increases with $\frac{r_{\text{Res}}}{r_1}$ and decreases with increasing $\frac{L_{\text{Res}}}{L_1}$. Based on these observation, the optimal oscillators should have maximum $\frac{r_{\text{Res}}}{r_1}$ and minimum $\frac{L_{\text{Res}}}{L_1}$, so that the width of the band gap is maximised.

However, in order to achieve the same tuned frequency, which is the natural frequency of the resonators, increasing the values of $\frac{r_{\text{Res}}}{r_1}$ and decreasing $\frac{L_{\text{Res}}}{L_1}$ will lead to an increase

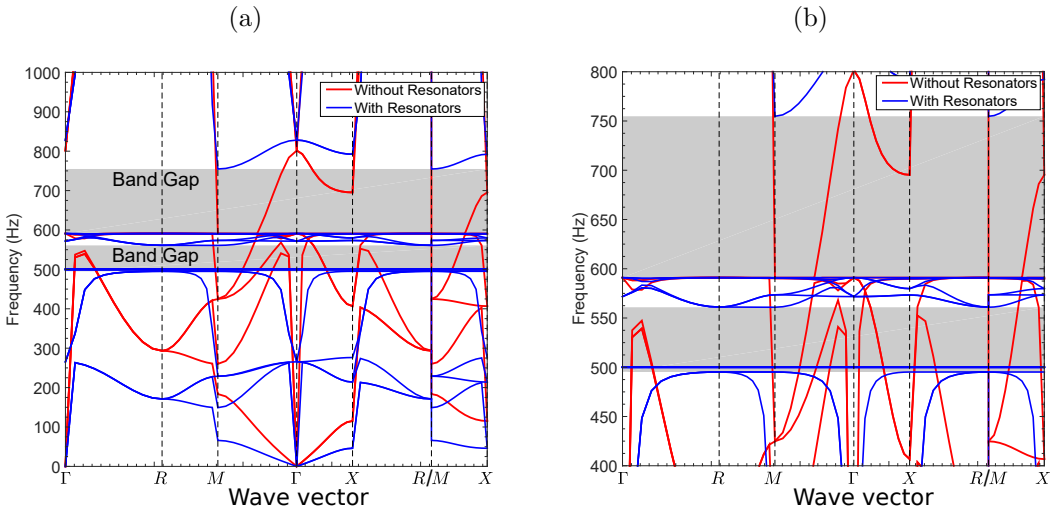



Figure 5.15: Band structures of simple cubic lattice studied with and without local resonators (a) 0 to 1000 Hz (b) 400 to 800 Hz.

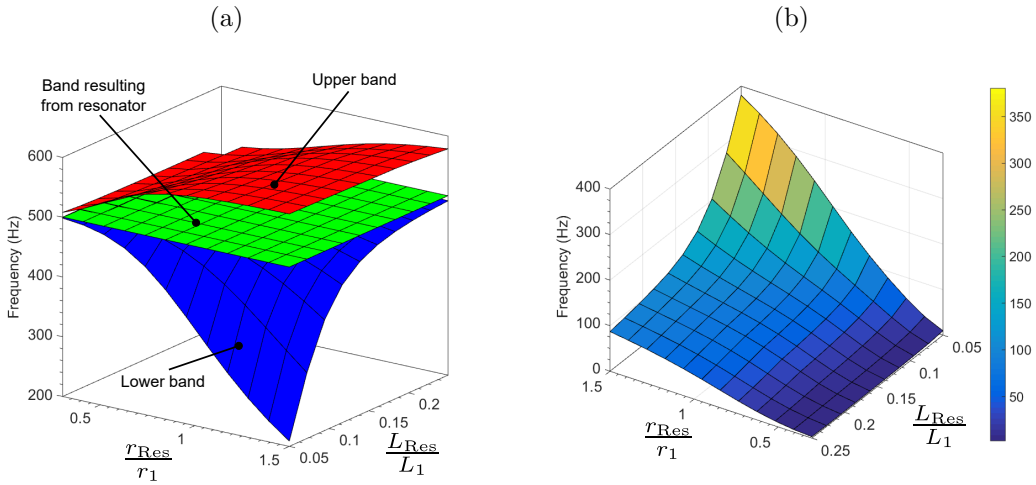



Figure 5.16: (a) Upper and lower bounds of the first band gaps (b) width of first band gap for different resonator configurations for simple cubic structure.

in the mass required for the resonators. This is because the increase in $\frac{r_{\text{Res}}}{r_1}$ and decrease in $\frac{L_{\text{Res}}}{L_1}$ will result in a stiffer beam for the resonator and an increase in mass is needed to maintain the same natural frequency. This can be seen in Figure 5.17, that shows the density increment, defined as the ratio of the increase in density to the original density of the lattice, for different geometries of the resonator beams. The required mass increases exponentially with increasing $\frac{r_{\text{Res}}}{r_1}$ and decreasing $\frac{L_{\text{Res}}}{L_1}$. This suggests that the increase in band gap width will also result in an increase in the density of the lattice, which is undesirable for light-weight applications.

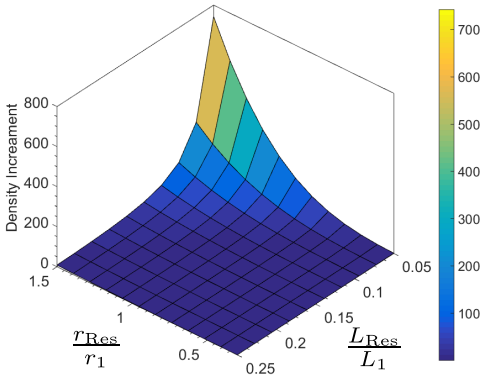



Figure 5.17: Density increment with the addition of resonators for simple cubic lattice.

As seen in Section 5.3.5, the parameters to be maximised are directly proportional to the inverse of density. Therefore, the increase in mass can still be justified if these parameters multiplied by $(1+\ \Delta\rho)$, is still significantly larger than unity, where $(1+\ \Delta\rho)$ is defined as follows.

$$P_{\text{With resonators}} = \frac{P_{\text{Without resonators}}}{(1+\Delta\rho)} \tag{5.16}$$

where $P$ is the strength or stiffness parameter ($\frac{\sigma_f^{\frac{2}{3}}}{\rho}$, $\frac{E^{\frac{1}{2}}}{\rho}$, $\frac{\sigma_f^{\frac{1}{2}}}{\rho}$, or $\frac{E^{\frac{1}{3}}}{\rho}$) as shown in Section 5.3.5 and $\Delta\rho$ is the density increment.

This is because the static properties for light-weight structural applications after the addition of the resonators are still better than the bulk material.

Since the optimal parameter for the simple cubic case is 72.13, as shown in Table 5.4, it is likely that this is possible. For example, an overlap of the contour plot of the density increment (the red lines) and the width of the band gaps (the other lines) in Figure 5.18 (a), shows that band gaps of more than 20 Hz is achievable, where the static parameter after adding the resonators is still larger than 10, although a mass of 5 times the original lattice is added to the system.

Furthermore, the band gap width per unit density increment contour plot, as shown

in Figure 5.18 (b), was studied to determine the beam configuration that will give the maximum band gap width while minimising the penalty of increasing density. As seen in Figure 5.18 (b), there is a peak at approximately $\frac{L_{\text{Res}}}{L_1} = 0.2$ and $\frac{r_{\text{Res}}}{r_1} = 0.4$ with a value of 50. This result suggests that there is a maximum band gap width per unit density increment for a tuned resonator and optimisation methods can be implemented to find this value.

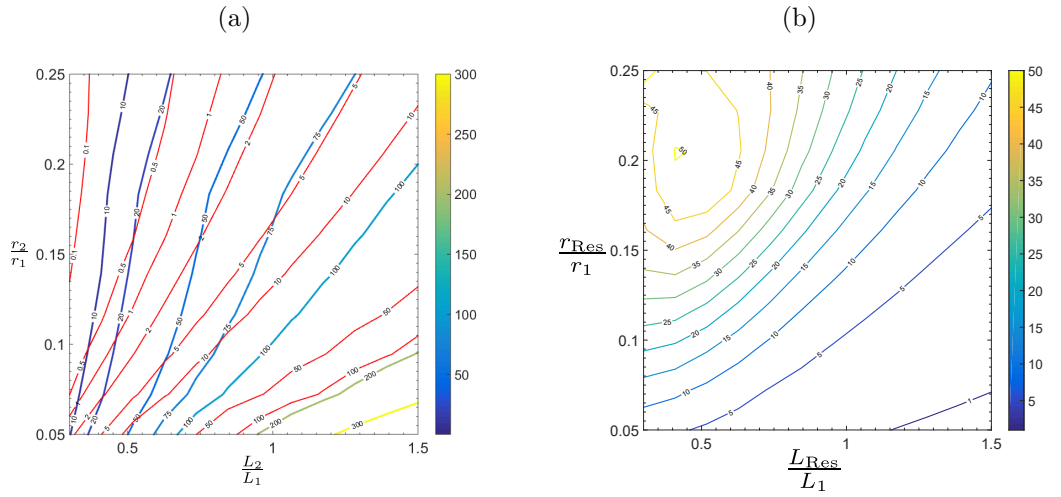



Figure 5.18: (a) Overlap of density increment and band gap width contour plot, red contour denote density increment while the other contour denotes band gap width (b) Band gap width per unit density increment contour plot for simple cubic structures.

### 5.4.2 Optimal lattice for strength constrained panel structure (octet lattice)

The upper and lower bounds of the optimal lattice for the strength constrained plate structure found in Section 5.3.5 are plotted in Figure 5.19 (a). The band structure for this lattice configuration share similar trends with the simple cubic structure discussed in the previous section. It has a pass band for all lengths and radii of the resonators at the tuned frequency of 500 Hz. The trends of the upper and lower bounds of the band gap, and subsequently the band gap width with respect to $\frac{r_{\text{Res}}}{r_1}$ and $\frac{L_{\text{Res}}}{L_1}$ follow the same trends as the ones for the simple cubic structure.

The density increment resulting from the addition of the resonators, shown in Figure 5.20, for this lattice configuration are also similar to the simple cubic structure. However, the density increment for the regular octet structure is lower due to the larger original density of the unit cell. The similar trends of this lattice and the simple cubic structure is expected because the same mechanism was used to produce the band gaps.

Although the density increment from the addition of the resonators is lower for the octet structure, the band gap width per unit density increment for the octet lattice,

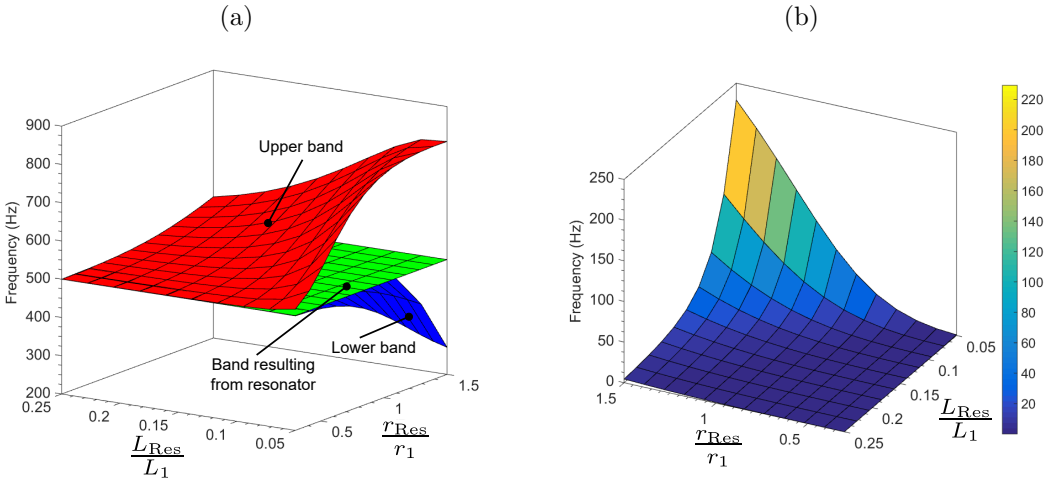



Figure 5.19: (a) Upper and lower bounds of the first band gaps (b) width of first band gap for different resonator configurations for regular octet lattice.

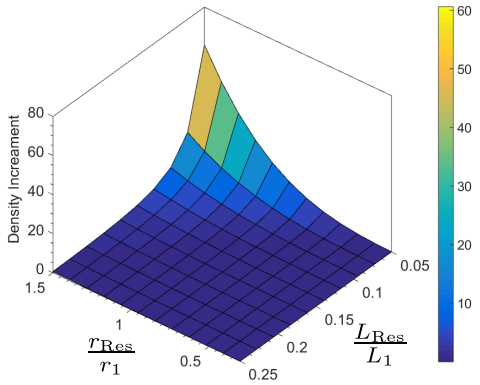



Figure 5.20: Density increment with the addition of resonators for regular lattice.

shown in Figure 5.21 (b), is significantly lower than that for the simple cubic structure in Figure 5.18 (b). The cause of this is the significantly smaller band gap width produced by the resonators as shown in Figure 5.21 (a). This result suggests that there is a positive correlation between the mass of the oscillators and the width of the band gap. Furthermore, no distinct peak was observed in Figure 5.21 (b), although it appears to have a region with relatively high values and the maximum appears to be outside the range that was investigated.

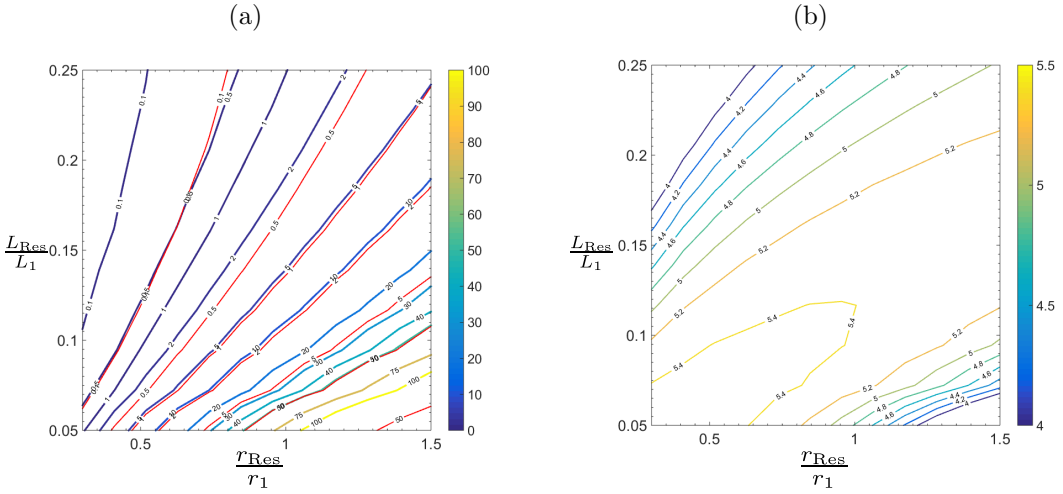



Figure 5.21: (a) Overlap of density increment and band gap width contour plot, red contour denote density increment while the other contour denotes band gap width (b) Band gap width per unit density increment contour plot for the regular octet lattice.

### 5.4.3 Optimal lattice for stiffness constrained beam structure (FCC lattice)

The optimal lattice structure for a stiffness constrained beam structure, which has an FCC topology, has a band gap from 411.3 to 485.6 Hz, as seen in Figure 5.22, even though no local resonators were present. The band gap without the local resonators will be referred to as the original gap herein, while the band gap with the resonators will be referred to as the resonator gap. The original gap produced via Bragg scattering. This is possible at a low frequency of 500 Hz as the length of the unit cell, $L_1$, and the density, $\rho$, is high while the stiffness, $E$, is relatively low for the structure studied here, which means that the wavelength of the elastic wave may be lower than the length of the unit cell at 500 Hz and the limitation for Bragg scattering have not been met.

The upper and lower bounds of the resonator gap and the original gap are shown in Figure 5.23 (a), while the band gap widths are shown in Figure 5.23 (b). Since the mechanism for the resonator gap is the same as the lattice structures shown previously, the general trend for the upper and lower bounds, and the band gap widths of the resonator

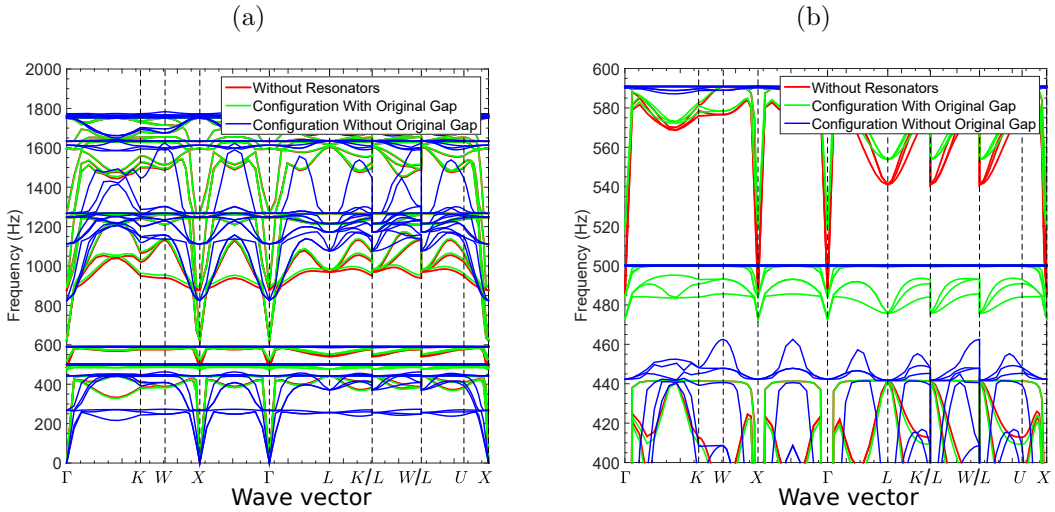



Figure 5.22: Band structures of FCC studied with and without local resonators (a) 0 to 2000 Hz (b) 400 to 600 Hz.

gap are similar to the previous structures. The density increment for the resonators in Figure 5.24 was also found to follow the trends of the other lattice structures.

However, the addition of the resonators affects the original gap. Firstly, the width of the original gap is reduced. Furthermore, the original gap appears to have the opposite trend of the resonator gap, as seen in Figure 5.23 (a) and (b), where the its width decreases with increasing $\frac{r_{\text{Res}}}{r_1}$ and decreasing $\frac{L_{\text{Res}}}{L_1}$ until it eventually closes. Increasing the width of the resonator gap will lead to a decrease in the original gap.

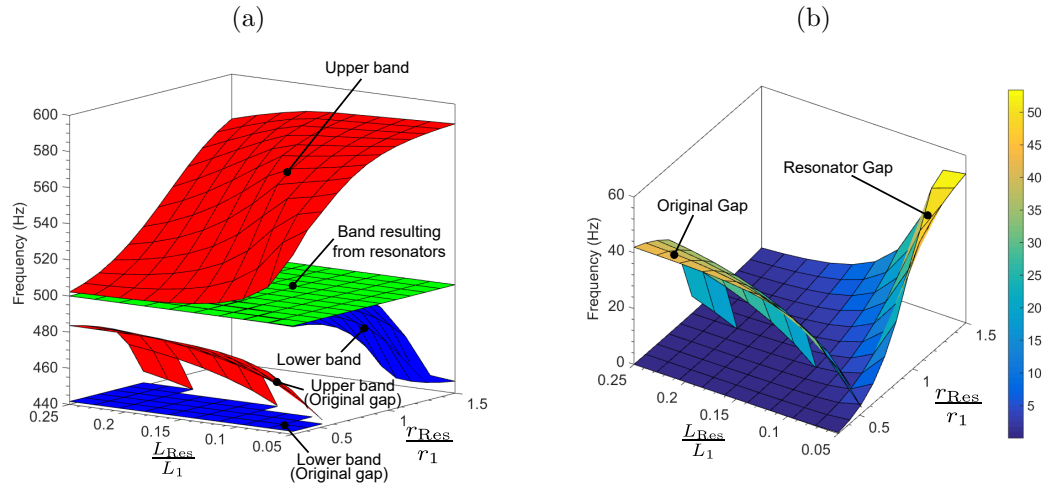



Figure 5.23: (a) Upper and lower bounds of the first band gaps (b) width of first band gap for different resonator configurations for the FCC structure.

Additionally, some differences in the band structure were observed for the case when the original gap is present, as seen in Figure 5.22. When the influence of the resonator

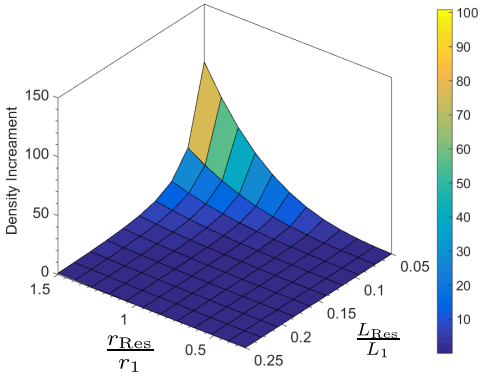



Figure 5.24: Density increment with the addition of resonators for FCC lattice.

gap is low, the band structure of the lattice is similar to the case without the resonators. The resonators generate a pass band at a frequency slightly lower than the tuned frequency, while creating an additional band gap above 500 Hz. On the other hand, when the effects of the resonators become significant, the band structure with the resonators differs significantly from the original case, this can be seen by comparing the green and blue curve shown in Figure 5.22.

The overlap of the band gap width contour plot and the density increment from the addition of the resonators are shown in Figure 5.25 (a) and (b) for the original gap and the resonator gap respectively. As seen in Figure 5.25 (a), the band gap width of the original gap appears to be reducing with density increment, contrary to the observation made in Figure 5.25 (b) for the resonator gap. There are no contours for the band gap width for the original gap at higher $\frac{r_{\text{Res}}}{r_1}$ values as the original gap closes. This observation is analogous to the original gap being "*cannibalised*" by the resonator gap when resonators with larger masses and larger resonator gap widths are used. Furthermore, since a large original gap can be achieved without the penalty of increasing the lattice's density, modifying the original structure to tune the band gap to the desired frequency ranges is a better strategy if band gaps are present in the original structure. Unfortunately, for this configuration, the band gap width resulting from the addition of the resonators is relatively low. For example, based on Figure 5.25 (b), the added resonators will result in an increase of 5 times the density of the lattice to achieve a 10 Hz band gap. This significantly reduces the original stiffness parameter from 22.54 to 3.75. Despite the static performance of the lattice structure still being better than the bulk material, the significant reduction in the stiffness parameter means the strategy of adding resonators may not be suitable for this configuration.

The band gap width per unit density increment for the original and resonator gaps are shown in Figure 5.26 (a) and (b) respectively. As expected, the trend observed for the

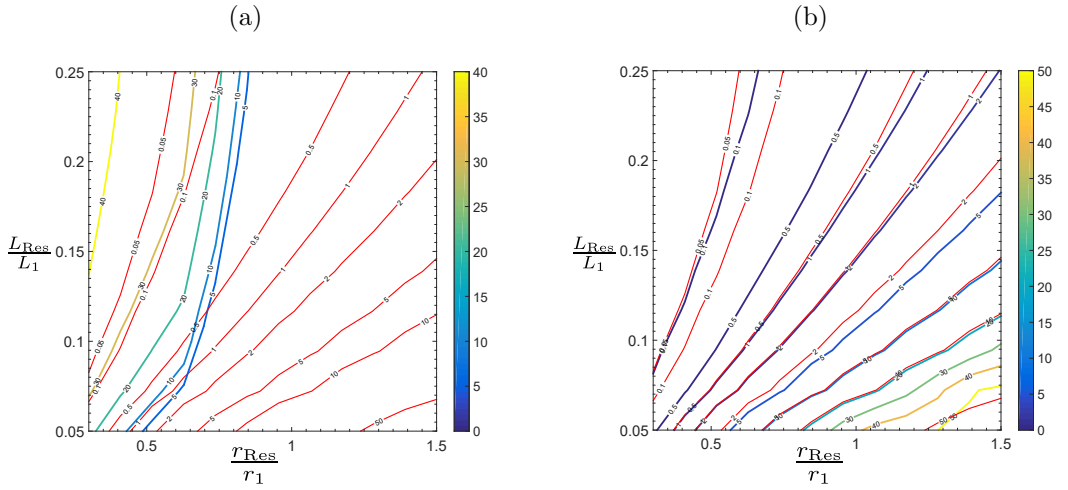



Figure 5.25: Overlap of density increment and band gap width contour plot, red contour denote density increment while the other contour denotes band gap width (a) Original gap (b) Resonator gap for the FCC lattice.

resonator gap in Figure 5.26 (b) is similar to that for the octet truss discussed previously. However, compared to the other lattice configurations, the band gap width per unit density increment for this FCC configuration, seen in Figure 5.26 (b), is significantly lower than the other lattice configurations, especially the simple cubic configuration. This result suggests that the addition of resonator does not provide large band gap widths for the increase in mass. However, by comparing Figure 5.26 (a) and (b), the band gap width per unit density increment for the orginal gap is approximately three orders of magnitude higher than that for the resonator gap. This result indicates that the original gap strategy should be pursued in favour of the addition of resonators if these gaps are present around the desired frequencies.

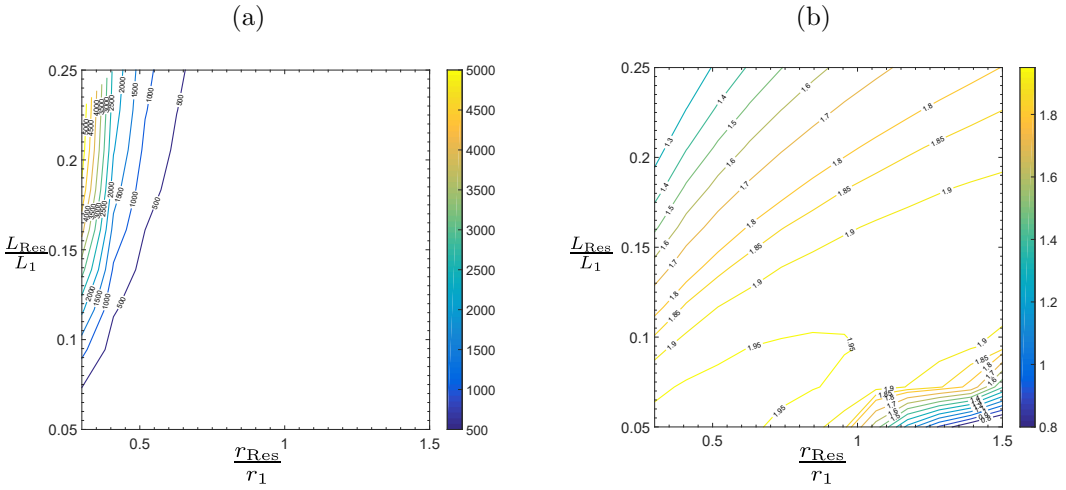



Figure 5.26: Band gap width per unit density increment contour plot (a) Original gap (b) Resonator gap for the FCC lattice.

### 5.4.4 Optimal lattice for strength constrained beam structure (FCC lattice)

The final configuration is the FCC lattice that has the optimal geometrical parameters for a strength constrained beam structure. The upper and lower bounds of the first band gap for this lattice topology and the width of the first band gap are shown in Figure 5.27 (a) and (b) respectively. As seen in Figure 5.27 (a), there is an additional band gap at low values of $\frac{L_{\text{Res}}}{L_1} = 0.05$. This band gap will not be investigated as the band gap of interest is the one related to the tuned frequency of 500 Hz. Additionally, unlike the previous FCC case, there are no band gaps present for this case when no resonators are added. Similar to the other lattice structures being investigated, the band gap follows the trends observed in the other lattices with a pass band from the resonators at the tuned frequency of 500 Hz, as seen in Figure 5.27 (a). The band gap width also increases with decreasing $\frac{L_{\text{Res}}}{L_1}$ and increasing $\frac{r_{\text{Res}}}{r_1}$, as seen in Figure 5.27 (b). However, the increase in band gap width is accompanied by an undesirable increase in density as indicated in Figure 5.28.

The overlap of the band gap width contour plot and the density increment from the addition of the resonators are shown in Figure 5.29 (a) and (b) respectively. Again, the trends shown in these figures are consistent with that for the band gaps in the other configurations. However, the optimal band gap width per unit density increment for this structure appears to be outside the range of values being studied. Lastly, the band gap width per unit density increment, shown in Figure 5.29 (b), also suggests that the resonators that were added are not efficient in generating the band gaps. This is undesirable, especially when the normalised strength parameter is already low at 3.11. A further investigation of Figure 5.29 (a) shows that in order to produce a band gap

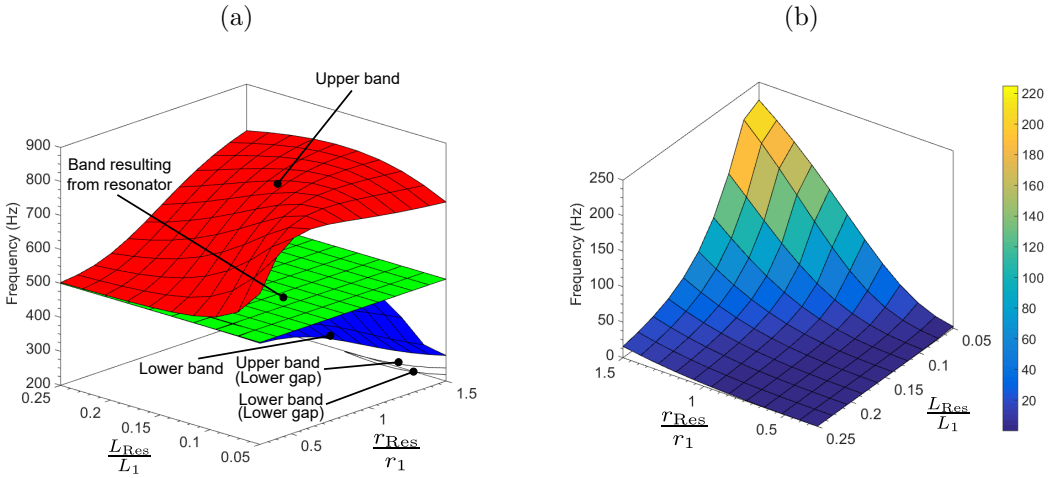



Figure 5.27: (a) Upper and lower bounds of the first band gaps (b) width of first band gap for different resonator configurations for the FCC lattice.

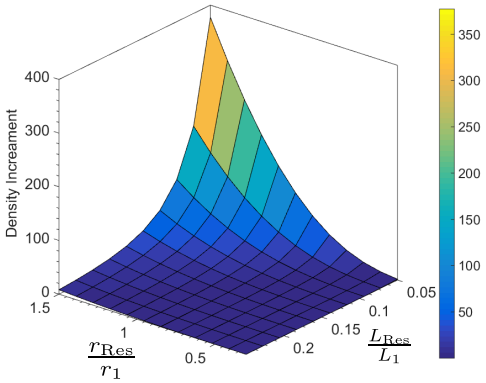



Figure 5.28: Density increment with the addition of resonators for the FCC lattice.

with a width of 5 Hz, the added mass will result in a density increment of 10 times the original density. This will lead to the strength parameter with the oscillators being reduced to 0.2828, which is significantly lower than that for the bulk material. Hence, the strategy of adding resonators is not a viable option for this case.

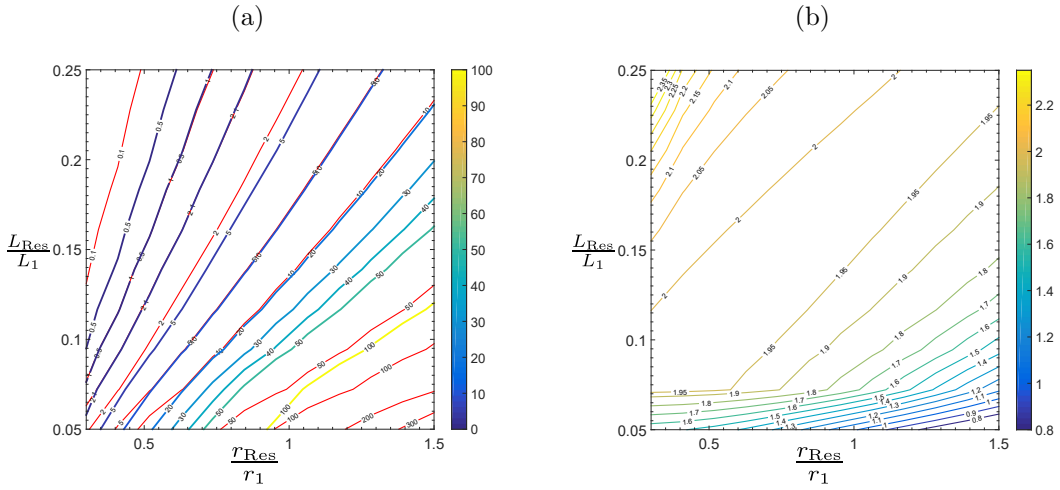



Figure 5.29: (a) Overlap of density increment and band gap width contour plot, red contour denote density increment while the other contour denotes band gap width (b) Band gap width per unit density increment contour plot for the FCC lattice.

### 5.4.5 General discussion on band gap behaviour of lattice with oscillators

Local resonators were added to the lattice structures with the optimal static properties from Section 5.3.5 in order to produce locally resonant (LR) band gaps. This method is similar to the method employed in [22]. The location of the band gaps were tuned to be 500 Hz and resonators of different lengths, radii, and masses were studied. Although the band gaps were tuned to be 500 Hz in this study, the general trends of the band gaps should be similar for resonators with other frequencies, with the differences being the location of the optimal band gap width per unit density being at different values of length and radius. The procedure introduced in this study can be used to determined the trends for resonators with other tuned frequencies.

The LR gaps produced by the addition of the resonators for all lattice topologies showed similar trends, in which the band gap width increases with increasing $\frac{r_{\text{Res}}}{r_1}$ and decreasing $\frac{L_{\text{Res}}}{L_1}$. However, the increase in the LR band gap width comes at a cost of an increase in the density, suggesting a positive correlation between the band gap width and the resonator mass. For cases where the static parameters are significantly better than the bulk material, such as the simple cubic and FCC lattices for the plate configurations, the normalised stiffness and strength parameters after adding the resonators may still be

significantly higher than the bulk material despite the increase in density. Conversely, for other cases especially where the static parameters are only marginally better than the bulk material, for example the FCC and octet structures for the beam configurations, the parameter may reduce below that for the bulk material and the strategy of adding local resonators is not viable. Hence, the increase in density is a key consideration when employing the strategy outlined in this chapter to produce multifunctional lightweight structural materials with elastic band gap properties.

Additionally, some lattice structures, such as one of the FCC lattice investigated here, have band gaps prior to the introduction of the resonators. These band gaps have far larger widths compared to that introduced by the resonators and do not come with a penalty on the density. Therefore, tuning the original band gap to the desired frequency is a more favourable solution to the addition of the local resonators when these band gaps are present.

There are several improvements that can be made to increase the band gap widths that can be studied further. One possible improvement is to design hybrid 3D cores, where two or more topologies are combined in a spatially periodic pattern that may increase the band gap width. Another possible strategy is to arrange the unit cells with different resonators in series with overlapping band gaps. This may result in a very wide band gap to effectively attenuate vibrations, for example as seen in [3]. Lastly, as in beam or panel configurations, the axial length is generally larger than the width or height of the system. Therefore, there is a potential to improve the band gap and static performance of the lattice structure by varying the width and height independently. These possible improvements are topics of future study in this field.

## 5.5 Conclusion

Lattice structures have huge potential for multifunctional applications. In this chapter, a parametric study was conducted in order to investigate the viability of cubic structures to be used as both a lightweight structural component with vibration isolation properties. The stiffness and strength properties of four different cubic lattice topologies to be used as core materials for sandwich beams and panels were investigated in order to determine the best topology and geometric parameters. In general, the normalised stiffness parameter was found to increase with the radius of the member struts for all topologies. The strength of the lattice topologies were determined by two failure mechanism, which are the yielding and buckling of the struts. The yielding parameter increases with increasing $\frac{r_2}{r_1}$ and decreases with increasing $\frac{r_1}{L_1}$, for all the topologies except the simple cubic lattice that has no diagonal struts. On the other hand, the normalised strength parameter for buckling increases with increasing $\frac{r_2}{r_1}$ and increasing $\frac{r_1}{L_1}$ for all topologies with the exception of the octet truss, which does not experience

buckling. The failure strength of the topologies was set to be the lower of the yielding and buckling failure modes. Therefore, the optimal topology for the strength was found to be the point in which the yield and buckling criteria are equal. The lattice topologies were found to be able to have superior static mechanical properties compared to that of the parent bulk material. Based on these findings, the optimal topology for each configuration was found.

After that, tuned resonators made from cantilever beams with masses at the end were added to the topologies to introduce band gaps via the local resonance mechanism. The resonators were tuned to have a natural frequency of 500 Hz. Since there are different parameters, such as the length, radius, and added mass, which can produce resonators of a given natural frequency, the effects of these geometrical parameters on the band gap widths were also studied. For all topologies, the band gap widths produced by the introduction of the resonators follow the same trend. The band gap width was found to be larger for increasing values of $\frac{r_{\text{Res}}}{r_1}$ and decreasing values of $\frac{L_2}{L_1}$ but this is accompanied by an increase in density. This is because the required changes to increase the band gap width will result in a stiffer beam and a larger mass is required to give the same natural frequency. With the increase in density resulting from the introduction of the oscillators, the strength and stiffness parameters for the lattice structures reduces. Based on the findings of this investigation, the addition of the resonators is justifiable if the stiffness or strength parameter is still significantly larger than that for the bulk material, as seen in some of the topologies investigated here. However, for other cases, such as the FCC for the strength constrained beam structure, the value falls below that for the bulk material and this strategy is not viable. Therefore, the increase in density and the decrease in the normalised stiffness and strength parameter are important factors to consider when adding resonators to such structural components.

Lastly, some topologies such as one of the FCC topology studied here have a band gap prior to the addition of the resonators. Since the addition of the resonators will only degrade the original gap, the best strategy is to make changes to the structure to achieve the desired band gap frequency because the original gap does not result in the addition of mass.

# 6 Design and testing of a three dimensional periodic lattice structure with elastic band gap

## 6.1 Introduction

In the previous chapter, a study on the design parameters of several periodic lattice structures with cubic topologies has been performed. In that study, the relationship of the design parameters, such as the beam thickness, on the elastic band gaps and effective mechanical properties of these structures were found. A large number of studies, [22, 23, 103, 106, 149, 221] have been conducted on the topic of band gap in lattice structures. In these studies, many designs were proposed and the band structures of the lattices were determined using models but the frequency response of the designs were either not analysed or calculated using finite element without performing any experiments. Only a few studies, [3, 22, 44], have performed experimental measurements on the frequency response function of lattice structures to demonstrate the presence of band gaps. The likely cause of the lack of experimental studies is that the difficulty in the manufacture of the lattices and huge confidence in the analytical solutions.

In this chapter, two three-dimensional cubic structures, one with local resonators to generate elastic band gaps and the other without local resonators as a comparison, have been manufactured using additive manufacturing, commonly known as 3D printing. The aim of this chapter is to demonstrate experimentally, that three dimensional periodic lattices can be manufactured to produce elastic band gaps. This is done by performing experiments on the structures and measuring their frequency response functions to show the presence of the elastic band gaps. Additionally, issues with the practical implementation of such designs will also be studied in this work.

This chapter is organised as follows. Firstly, the selected design and its analysis will be presented. This is followed by the description of the manufactured lattice structures and experimental setup. After that, the results of the experimental will be presented and discussed before concluding this chapter.

## 6.2 Design of periodic lattice structure

### 6.2.1 Selected topology and geometry

The lattice topology selected in this study is the simple cubic structure as described in Section 5.2.1, and shown in Figure 5.1 (a). The reason for the selection of the simple cubic topology is mainly due to its simplicity, which facilitates the manufacturing process. In this study, the cubic structure was manufactured using stereolithography (SLA) by CRDM, a company specialising in additive manufacturing. The main body of the structure and struts were made from Acura 55, which is an acrylonitrile butadiene styrene (ABS) polymer, and the material properties are given in Table 5.3 in the previous chapter. Low carbon steel ball bearings were used as the masses for the resonators and were attached to the ends of the resonator struts using adhesives. The density of the ball bearings was taken to be 7800 kg $m^{-3}$.

Since the main aim of this study is to demonstrate the presence of the elastic band gaps created via the local resonators, the geometry of the main structure of the lattice, which are the length of the unit cell, $L_1$, and the radius of the main structure, $r_1$, are selected based on the limitations of the SLA process. In this study, $L_1$ was selected to be 50 mm so that the entire structure can be printed. The manufactured structure has a total of 7 unit cells across its length and 2 unit cells in the two directions perpendicular to its length, as seen in Figure 6.1. Although the static mechanical properties of the lattice are not studied here, the value of $r_1$ was selected to be 1 mm because based on the findings of Section 5.3.1, this value should be minimised to achieve maximum specific stiffness. The value of 1 mm is limited by the resolution of the 3D printer.

In this study, the band gaps were designed to be around a frequency of 500 Hz. Therefore, the local resonators were designed to have a natural frequency of 500 Hz. In order to determine the geometric parameters required for the oscillators, finite element analyses were performed. The finite element analyses performed are described in the next section.

### 6.2.2 Finite element and band structure calculations

In this study, finite element analysis has been implemented to find the natural frequency of the local resonator, to determine the band structure of the periodic lattice, and to calculate the frequency response function for the periodic lattice used in the experiments.

As stated in the previous section, the local resonators need to have a natural frequency of 500 Hz to produce a band gap around 500 Hz. The three parameters that can be tuned are the mass of the ball bearing, $m$, the radius of the local resonator, $r_{\text{Res}}$, and the length of the local resonator, $L_{\text{Res}}$. In order to determine suitable values for these parameters, a finite element model of 10 elements were used to model the beam while the steel ball bearing was treated as a point mass, as shown in Figure 6.1. For a given

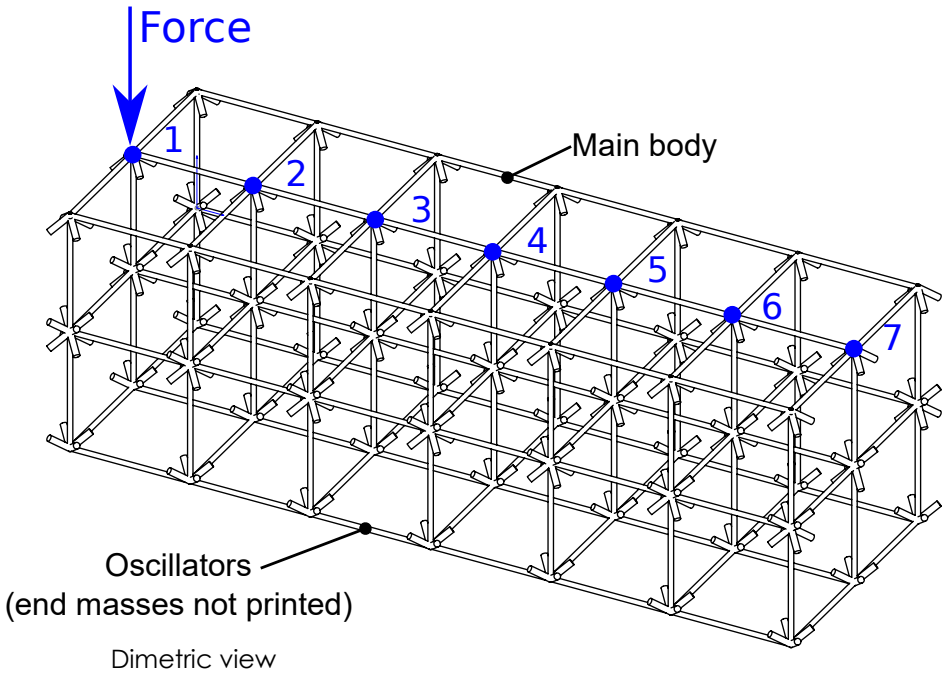



Figure 6.1: Finite structure that is printed and boundary conditions in finite element analysis.

value of $r_{\text{Res}}$ and $L_{\text{Res}}$, the natural frequencies of the first mode, in which one end is treated as a built in part, were calculated for different values of mass and the masses that gives natural frequencies of 500 Hz were recorded. This is repeated for a range of $r_{\text{Res}}$ and $L_{\text{Res}}$. The natural frequencies of the local resonator, $\omega_n$, were found by solving the following eigenvalue problem .

$$\mathbf{K} - \omega_n^2 \mathbf{M} = \mathbf{0} \tag{6.1}$$

where $\mathbf{K}$ is the stiffness matrix and $\mathbf{M}$ is the mass matrix obtained from finite element analysis.

The surface in Figure 6.2, shows all possible values for the local resonators to give a natural frequency of 500 Hz. A steel ball bearing with a diameter of 8 mm was selected to be the mass as a larger diameter will lead to the mass being easier to be attached. 8 mm is a suitable compromise between this requirement and the space it occupies. The steel ball bearing with 8 mm diameter has a mass of 2.1 grams and this is shown by the red curve in Figure 6.2. Based on this analysis, $r_{\text{Res}}$ and, $L_{\text{Res}}$ were selected to be 1.25 mm and 10 mm respectively.

Once the local resonators were selected, the band structure of the periodic lattice structure was calculated using the method described in Section 5.2.3. The length of the structure in the experiment, as seen in Figure 6.1, is significantly longer than the

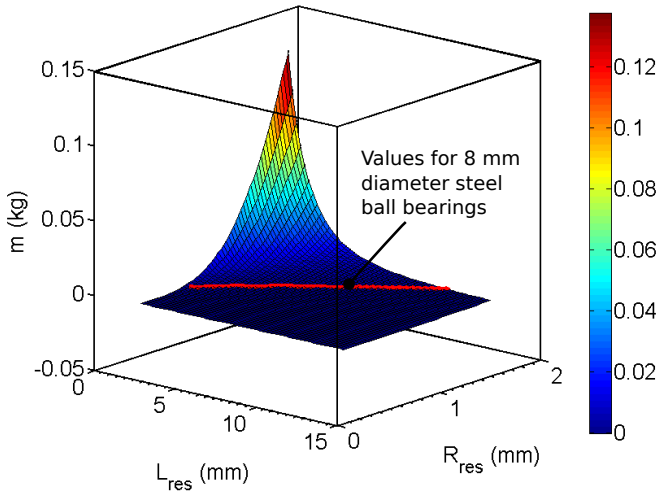



Figure 6.2: Surface showing values that gives the local resonators a natural frequency of 500 Hz.

width and thickness of the system and the wave propagation will propagate in one direction which is across the length of the structure. Therefore, the unit cell as shown in Figure 6.3 was used to find the band structure of the system in this study, where the points with the Bloch wave boundary conditions are also illustrated. Due to the lattice structure having a number of nodes that is much larger than 2, the wave superposition method developed in Chapter 3 cannot measure the band gaps within the structure accurately and was not used in this study.

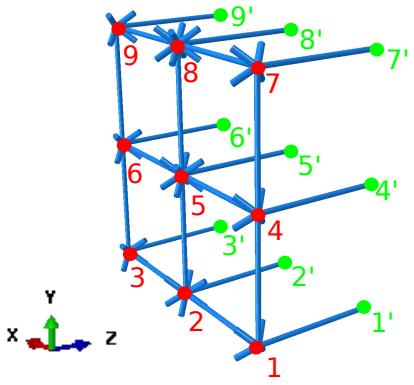



Figure 6.3: Unit cell used to calculate band structure where the nodes denoted by prime have Bloch wave periodic conditions.

The band structure of the system is shown in Figure 6.4. As seen in Figure 6.4 (a), the structure with the local resonators have a band gap of 476 to 579 Hz. However, no band gaps are present in the structure with no local oscillators in Figure 6.4 (b). This result demonstrates that the band gaps are produced by the addition of the local

resonators.

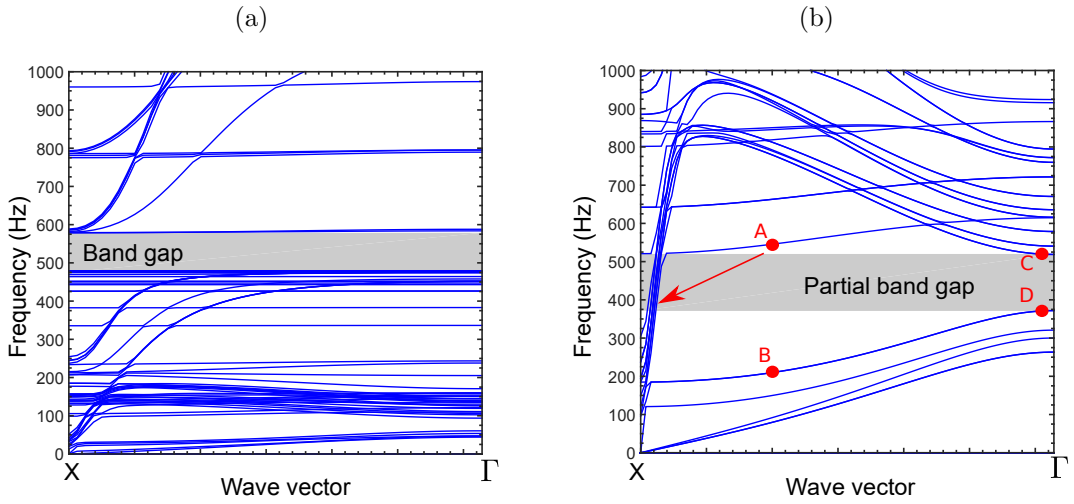


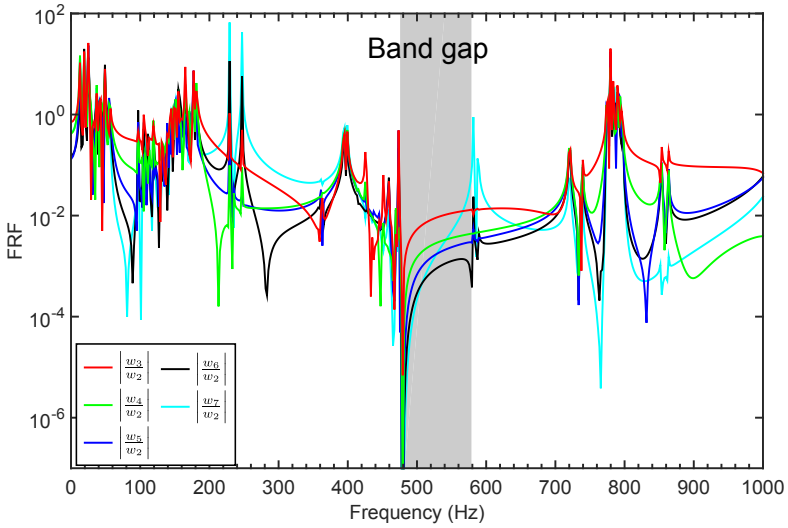

Figure 6.4: Band structure of structure (a) with local resonators (b) without local resonators.

Since an experiment was conducted to measure the frequency response function of the the structure, a finite element analysis was performed to calculate the frequency response function. The finite element model of the structure was made from Timoshenko beam elements and each strut was modelled by 20 elements. The boundary conditions for the model are shown in Figure 6.1, where the structure is free with a periodic force being applied at one end. The frequency response at the points shown in Figure 6.1 were calculated. The values at these points were also measured in the experiment. The finite element analysis was performed using commercial finite element software, Abaqus.

The frequency response functions of the structures calculated from the finite element models are plotted in Figure 6.5 and this result was used as a comparison with the experiments. As seen in Figure 6.5 (a), the frequency response function at the band gaps predicted in Figure 6.4 (a), are low compared to the other frequencies with the exception of the frequency response at the final node, $\left|\frac{w_7}{w_2}\right|$ which was caused by the wave being reflected back at the end of the structure. This demonstrates that the local resonators may be effective in attenuating vibrations. However, the addition of the resonators, that acts as dynamic absorbers, have also result in a larger number of resonator modes as seen with the large number of peaks at frequencies from 0 to 200 Hz in Figure 6.5 (a). These vibration modes may be detrimental to the structure in practical applications and should be considered while attempting to use local resonators to produce band gaps, while damping can be introduced to the dynamic absorbers to reduce the amplitudes at these resonances. These results will be compared further with the experimental results in Section 6.4.

Although there are no full band gaps predicted in the structure without the local

(a)




(b)

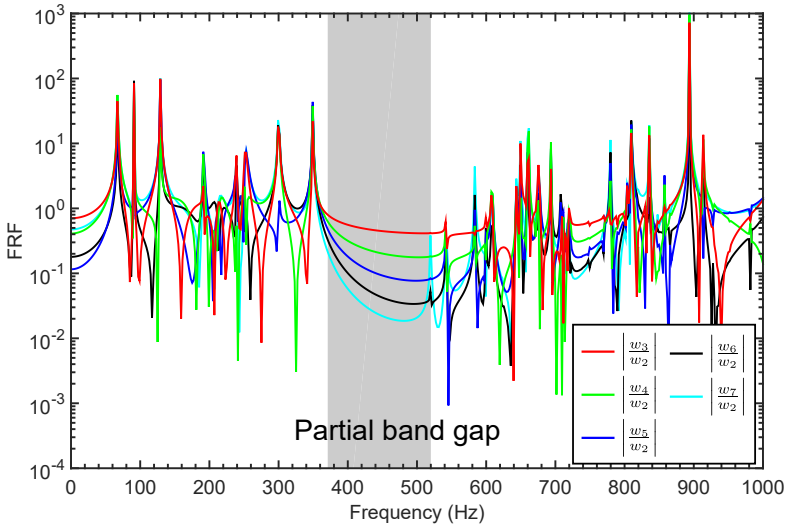



Figure 6.5: Frequency response functions from finite element calculations (a) with local resonators (b) without local resonators.

resonators, shown in Figure 6.4 (b), the frequency response at several ranges of frequencies, for example 371 to 520 Hz, in Figure 6.5 (b) are also low. The reason for this is because of the presence of partial band gaps. The Bloch modes of the structure for the different bands in Figure 6.4 (b) are shown in Figure 6.6. The mode shapes for the same band, for example the band with Points B and D in Figure 6.4 (b), are similar as seen in Figure 6.6 (b) and (d). Since for the bands in the partial band gap region of 371 to 520 Hz are for waves that do not propagate across the length of the structure, as shown in Figure 6.6 (a), where the amplitude of the Bloch wave at the end of the unit cell is negligible, these modes will not be excited with the loading conditions used in the finite element analysis leading to the low frequency response and hence the partial band gap. The partial band gaps will also be able to attenuate vibrations provided that the modes within these partial band gaps are not excited. Additionally, the partial band gap (371-520 Hz) was found to be larger to the band gap introduced by the local resonators (476-579 Hz), but it is important to point out that the partial band gap will only prevent the propagation of waves in the axial direction while a full band gap produced by the local resonators will prevent vibration from being transmitted in all directions.

## 6.3 Experimental set up

An experiment was performed in order to demonstrate that the presence of elastic band gaps are capable of attenuating vibrations. Two lattice structures, one with the local resonators and one without the local resonators, were tested in the experiment. The experiment was set up by hanging the structure onto a frame via wires while a shaker was used to excite one end of the structure. The point in which the shaker was attached to was designated as Point 1 and the subsequent points were designated with increasing numbers. The shaker was attached to the structure via a stinger, a load cell, and an aluminium plate. The aluminium plate was required as the load cell cannot be directly attached to the lattice structure directly because of its limited surface area. An accelerometer was then attached to the point of interest within the structure in order to measure the acceleration. The experimental setup is as shown in Figure 6.7.

A stepped sweep was performed by inputting a sinusoidal signal to the shaker from 100 to 1000 Hz, and the acceleration was measured with the accelerometer for a single point (Point 2). This is repeated until the acceleration for all the necessary points (Points 3 to 7) were measured.

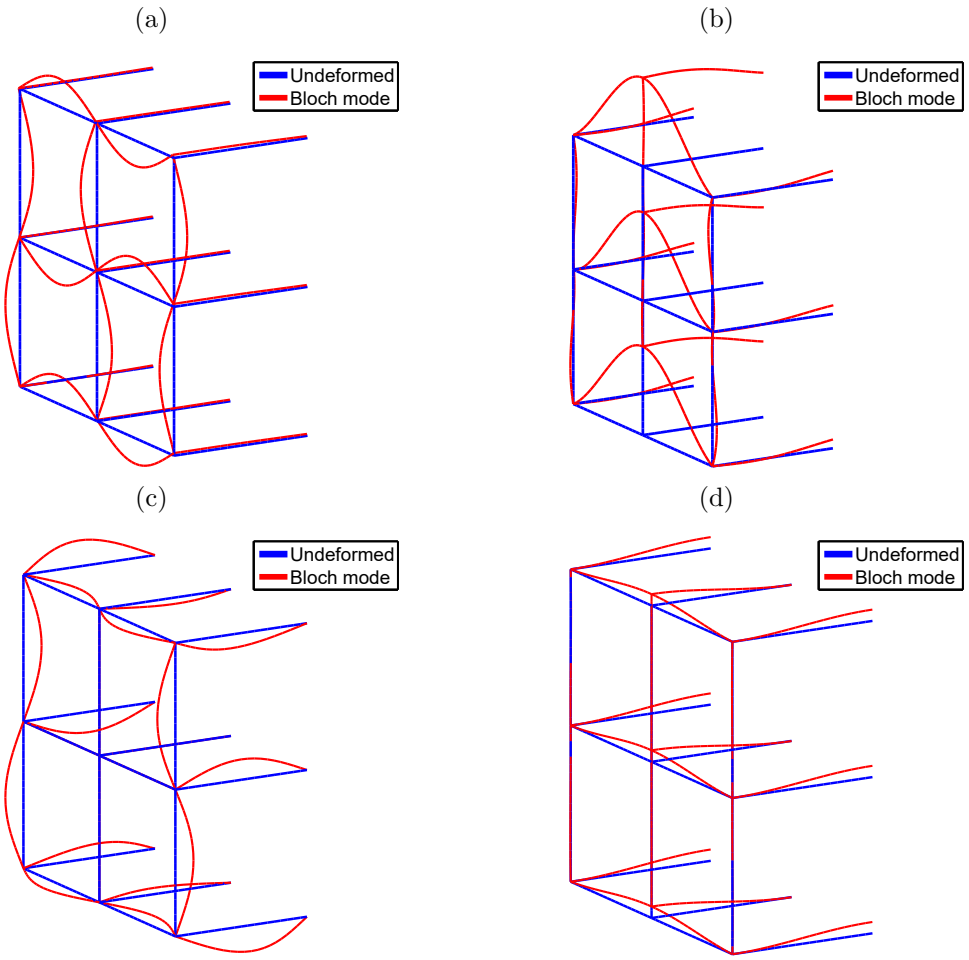



Figure 6.6: Bloch modes at the points shown in Figure 6.4 (a) Point A (b) Point B (c) Point C (d) Point D.

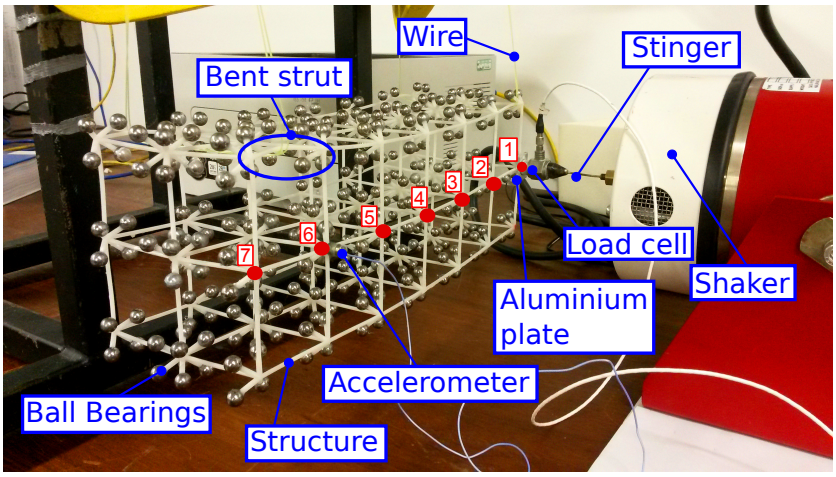



Figure 6.7: Experimental setup.

## 6.4 Results and discussion

The frequency response functions for the structure from the experiment are shown in Figure 6.8. The result in these figures differs from the predictions made using finite element analysis in Figure 6.5.

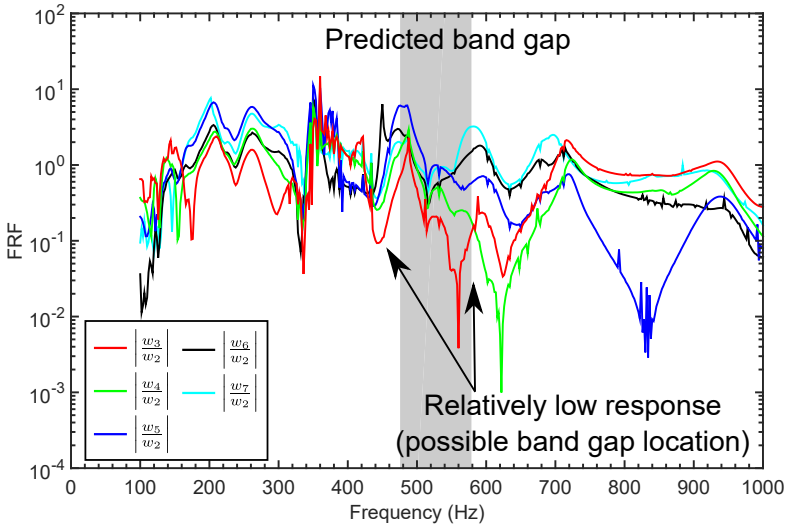
There are several possible reasons for the discrepancies. One possible reason is that the loading in the experiment on the structure was across an area with an aluminium plate, instead of the point force boundary conditions used in the finite element analysis. In addition, the struts at the points where the wires go through the structure for the structure with the local resonators have severely bent under the weight of the structure due to the addition of the masses, as seen in Figure 6.7. Furthermore, material damping that was not taken into account in the finite element analysis, which will lead to lower frequency responses, especially at higher frequencies of the structure with no local resonators in Figure 6.8 (b). Lastly, manufacturing defects, such as struts of different lengths for the local resonators and also broken struts may have also lead to the finite element analysis being different.

Despite the differences in the predictions using the finite element analysis, the band gap phenomenon does not apply specifically to a single mode and can attenuate vibrations across a range instead. Therefore, the structures should also be able to attenuate vibrations across the frequencies at the band gaps, although there are discrepancies in the finite element predictions that are sensitive to loading conditions.

Based on the results shown in Figure 6.8 (b), the frequency response of the structure without the local resonators appear to be low at the predicted partial band gaps. This result suggests that the low frequency response is likely to be caused by the partial band gap and that partial band gaps are capable of attenuating vibrations. The band gap phenomenon that attenuates vibrations based on frequency ranges instead of targeted modes has the benefit of not requiring accurate calculations of the structural modes and frequency response in the design of these systems. This facilitates the design process of the structures for vibration attenuation compared to other solutions, such as modifying the main structure to avoid resonances at given frequencies or active control.

Unfortunately, the frequency response function of the structure with the local resonators do not appear to have a clear region of frequencies with low frequency response, as seen in Figure 6.8 (a), including the region with the predicted band gap. Although there are several regions in Figure 6.8 (a) that appear to have lower magnitudes of vibration, it cannot be confirmed that this is due to the band gap phenomenon. The lack of a clear low response region can be attributed to manufacturing defects in the physical structure. Firstly, unlike the struts for the main structure, the struts for the local resonators have larger variations in lengths and similarly the ball bearings are also likely to have large variations in mass because these components were filed down, so that

(a)




(b)

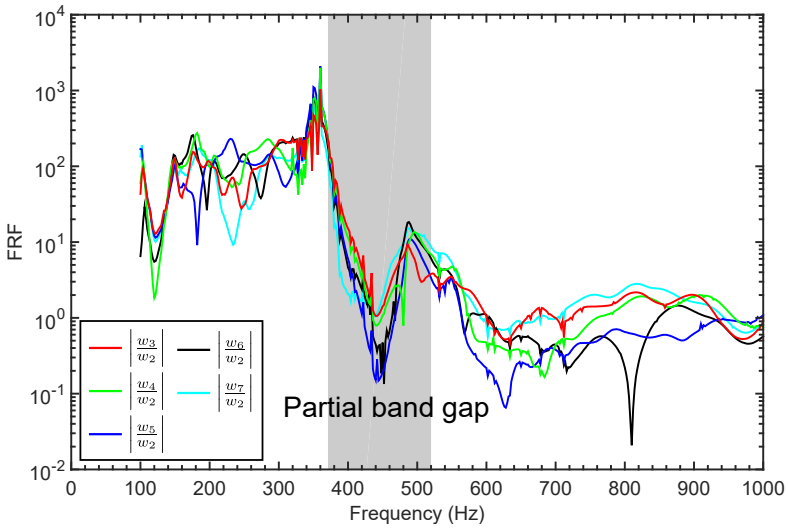



Figure 6.8: Frequency response functions from experiments (a) with local resonators (b) without local resonators, band gaps are predicted based on the finite element analysis.

they can be attached with adhesives. The amount of variation within the defects are not similar for different parts of the structure, which means that the structure is no longer periodic and the errors are expected to be large as the band gap calculations assumed that the structures are periodic. Additionally, the nodes where the struts intersect are also much larger and stiffer, especially when compared to the structure with no local resonators. The higher stiffness and size of the nodes were not accounted for in the finite element analysis. Lastly, the bent struts around the wires also leads to discontinuity in the loading conditions within the structure. These problems were less significant in the case of the structure with no local resonators that is considerably simpler in its design and have less variations in dimensions and mass as no parts requires filing or adhesives.

Although the variations in geometry and mass of the local resonators may result in a wider but less effective band gap, which could explain the regions with lower magnitudes of response in Figure 6.8 (a), this is likely to be ineffective as a solution for a structure with a limited number of unit cells. The problems faced during the structure with local resonators highlights one of the key issues with implementing periodic structures for vibration attenuation, which is the manufacturing process. Although current rapid prototyping technologies are capable of printing three dimensional lattice structure, the technology to manufacture these structures with stiffer materials, such as steel or titanium, is still not widely available. Additionally, further improvements can be made to manufacturing techniques to allow the printing of multiple materials as there is a requirement to use different materials, especially when the local resonators have slightly higher mass.

Finally, the findings in this study have also shown that even though the local resonators can be used to create band gaps at desired locations easily, manufacturing the parts with local resonators might be difficult. Therefore, it is more beneficial to design the lattice structure to have band gaps via the Bragg scattering effect when possible. This is because Bragg scattering that does not require local resonators are easier to produce and are less prone to manufacturing defects. Since partial band gaps can be used to attenuate vibrations when several Bloch modes are not excited, it is useful to evaluate for the Bloch modes, while calculating the band structure to take advantage of this.

## 6.5 Summary and conclusion

Two simple cubic periodic lattice structures, one with local resonators and one without local resonators, were designed, manufactured, and tested in this study in order to demonstrate that the band gap phenomenon can be used to attenuate vibrations. The periodic lattice structures were made from ABS and manufactured using SLA. The geometry of the main portion of the structures were determined from the findings in

Chapter 5 and the key parameters of the local resonators, which is a strut with a ball bearing attached to one end, were determined by finding the natural frequency of its first mode. The location of the band gap was targeted to be 500 Hz. The band structure was calculated and finite element analyses were performed to show that the structure have band gaps at this region prior to the manufacture of the structures. Additionally, the structure without the local resonators was found to possess a partial band gap that can also be used to attenuate vibrations.

The manufactured structures were then hung freely from a structure with wires and a shaker was attached to one end and a stepped sweep was performed. The frequency response functions at regular intervals were measured using an accelerometer. The discrepancies between the measured frequency response function and the results of the finite element analysis were attributed to the difference in boundary conditions and manufacturing defects. However, since the band gap phenomenon attenuates vibrations independently from the vibration modes of the structure, the band gaps should still appear within the finite structure. This was observed for the structure without the local resonators, where the frequency response at the predicted band gap is lower at the partial band gap. However, no obvious low vibration regions were found for the structure with the local resonators, including the predicted band gap region. The likely cause for this is the simplifications made during the analysis, the variations in strut length and masses of the local resonators, and severe bending of the struts. These issues were less significant for the structure without the local resonators that is much simpler.

The problems encountered in this study have suggested that the manufacturing techniques to produce accurate lattice structures should be a focus in this field, so that structures with band gaps can be produced using local resonators. Additionally, if possible the Bragg scattering effect, which does not require the use of local resonators, should be used instead as structures without the local resonators are easier to manufacture. Lastly, the partial band gaps can also be used to attenuate vibrations. Hence, calculating the Bloch modes to locate these band gaps can further improve the performance of these structures.

# 7 Conclusions and future work

## 7.1 Summary and conclusion

Vibrations are a major issue in engineering, as they cause a variety of problems including structural damage and fatigue. Due to weight reduction and load bearing requirements, structural components today have been designed to be light and stiff. However, high damping and vibration attenuation are commonly associated with materials that have moderate to low stiffness, making them unsuitable for structural component applications [3]. Among the different types of lightweight structural, periodic lattice structures can be designed to have elastic band gaps that are capable of preventing the transmission of vibrations within a range of frequencies via the Bragg scattering or local resonance mechanism. Although many studies have been performed on the elastic band gaps and the static mechanical properties of periodic structures, not many studies have been conducted on both of these properties in tandem. The work done in this thesis aims to develop techniques and perform analyses to promote the implementation of periodic lattices in practical applications to have both excellent static mechanical properties and the ability to attenuate vibrations.

Firstly, a literature review has been performed on the techniques used to calculate the band structure in order to determine the width and location of the band structures. Key techniques found in the literature are the plane wave expansion (PWE) method, extended plane wave expansion (EPWE) method, the finite element method (FEM), transfer matrix (TM) method, and finite difference time domain (FDTD) method. The majority of these methods make use of the Bloch wave theory by either applying Bloch wave boundary conditions or expanding the stress and strain fields in terms of Bloch waves within the material constitutive equations and then reformulating the equations into an eigenvalue problem. Solving the eigenvalue problem will give the band structure of the system. Additionally, each of these methods comes with their respective benefits and disadvantages. For example, the PWE and EPWE methods have a theoretical basis but they may be badly conditioned and are affected by the Gibbs phenomenon. Additionally, the expansion of the stiffness and density terms may not be easily found when the structures are complicated. On the other hand, the FEM is simple to apply and can be used for complicated structures but it has the common problems associated with FEM, such as discretisation errors. The finite time domain method can be used to

overcome the badly conditioned problems with PWE and EPWE, but is computationally expensive.

A common characteristic with all the methods to determine the band structure found in the literature with the exception of the two dimensional Fourier transform, is that all these techniques require a model for the material. Therefore, these methods cannot be used to determine the band structure from experimental measurements. Although the two dimensional Fourier transform can be used to measure the band structure, it requires equipment with high temporal and spatial resolution. Therefore, there is an imperative to develop a method to measure the band structure using very simple equipment.

In addition to the techniques for calculating the band structure, homogenisation techniques to determine the effective mechanical properties, mainly strength and stiffness, of periodic structures have also been reviewed. The homogenisation techniques can be separated into a few categories: analytical methods, matrix based techniques, asymptotic homogenisation, and discrete homogenisation.

A method to determine the band structure of periodic structures using only the responses from a limited number of points was developed. The technique was named the wave superposition method (WSM) as it is based on the superposition of Bloch waves and it does not require knowledge of the material properties. The response of a one dimensional finite periodic structure is the sum of Bloch waves and can be separated into a forward moving wave and a reverse wave. By exploiting the superposition principle, the relationship between the response at every node can be found and the equations for the band structure were determined by eliminating the unknowns using these relationships. A numerical study using the analytical solutions of a Timoshenko beam was used to validate the technique and the band structure calculated using the WSM and transfer matrix were found to be identical. The WSM was also extended to determine the frequency response of the beams from the band structure and the response at only two points of the system. After that, an attempt was made to extend the method for materials with more dimensions. The WSM was found to be accurate for lower bands but has a larger scatter and errors for higher bands. Furthermore, the WSM can only measure a portion of the dispersion surface for materials with more dimensions and this depends on the boundary conditions. Despite these limitations, the WSM is the only method that can measure the imaginary part of the band structure from experiments and can be useful in the study of periodic structures with damping.

An experiment was then performed to measure the band structure of periodic structures with the WSM to validate the method. Two beams, a bi-material beam and an aluminium beam with varying widths were tested. The beams were hung freely from a structure and one end of the structure was excited with a shaker. A stepped sweep was performed, and the acceleration at regular intervals of the beam were measured using

a single accelerometer. The frequency response functions of the beams were found to agree with the analytical solutions with the exception of regions around the natural frequencies of the torsional modes. Since beam bending is composed of two coupled waves, the WSM measured two sets of waves where one set of waves is mainly evanescent and the other set is mainly propagating wave. The band structure measured using WSM was found to be fairly accurate for the bands of the propagating waves but the measured band structure for the evanescent waves are noisy and inaccurate. The inaccuracies in the evanescent waves were attributed to the WSM being very sensitive to noise and the effects of the torsional modes being measured by the accelerometer. This result highlights a key issue with the WSM, which is its inability to reject errors. However, as the band gaps are only determined from the lack of a propagating wave, the bands for the evanescent waves can be neglected. Additionally, the frequency response of all the nodes of the beams were predicted using the measured band structure and the frequency response at two points of the beam. The predicted results are overall accurate with the exception of regions around the torsional modes, where the band structure was inaccurate. The results from the experiments agree well with the analytical results and validated the WSM.

A parametric study to determine the optimal geometric parameters to give the a periodic lattice structure that will have excellent properties and band gaps was also performed. The relationship of the normalised specific stiffness and strength properties with the normalised geometric properties for four different cubic lattice topologies: simple cubic, BCC, FCC, and regular octet, was first studied. The relationship for the stiffness is straightforward, where the normalised stiffness parameter was found to increase with the radius, $r_1$, of the member struts for all topologies.

In general, the normalised stiffness parameter was found to increase with the radius, $r_1$, of the member struts for all topologies. On the other hand, the periodic lattices were considered to have failed when the struts yield or buckle. The lattice structure was found to have higher yield strengths with increasing radius of the main struts, $r_1$, and decreasing radius of the diagonal struts. Conversely, the opposite trend was found for the buckling strength for all topologies with the exception of the octet truss that does not buckle. The optimal topology for the strength was the value when the yield and buckling strengths are equal. The optimal topology and geometric parameters to give the optimal static properties were found based on this analysis. After that, local resonators, in the form of cantilever beams with a mass attached, tuned to give band gaps at 500 Hz, were added to the optimal lattices. The trends of the local resonator parameters, which are the lengths, radius, and added mass, on the band gap width and increase in density of the materials were found. The study showed that the local resonators will increase the density of the lattice structure significantly, and therefore the addition of these are only sensible when the stiffness and strength parameters with the

local resonators is still higher than that of the bulk materials. Furthermore, some of the topologies have produced band gaps at the desired frequency when no local resonators were added. These band gaps were produced via the Bragg scattering effect and since it does not increase the density of the material, it is the preferred method of producing band gaps when lightweight applications are required.

Lastly, two periodic lattices, one with local resonators and one without local resonators, were designed and manufactured using the findings in the previous analysis. The lattice structures were tested in order to demonstrate the presence of the elastic band gaps and assess their ability to attenuate vibrations. The periodic lattice structures were manufactured using SLA and the struts were made of ABS, while steel ball bearings were used as the masses of the local oscillators. The structures were designed to have a band gap around 500 Hz and the band structures found using finite element analysis showed that the structure with the local resonators has a full band gap at 475.6 to 578.7 Hz and the structure without the local resonators has a partial band gap at 371 to 520 Hz. The experiments conducted to measure the frequency response of the lattice structures were identical to the experiment performed to validate the WSM. The measured response of the lattice structure without local resonators have low amplitudes at the predicted partial band gaps, validating the presence of band gaps. On the other hand, there are no clear region with low amplitudes of vibrations, including the predicted band gap frequencies for the structure with the local resonators. The likely cause of this is the variations in the strut lengths and mass of the local oscillators as these parts were filed down so that they can be attached with adhesives. This problem is made further severe by the low number of unit cells within the lattice structure of 7. Additionally, simplifications in the model that treat the ball bearings as a point mass may also lead to discrepancies with the results. The issues faced for the structure with local resonators highlighting a key issue in the implementation of the periodic lattice structures in practice, which is the requirement of accurate manufacturing and joining. Therefore, there is a need to improve rapid prototyping techniques to facilitate the implementation of the concept of using periodic lattice structures to attenuate vibrations. Lastly, partial band gaps can also be used to attenuate vibrations and may be advantageous if the partial band gaps do not require the addition of local resonators, as this would lead to a lighter structure and a structure that can be produced more accurately.

In summary, the techniques and findings in this thesis have laid the foundations for future development of periodic lattice structures for combined lightweight structural and vibration isolation applications. The WSM will simplify the experimental measurement of the band structure, encouraging more research to be conducted in this field. Additionally, the parametric study to determine the effects of geometrical parameters on the static and dynamic performance of lattice structures can be used as a guideline in the design of such structures and may serve as a framework for similar analysis with

other topologies. The experiments have also demonstrated that these periodic lattice structures can effectively isolate vibrations. Lastly, since the concept of using periodic lattice structures for both vibration attenuation and structural applications is relatively new, there is a lot of room for development of the concept. The techniques and analysis performed in this thesis can also be improved further. This possible future work to be done on this topic will be discussed next.

## 7.2 Suggestions for future work

There are several suggestions for future work to be built upon the work done in this thesis. One of the key contributions in this thesis is the WSM developed in Chapter 3. Firstly, the WSM allows for the measurements of band structure including the imaginary part of the band structure. Since there is significant interest in the effects of damping on the band gaps in phononic crystals and elastic metamaterials, many studies [99, 100, 188] have performed analyses on this topic, but only a small portion of them are experimental. The WSM will allow experiments to be performed on phononic crystals and metamaterials composed of materials with damping, allowing comparisons between the band structure from analytical models and experimental measurements. Additionally, the WSM can be used to study the band structure of complicated structures and compare analytical models with actual systems.

Although, the WSM will be significantly more useful if it can be extended for periodic materials with more dimensions but as discussed in Section 3.5, the full dispersion surface or volume of the band structure cannot be measured from the response of a finite structure as only a part of the band structure will be measured. However, part of the dispersion curve for structures with two and three dimensions can be measured by aligning these structures in a single line. However, the WSM in Chapter 3 was developed for cases with two sets of waves and when applied to structures with more than two sets of waves, the measured band structure will have errors and scatter. Therefore, the WSM can be extended to more than two set of waves using the same framework in Chapter 3. This task is not trivial as the equations becomes significantly more complicated with each additional wave. The WSM will be more accurate when more waves are taken into account.

Apart from that, from the experiment performed in Chapter 4, it was discovered that band structure measured with the WSM is noisy for the evanescent waves. This is a result of the equations being fully determined and a small error in the response function results in a large error in the calculated band structure. Therefore, the technique can be improved by taking more measurement points and modifying the method using regression analysis. This will allow for the WSM to reject errors in the measurements and give better measurements of the band structure.

Furthermore, in Chapter 5 the parametric studies were performed for periodic cubic lattices and the effects of varying the geometrical parameters on the static and dynamic characteristics of the cubic lattices were found. However, there are many other topologies for the lattice structures and the same analysis can be performed for structures with other topologies using the steps described in Chapter 5. The analysis in Chapter 5 can also be extended to include material damping to also study the effects of damping on the band structures.

Lastly, the experiment in Chapter 6 has also pointed out a key problem with implementing periodic structures for vibration attenuation, which is current manufacturing processes are unable to produce complicated structures accurately and cost effectively. Therefore, further development in rapid prototyping technologies are needed to aid the implementation of periodic lattice structures for structural and vibration attenuation applications. As mentioned in Chapter 6, periodic structures with band gaps may be made from multiple materials and rapid prototyping processes, such as the one in [222], can be further developed to produce elastic metamaterials properly.

# Bibliography


[1] D. J. Inman, *Engineering Vibration*, 2nd ed. Upper Saddle River, New Jersey: Pearson Education, 2001.

[2] E. Baravelli, M. Carrara, and M. Ruzzene, "High stiffness, high damping chiral metamaterial assemblies for low-frequency applications," *Proc. SPIE 8695, Health Monitoring of Structural and Biological Systems*, 2013.

[3] E. Baravelli and M. Ruzzene, "Internally resonating lattices for bandgap generation and low-frequency vibration control," *Journal of Sound and Vibration*, vol. 332, no. 25, pp. 6562–6579, 2013.

[4] R. Ibrahim, "Recent advances in nonlinear passive vibration isolators," *Journal of Sound and Vibration*, vol. 314, no. 3-5, pp. 371–452, 2008.

[5] K. Wilde, P. Gardoni, and Y. Fujino, "Base isolation system with shape memory alloy device for elevated highway bridges," *Engineering Structures*, vol. 22, no. 3, pp. 222–229, 2000.

[6] R. DesRoches, J. McCormick, and M. Delemont, "Cyclic Properties of Superelastic Shape Memory Alloy Wires and Bars," *Journal of Structural Engineering*, vol. 130, no. 1, pp. 38–46, 2004.

[7] M. Dolce, D. Cardone, and R. Marnetto, "Implementation and testing of passive control devices based on shape memory alloys," *Earthquake Engineering and Structural Dynamics*, vol. 29, no. 7, pp. 945–968, 2000.

[8] M. D. Rao, "Recent applications of viscoelastic damping for noise control in automobiles and commercial airplanes," *Journal of Sound and Vibration*, vol. 262, no. 3, pp. 457–474, 2003.

[9] J. Soovere and M. Drake, "Aerospace Structures Technology Damping Design Guide. Volume 2. Design Guide," Air Force Wright Aeronautical Laboratories, Dayton, Tech. Rep., 1985.

[10] P. Gardonio, "Review of Active Techniques for Aerospace Vibro-Acoustic Control," *Journal of aircraft*, vol. 39, no. 2, pp. 206–214, 2002.

[11] J. Scheuren, "Active Control of Sound and Vibrations," in *Handbook of Engineering Acoustics*, G. Muller and M. Moser, Eds., Berlin, 2013, pp. 301–334.

[12] T. Gorishnyy, M. Maldovan, C. Ullal, and E. Thomas, "Sound ideas," *Physics World*, 2005.

[13] L. Brillouin, *Wave Propagation In Periodic Structures*. McGraw-Hill Book Company, 1946.

[14] D. Mead, "Wave Propagation in Continuous Periodic Structures: Research Contributions From Southampton, 1964 to 1995," *Journal of Sound and Vibration*, vol. 190, no. 3, pp. 495–524, 1996.

[15] Y. Xiao, J. Wen, and X. Wen, "Flexural wave band gaps in locally resonant thin plates with periodically attached springmass resonators," *Journal of Physics D: Applied Physics*, vol. 45, no. 19, p. 195401, 2012.

[16] P. Sheng, X. Zhang, Z. Liu, and C. Chan, "Locally resonant sonic materials," *Physica B: Condensed Matter*, vol. 338, no. 1-4, pp. 201–205, 2003.

[17] H. von Helmholtz and A. J. Ellis, *On the Sensations of Tone as a Physiological Basis for the Theory of Music*. Longmans, Green, 1885.

[18] J. J. Keller and E. Zauner, "On the use of Helmholtz resonators as sound attenuators," *ZAMP Zeitschrift für angewandte Mathematik und Physik*, vol. 46, no. 3, pp. 297–327, 1995.

[19] J. B. Pendry, A. J. Holden, D. J. Robbins, and W. J. Stewart, "Magnetism from conductors and enhanced nonlinear phenomena," *IEEE Transactions on Microwave Theory and Techniques*, vol. 47, no. 11, pp. 2075–2084, 1999.

[20] Z. Liu, X. Zhang, Y. Mao, Y. Zhu, Z. Yang, C. Chan, and S. Ping, "Locally Resonant Sonic Materials," *Science*, vol. 289, pp. 1734–1736, 2000.

[21] Y. L. Xu, C. Q. Chen, and X. G. Tian, "Wave Characteristics of Two-Dimensional Hierarchical Hexagonal Lattice Structures," *Journal of Vibration and Acoustics*, vol. 136, no. 1, p. 011011, 2013.

[22] W. Liu, J. W. Chen, and X. Y. Su, "Local resonance phononic band gaps in modified two-dimensional lattice materials," *Acta Mechanica Sinica*, vol. 28, no. 3, pp. 659–669, 2012.

[23] M. J. Leamy, "Exact wave-based Bloch analysis procedure for investigating wave propagation in two-dimensional periodic lattices," *Journal of Sound and Vibration*, vol. 331, no. 7, pp. 1580–1596, 2012.

[24] L. Raghavan and S. Phani, "Bandgap formation mechanisms in periodic materials and structures," in *Proceedings of Meetings on Acoustics*, vol. 19, Montreal, 2013, p. 045021.

[25] A. Phani, J. Woodhouse, and N. Fleck, "Wave propagation in two-dimensional periodic lattices," *The Journal of the Acoustical Society of America*, vol. 119, no. 4, p. 1995, 2006.

[26] Y. Liu, X. Z. Sun, W. Z. Jiang, and Y. Gu, "Tuning of Bandgap Structures in Three-Dimensional Kagome-Sphere Lattice," *Journal of Vibration and Acoustics*, vol. 136, no. 2, p. 021016, 2014.

[27] E. Dragoni, "Optimal mechanical design of tetrahedral truss cores for sandwich constructions," *Journal of Sandwich Structures and Materials*, vol. 15, no. 4, pp. 464–484, 2013.

[28] J.-E. Choi, G.-D. Ko, and K.-J. Kang, "Taguchi method-based sensitivity study of design parameters representing specific strength of wire-woven bulk Kagome under compression," *Composite Structures*, vol. 92, no. 10, pp. 2547–2553, 2010.

[29] A. Vigliotti and D. Pasini, "Stiffness and strength of tridimensional periodic lattices," *Computer Methods in Applied Mechanics and Engineering*, vol. 229, pp. 27–43, 2012.

[30] R. A. W. Mines, "On the Characterisation of Foam and Micro-lattice Materials used in Sandwich Construction," *Strain*, vol. 44, no. 1, pp. 71–83, 2008.

[31] V. Deshpande, N. Fleck, and M. Ashby, "Effective properties of the octet-truss lattice material," *Journal of the Mechanics and Physics of Solids*, vol. 49, pp. 1747–1769, 2001.

[32] J. Wallach and L. Gibson, "Mechanical behavior of a three-dimensional truss material," *International Journal of Solids and Structures*, vol. 38, no. 40-41, pp. 7181–7196, 2001.

[33] E. Ptochos and G. Labeas, "Elastic modulus and Poissons ratio determination of micro-lattice cellular structures by analytical, numerical and homogenisation methods," *Journal of Sandwich Structures and Materials*, vol. 14, no. 5, pp. 597–626, 2012.

[34] ——, "Shear Modulus Determination of Cuboid Metallic Open-Lattice Cellular Structures by Analytical, Numerical and Homogenisation Methods," *Strain*, vol. 48, no. 5, pp. 415–429, 2012.

[35] F. Scarpa, M. Ouisse, M. Collet, and K. Saito, "Kirigami Auxetic Pyramidal Core: Mechanical Properties and Wave Propagation Analysis in Damped Lattice," *Journal of Vibration and Acoustics*, vol. 135, no. 4, p. 041001, 2013.

[36] X. Liu, G. Hu, C. Sun, and G. Huang, "Wave propagation characterization and design of two-dimensional elastic chiral metacomposite," *Journal of Sound and Vibration*, vol. 330, pp. 2536–2553, 2011.

[37] M. I. Hussein, M. J. Leamy, and M. Ruzzene, "Dynamics of Phononic Materials and Structures: Historical Origins, Recent Progress, and Future Outlook," *Applied Mechanics Reviews*, vol. 66, no. 4, p. 040802, 2014.

[38] J. Rayleigh, *The Theory of Sound. Volume 1.* New York: Dover Publications, 1945.

[39] J. W. Miles, "Vibrations of beams on many supports," *Journal of the Engineering Mechanics Division*, vol. 82, no. 1, pp. 1–9, 1956.

[40] M. Heckl, "Investigations on the Vibrations of Grillages and Other Simple Beam Structures," *The Journal of the Acoustical Society of America*, vol. 36, no. 7, pp. 1335–1343, 1964.

[41] E. E. Ungar, "Steady-State Responses of One-Dimensional Periodic Flexural Systems," pp. 887–894, 1966.

[42] R. Martínez-Sala, J. Sancho, J. V. Sánchez, V. Gómez, J. Llinares, and F. Meseguer, "Sound attenuation by sculpture," *Nature*, vol. 378, no. 6554, pp. 241–241, 1995.

[43] J. Wen, G. Wang, D. Yu, H. Zhao, and Y. Liu, "Theoretical and experimental investigation of flexural wave propagation in straight beams with periodic structures: Application to a vibration isolation structure," *Journal of Applied Physics*, vol. 97, no. 11, p. 114907, 2005.

[44] S. M. Jeong and M. Ruzzene, "Experimental Analysis of Wave Propagation in Periodic Grid-like Structures," *Proceedings of the SPIE*, vol. 5760, no. 404, pp. 518–525, 2005.

[45] Y. Gao, F. Sui, and S. Daley, "Elastic metamaterials with local resonances for broadband vibration isolation," in *First Euro-Mediterranean Conference on Structural Dynamics and Vibroacoustics*, Marrakech, 2013, pp. 23–26.

[46] H. Sun, X. Du, and F. Pai, "Theory of Metamaterial Beams for Broadband Vibration Absorption," *Journal of intelligent material systems and structures*, vol. 21, no. 11, pp. 1085–1101, 2010.

[47] Z.-J. Wu, Y.-Z. Wang, and F.-M. Li, "Analysis on band gap properties of periodic structures of bar system using the spectral element method," *Waves in Random and Complex Media*, vol. 23, pp. 349–372, 2013.

[48] J. Wen, G. Wang, D. Yu, H. Zhao, and Y. Liu, "Vibration isolation structure with the idea of phononic crystals," in *The Thirteenth International Congress on Sound and Vibration*, J. Eberhardsteiner, H. A. Mang, and H. Waubke, Eds., Vienna, 2006.

[49] F. H. D. Policarpo, "Numerical and experimental models for vibration attenuation using cork composite materials," Ph.D. dissertation, Universidade de Lisboa, 2013.

[50] H. Policarpo, "A steel-composition cork phononic device for low frequency vibration isolation," *II LAETA Young Researchers Meeting, Porto, April 2012*, 2012.

[51] R. Zhu, X. Liu, G. Hu, C. Sun, and G. Huang, "A chiral elastic metamaterial beam for broadband vibration suppression," *Journal of Sound and Vibration*, vol. 333, no. 10, pp. 2759–2773, 2014.

[52] A. Spadoni, M. Ruzzene, S. Gonella, and F. Scarpa, "Phononic properties of hexagonal chiral lattices," *Wave Motion*, vol. 46, no. 7, pp. 435–450, 2009.

[53] X. Liu, Y. Wang, Y. Wang, and C. Zhang, "Wave propagation in a sandwich plate with a periodic composite core," *Journal of Sandwich Structures and Materials*, vol. 16, no. 3, pp. 319–338, 2014.

[54] Y. F. Wang and Y. S. Wang, "Complete Bandgap in Three-Dimensional Holey Phononic Crystals With Resonators," *Journal of Vibration and Acoustics*, vol. 135, no. 4, p. 041009, 2013.

[55] J. F. Abel, J. R. Cooke, G. M. Hulbert, E. Dede, C. Yilmaz, Z. D. Ma, and N. Kikuchi, "Analysis and design of materials and structures for attenuating vibration and acoustic response," in *Proceedings of the 6th International Conference on Computation of Shell and Spatial Structures*, J. F. Abel and J. R. Cooke, Eds., New York, 2008, pp. 1–4.

[56] M. I. Hussein, K. Hamza, G. M. Hulbert, and K. Saitou, "Optimal synthesis of 2D phononic crystals for broadband frequency isolation," *Waves in Random and Complex Media*, vol. 17, no. 4, pp. 491–510, 2007.

[57] M. I. Hussein, "Tailoring of two-dimensional band-gap materials for broadband frequency isolation," in *Proceedings of the ASME 2007 International Design Engineering Technical Conferences & Computers and Information in Engineering Conference*, Las Vegas, 2007.

[58] Z. B. Cheng, Y. Q. Yan, F.-y. Menq, Y. L. Mo, H. J. Xiang, Z. F. Shi, and K. H. Stokoe, "3D Periodic Foundation-based Structural Vibration Isolation," in *Proceedings of the World Congress on Engineering*, vol. 3, London, 2013.

[59] Z. Cheng and Z. Shi, "Novel composite periodic structures with attenuation zones," *Engineering Structures*, vol. 56, pp. 1271–1282, 2013.

[60] P. Wang, J. Shim, and K. Bertoldi, "Effects of geometric and material nonlinearities on tunable band gaps and low-frequency directionality of phononic crystals," *Physical Review B*, vol. 88, no. 1, p. 014304, 2013.

[61] S. Chen, G. Wang, J. Wen, and X. Wen, "Wave propagation and attenuation in plates with periodic arrays of shunted piezo-patches," *Journal of Sound and Vibration*, vol. 332, no. 6, pp. 1520–1532, 2013.

[62] H. Zhang, J.-H. Wen, S.-B. Chen, G. Wang, and X.-S. Wen, "Flexural wave band-gaps in phononic metamaterial beam with hybrid shunting circuits," *Chinese Physics B*, vol. 24, no. 3, p. 036201, 2015.

[63] F. Tateo, B. S. Beck, M. Collet, M. Ouisse, K. a. Cunefare, and M. N. Ichchou, "Vibration control of plates through a periodic array of shunted piezoelectric patches with negative capacitance circuits," *Active and Passive Smart Structures and Integrated Systems*, vol. 9057, p. 90572E, 2014.

[64] Y. Z. Wang, F. M. Li, K. Kishimoto, Y. S. Wang, and W. H. Huang, "Elastic wave band gaps in magnetoelectroelastic phononic crystals," *Wave Motion*, vol. 46, no. 1, pp. 47–56, 2009.

[65] O. Bou Matar, J. F. Robillard, J. O. Vasseur, A. C. Hladky-Hennion, P. A. Deymier, P. Pernod, and V. Preobrazhensky, "Band gap tunability of magneto-elastic phononic crystal," *Journal of Applied Physics*, vol. 111, no. 5, p. 054901, 2012.

[66] A. Bayat and F. Gordaninejad, "Dynamic response of a tunable phononic crystal under applied mechanical and magnetic loadings," *Smart Materials and Structures*, vol. 24, no. 6, p. 065027, 2015.

[67] B. S. Beck, "Negative capacitance shunting of piezoelectric patches for vibration control of continous systems," Ph.D. dissertation, Georgia Institute of Technology, 2012.

[68] S. Asiri, "Tunable mechanical filter for longitudinal vibrations," *Shock and Vibration*, vol. 14, pp. 377–391, 2007.

[69] M. Reynolds and S. Daley, "An active viscoelastic metamaterial for isolation applications," *Smart Materials and Structures*, vol. 23, no. 4, p. 045030, 2014.

[70] C. Yilmaz, G. Hulbert, and N. Kikuchi, "Phononic band gaps induced by inertial amplification in periodic media," *Physical Review B*, vol. 76, no. 5, p. 054309, 2007.

[71] G. Acar and C. Yilmaz, "Experimental and numerical evidence for the existence of wide and deep phononic gaps induced by inertial amplification in two-dimensional solid structures," *Journal of Sound and Vibration*, vol. 332, no. 24, pp. 6389–6404, 2013.

[72] S. Taniker and C. Yilmaz, "Phononic gaps induced by inertial amplification in BCC and FCC lattices," *Physics Letters A*, vol. 377, pp. 1930–1936, 2013.

[73] J. Yin, J. Huang, S. Zhang, H. Zhang, and B. Chen, "Ultrawide low frequency band gap of phononic crystal in nacreous composite material," *Physics Letters A*, vol. 378, no. 32-33, pp. 2436–2442, 2014.

[74] J. Yin, H. Peng, S. Zhang, H. Zhang, and B. Chen, "Design of nacreous composite material for vibration isolation based on band gap manipulation," *Computational Materials Science*, vol. 102, pp. 126–134, 2015.

[75] H. Xiuchang, J. Aihua, Z. Zhiyi, and H. Hongxing, "Design and optimization of periodic structure mechanical filter in suppression of foundation resonances," *Journal of Sound and Vibration*, vol. 330, no. 20, pp. 4689–4712, 2011.

[76] A. Gupta, "A review on sonic crystal, its applications and numerical analysis techniques," *Acoustical Physics*, vol. 60, no. 2, pp. 223–234, 2014.

[77] J. O. Vasseur, P. A. Deymier, A. Sukhovich, B. Merheb, A. C. Hladky-Hennion, and M. I. Hussein, "Phononic Band Structures and Transmission Coefficients: Methods and Approaches," in *Acoustic Metamaterials and Phononic Crystals*, Berlin, 2013, pp. 329–372.

[78] M. S. A. Elsayed, "The Blochs Theorem," *Technical Report No. TR-MDOG-09-01. McGill University.*, pp. 1–35, 2009.

[79] L. Junyi and D. Balint, "An inverse method to determine the dispersion curves of periodic structures based on wave superposition," *Journal of Sound and Vibration*, vol. 350, pp. 41–72, 2015.

[80] M. Sigalas and E. Economou, "Elastic and acoustic wave band structure," *Journal of Sound and Vibration*, vol. 158, no. 2, pp. 377–382, 1992.

[81] ——, "Band structure of elastic waves in two dimensional systems," *Solid State Commun.*, vol. 86, no. 3, p. 141, 1993.

[82] M. Kushwaha and P. Halevi, "Acoustic band structure of periodic elastic composites," *Physical Review Letters*, vol. 71, no. 13, pp. 2022–2025, 1993.

[83] Y. Li, J. Chen, X. Han, K. Huang, and J. Peng, "Large complete band gap in two-dimensional phononic crystal slabs with elliptic inclusions," *Physica B: Condensed Matter*, vol. 407, no. 8, pp. 1191–1195, 2012.

[84] Y. Wang, F. Li, Y. Wang, K. Kishimoto, and W. Huang, "Tuning of band gaps for a two-dimensional piezoelectric phononic crystal with a rectangular lattice," *Acta Mechanica Sinica*, vol. 25, no. 1, pp. 65–71, 2008.

[85] H. Pichard, O. Richoux, and J. P. Groby, "Experimental demonstrations in audible frequency range of band gap tunability and negative refraction in two-dimensional sonic crystal," *The Journal of the Acoustical Society of America*, vol. 132, no. 4, pp. 2816–2822, 2012.

[86] V. Laude, M. Wilm, S. Benchabane, and A. Khelif, "Full band gap for surface acoustic waves in a piezoelectric phononic crystal," *Physical Review E*, vol. 71, no. 3, p. 036607, 2005.

[87] M. M. Sigalas and E. N. Economou, "Elastic waves in plates with periodically placed inclusions," *Journal of Applied Physics*, vol. 75, no. 6, p. 2845, 1994.

[88] H. Zhu and F. Semperlotti, "Metamaterial based embedded acoustic filters for structural applications," *AIP Advances*, vol. 3, no. 9, p. 092121, 2013.

[89] Y. Z. Wang, F. M. Li, K. Kishimoto, Y. S. Wang, and W. H. Huang, "Band gaps of elastic waves in three-dimensional piezoelectric phononic crystals with initial stress," *European Journal of Mechanics - A/Solids*, vol. 29, no. 2, pp. 182–189, 2010.

[90] T. T. Wu, J. C. Hsu, and J. H. Sun, "Phononic plate waves." *IEEE transactions on ultrasonics, ferroelectrics, and frequency control*, vol. 58, no. 10, pp. 2146–61, 2011.

[91] X. Y. Zou, Q. Chen, and J. C. Cheng, "The band gaps of plate-mode waves in one-dimensional piezoelectric composite plates: polarizations and boundary conditions." *IEEE transactions on ultrasonics, ferroelectrics, and frequency control*, vol. 54, no. 7, pp. 1430–6, 2007.

[92] J. C. Hsu and T. T. Wu, "Calculations of Lamb wave band gaps and dispersions for piezoelectric phononic plates using mindlin's theory-based plane wave expansion

method." *IEEE transactions on ultrasonics, ferroelectrics, and frequency control*, vol. 55, no. 2, pp. 431–41, 2008.

[93] J. Vasseur, P. Deymier, B. Djafari-Rouhani, Y. Pennec, and A. C. Hladky-Hennion, "Absolute forbidden bands and waveguiding in two-dimensional phononic crystal plates," *Physical Review B*, vol. 77, no. 8, p. 085415, 2008.

[94] M. Wilm, A. Khelif, S. Ballandras, V. Laude, and B. Djafari-Rouhani, "Out-of-plane propagation of elastic waves in two-dimensional phononic band-gap materials," *Physical Review E*, vol. 67, no. 6, p. 065602, 2003.

[95] J. G. Hu and W. Xu, "Band structures of phononic crystal composed of lattices with different periodic constants," *Physica B: Condensed Matter*, vol. 441, pp. 89–93, 2014.

[96] Y. Yan, A. Laskar, Z. Cheng, F. Menq, Y. Tang, Y. L. Mo, and Z. Shi, "Seismic isolation of two dimensional periodic foundations," *Journal of Applied Physics*, vol. 116, no. 4, p. 044908, 2014.

[97] K. Ho, C. Chan, and C. Soukoulis, "Existence of a photonic gap in periodic dielectric structures," *Physical Review Letter*, vol. 65, no. 25, pp. 3152–3155, 1990.

[98] A. Jeffery, *Advanced Engineering Mathematics*. Burlington, MA: Harcourt/Acedemic Press, 2002.

[99] R. P. Moiseyenko and V. Laude, "Material loss influence on the complex band structure and group velocity in phononic crystals," *Physical Review B*, vol. 83, no. 6, p. 064301, 2011.

[100] V. Laude, Y. Achaoui, S. Benchabane, and A. Khelif, "Evanescent Bloch waves and the complex band structure of phononic crystals," *Physical Review B*, vol. 80, no. 9, p. 092301, 2009.

[101] V. Laude, J. M. Escalante, and A. Martínez, "Effect of loss on the dispersion relation of photonic and phononic crystals," *Physical Review B*, vol. 88, no. 22, p. 224302, 2013.

[102] V. Romero-Garcia, J. V. Sanchez-Perez, S. Castineira-Ibanez, and L. M. Garcia-Raffi, "Evidences of evanescent Bloch waves in phononic crystals," *Applied Physics Letters*, vol. 96, no. 12, p. 124102, 2010.

[103] A. S. Phani, "On elastic waves and related phenomena in lattice materials and structures," in *AIP Advances*, vol. 1. AIP, 2011, p. 41602.

[104] Y. Song, J. Wen, D. Yu, and X. Wen, "Analysis and enhancement of torsional vibration stopbands in a periodic shaft system," *Journal of Physics D: Applied Physics*, vol. 46, no. 14, p. 145306, 2013.

[105] C. H. Wang and M. W. Brown, "Life Prediction Techniques for Variable Amplitude Multiaxial Fatigue Part 1 : Theories," *Journal of Engineering Materials and Technology*, vol. 118, pp. 367–370, 1996.

[106] Y. Chen, H. Yao, and L. Wang, "Acoustic band gaps of three-dimensional periodic polymer cellular solids with cubic symmetry," *Journal of Applied Physics*, vol. 114, no. 4, 2013.

[107] Y. L. Xu, X. G. Tian, and C. Q. Chen, "Band structures of two dimensional solid/air hierarchical phononic crystals," *Physica B: Condensed Matter*, vol. 407, no. 12, pp. 1995–2001, 2012.

[108] S. Halkjær, O. Sigmund, and J. S. Jensen, "Maximizing band gaps in plate structures," *Structural and Multidisciplinary Optimization*, vol. 32, no. 4, pp. 263–275, 2006.

[109] C. C. Claeys, K. Vergote, P. Sas, and W. Desmet, "On the potential of tuned resonators to obtain low-frequency vibrational stop bands in periodic panels," *Journal of Sound and Vibration*, vol. 332, no. 6, pp. 1418–1436, 2013.

[110] S. Zhang, J. Hui Wu, and Z. Hu, "Low-frequency locally resonant band-gaps in phononic crystal plates with periodic spiral resonators," *Journal of Applied Physics*, vol. 113, no. 16, p. 163511, 2013.

[111] Z.-G. Huang and Z.-Y. Chen, "Acoustic Waves in Two-Dimensional Phononic Crystals With Reticular Geometric Structures," *Journal of Vibration and Acoustics*, vol. 133, no. 3, p. 031011, 2011.

[112] O. Bilal and M. Hussein, "Trampoline metamaterials: Local resonance enhancement by springboards," *Applied Physics Letters*, vol. 103, p. 111901, 2013.

[113] Y.-F. Wang and Y.-S. Wang, "Multiple wide complete bandgaps of two-dimensional phononic crystal slabs with cross-like holes," *Journal of Sound and Vibration*, vol. 332, no. 8, pp. 2019–2037, 2013.

[114] A. Spadoni, M. Ruzzene, and K. Cunefare, "Vibration and Wave Propagation Control of Plates with Periodic Arrays of Shunted Piezoelectric Patches," *Journal of Intelligent Material Systems and Structures*, vol. 20, no. 8, pp. 979–990, 2009.

[115] H. Shen, J. Wen, M. P. Païdoussis, D. Yu, M. Asgari, and X. Wen, "Control of sound and vibration for cylindrical shells by utilizing a periodic structure of

functionally graded material," *Physics Letters A*, vol. 376, no. 45, pp. 3351–3358, 2012.

[116] Y. Xiao, J. Wen, D. Yu, and X. Wen, "Flexural wave propagation in beams with periodically attached vibration absorbers: Band-gap behavior and band formation mechanisms," *Journal of Sound and Vibration*, vol. 332, pp. 867–893, 2013.

[117] O. Richoux, A. Maurel, and V. Pagneux, "Disorder persistent transparency within the bandgap of a periodic array of acoustic Helmholtz resonators," *Journal of Applied Physics*, vol. 117, no. 10, p. 104902, 2015.

[118] G. Wang, S. Chen, and J. Wen, "Low-frequency locally resonant band gaps induced by arrays of resonant shunts with Antonious circuit: experimental investigation on beams," *Smart Materials and Structures*, vol. 20, no. 1, p. 015026, 2011.

[119] S. Fomenko, M. Golub, C. Zhang, T. Bui, and Y. S. Wang, "In-plane elastic wave propagation and band-gaps in layered functionally graded phononic crystals," *International Journal of Solids and Structures*, vol. 51, no. 13, pp. 2491–2503, 2014.

[120] V. Laude, R. P. Moiseyenko, S. Benchabane, and N. F. Declercq, "Bloch wave deafness and modal conversion at a phononic crystal boundary," *AIP Advances*, vol. 1, no. 4, p. 041402, 2011.

[121] J. Lee, "Vibration absorption systems and energy absorption structures. Technical Report March 2015." 2015.

[122] Y. F. Wang, Y. S. Wang, and X. X. Su, "Large bandgaps of two-dimensional phononic crystals with cross-like holes," *Journal of Applied Physics*, vol. 110, no. 11, p. 113520, 2011.

[123] J. W. Wang, G. Wang, S. B. Chen, and J. H. Wen, "Broadband Attenuation in Phononic Beams Induced by Periodic Arrays of Feedback Shunted Piezoelectric Patches," *Chinese Physics Letters*, vol. 29, no. 6, p. 064302, 2012.

[124] Y. Xiao, J. Wen, G. Wang, and X. Wen, "Theoretical and Experimental Study of Locally Resonant and Bragg Band Gaps in Flexural Beams Carrying Periodic Arrays of Beam-Like Resonators," *Journal of Vibration and Acoustics*, vol. 135, no. 4, p. 041006, 2013.

[125] D. Yu, Y. Liu, H. Zhao, G. Wang, and J. Qiu, "Flexural vibration band gaps in Euler-Bernoulli beams with locally resonant structures with two degrees of freedom," *Physical Review B*, vol. 73, no. 6, p. 064301, 2006.

[126] D. Yu, J. Wen, H. Zhao, Y. Liu, and X. Wen, "Vibration reduction by using the idea of phononic crystals in a pipe-conveying fluid," *Journal of Sound and Vibration*, vol. 318, pp. 193–205, 2008.

[127] Y. Xiao, J. Wen, and X. Wen, "Longitudinal wave band gaps in metamaterial-based elastic rods containing multi-degree-of-freedom resonators," *New Journal of Physics*, vol. 14, no. 3, p. 033042, 2012.

[128] C. Liu, S. Hu, and S. Shen, "Effect of Flexoelectricity on Band Structures of One-Dimensional Phononic Crystals," *Journal of Applied Mechanics*, vol. 81, no. 5, p. 051007, 2013.

[129] C. Y. Lee, M. J. Leamy, and J. H. Nadler, "Frequency band structure and absorption predictions for multi-periodic acoustic composites," *Journal of Sound and Vibration*, vol. 329, no. 10, pp. 1809–1822, 2010.

[130] L. Han, Y. Zhang, Z. Q. Ni, Z. M. Zhang, and L. H. Jiang, "A modified transfer matrix method for the study of the bending vibration band structure in phononic crystal Euler beams," *Physica B: Condensed Matter*, vol. 407, no. 23, pp. 4579–4583, 2012.

[131] P. F. Hsieh, T. T. Wu, and J. H. Sun, "Three-dimensional phononic band gap calculations using the FDTD method and a PC cluster system." *IEEE transactions on ultrasonics, ferroelectrics, and frequency control*, vol. 53, no. 1, pp. 148–158, 2006.

[132] Y. Liu, J. Y. Su, Y. L. Xu, and X. C. Zhang, "The influence of pore shapes on the band structures in phononic crystals with periodic distributed void pores." *Ultrasonics*, vol. 49, no. 2, pp. 276–80, 2009.

[133] Y. Tanaka, Y. Tomoyasu, and S. Tamura, "Band structure of acoustic waves in phononic lattices: Two-dimensional composites with large acoustic mismatch," *Physical Review B*, vol. 62, no. 11, pp. 7387–7392, 2000.

[134] Y. Kanno, K. Tsuruta, K. Fujimori, H. Fukano, and S. Nogi, "Phononic-Crystal Acoustic Lens by Design for Energy-Transmission Devices," *Electronics and Communications in Japan*, vol. 97, no. 1, pp. 22–27, 2014.

[135] D. García-Pablos, M. Sigalas, F. Montero de Espinosa, M. Torres, M. Kafesaki, and N. García, "Theory and Experiments on Elastic Band Gaps," *Physical Review Letters*, vol. 84, no. 19, pp. 4349–4352, 2000.

[136] T. Kurose, K. Tsuruta, C. Totsuji, and H. Totsuji, "Negative Refraction of Acoustic Waves in a Two-Dimensional Phononic Crystal via FDTD Simulation," *Materials Transactions*, vol. 50, no. 5, pp. 1004–1007, 2009.

[137] J. Vasseur, P. Deymier, B. Chenni, B. Djafari-Rouhani, L. Dobrzynski, and D. Prevost, "Experimental and Theoretical Evidence for the Existence of Absolute Acoustic Band Gaps in Two-Dimensional Solid Phononic Crystals," *Physical Review Letters*, vol. 86, no. 14, pp. 3012–3015, 2001.

[138] L. Airoldi and M. Ruzzene, "Design of tunable acoustic metamaterials through periodic arrays of resonant shunted piezos," *New Journal of Physics*, vol. 13, no. 11, p. 113010, 2011.

[139] M. Bavencoffe, B. Morvan, A. C. Hladky-Hennion, and J. L. Izbicki, "Experimental and numerical study of evanescent waves in the mini stopband of a 1D phononic crystal." *Ultrasonics*, vol. 53, no. 2, pp. 313–9, 2013.

[140] L. De Marchi, A. Marzani, S. Caporale, and N. Speciale, "Ultrasonic guided-waves characterization with warped frequency transforms," *IEEE Transactions on Ultrasonics, Ferroelectrics, and Frequency Control*, vol. 56, no. 10, pp. 2232–2240, 2009.

[141] Z. Y. Liu, C. T. Chan, P. Sheng, A. L. Goertzen, and J. H. Page, "Elastic wave scattering by periodic structures of spherical objects: Theory and experiment," *Physical Review B*, vol. 62, no. 4, pp. 2446–2457, 2000.

[142] J. D. Achenbach, "Reflection and transmission of an obliquely incident wave by an array of spherical cavities," *The Journal of the Acoustical Society of America*, vol. 80, p. 1209, 1986.

[143] ——, "Harmonic waves in a solid with a periodic distribution of spherical cavities," *The Journal of the Acoustical Society of America*, vol. 81, p. 595, 1987.

[144] Y. Lai, X. Zhang, and Z. Q. Zhang, "Engineering acoustic band gaps," *Applied Physics Letters*, vol. 79, pp. 3224–3226, 2001.

[145] A. Gonis and W. H. Butler, *Multiple Scattering in Solids*. New York: Springer-Verlag, 2000.

[146] A. Bostrom, "Multiple scattering of elastic waves by bounded obstacles," *Journal of the Acoustical Society of America*, vol. 67, no. 2, pp. 399–413, 1980.

[147] J.-Q. Chen, P.-N. Wang, Z.-M. Lu, and X.-B. Wu, *Tables of the Clebsch-Gordan, Racah, and Subduction Coefficients of SU(n) Groups*. Singapore: World Scientific Publishing, 1987.

[148] P. C. Waterman, "Matrix theory of elastic wave scattering," *Journal of the Acoustical Society of America*, vol. 01803, no. 3, pp. 567–580, 1976.

[149] Z. J. Wu, F. M. Li, and C. Z. Zhang, "Vibration band-gap properties of three-dimensional Kagome lattices using the spectral element method," *Journal of Sound and Vibration*, vol. 341, pp. 162–173, 2015.

[150] J. Bin, W. S. Oates, and M. Yousuff Hussaini, "An analysis of a discontinuous spectral element method for elastic wave propagation in a heterogeneous material," *Computational Mechanics*, pp. 789–804, 2015.

[151] S. R. Wen, N. L. Lu, and Z. J. Wu, "Dynamic property analysis of the space-frame structure using the spectral element method," *Waves in Random and Complex Media*, vol. 24, no. 4, pp. 404–420, 2014.

[152] Z. J. Wu, F. M. Li, and Y. Z. Wang, "Vibration band gap properties of periodic Mindlin plate structure using the spectral element method," *Meccanica*, 2013.

[153] U. Lee, J. Kim, and A. Y. T. Leung, "The Spectral Element Method in Structural Dynamics," *The Shock and Vibration Digest*, vol. 32, no. 6, pp. 451–465, 1997.

[154] M. Ruzzene and F. Scarpa, "Directional and band-gap behavior of periodic auxetic lattices," *Physica Status Solidi (B)*, vol. 242, no. 3, pp. 665–680, 2005.

[155] P. Wang, F. Casadei, S. H. Kang, and K. Bertoldi, "Locally resonant band gaps in periodic beam lattices by tuning connectivity," *Physical Review B*, vol. 020103, pp. 2–5, 2015.

[156] C. Yilmaz and G. Hulbert, "Theory of phononic gaps induced by inertial amplification in finite structures," *Physics Letters A*, vol. 374, no. 34, pp. 3576–3584, 2010.

[157] P. Celli and S. Gonella, "Laser-enabled experimental wavefield reconstruction in two-dimensional phononic crystals," *Journal of Sound and Vibration*, vol. 333, no. 1, pp. 114–123, 2014.

[158] M. F. Ashby, A. G. Evans, N. A. Fleck, L. J. Gibson, J. W. Hutchinson, and H. N. G. Wadley, *Metal Foams: A Design Guide*. Butterworth-Heinemann, 2000.

[159] N. Fleck, V. Deshpande, and M. Ashby, "Micro-architectured materials: past, present and future," *Proceedings of the Royal Society A: Mathematical, Physical and Engineering Sciences*, vol. 466, no. 2121, pp. 2495–2516, 2010.

[160] S. Arabnejad and D. Pasini, "Mechanical properties of lattice materials via asymptotic homogenization and comparison with alternative homogenization methods," *International Journal of Mechanical Sciences*, vol. 77, pp. 249–262, 2013.

[161] L. J. Gibson and M. F. Ashby, *Cellular Solids: Structure and Properties*, 2nd ed. Cambridge: Cambridge University Press, 1997.

[162] I. G. Masters and K. E. Evans, "Models for the elastic deformation of honeycombs," *Composite Structures*, vol. 35, no. 1996, pp. 403–422, 1996.

[163] R. Christensen, "Mechanics of cellular and other low-density materials," *International Journal of Solids and Structures*, vol. 37, no. 1-2, pp. 93–104, 2000.

[164] A. J. Wang and D. L. McDowell, "In-Plane Stiffness and Yield Strength of Periodic Metal Honeycombs," *Journal of Engineering Materials and Technology*, vol. 126, no. 2, p. 137, 2004.

[165] C. Chen, T. J. Lu, and N. A. Fleck, "Effect of imperfections on the yielding of two-dimensional foams," *Journal of the Mechanics and Physics of Solids*, vol. 47, pp. 2235–2272, 1999.

[166] R. Hutchinson and N. Fleck, "The structural performance of the periodic truss," *Journal of the Mechanics and Physics of Solids*, vol. 54, no. 4, pp. 756–782, 2006.

[167] M. S. Elsayed and D. Pasini, "Analysis of the elastostatic specific stiffness of 2D stretching-dominated lattice materials," *Mechanics of Materials*, vol. 42, no. 7, pp. 709–725, 2010.

[168] S. Pellegrino and C. Calladine, "Matrix analysis of statically and kinematically indeterminate frameworks," *International Journal of Solids and Structures*, 1986.

[169] R. K. Livesley, *Matrix methods of structural analysis*, ser. Commonwealth and international library: Structures and solid body mechanics division. Pergamon Press, 1964.

[170] N. Triantafyllidis and W. Schnaidt, "Comparison of microscopic and macroscopic instabilities in a class of two-dimensional periodic composites," *Journal of the Mechanics and Physics of Solids*, 1993.

[171] J. Cornwell, *Group Theory in Physics: An Introduction.* San Diego: Academic Press Inc, 1997.

[172] S. Crandall, N. Dahl, and T. Lardner, *An Introduction to the Mechanics of Solids.* New York: McGraw-Hill Book Company, 1978.

[173] R. Cook, D. Malkus, and M. Plesha, *Concepts and appplications of finite element analysis.* New York: John Wiley & Sons, 1989.

[174] A. L. Kalamkarov, I. V. Andrianov, and V. V. Danishevskyy, "Asymptotic Homogenization of Composite Materials and Structures," *Applied Mechanics Reviews*, vol. 62, no. 3, p. 030802, 2009.

[175] B. Hassani and E. Hinton, "A review of homogenization and topology optimization Ihomogenization theory for media with periodic structure," *Computers & Structures*, vol. 69, no. 6, pp. 707–717, 1998.

[176] J. Guedes and N. Kikuchi, "Preprocessing and postprocessing for materials based on the homogenization method with adaptive finite element methods," *Computer Methods in Applied Mechanics and Engineering*, vol. 83, no. 2, pp. 143–198, 1990.

[177] J. Stefan, "Homogenized nonlinear constitutive properties and local stress concentrations for composites with periodic internal structure," *International Journal of Solids and Structures*, vol. 29, no. 17, pp. 2181–2200, 1992.

[178] F. Dos Reis and J. Ganghoffer, "Equivalent mechanical properties of auxetic lattices from discrete homogenization," *Computational Materials Science*, vol. 51, no. 1, pp. 314–321, 2012.

[179] F. D. Reis and J. F. Ganghoffer, "Discrete homogenization of architectured materials : Implementation of the method in a simulation tool for the systematic prediction of their effective elastic properties," *Technische Mechanik*, vol. 30, pp. 85–109, 2010.

[180] F. Pradel and K. Sab, "Cosserat modelling of elastic periodic lattice structures," *Comptes Rendus de l'Academie de Sciences - Serie IIb: Mecanique, Physique, Chimie, Astronomie*, vol. 326, pp. 699–704, 1998.

[181] M. Assidi, F. Dos Reis, and J.-F. Ganghoffer, "Equivalent mechanical properties of biological membranes from lattice homogenization," *Journal of the Mechanical Behavior of Biomedical Materials*, vol. 4, no. 8, pp. 1833–1845, 2011.

[182] C. Florence and K. Sab, "A rigorous homogenization method for the determination of the overall ultimate strength of periodic discrete media and an application to general hexagonal lattices of beams," *European Journal of Mechanics - A/Solids*, vol. 25, no. 1, pp. 72–97, 2006.

[183] T. Ziegler, A. Neubrand, and R. Piat, "Multiscale homogenization models for the elastic behaviour of metal/ceramic composites with lamellar domains," *Composites Science and Technology*, vol. 70, no. 4, pp. 664–670, 2010.

[184] M. Hori and S. Nemat-Nasser, "On two micromechanics theories for determining micro-macro relations in heterogeneous solids," *Mechanics of Materials*, vol. 31, no. 10, pp. 667–682, 1999.

[185] E. Andreassen, "Analysis of Phononic Bandgap Structures With Dissipation," *Journal of Vibration and Acoustics*, vol. 135, p. 041015, 2013.

[186] A. Phani and J. Woodhouse, "Elastic Boundary Layers in Two-Dimensional Isotropic Lattices," *Journal of Applied Mechanics*, vol. 75, p. 021020, 2008.

[187] X. Liu, G. Huang, and G. Hu, "Chiral effect in plane isotropic micropolar elasticity and its application to chiral lattices," *Journal of the Mechanics and Physics of Solids*, vol. 60, no. 11, pp. 1907–1921, 2012.

[188] M. I. Hussein and M. J. Frazier, "Metadamping: An emergent phenomenon in dissipative metamaterials," *Journal of Sound and Vibration*, vol. 332, no. 20, pp. 4767–4774, 2013.

[189] L. Liu and M. I. Hussein, "Wave Motion in Periodic Flexural Beams and Characterization of the Transition Between Bragg Scattering and Local Resonance," *Journal of Applied Mechanics*, vol. 79, p. 011003, 2012.

[190] D. Bigoni, S. Guenneau, a. B. Movchan, and M. Brun, "Elastic metamaterials with inertial locally resonant structures: Application to lensing and localization," *Physical Review B*, vol. 87, no. 17, p. 174303, 2013.

[191] H. Policarpo, M. Neves, and A. Ribeiro, "Dynamical response of a multi-laminated periodic bar: Analytical, numerical and experimental study," *Shock and Vibration*, vol. 17, pp. 521–535, 2010.

[192] E. Kim and J. Yang, "Wave propagation in single column woodpile phononic crystals: Formation of tunable band gaps," *Journal of the Mechanics and Physics of Solids*, vol. 71, pp. 33–45, 2014.

[193] S.-B. Chen, J.-H. Wen, G. Wang, and X.-S. Wen, "Tunable band gaps in acoustic metamaterials with periodic arrays of resonant shunted piezos," *Chinese Physics B*, vol. 22, no. 7, p. 074301, 2013.

[194] H. Policarpo, M. Neves, and N. Maia, "A simple method for the determination of the complex modulus of resilient materials using a longitudinally vibrating three-layer specimen," *Journal of Sound and Vibration*, vol. 332, no. 2, pp. 246–263, 2013.

[195] C. Mei and B. R. Mace, "Wave Reflection and Transmission in Timoshenko Beams and Wave Analysis of Timoshenko Beam Structures," *Journal of Vibration and Acoustics*, vol. 127, no. 4, p. 382, 2005.

[196] M. I. Hussein, "Reduced Bloch mode expansion for periodic media band structure calculations," *Proceedings of the Royal Society A: Mathematical, Physical and Engineering Sciences*, vol. 465, no. 2109, pp. 2825–2848, 2009.

[197] S.-B. Chen, J.-H. Wen, D.-L. Yu, G. Wang, and X.-S. Wen, "Band gap control of phononic beam with negative capacitance piezoelectric shunt," *Chinese Physics B*, vol. 20, no. 1, p. 014301, 2011.

[198] Y. Y. Chen, G. L. Huang, and C. T. Sun, "Band Gap Control in an Active Elastic Metamaterial With Negative Capacitance Piezoelectric Shunting," *Journal of Vibration and Acoustics*, vol. 136, no. 6, p. 061008, 2014.

[199] M. Brun, "Phononic Band Gap Systems in Structural Mechanics: Finite Slender Elastic Structures and Infinite Periodic Waveguides," *Journal of Vibration and Acoustics*, vol. 135, no. 4, p. 041013, 2013.

[200] M. Collet, K. Cunefare, and M. Ichchou, "Wave Motion Optimization in Periodically Distributed Shunted Piezocomposite Beam Structures," *Journal of Intelligent Material Systems and Structures*, vol. 20, no. 7, pp. 787–808, 2008.

[201] J. Humar, *Dynamics of Structures*, 2nd ed. AK Leiden: Taylor and Francis Group Plc, 2002.

[202] C. W. de Silva, *Vibration Damping, Control and Design.* Oxford, United Kingdom: CRC Press, 2007.

[203] Granta Design, "Cambridge Engineering Selector Edupack 2012," 2012.

[204] Y. Zhang, L. Han, and L. H. Jiang, "Transverse vibration bandgaps in phononic-crystal Euler beams on a Winkler foundation studied by a modified transfer matrix method," *Physica Status Solidi (B)*, vol. 250, no. 7, pp. 1439–1444, 2013.

[205] D. Yu, J. Fang, L. Cai, X. Han, and J. Wen, "Triply coupled vibrational band gap in a periodic and nonsymmetrical axially loaded thin-walled BernoulliEuler beam including the warping effect," *Physics Letters A*, vol. 373, no. 38, pp. 3464–3469, 2009.

[206] M. I. Hussein, G. M. Hulbert, and R. A. Scott, "Dispersive elastodynamics of 1D banded materials and structures: analysis," *Journal of Sound and Vibration*, vol. 307, no. 3-5, pp. 0–60, 2007.

[207] J. Wang, G. Wang, J. Wen, and X. Wen, "Flexural vibration band gaps in periodic stiffened plate structures," *Mechanika*, vol. 18, no. 2, pp. 186–191, 2012.

[208] C. A. Steeves, C. Mercer, E. Antinucci, M. Y. He, and A. G. Evans, "Experimental investigation of the thermal properties of tailored expansion lattices," *International Journal of Mechanics and Materials in Design*, vol. 5, no. 2, pp. 195–202, 2009.

[209] C. A. Steeves, S. L. dos Santos e Lucato, M. He, E. Antinucci, J. W. Hutchinson, and A. G. Evans, "Concepts for structurally robust materials that combine low thermal expansion with high stiffness," *Journal of the Mechanics and Physics of Solids*, vol. 55, no. 9, pp. 1803–1822, 2007.

[210] J. Berger, C. Mercer, R. M. McMeeking, and A. G. Evans, "The Design of Bonded Bimaterial Lattices that Combine Low Thermal Expansion with High Stiffness," *Journal of the American Ceramic Society*, vol. 94, pp. S42–S54, 2011.

[211] D. C. Lagoudas, J. J. Mayes, and M. M. Khan, "Simplified Shape Memory Alloy (SMA) Material Model for Vibration Isolation," *Smart Structures and Materials*, pp. 452–461, 2001.

[212] M. F. Ashby, "The properties of foams and lattices." *Philosophical transactions. Series A, Mathematical, physical, and engineering sciences*, vol. 364, no. 1838, pp. 15–30, 2006.

[213] ——, *Materials Selection in Mechanical Design*, 3rd ed. Burlington, MA: Butterworth-Heinemann, 2005.

[214] S. Shaffer, K. Yang, J. Vargas, M. A. Di Prima, and W. Voit, "On reducing anisotropy in 3D printed polymers via ionizing radiation," *Polymer (United Kingdom)*, vol. 55, no. 23, pp. 5969–5979, 2014.

[215] A. Bellini and S. Guceri, "Mechanical characterization of parts fabricated using fused deposition modeling," *Rapid Prototyping Journal*, vol. 9, no. 4, pp. 252–264, 2003.

[216] H. Wadley, "Cellular Metals Manufacturing," *Advanced Engineering Materials*, vol. 4, no. 10, pp. 726–733, 2002.

[217] 3D Systems Corporation, "Accura 55 plastic broucher," 2007.

[218] A. Vigliotti and D. Pasini, "Mechanical properties of hierarchical lattices," *Mechanics of Materials*, vol. 62, pp. 32–43, 2013.

[219] B. K. Lee and K. J. Kang, "A parametric study on compressive characteristics of Wire-woven bulk Kagome truss cores," *Composite Structures*, vol. 92, pp. 445–453, 2010.

[220] M. Petyt, *Introduction to Finite Element Vibration Analysis.* Cambridge University Press, 1998.

[221] B. Tian, B. Tie, D. Aubry, and X. Su, "Elastic Wave Propagation in Periodic Cellular Structures," *Computer Modeling in Science and Engineering*, vol. 76, no. 4, pp. 217–233, 2011.

[222] I. Raza, L. Iannucci, and P. Curtis, "Additive Manufacturing of Locally Resonant Acoustic Metamaterials," in *Third International Conference on Phononic Crystals/Metamaterials, Phonon Transport and Phonon Coupling*, Paris, France, 2015.

# A Appendices

## A.1 Solution for two waves with one degree of freedom

The solutions to determine the band structure for a periodic structure with two waves when only one degree of freedom is measured are listed in this appendix. The two final equations prior to eliminating one of the $\lambda$ are as follows.

$$\begin{aligned}
&[W_3\lambda_A^2-(W_2+W_4)\lambda_A+W_3]\lambda_A\lambda_B^4+\\
&\quad[W_3\lambda_A^4-(2W_2+W_4)\lambda_A^3+(W_1+3W_3)\lambda_A^2-(2W_2+W_4)\lambda_A+W_3]\lambda_B^3+\\
&[-(W_2+W_4)\lambda_A^4+(W_1+3W_3)\lambda_A^3-(3W_2+2W_4-W_6)\lambda_A^2+(W_1+3W_3)\lambda_A-(W_2+W_4)]\lambda_B^2\\
&\quad[W_3\lambda_A^4-(2W_2+W_4)\lambda_A^3+(W_1+3W_3)\lambda_A^2-(2W_2+W_4)\lambda_A+W_3]\lambda_B+\\
&\qquad[W_3\lambda_A^2-(W_2+W_4)\lambda_A+W_3]\lambda_A=0 \qquad \text{(A.1)}
\end{aligned}$$

$$\begin{aligned}
&[W_3\lambda_A^2-(W_2+W_4)\lambda_A+W_3]\lambda_B^2+\\
&\quad[-(W_2+W_4)\lambda_A^2+(W_1+2W_3+W_5)\lambda_A+-(W_2+W_4)]\lambda_B\\
&\qquad[W_3\lambda_A^2-(W_2+W_4)\lambda_A+W_3]\lambda_A=0 \qquad \text{(A.2)}
\end{aligned}$$

By solving Eq. (A.1) and Eq. (A.2), the values of $\lambda$ needed to find the band structure was calculated using Maple and described by Eqs. (A.3) and (A.4).

$$\lambda_{1,2}=\frac{1}{4b_1}(b_2\pm\sqrt{b_3})+\frac{1}{4b_1}\sqrt{2(b_4\pm b_2\sqrt{b_3}+b_5)} \qquad \text{(A.3)}$$

$$\lambda_{3,4}=\frac{1}{4b_1}(b_2\pm\sqrt{b_3})-\frac{1}{4b_1}\sqrt{2(b_4\pm b_2\sqrt{b_3}+b_5)} \qquad \text{(A.4)}$$

where the unknowns, $b_1$, $b_2$, $b_3$, $b_4$ and $b_5$ are given in Eqs. (A.5) to (A.9).

$$b_1=W_2W_4-W_3^2-W_3W_5+W_4^2 \qquad \text{(A.5)}$$

$$b_2=W_1W_4-W_2W_3-W_3W_6+W_4W_5 \qquad \text{(A.6)}$$

$$
\begin{aligned}
b_3 = \\
& W_1^2W_4^2 - 6W_1W_2W_3W_4 - 4W_1W_2W_4W_5 + 4W_1W_3^3 + 8W_1W_3^2W_5 \\
& - 4W_1W_3W_4^2 - 2W_1W_3W_4W_6 + 4W_1W_3W_5^2 - 2W_1W_4^2W_5 + 4W_2^3W_4 \\
& - 3W_2^2W_3^2 - 4W_2^2W_3W_5 + 16W_2^2W_4^2 + 4W_2^2W_4W_6 - 20W_2W_3^2W_4 \\
& - 2W_2W_3^2W_6 - 26W_2W_3W_4W_5 - 4W_2W_3W_5W_6 + 20W_2W_4^3 \\
& + 8W_2W_4^2W_6 - 4W_2W_4W_5^2 + 8W_3^4 + 20W_3^3W_5 - 16W_3^2W_4^2 \\
& - 4W_3^2W_4W_6 + 16W_3^2W_5^2 + W_3^2W_6^2 - 20W_3W_4^2W_5 \\
& - 6W_3W_4W_5W_6 + 4W_3W_5^3 + 8W_4^4 + 4W_4^3W_6 - 3W_4^2W_5^2
\end{aligned} \tag{A.7}
$$

$$
\begin{aligned}
b_4 = \\
& 2W_1W_3^3 + 2W_2^3W_4 - 6W_2W_4^3 - 6W_3^3W_5 - 4W_3^4 - 4W_4^4 - 2W_1W_3W_4W_6 \\
& - 4W_3W_4W_5W_6 - 2W_1W_2W_4W_5 - 2W_2W_3W_5W_6
\end{aligned} \tag{A.8}
$$

$$
\begin{aligned}
b_5 = \\
& W_1^2W_4^2 + W_3^2W_6^2 - W_4^2W_5^2 + 2W_3W_5^3 + 2W_4^3W_6 - 2W_2^2W_3W_5 \\
& - 2W_1W_3W_4^2 + 4W_1W_3^2W_5 + 6W_3W_4^2W_5 + 6W_4W_3^2W_2 + 8W_4^2W_3^2 \\
& - W_3^2W_2^2 + 2W_1W_3W_5^2 + 2W_2^2W_4W_6 + 4W_2W_4^2W_6 \\
& - 2W_2W_4W_5^2 - 2W_3^2W_4W_6 - 4W_1W_2W_3W_4 + 2W_2W_3W_4W_5
\end{aligned} \tag{A.9}
$$

## A.2 Example of eigenvector component calculations using force measurements

The general equation to calculate the components of the eigenvectors are given in Section 3.2.5. In this appendix, an example of calculating the eigenvectors using two different boundary conditions will be briefly described.

In this example, the two boundary conditions used to calculate the eigenvector components are the free-free and free-fixed conditions described in Section 3.3. The main reason that these conditions were selected is that the measurements of forces for these two configurations can be set up in practice and these conditions were used to find the results in Section 3.4.3 of this work. As described in Section 3.2.5, the force measure-

ments at both ends of the beam can be substituted into Eq. (3.48) in Section 3.2.5 to give the following equations.

$$F_0^{\text{Free}} = v_{F,A}^{\text{Forward}} W_{FA0}^{\text{Free}} + v_{F,B}^{\text{Forward}} W_{FB0}^{\text{Free}} + v_{F,A}^{\text{Reverse}} W_{RA0}^{\text{Free}} + v_{F,B}^{\text{Reverse}} W_{RB0}^{\text{Free}} \tag{A.10}$$

$$\begin{aligned} 0 = \lambda_A^N v_{F,A}^{\text{Forward}} W_{FA0}^{\text{Free}} + \lambda_B^N v_{F,B}^{\text{Forward}} W_{FB0}^{\text{Free}} + \\ \lambda_A^{-N} v_{F,A}^{\text{Reverse}} W_{RA0}^{\text{Free}} + \lambda_B^{-N} v_{F,B}^{\text{Reverse}} W_{RB0}^{\text{Free}} \end{aligned} \tag{A.11}$$

$$F_0^{\text{Fixed}} = v_{F,A}^{\text{Forward}} W_{FA0}^{\text{Fixed}} + v_{F,B}^{\text{Forward}} W_{FB0}^{\text{Fixed}} + v_{F,A}^{\text{Reverse}} W_{RA0}^{\text{Fixed}} + v_{F,B}^{\text{Reverse}} W_{RB0}^{\text{Fixed}} \tag{A.12}$$

$$\begin{aligned} F_N^{\text{Fixed}} = \lambda_A^N v_{F,A}^{\text{Forward}} W_{FA0}^{\text{Fixed}} + \lambda_B^N v_{F,B}^{\text{Forward}} W_{FB0}^{\text{Fixed}} + \\ \lambda_A^{-N} v_{F,A}^{\text{Reverse}} W_{RA0}^{\text{Fixed}} + \lambda_B^{-N} v_{F,B}^{\text{Reverse}} W_{RB0}^{\text{Fixed}} \end{aligned} \tag{A.13}$$

The superscripts "Free" and "Fixed" in Eqs. (A.10) to (A.13) denote the free-free and free-fixed boundary conditions respectively. The wave functions, $W_{FA}$, $W_{FB}$ , $W_{RA}$ and $W_{RB}$ are dependent on boundary conditions. However, the wave functions can be determined from the displacement measurements and Eq. (3.47). Additionally, the forces at both ends at the left hand side of Eqs. (A.10) to (A.13) are also measured. Therefore, the only unknowns in Eqs. (A.10) to (A.13) are the eigenvector components. Since, the eigenvector components in Eqs. (A.10) to (A.13) are linear, these four equations can be solved using linear algebra. The same procedure can be used to find the eigenvector components relating the other physical quantities, $\phi$ and $M$, by using the measurements for these physical quantities instead.

## A.3 Publications

This appendix is a list of publications relating to the work done in the thesis.

### Journal papers

Junyi L, Balint DS. A wave superposition method to determine the band structure of phononic crystals and acoustic metamaterials. *Journal of Sound and Vibration.* 2015; 350: 41-72.

Junyi L, Balint DS, Ruffini V. Measuring the band structures of periodic beams using the wave superposition method. *International Journal of Solids and Structures*. Submitted for publication (Minor revision).

Junyi L, Balint DS. A parametric study of the mechanical and dispersion properties of cubic lattice structures. *International Journal of Solids and Structures*. Submitted for publication (Minor revision).

Junyi L, Balint DS. Optimal shunt parameters for maximising wave attenuation with periodic piezoelectric patches. *Journal of Intelligent Material Systems and Structures*. Submitted for publication (Major revision).

**Conferences**

Junyi L, Balint DS, Ruffini V. Determining Band Structures from a Small Number of Frequency Response Measurements. *Phononics 2015: Third International Conference on Phononic Crystals/Metamaterials, Phonon Transport and Phonon Coupling*, 31 May – 5 June 2015, Paris, France.